Maximilian Häberle

A new kinematic view of the globular cluster ω Centauri

A study in three velocity dimensions based on observations
with the Hubble Space Telescope, the VLT MUSE instrument,
and the newly constructed SDSS-V Local Volume Mapper

Dissertation

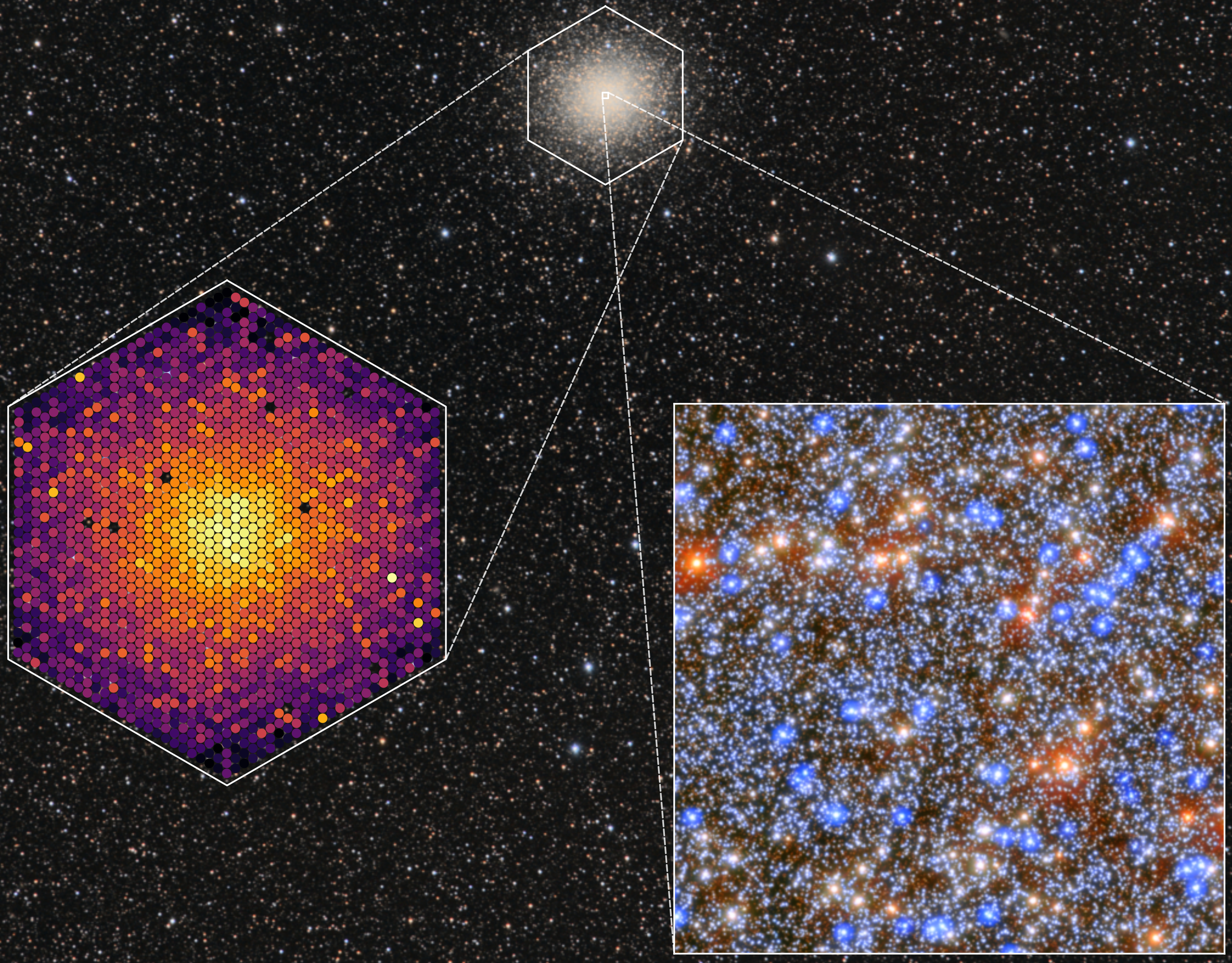

Dissertation
submitted to the
Combined Faculty of Mathematics, Engineering and Natural Sciences
of Heidelberg University, Germany
for the degree of
Doctor of Natural Sciences

Put forward by
MAXIMILIAN HÄBERLE
born in: Heidelberg, Germany
Oral examination: 24.04.2025

The cover shows a wide field ($\sim$4.8° × 7.2°) image of ω Cen and its surroundings, taken with a 300 mm telephoto lens during the LVM telescope commissioning campaign at Las Campanas Observatory in 2023. The hexagonal inset shows the flux distribution in a single LVM pointing. The square inset shows a 1×1 arcminute wide crop of the stacked image created using the Hubble Space Telescope observations of ω Cen used in this thesis.

The back cover shows the full HST image spanning 9.16×9.16 arcminutes.
Image Credit: ESA/Hubble & NASA, M. Häberle (MPIA)

A new kinematic view of the globular cluster ω Centauri

A study in three velocity dimensions based on observations with the Hubble Space Telescope,
the VLT MUSE instrument, and the newly constructed SDSS-V Local Volume Mapper

Referees:	Dr. Nadine Neumayer
	Prof. Dr. Michela Mapelli

ABSTRACT

Omega Centauri (ω Cen) is the most massive globular cluster of the Milky Way. Due to its complex stellar populations, it is believed to be the stripped nucleus of an accreted dwarf galaxy, making it not only an important witness of the Milky Way's merger history but also the closest galactic nucleus to us on Earth. Many of its properties are still under active investigation, including the origin and kinematics of its multiple stellar populations, the mass distribution in its center, and the potential connection with the debris of its former host galaxy. As a stripped nucleus, ω Cen has also been a candidate for hosting an intermediate-mass black hole, but previous searches have remained inconclusive.

In this thesis, I present a novel, comprehensive astrometric and photometric catalog based on 20 years of archival and new Hubble Space Telescope observations. The underlying dataset contains over 800 individual images and allows for the measurement of precise proper motions for around 1.4 million stars within the half-light radius (r_{HL} =5') of ω Cen.

Within the new dataset, I discovered 7 fast-moving stars within a radius of just 3 arcseconds (0.1pc) around the cluster center. These stars move faster than the expected local escape velocity, and their presence can be best explained by being bound to a black hole with a mass of at least 8200 solar masses. These results make a strong case for ω Cen hosting an intermediate-mass black hole, a long-sought missing link between stellar mass and supermassive black holes.

To study the overall kinematics of ω Cen, I combined the astrometric dataset with a recent spectroscopic catalog, allowing the determination of the full 3-dimensional velocity vector for thousands of stars. This analysis provides improved measurements of the velocity dispersion profile, the rotation curve, and the state of energy equipartition of ω Cen. By combining proper motions with line-of-sight velocities, I calculated an improved kinematic distance estimate of (5445 ± 41) pc, the most precise distance to ω Cen available.

In the final scientific chapter, I present preparatory efforts for the guiding system of the new SDSS-V Local Volume Mapper (LVM). This novel wide-field integral field spectrograph celebrated its first light in 2023. While the primary goal of this instrument is to map interstellar gas within the Milky Way and the Magellanic Clouds, it can also study the integrated light of star clusters such as ω Cen, benchmarking unresolved extragalactic studies. I present preliminary results of the overall line-of-sight kinematics measured with the LVM, which agree with our resolved results.

The results of this thesis are an important step towards a better understanding of the formation history of ω Cen and low mass galactic nuclei in general. The large astro-photometric catalog is already being used for detailed studies of the age-metallicity relation, the abundances, and the subpopulations of ω Cen. The precise kinematic measurements will be followed-up with detailed dynamical models. Finally, the detection of fast-moving stars marks a breakthrough in the search for local intermediate-mass black holes in star clusters and can serve as a blueprint for future searches in other clusters, although new instrumentation such as ELT MICADO will be required.

Zusammenfassung

Omega Centauri (ω Cen) ist der massereichste Kugelsternhaufen in der Milchstraße. Aufgrund seiner komplexen Sternpopulationen wird vermutet, dass er der Kern einer Zwerggalaxie ist, deren Außenbereiche durch die Verschmelzung mit der Milchstraße abgestreift wurden. Dies macht ihn nicht nur zu einem wichtigen Zeugen der Entstehungsgeschichte der Milchstraße, sondern auch zu einem einzigartigen Beispiel für einen massearmen Galaxienkern.

Viele seiner Eigenschaften sind Gegenstand der aktuellen Forschung, darunter der Ursprung und die Kinematik seiner vielfältigen Sternpulationen, die Massenverteilung in seinem Zentrum und die mögliche Verbindung mit den Überresten seiner ehemaligen Galaxie. Ein mögliches mittelschweres Schwarzes Loch im Zentrum von ω Cen wird seit Längerem kontrovers diskutiert.

In dieser Arbeit stelle ich einen umfassenden neuen astrometrischen und photometrischen Katalog vor, der auf 20 Jahren archivierter und neuer Beobachtungen mit dem Hubble-Weltraumteleskop basiert. Der zugrundeliegende Datensatz enthält über 800 Einzelbilder und ermöglicht die Messung präziser Eigenbewegungen für etwa 1,4 Millionen Sterne innerhalb des Halblichtradius von ω Cen.

In dem neuen Datensatz habe ich 7 sich schnell bewegende Sterne in einem Radius von nur 3 Bogensekunden (0,1 pc) um das Zentrum des Haufens entdeckt. Diese Sterne bewegen sich schneller als die erwartete lokale Fluchtgeschwindigkeit, und die wahrscheinlichste Erklärung für ihr Vorkommen ist, dass sie an ein Schwarzes Loch mit einer Masse von mindestens 8200 Sonnenmassen gebunden sind. Diese Ergebnisse sprechen dafür, dass ω Cen ein sogenanntes mittelschweres Schwarzes Loch beherbergt, ein lange gesuchtes fehlendes Bindeglied zwischen stellaren und supermassereichen Schwarzen Löchern.

Um die Gesamtkinematik von ω Cen zu untersuchen, habe ich den astrometrischen Datensatz mit einem aktuellen spektroskopischen Katalog kombiniert, was die Bestimmung des vollständigen 3-dimensionalen Geschwindigkeitsvektors für Tausende von Sternen ermöglicht. Diese Analyse liefert verbesserte Messungen des Geschwindigkeitsdispersionsprofils, der Rotationskurve und des Zustands der Energieäquipartition von ω Cen. Durch den Vergleich von Eigenbewegungen mit Sichtliniengeschwindigkeiten habe ich eine verbesserte kinematische Entfernungsschätzung von 5445 ± 41 pc berechnet. Dies ist die bisher genaueste Abschätzung für die Enfernung von ω Cen.

In einem letzten Abschnitt stelle ich die Vorbereitungen für das Nachführungssystem des neuen SDSS-V Local Volume Mappers (LVM) vor. Dieser neue Weitwinkel Integralfeld-Spektrograph wurde im Jahr 2023 in Betrieb genommen. Während das primäre Ziel dieses Instruments die Kartierung von interstellarem Gas in der Milchstraße und den Magellanschen Wolken ist, kann es auch dazu verwendet werden, das integrierte Licht von Sternhaufen wie Omega Centauri zu untersuchen, um ein Benchmarking für unaufgelöste extragalaktische Studien durchzuführen. Ich präsentiere vorläufige Ergebnisse für LVM Messungen der Kinematik von ω Cen, die mit unseren aufgelösten Ergebnissen übereinstimmen.

Die Ergebnisse dieser Arbeit sind ein wichtiger Schritt zu einem besseren Verständnis der Entstehungsgeschichte von ω Cen und anderen massearmen Galaxiekernen. Der astrophotometrische Katalog wird bereits für detaillierte Studien der Alters-Metallizitäts-Beziehung, der Elementhäufigkeiten und der Sternpopulationen von ω Cen verwendet. Die präzisen kinematischen Messungen werden mit detaillierten dynamischen Modellen weiterverfolgt. Die Entdeckung der schnellen Sterne im Zentrum von ω Cen markiert einen Durchbruch bei der Suche nach mittelschweren Schwarzen Löchern in Sternhaufen und kann als Vorlage für die künftige Suche in anderen Sternhaufen dienen, auch wenn dafür neue Instrumente wie ELT MICADO erforderlich sein werden.

Acknowledgments

The submission of this thesis marks the end of an exciting four-and-a-half-year-long journey that would not have been possible without the help of many great people.

First of all, I want to thank my supervisor, Nadine Neumayer, whose scientific vision started this exciting project. Your patient support during the first three years of data reduction, your calm and supportive mentoring style, and your great advice on all aspects of scientific life have brought me where I am today and I am looking forward to our future projects.

Next, I want to thank Anil Seth for his scientific guidance, enthusiasm, countless revisions of papers and proposals, and hospitality in Salt Lake City. I also want to thank the rest of the oMEGACat collaboration for many encouraging discussions and helpful suggestions during all phases of the project.

The creation of the oMEGACat II catalog would not have been possible without Andrea Bellini and Mattia Libralato teaching me everything about high-precision astrometry with the Hubble Space Telescope and without Selina Nitschai and Callie Clontz, who were the early adopters of the catalog and helped to substantially improve it.

I also want to thank Tom Herbst and the MPIA LVM team for the unique experience we shared during the construction of the LVM telescopes. Going from the drawing board, over experiments in a tent on foggy Königstuhl, to an intense and successful commissioning campaign at the observatory in just under 3 years was quite a ride and I learned so much about building a new instrument. The resulting LVM data is beautiful.

The Thesis and PhD Advisory committees are important institutions, and I want to thank Jörg-Uwe Pott, Rainer Spurzem, and all volunteer PAC members for their time and advice, which gave me general orientation and helped keeping the thesis on track. I also want to thank Michela Mapelli for her interest in my work and her willingness to be the second examiner for the thesis, and Hans-Walter Rix and Werner Aeschbach for forming my examination committee.

In addition to the exciting scientific work, the last years would not have been half as fun without the other students at MPIA. I want to thank Eric, Nico, Evert, Verena, Selina, Liang, Callie, Richard, and Nils for all the great moments we had in the office, on the bike, or during our nice retreats. We are already dispersing, but I hope to stay in touch with you. A special thanks goes to Eric, Callie and Peter who read chapters of this thesis and helped to make it more comprehensive and understandable.

Throughout all this time, I could count on the support of my friend Jan and my family: my parents, Eva and Tilmann, and my sisters, Theresa and Elisabeth, who were always there in times of need.

Finally, I want to thank my wife, Frida, who is my rock and my safe haven. Our daughter Isabella was born right in the middle of the PhD, and the two of you are the most important people in my life. Without your support nothing of this would have been possible. At the same time, I am very proud of what you have achieved in the last years, and I am even more excited about what you can do in the future. ¡Te amo!

CONTENTS

I. INTRODUCTION

MOTIVATION

We live in an exciting era of new discoveries in astronomy and astrophysics. In recent years, enormous progress has been made in many different fields both in the local and the distant Universe. Much of that progress has been driven by the development of new astronomical instrumentation and techniques. One specific subfield where the influence of advances in technology has been especially apparent is the study of black holes (Genzel et al., 2024): In about one hundred years, we went from the first theoretical descriptions (Schwarzschild, 1916) to the first observational clues in the form of X-Ray binaries and luminous quasars (e.g. Webster & Murdin, 1972; Bolton, 1972; Schmidt, 1963; Rees, 1984), to a detailed and diverse picture spanning many orders of magnitude in mass.

At the low mass end, recent highlights include the detection of numerous black hole binary mergers via their gravitational wave emission (see e.g. Abbott et al., 2016, 2023), but also the detection of black holes in stellar binary systems, thanks to the Gaia satellite (El-Badry et al., 2023a,b; Gaia Collaboration et al., 2024). At higher masses, the central black hole in the Milky Way has been probed with detailed interferometric observations of stellar orbits in the near-infrared (GRAVITY Collaboration et al., 2018, 2020a), and long-baseline interferometry at millimeter wavelengths has allowed to image the region close to the event horizon for both Sgr A* (Event Horizon Telescope Collaboration et al., 2022a), but also the thousand times more massive and more distant central black hole of M87 (Event Horizon Telescope Collaboration et al., 2019). At even larger distances, the James Webb Space Telescope is detecting massive black holes in very early states of their evolution (Maiolino et al., 2024).

All these spectacular results and detections lead to further questions: Where is the location of the binary black hole mergers? How did the first supermassive black holes form? How could they accrete such large masses in relatively short periods of time? Is there are population of intermediate mass black holes bridging the gap between observed stellar mass and supermassive black holes? Answering these questions is also important for our understanding of galaxy formation in general, as is demonstrated by the tight correlations between galaxy properties with the mass of their central black holes.

Much effort is invested in high-redshift observations, but another pathway is to look at cosmic fossils in the local Universe. Massive star clusters, such as globular clusters, but also nuclear star clusters in the centers of galaxies, belong to the oldest surviving structures that we can observe. Their stellar populations encode their formation history, and their internal kinematics can reveal information about their unseen content.

The main focus of this thesis is Omega Centauri (ω Cen), the most massive globular cluster of the Milky Way. ω Cen is believed to be the stripped nucleus of a dwarf galaxy that has been accreted by the Milky Way and, as such, provides both an important witness of the early history of our Galaxy and also a unique laboratory to study the closest known galaxy nucleus.

OUTLINE

In Chapter 1 of this thesis, I provide a brief overview of the different types of astrophysical black holes and the corresponding observational evidence. I then introduce different formation scenarios for supermassive black holes in the early Universe and describe how observations of intermediate-mass black holes in the local Universe can help to constrain them. Chapter 2 focuses on massive star clusters, one promising location for the search for intermediate-mass black holes. I then introduce ω Cen, the most massive globular cluster of the Milky Way, and the main object of study of this thesis.

After the introduction, I present the main scientific results in 4 individual chapters, each of which is based on a publication written during my PhD. Chapter 3 describes the creation of a new proper motion and photometric catalog for ω Cen with high precision measurements for around 1.4 million individual stars. Chapter 4 describes the discovery of several fast-moving stars in the very center ω Cen. We use these stars to place a lower limit on the presence of an intermediate-mass black hole in the cluster center. Chapter 5 describes an analysis of the overall kinematic properties of ω Cen based on a combination of the new proper motion catalog with line-of-sight velocities. We measure the velocity dispersion and its anisotropy, the kinematic distance, and the state of energy equipartition with unreached resolution and precision.
The last scientific chapter (Chapter 6) leaves the field of black holes and star clusters and describes efforts undertaken in preparation for the SDSS-V Local Volume Mapper instrument.

A concluding summary of the main scientific results of this thesis is given in Chapter 7.

In Chapter 8 I give an overview of other ongoing studies based on the oMEGACat data. This is followed by a brief outlook on how the SDSS-V Local Volume Mapper instrument can be used to observe the kinematics of the outskirts of globular clusters. Finally, I sketch possible pathways for further constraints on the intermediate-mass black hole in ω Cen, but also the overall IMBH population in globular clusters using current and future instrumentation.

ABBREVIATIONS

ACS	Advanced Camera for Surveys
ADU	Analog-digital-converter units
AGN	Active galactic nucleus
A&G	Acquisition and guiding
ALMA	Atacama Large Millimeter/submillimeter Array
AO	Adaptive optics
BH	Black hole
BPT	Baldwin, Phillips & Terlevic
CCD	Charge-coupled device
CMOS	Complementary metal-oxide semiconductor
ESO	European Southern Observatory
FoV	Field of view
FWHM	Full width at half maximum
Gyr	Giga (10^9) years
HST	Hubble Space Telescope
HRC	High Resolution Channel
IFU	Integral field unit
IMBH	Intermediate-mass black hole
IMF	Initial mass function
JWST	James Webb Space Telescope
LOS	Line-of-sight
LVM	Local Volume Mapper
mas	Milliarcsecond
MCMC	Markov chain Monte Carlo
MUSE	Multi Unit Spectroscopic Explorer
Myr	Mega (10^6) years
NFM	Narrow Field Mode
NGC	New General Catalogue
NIR	Near-Infrared
PA	Position angle
P-V	Peak-to-Valley
PSF	Point-spread function
RMS	Root mean square
SMBH	Supermassive black hole
S/N	Signal to noise ratio
SDSS	Sloan Digital Sky Survey
SED	Spectral energy distribution
UV	Ultraviolet
UT	Unit Telescope
VLT	Very Large Telescope
VLTI	Very Large Telescope Interferometer
WFC3	Wide Field Camera 3
WFM	Wide Field Mode

1 Black holes across the mass spectrum

Black holes are some of the most extreme astrophysical objects in the Universe. Their densities are so high that there is a certain radius from within not even light can escape their gravitational influence. The extent of this "Event Horizon" is the Schwarzschild radius (r_{S}) and can be calculated using:

$$r_{\mathrm{S}} = \frac{2GM_{\mathrm{BH}}}{c^2} \tag{1.1}$$

where G, M_{BH}, and c are the gravitational constant, the mass of the black hole, and the speed of light. Early ideas of "dark stars" that are heavy enough to even attract light date back to the 18th century (Michell, 1784), but it took until Einstein's formulation of General Relativity (Einstein, 1916) to have a mathematical framework capable of describing what later would be called "Black Hole". Shortly after, Karl Schwarzschild formulated the solution of the Einstein field equations for a homogeneous non-spinning sphere (Schwarzschild, 1916). The solution was expanded to rotating black holes (Kerr, 1963) and to black holes holding an electrical charge (Newman et al., 1965).

As no light and, therefore, no information can return from beyond the event horizon, most empirical evidence for black holes in the Universe comes from observations of matter surrounding the black hole. These observations are typically either searching for signs of accretion of gas onto a black hole or probing for the dynamic influence of the black hole on the gas and stars surrounding it. With the recent advancements of laser interferometer gravitational wave detectors, observations of gravitational waves are now able to provide complementary information on the properties of merging binary black holes.

In the following chapter, I discuss observational evidence for the two known main classes of observed astrophysical black holes: stellar mass black holes and supermassive black holes. I then introduce intermediate-mass black holes and their theorized formation channels, which could bridge the gap between the two separate mass regimes.

1.1 Stellar mass black holes

1.1.1 Formation and demographics

Stellar-mass black holes are believed to be the remnants of massive ($M \gtrsim 8\,\mathrm{M}_{\odot}$) stars that have exhausted their nuclear fuel (see Mapelli, 2021, for a textbook introduction). Due to the resulting lack of energy production, the core of the star begins to contract until it is stabilized by electron degeneracy pressure. If the core mass exceeds the Chandrasekhar limit ($M \sim 1.4\,\mathrm{M}_{\odot}$) gravity overpowers the degeneracy pressure and the core implodes on very rapid timescales, leading to core-collapse. The collapse is only halted when nuclear like densities are reached. The energy production by subsequent nuclear reactions leads to a rebound shock, which disrupts the outer stellar layers and leads to an observable supernova explosion. Depending on the mass of the progenitor and the core-collapse mechanism, a compact remnant is left behind that is either a neutron star or a stellar-mass black hole (e.g. Fryer et al., 2012).

At even higher stellar masses (main sequence masses of $\sim 70 - 260\,\mathrm{M}_\odot$, Helium core masses $> 30\,\mathrm{M}_\odot$), the process of electron-positron pair production leads to an unstable stellar core (Fowler & Hoyle, 1964) which rapidly implodes. At the highest core masses ($\mathrm{M}_{\mathrm{core}} > 133\,\mathrm{M}_\odot$), the core can directly collapse to a stellar-mass black hole. For core masses above $> 64\,\mathrm{M}_\odot$, the subsequent nuclear reaction leads to a single violent pulse that disrupts the star in a so called "pair-instability supernova", that produces no compact remnant. At lower masses ($30\,\mathrm{M}_\odot < \mathrm{M}_{\mathrm{core}} < 64\,\mathrm{M}_\odot$), the energy produced by the collapsing core is not enough to disrupt the star, which can lead to a series of pulsations which lead to additional mass loss and can have a diverse set of durations and transient observable phenomena (Spera & Mapelli, 2017; Woosley, 2017).

Besides the diversity of supernova mechanisms, the resulting mass distribution of stellar-mass black holes is also influenced by metallicity-dependent stellar evolution, such as significant mass-loss due to stellar winds (e.g. Fryer & Kalogera, 2001; Belczynski et al., 2010; Mapelli, 2021).

The inference of black hole distributions by observations is further complicated by the fact that almost all detected stellar-mass black holes are in binary systems (see below). However, these binary systems likely only make up a tiny fraction of the $10^8 - 10^9$ stellar mass black holes expected within the Galaxy (e.g. Brown & Bethe, 1994; Olejak et al., 2020). Understanding the formation channels of these binaries, their evolution, and their interaction with their surroundings is important to be able to constrain the formation mechanisms of stellar mass black holes (Mapelli et al., 2022).

1.1.2 DETECTIONS

1.1.2.1 X-RAY BINARIES

The first observational evidence for stellar-mass black holes came in the discovery of the strong X-ray source Cygnus X-1 (Giacconi et al., 1962). The identification of a stellar companion (Webster & Murdin, 1972; Bolton, 1972) and subsequent measurement of the orbital parameters of the binary system allowed dynamical mass measurements of around $21\,\mathrm{M}_\odot$ (Miller-Jones et al., 2021). Since then, around 20 (Remillard & McClintock, 2006; Wiktorowicz et al., 2014) other black holes in X-ray binaries have been discovered, spanning masses from $\sim 5 - 20\,\mathrm{M}_\odot$. In X-ray binaries, the black hole is identified by the electromagnetic emission of heated gas that is being accreted. This is not possible for so-called "dormant" or "quiescent" black holes, which do not show any signs of accretion.

1.1.2.2 Dynamical detections of BH-Star binaries

Even if there is no black hole accretion, it is possible to detect black holes via their gravitational influence on the dynamics of a binary stellar companion. If the orbital parameters of this system can be determined, the mass of the unseen companion can be measured. At the time of writing, three such black holes have been detected using astrometric data from the ESA Gaia satellite: Gaia BH1 has a mass of around 9.6 $M_\odot$ and is the closest known black hole (El-Badry et al., 2023a). It is orbited by a sun-like star with a period of P_{orb}=185.6 days. With M=8.9 $M_\odot$, Gaia BH2 (El-Badry et al., 2023b) is slightly more massive and is orbited by a red-giant star (P_{orb} = 1277 d). The most recent of the Gaia Black Holes (BH3; Gaia Collaboration et al. 2024) is especially interesting to due its high mass (M_{BH}=33 $M_\odot$), the stark mass difference with its stellar companion ($M_\star$=0.8 $M_\odot$) and the low metallicity of the companion. The binary system can be associated with the ED-2 stream, indicating a potential dynamic formation scenario (Balbinot et al., 2024; Marín Pina et al., 2024), however other works also demonstrate formation scenarios via isolated binary evolution (Iorio et al., 2024). Earlier dynamical detections were made in the globular cluster NGC 3201 using multi-epoch spectroscopy with VLT MUSE (Giesers et al., 2018, 2019).

1.1.2.3 Gravitational wave events

Another prediction by General Relativity is that two orbiting masses lose energy by emitting gravitational waves, propagating disturbances of space-time (Einstein, 1918). The first evidence for this process was the detection of the spin-down of the binary pulsar PSR 1913+16 (Hulse & Taylor, 1975; Taylor & Weisberg, 1982). The direct detection of gravitational waves required the development of second-generation interferometric gravitational wave detections, such as Advanced LIGO (LIGO Scientific Collaboration et al., 2015), Advanced Virgo (Acernese et al., 2015) and KAGRA (Kagra Collaboration et al., 2019).

In September 2015 the two LIGO detectors detected the gravitational wave signal of the orbital decay of two coalescing black holes with masses of 36 $M_\odot$ and 29 $M_\odot$ and the subsequent ring-down of the remaining black hole which was calculated to have a mass of 62 $M_\odot$ (Abbott et al., 2016). This event, named GW150914, marked the beginning of a new era in gravitational wave astronomy. Since this initial detection, dozens of other black holes - black hole mergers (and some mergers including neutron stars) have been observed (Abbott et al., 2023). A compilation of all binary black hole mergers is shown in Figure 1.1. So far the event GW190521 (Abbott et al., 2020) produced the most massive remnant black hole. With a post-merger mass of approximately 142 $M_\odot$, it reaches into the low intermediate-mass regime. At the time of writing, the existing gravitational wave detectors are conducting their fourth coordinated observing campaign and many additional detections are expected.

1.1.2.4 Detection of isolated stellar mass black holes via microlensing

All methods for the detection of stellar mass black holes share the limitation of being able to only detect black holes in binary systems. One way of overcoming this limitation would be to use the

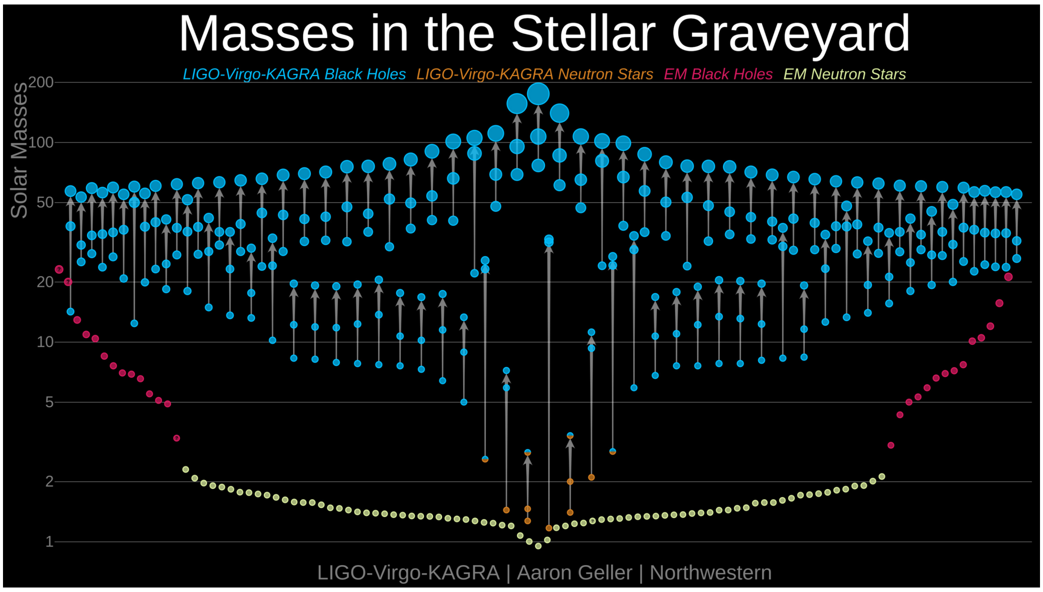

Figure 1.1: This figure summarizes the known population of compact object binaries. Light yellow circles indicate electromagnetic neutron star detections (such as pulsars), red circles indicate black holes in x-ray binaries, and blue (orange) circles indicate black-hole (neutron star) binary mergers observed by their gravitational wave emission with both their initial masses and their post-merger mass. *Image Source:* https://www.ligo.caltech.edu/image/ligo20211107a

relativistic effects of microlensing to detect the chance alignment between a stellar background source and an isolated black hole. At the moment, there is one promising candidate using the latter method (Lam et al., 2022; Sahu et al., 2022) and there is also some hope to apply this technique to search for black holes in globular clusters (see Subsection 8.1.8).

1.2 SUPER-MASSIVE BLACK HOLES

1.2.1 ACTIVE GALACTIC NUCLEI (AGN) AND QUASARS

The discovery of the first quasar (Schmidt, 1963), a powerful point-like emission source at a cosmological distance, marked the beginning of studies of supermassive black holes (SMBHs). Already Salpeter (1964) and Zel'dovich (1964) suggested that this emission could be powered by the accretion of gas by massive compact objects and Lynden-Bell (1969) made the connection between distant quasars and the active central regions of nearby galaxies. An early review of the accretion mechanism on supermassive black holes is given in Rees (1984). Measuring the mass of these objects requires observations of the dynamics of gas or stars within the radius of influence of the central black hole. This was pioneered by Young et al. (1978) and Sargent et al. (1978) with velocity dispersion measurements of the central region of the massive elliptical galaxy M 87. In the following years, several candidates for supermassive black holes in galaxy centers were discovered with masses between 10^6-$10^{9.5}$ $M_\odot$ (Kormendy & Richstone, 1995). Until the mid-nineties, these detections were based on seeing-limited ground-based observations of the stellar dynamics or radio observations of gas dynamics. The high resolution of the

Hubble Space Telescope enabled further detections and more robust measurement, see Kormendy & Gebhardt (2001); Kormendy & Ho (2013) for reviews.

The most detailed observations for accreting supermassive black holes to date have been obtained using the "Event Horizon Telescope", a network of radio-telescopes spread around the Globe, that perform very-long baseline interferometry at millimeter wavelengths. The unprecedented resolution of just 25 μas allowed to resolve structures close to the event horizon of the central black hole in the giant elliptical galaxy M87 (Event Horizon Telescope Collaboration et al., 2019) and for Sgr A* (Event Horizon Telescope Collaboration et al., 2022a), the central black hole of the Milky Way (see next section).

1.2.2 The closest supermassive black hole: Sgr A*

One special and unique case among the supermassive black holes is Sgr A*, the central black hole of the Milky Way. With a distance of $8.178 \pm 0.013_{\mathrm{stat.}} \pm 0.022_{\mathrm{sys.}}$ kpc (GRAVITY Collaboration et al., 2019), it is two orders of magnitude closer than any other SMBH in the local Universe, which allows us to study its surroundings in much greater detail. Compared to other supermassive black holes, it shows only very low AGN activity, with a bolometric luminosity of just $\lesssim 10^{36}$ erg s^{-1}, corresponding to an Eddington rate of $L/L_{\mathrm{Edd.}} \sim 10^{-9}$ (see Subsection 1.2.4 for the definition of the Eddington ratio).

Its radio emission was first observed by Balick & Brown (1974) and early observations of gas- (Wollman et al., 1977; Lacy et al., 1980) and stellar- (McGinn et al., 1989; Krabbe et al., 1995; Haller et al., 1996) dynamics showed signs for a central mass of the order of several 10^6 M$_\odot$.

The further history of the study of the stellar motions in the vicinity of Sgr A* is closely related to the development of ground-based, high-resolution, infrared astronomy. Using infrared observations is a necessary requirement due to the strong extinction towards the Galactic Center. Observations started with lucky imaging instruments such as SHARP at the ESO NTT (Hofmann et al., 1992), which were later superseded by AO-assisted imaging and spectroscopic observations at the 8m ESO Very Large Telescope and the 10m Keck telescope[1]. Initially, these observations led to the discovery of stars with high proper motions (Eckart & Genzel, 1996; Genzel et al., 1997; Ghez et al., 1998), but with longer temporal baselines, precise orbits for dozens of stars were measured (Ghez et al., 2008; Gillessen et al., 2009, 2017), including the S2 star with a period of just 15 years (Schödel et al., 2002).

The near-infrared observations culminated with the interferometric VLT GRAVITY instrument (GRAVITY Collaboration et al., 2017). By coherently combining light from all four unit telescopes of the VLT, it reaches spatial resolutions of 3 milliarcseconds (mas) and an astrometric precision of 10-100 μas. Observations of the pericenter passage of S2 in 2018 with GRAVITY allowed the detection of relativistic effects such as gravitational redshift (GRAVITY Collaboration et al., 2018)

---

[1] The used instruments at the VLT were NAOS-CONICA (Lenzen et al., 2003; Rousset et al., 2003) and the integral field spectrograph SINFONI (Eisenhauer et al., 2003). At Keck, the instrument for Speckle observations was the Keck Facility Near Infrared Camera (Matthews et al., 1996). The monitoring was continued using the laser guide star adaptive optics system (Wizinowich et al., 2006) in front of the NIRC2 imager and the NIRSPEC (McLean et al., 1998) and OSIRIS (Larkin et al., 2006) spectrographs.

and Schwarzschild Precession (GRAVITY Collaboration et al., 2020a). Finally, astrometric and polarimetric observations of the near-infrared flares of Sgr A* have allowed to dynamically probe the black hole at scales similar to the ones probed with the Event Horizon Telescope (Gravity Collaboration et al., 2023).

1.2.3 Scaling relations

Once a sufficiently large statistical sample of precise black hole mass measurements became available, several tight scaling relations between the black hole mass and properties of its host galaxy were discovered. This includes the $M_{\mathrm{BH}}-\sigma$ relation (Ferrarese & Merritt, 2000; Gebhardt et al., 2000), that connects the black hole mass M_{BH} with the central velocity dispersion σ of the host galaxy. Another tight relation was found between the black hole mass and the bulge luminosity L_{Bulge} (Magorrian et al., 1998) and the black hole mass with the mass of the central stellar bulge M_{Bulge} (Häring & Rix, 2004). These correlations are likely a consequence of the coevolution between the central black holes and their host galaxy, but also of the merger history of galaxies. A review of the different scaling relations and potential explanations is given in Kormendy & Ho (2013). How the scaling relations extend to the lowest black hole masses is still an open question (see Greene et al., 2020), but extrapolating e.g. the $M_{\mathrm{BH}}-M_{\mathrm{Bulge}}$ relation to globular clusters would yield intermediate-mass black holes (see Section 1.3) at $10^3-10^4\,\mathrm{M}_\odot$.

1.2.4 Observational evidence for early SMBH formation

Due to their high luminosities, quasars can be detected at large distances and offer a unique way to probe the conditions in the early Universe. The observational frontier for quasars has been shifted to higher and higher redshifts; see Fan et al. (2023) for a recent review. Hundreds of quasars have been found at redshifts $z>6$ and the current record holder has a redshift of $z=7.642$ and a black hole mass of $(1.6\pm0.4)\times10^9\,\mathrm{M}_\odot$ (Wang et al., 2021). Observations with JWST also allowed to detect a rapidly accreting black hole in GN-z11, a galaxy at redshift $z=10.6$ (Maiolino et al., 2024).

These extreme objects provide an intriguing challenge for our understanding of SMBH growth and formation. What provided the seeds for these black holes? And how could they accrete their mass in such a relatively short period of time?

Normally, it is assumed that the growth rate of a black hole cannot exceed the so-called Eddington limit, at which the radiation pressure is equal to the gravitational force. Assuming spherical symmetry and pure hydrogen gas yields the following expression for the Eddington luminosity $L_{\mathrm{Edd.}}$ (Fan et al., 2023):

$$L_{\mathrm{Edd.}}=\frac{4\pi G m_p M_{\mathrm{BH}}}{\sigma_T}=1.26\times10^{38}\,\mathrm{erg\,s^{-1}}\left(\frac{M_{\mathrm{BH}}}{M_\odot}\right) \tag{1.2}$$

with the speed of light c, the gravitational constant G, the proton mass m_p and the Thomson cross-section σ_T. The Eddington ratio between the observed bolometric luminosity $L_{\mathrm{Bol.}}$ and $L_{\mathrm{Edd.}}$ gives a measure for the accretion state of the black hole. Taking the observed masses of massive quasars at high redshift and assuming constant accretion at the Eddington limit gives us minimum masses for

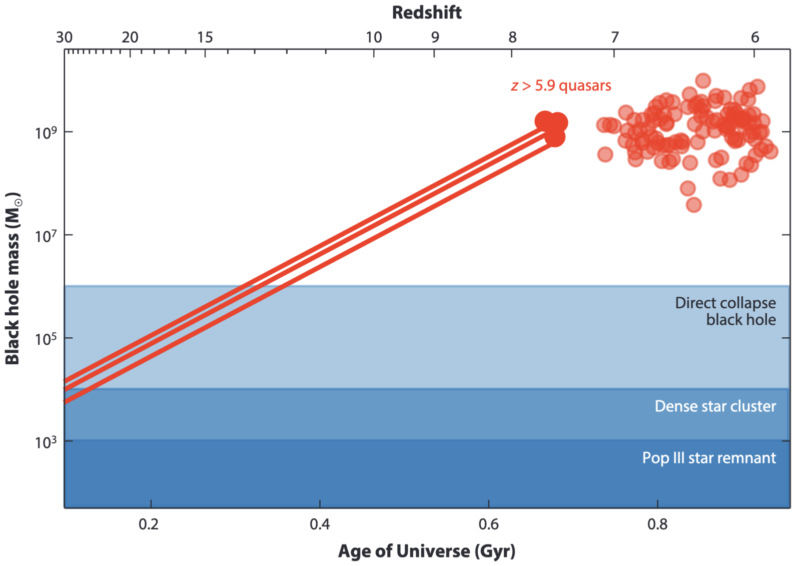

Figure 1.2: This figure shows the masses and redshifts of known high red-shift quasars (red circles). The red tracks indicate how the mass of black hole seeds would grow assuming constant accretion at the Eddington limit.
Figure from Fan et al. (2023).

the seeds of the black holes and their formation time, see Figure 1.2. A recent review of the different formation channels for SMBHs is given in Inayoshi et al. (2020), the main seed formation scenarios are also presented in the next section.

1.3 INTERMEDIATE MASS BLACK HOLES AS SEEDS FOR SUPERMASSIVE BLACK HOLES

While black holes in the stellar and the super-massive mass range have been studied in great detail and we have started to understand their overall populations, the intermediate mass range between around $100 - 10^5\ \mathrm{M}_\odot$ is still quite unconstrained (see Greene et al., 2020, for a comprehensive review). Namely, it is unclear whether there is a continuous spectrum of black hole masses or whether there is a clear split into the different mass regimes. Constraining the local population of intermediate-mass black holes could help to understand the origin of SMBHs and to discern between light- and heavy-seeding formation scenarios for SMBHs. In the following, I present the different possible formation channels for supermassive black holes seeds with an emphasis on intermediate-mass black hole formation in dense star clusters. Afterward, I give an overview of the existing observational evidence for intermediate-mass black holes.

Three primary theoretical formation channels for seeds are discussed in the literature:

1.3.1 Pop III stars

The first stars formed from gas that was free of any metals (Klessen & Glover, 2023) and at redshifts $z \gtrsim 30$. The initial mass function (IMF) of these stars likely was very different than the present day IMF. Although there are still many uncertainties, the Pop III IMF is expected to be top heavy and reach up to stars with masses of several hundred $\mathrm{M}_\odot$. As discussed above, these massive stars end their lives as supernovae with stellar-mass black holes as remnants. For massive Pop III stars, these remnants could reach masses on the order of $\sim$100 $\mathrm{M}_\odot$. Depending on their frequency, their number of density could match the number density of SMBHs in the local Universe (Madau & Rees, 2001) making them one potential category of seeds for SMBHs. However, super-Eddington accretion may be required to grow from $\sim$ 100 $\mathrm{M}_\odot$ to massive (10^9 $\mathrm{M}_\odot$) high-redshift quasars (Haiman & Loeb, 2001).

1.3.2 Direct collapse models

Rather than forming a Pop III star, a collapsing gas cloud may collapse directly into a SMBH (Loeb & Rasio, 1994; Bromm & Loeb, 2003; Begelman et al., 2006), perhaps with a brief, intermediate stellar phase. This is only possible in primordial, metal-free gas without efficient cooling or fragmentation channels. While the SMBH seed masses $\sim 10^{3-6}$ $\mathrm{M}_\odot$ would no longer require super Eddington accretion to reach the SMBHs in high-z quasars, it is unclear if a gas cloud could, in fact, directly collapse into an SMBH without first fragmenting (Klessen & Glover, 2023).

1.3.3 Dynamical formation in dense star clusters

A third scenario for the formation of seed black holes consists of a gravitational runaway of stars or stellar mass black holes happening in the center of massive, dense star clusters. Depending on the timescale on which this process happens, the scenario is typically split in a fast (few Myrs) and a slow (100-1000 Myr) channel (see also Askar et al. 2023 for a review of the different physical mechanisms at play):

1.3.3.1 The slow runaway channel

In the slow runaway scenario (introduced by Miller & Hamilton, 2002), stellar mass black holes (that are significantly more massive than the average star) accumulate in the center of the cluster due to mass segregation. In this very dense subcluster, black hole binaries form due to dynamic interactions and are subsequently hardened until they start to coalesce due to gravitational wave emission, forming more massive "second generation" black holes. Due to further interaction with other black holes, there is a hierarchical growth of the black hole and masses over 10^3 $\mathrm{M}_\odot$ can be reached.

The efficiency of this formation channel depends sensitively on the retention fraction of the first-generation black holes (as they might be ejected from the star cluster due to supernova recoil kicks) but also the retention fraction of black hole merger products (as there is also a recoil kick following gravitational wave emission). Therefore, this channel is likely more feasible in more massive cluster with escape velocities on the order of or larger than 100 $\mathrm{km\,s^{-1}}$ (Antonini et al., 2019).

1.3.3.2 Fast runaway

In the fast runaway scenario (Portegies Zwart & McMillan, 2002; Portegies Zwart et al., 2004; Fujii et al., 2024; Rantala et al., 2024) massive stars migrate to the cluster center on short timescales (few Myrs) and before they evolve into stellar mass black holes. Due to their large radii, they then collide and merge with other stars in the cluster center, forming a super massive star weighting up to several thousand solar masses. Due to repeated mergers with other stars, this very massive star can grow to thousands of solar masses. The further evolution of this very massive star then depends strongly on its metallicity (at higher metallicities, large amounts of mass can be lost again due to stellar winds), but eventually, it can directly collapse to an intermediate-mass black hole.

Another interesting implication of this scenario is that due to the high temperatures within supermassive stars and subsequent mass ejection due to stellar winds, they might also be responsible for the pollution of the intracluster medium, leading to the known chemical variations between different generations of stars within globular clusters (Gieles et al., 2018b, 2025).

1.4 Observations

A better understanding of the present-day population of intermediate-mass black holes could help to constrain seeding mechanisms in the early Universe (Greene et al. 2019, 2020; see also see Figure 1.3 for a schematic). While light-seeding scenarios such as Pop III stars would produce a broad range of IMBH masses and a high occupation fraction even in low-mass galaxies, heavy-seed scenarios would lead to a lower limit on observable IMBH masses and a smaller occupation fraction of black holes in low mass galaxies.

These implications for SMBH formation mechanisms have sparked the long search for intermediate-mass black holes. In the following, I summarize the different observational efforts and some of the most promising candidates.

1.4.1 Searches in low mass galactic nuclei

Various methods have been employed to search for intermediate-mass black holes in dwarf galaxies (Reines, 2022). These searches have led to a considerable sample of $\sim 10^{5-6}\,\mathrm{M}_{\odot}$ candidates (see Greene et al. 2020 for a list). However, evidence for black holes below $10^{5}\,\mathrm{M}_{\odot}$ remains sparse.

1.4.1.1 Dynamical measurements of black hole masses in dwarf galaxies

Dynamical measurements of black hole masses observe the kinematics of stars or gas in the vicinity of the potential black hole. The advantage of this method is that it works with relatively few assumptions and is independent of the black hole accretion rate, meaning that it works equally well for quiescent black holes. However, several challenges must be overcome in the case of IMBHs in dwarf galaxies: To be able to measure the dynamical mass, the sphere of influence of the potential black hole has to be

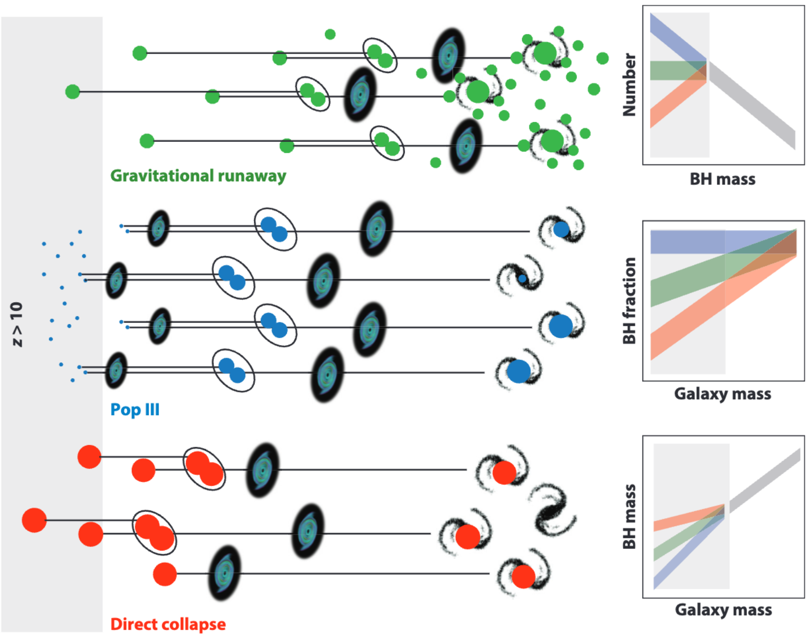

Figure 1.3: This figure summarizes the three main formation channels for for supermassive black holes formation and their predicted consequence on present-day intermediate-mass black hole populations. *Figure from Greene et al. 2020*

resolved. The size of the sphere of influence $r_{\text{infl.}}$ scales with the black hole mass M_{BH} and the stellar velocity dispersion σ (Peebles, 1972):

$$r_{\text{infl.}} = \frac{GM_{\text{BH}}}{\sigma^2} \tag{1.3}$$

Due to the comparatively low mass of IMBHs, this sphere of influence is typically on the order of ~ 1 pc and, therefore, only resolvable in the local Universe. Other challenges for this type of measurement include the need for a precise estimate of the M/L ratio of the galaxy (which can be complicated in the case of recent star formation) and the exact position of the exact center in case of irregular late-type galaxies (see e.g. the large uncertainty on the center of the Large Magellanic Cloud, van der Marel & Kallivayalil 2014). Dynamical black hole mass measurements or upper limits for several local dwarf galaxies (including the LMC and M33) have been published in Gebhardt et al. (2001); Neumayer & Walcher (2012); den Brok et al. (2015); Boyce et al. (2017); Nguyen et al. (2017, 2018, 2019). In half of the cases, black hole masses of $10^5 - 10^6\ \text{M}_\odot$ could be measured (indicating a high black hole occupation fraction), while in the other cases, upper limits on the order of $M \lesssim 10^5\ \text{M}_\odot$ were derived. Although the sample is still small and there is significant scatter, the results are compatible with black hole scaling relations continuing unbroken to lower black hole masses.

1.4.1.2 AGN EMISSION

Another route to detect IMBHs, which is not limited to close distances, is the spectroscopic identification of AGN emission from the centers of low-mass galaxies. This can be done by the identification of broad Hα lines emitted by gas orbiting the black hole (Greene & Ho, 2004, 2005), and hundreds of candidate black holes have been identified by searches within large sky surveys such as SDSS (Dong et al., 2012; Chilingarian et al., 2018; Liu et al., 2018). Another way to identify AGN emission is to probe the ionization state of the central region of a galaxy using line-ratio diagnostics such as Baldwin-Phillips-Terlevich (BPT) diagrams (Baldwin et al., 1981). This has been applied in, for example, Reines et al. (2013). In both cases, the AGN emission can only be detected with sufficiently strong accretion on the potential black hole, a condition that is only met for a small fraction ($\sim$1%) of dwarf galaxies, making it challenging to study the underlying population of more quiescent black holes. Another complication, that limits the robust detectability of AGN is that star formation at low metallicities can mimic AGN signatures in the BPT diagram (see e.g. Stasińska et al. 2006; Trump et al. 2015 but also the discussion in Greene et al. 2020 and references therein). One remarkable candidate selected using this technique is a 50 000 $M_\odot$ black hole in the galaxy RGG 118 (Baldassare et al., 2015).

1.4.1.3 X-RAY AND RADIO OBSERVATIONS

While optically selected AGN are typically in a state of high accretion, searches for AGN signatures at radio and X-ray wavelengths have the advantage that they can probe AGNs with lower accretion rates. Several studies have targeted hundreds of dwarf galaxies searching for X-ray signatures (see Miller et al. 2015 as an example and references in Greene et al. 2020) and in general found a significant black hole occupation fraction, although uncertainties such as the distribution of Eddington ratios remain. Additional radio observations can help to constrain to masses of black holes via the fundamental plane of radio activity (Merloni et al., 2003), see e.g. the low-mass galaxy NGC 404 (Nyland et al., 2012, 2017).

1.4.1.4 VARIABILITY

The optical variability of AGN is another tool that can be used to select samples of potential AGN in low mass galaxies (see e.g. Morokuma et al. 2016; Heinis et al. 2016; Baldassare et al. 2018, 2020). Future time-domain surveys like the Legacy Survey of Space and Time (LSST Science Collaboration et al., 2009) can enable these searches for a much larger sample of galaxies.

At the same time, the time delay between continuum and line emission (emitted from the accretion disk and the broad line region) can be used to measure black hole masses using the reverberation mapping technique (Peterson, 2014). This has been applied to low-mass AGN e.g. in Desroches et al. (2006). For the mass derivation empirical calibration factors that account for the geometry of the AGN are needed. Therefore, the selection of galaxies used for this calibration and the extrapolation to low masses might lead to significant systematic uncertainties (see e.g. Ho & Kim 2014).

1.4.1.5 Transient events

Stars that pass the tidal radius of a black hole can be disrupted in a "tidal disruption event", creating a bright transient flare that can last for several years (Rees, 1988). The shape of the light curve can serve as a way to measure the black hole mass (e.g. Mockler et al., 2019). Although exact TDE rates are still quite unconstrained, they might be quite high and contribute a significant part of black hole growth in dwarf galaxies (Zubovas, 2019). Searches for TDEs by intermediate-mass black hole have already started (Gomez & Gezari, 2023; Pomeroy & Norris, 2024) using the Zwicky Transient Facility (Bellm et al., 2019), but will be boosted by the new observational capabilities of the Rubin observatory with first light expected this year (2025).

The other important class of transient events that can be used to detect IMBHs are gravitational waves. The most massive event detected with the current detector generation (GW190521, Abbott et al. 2020) already reaches into the IMBH regime with a resulting BH mass of 142 $M_\odot$. Mergers between IMBHs or also intermediate-mass ratio inspirals (IMRIs) of stellar-mass black holes onto IMBHs have gravitational wave frequencies that are too low for the existing generation of detectors. This will change in the next decade when the ESA Laser Interferometer Space Antenna (Colpi et al., 2024) and the ground-based Einstein Telescope (Punturo et al., 2010) will be sensitive to gravitational waves at much lower frequency.

1.4.2 Searches in globular clusters

Intermediate-mass black holes might form in globular clusters via the gravitational runaway channels discussed above. However, detecting them turns out to be even more challenging than in the case of dwarf galaxies: The expected IMBH masses are even lower, and due to the low gas density within globular clusters, any accretion signal would be very weak. On the other hand, many globular clusters are at comparatively close distances, where individual stars can be resolved.

1.4.2.1 Dynamical searches

The stellar kinematics of globular clusters can be probed using various observational techniques: early works used unresolved spectroscopic observations of their line-of-sight velocities (see e.g. Noyola et al. 2008; Lützgendorf et al. 2013). With sufficient spatial resolution, individual stellar motions can be measured either as proper motions measured using multi-epoch high-resolution imaging (see e.g. McLaughlin et al. 2006; Anderson & van der Marel 2010; Häberle et al. 2021; Vitral et al. 2023), or line-of-sight velocities of individual stars (Kamann et al., 2014, 2016). Another recent channel is the observation of millisecond pulsars, which allow for a direct measure of the cluster's potential via their timing solutions (Kızıltan et al., 2017; Perera et al., 2017; Smith et al., 2024; Bañares-Hernández et al., 2025).

To infer the presence of a potential IMBH (or also the mass contribution of other unseen components), the kinematic measurements then have to be compared or fit to dynamical models. One standard tool is to use isotropic or anisotropic Jeans models (e.g. Cappellari, 2008). However, orbit-superposition models (e.g. Gebhardt et al., 2002), distribution function-based models (Gieles & Zocchi, 2015; Zocchi et al., 2017) and comparisons with grids of N-Body models (Baumgardt, 2017) have also been used. The exact choice of model is a trade-off between speed, flexibility, and evolutionary information (that naturally is taken into account, e.g., in N-body models).

Various studies have searched for kinematic evidence for IMBHs in individual globular clusters in the Milky Way, but also around M31 (see Table 1.1 for an overview and references). Other studies have done systematic searches by systematically modeling larger samples of globular clusters (Baumgardt, 2017; Dickson et al., 2024). In several works, potential IMBH signatures were detected with ω Cen and 47 Tuc being the most debated cases. However, other studies could not reproduce these results or noted various degeneracies in the model due to anisotropy or the mass contribution of stellar remnants.

One common challenge for all modeling techniques is the potential degeneracy between the kinematics influence of a central intermediate-mass black hole and the presence of a compact cluster of stellar remnants (Zocchi et al., 2019; Baumgardt et al., 2019b; Dickson et al., 2023; Bañares-Hernández et al., 2025). It can only be overcome with observations of the innermost region of a star cluster, where the signal of an IMBH would dominate over a stellar-mass black hole population.

1.4.2.2 ACCRETION CONSTRAINTS

Analog to active galactic nuclei, which have been studied in large numbers using their radio and x-ray emission, there have been searches for accretion signals from IMBHs in globular clusters. This accretion could be detectable via synchrotron emission at radio frequencies (Maccarone, 2004, 2005; Maccarone & Servillat, 2008). Various deep and systematic searches have been conducted (Strader et al., 2012; Tremou et al., 2018) without significant detections, yielding typical upper limits on black hole masses on the order of $M_{BH} < 1000\,M_\odot$. There are three viable explanations for these non-detections: Either there truly are no IMBHs in the cluster centers, the gas content of the cluster is overestimated, or the accretion onto the black holes is very inefficient. One remarkable recent result is the detection of a central radio source in the globular cluster 47 Tuc (Paduano et al., 2024) using $\sim$480 hours of observations with the Australia Telescope Compact Array. No optical counterpart is detected, and the authors give accretion emission by a $\sim 54 - 6000 M_\odot$ black hole as the most likely explanation.

Other searches have used deep X-ray observations (Haggard et al. 2013 targeting ω Cen; Bhattacharya et al. 2017 targeting 47 Tuc), but so far no IMBH detection within a Milky Way globular cluster has been confirmed. The massive cluster G1 shows X-Ray emission (Pooley & Rappaport, 2006) and some signs of radio emission (Ulvestad et al., 2007), however later simultaneous multi-wavelength observations showed that the emission could be explained by regular stellar mass black hole X-ray binaries (Miller-Jones et al., 2012).

Table 1.1: List of dynamical IMBH constraints derived for globular clusters sorted by NGC numbers. Filled circles in the first column indicate claimed detections, while open circles indicate upper limits or non-detections. If both are shown the authors presented different scenarios with and without an IMBH.

	Object	Mass constraints	Data	Modelling method	Reference
○	NGC 104 (47 Tuc)	$< 1.5 \times 10^3\,M_\odot$	PMs	Isotropic Jeans Models	McLaughlin et al. (2006)
●	NGC 104 (47 Tuc)	$2300^{+1500}_{-850}\,M_\odot$	Pulsars	N-Body Models	Kızıltan et al. (2017)
○	NGC 104 (47 Tuc)	no detection	PMs	Isotropic Jeans Models	Mann et al. (2019)
○	NGC 104 (47 Tuc)	$< 578\,M_\odot$	LOS & PMs	Distr. Functions	Della Croce et al. (2024)
○	NGC 1851	$< 2 \times 10^3\,M_\odot$	LOS (integr.)	Isotropic Jeans models	Lützgendorf et al. (2013)
●	NGC 1904 (M79)	$(3 \pm 1) \times 10^3\,M_\odot$	LOS (integr.)	Isotropic Jeans models	Lützgendorf et al. (2013)
●	NGC 5139 (ω Cen)	$(4.0^{+0.75}_{-1.0}) \times 10^4\,M_\odot$	LOS (integr.)	Isotropic Jeans models	Noyola et al. (2008)
●	NGC 5139 (ω Cen)	$(4.7 \pm 1.0) \times 10^4\,M_\odot$	LOS (integr.)	Isotropic Jeans models	Noyola et al. (2010)
○	NGC 5139 (ω Cen)	$< 1.2 \times 10^4\,M_\odot$	PMs	Anisotropic Jeans models	van der Marel & Anderson (2010)
●	NGC 5139 (ω Cen)	$5 \times 10^4\,M_\odot$	PMs	N-Body Models	Jalali et al. (2012)
○	NGC 5139 (ω Cen)	no detection	PMs	Distr. Function	Zocchi et al. (2019)
○	NGC 5139 (ω Cen)	no detection	PMs	N-Body model	Baumgardt et al. (2019b)
●	NGC 5139 (ω Cen)	$> 8.2 \times 10^3\,M_\odot$	PMs	Velocities of fast stars	Häberle et al. (2024a)
○	NGC 5139 (ω Cen)	$< 6 \times 10^3\,M_\odot$	Pulsars, PMs, LOS	Anisotropic Jeans models	Bañares-Hernández et al. (2025)
○	NGC 5272 (M3)	$< 5300\,M_\odot$	resolved LOS	Isotropic Jeans models	Kamann et al. (2014)
●	NGC 5286	$(1.5 \pm 1.0) \times 10^3\,M_\odot$	LOS (integr.)	Anisotropic Jeans models	Feldmeier et al. (2013)
○	NGC 5694	$< 8 \times 10^3\,M_\odot$	LOS (integr.)	Isotropic Jeans models	Lützgendorf et al. (2013)
○	NGC 5824	$< 6 \times 10^3\,M_\odot$	LOS (integr.)	Isotropic Jeans models	Lützgendorf et al. (2013)
○	NGC 6093 (M80)	$< 800\,M_\odot$	LOS (integr.)	Isotropic Jeans models	Lützgendorf et al. (2013)
●○	NGC 6121 (M4)	$(800 \pm 300)\,M_\odot$	resolved LOS	Anisotropic Jeans models	Vitral et al. (2023)
○	NGC 6205 (M13)	$< 8600\,M_\odot$	resolved LOS	Isotropic Jeans models	Kamann et al. (2014)
●	NGC 6266 (M62)	$(2 \pm 1) \times 10^3\,M_\odot$	LOS (integr.)	Isotropic Jeans models	Lützgendorf et al. (2013)
○	NGC 6341 (M92)	$< 980\,M_\odot$	resolved LOS	Isotropic Jeans models	Kamann et al. (2014)
●	NGC 6388	$(17 \pm 9) \times 10^3\,M_\odot$	LOS (integr.)	Isotropic Jeans models	Lützgendorf et al. (2011)
○	NGC 6388	$< 2000\,M_\odot$	resolved LOS	Isotropic Jeans models	Lanzoni et al. (2013)
●	NGC 6388	$(2.8 \pm 0.4) \times 10^4\,M_\odot$	LOS (integr.)	Isotropic Jeans models	Lützgendorf et al. (2015)
●○	NGC 6397	$600\,M_\odot$	resolved LOS	Isotropic Jeans models	Kamann et al. (2016)
○	NGC 6441	$< 1.32 \times 10^4\,M_\odot$	PMs	Anisotropic Jeans models	Häberle et al. (2021)
●	NGC6624	$> 7500\,M_\odot$	1 Pulsar	Orbital solution	Perera et al. (2017)
○	NGC6624	no detection	PMs	Distr. Functions	Gieles et al. (2018a)
●○	NGC 6715 (M54)	$9400\,M_\odot$	LOS (integr.)	Anisotropic Jeans models	Ibata et al. (2009)
○	NGC 7078 (M15)	$(3.9 \pm 2.2) \times 10^3\,M_\odot$	resolved LOS	Isotropic Jeans models	Gerssen et al. (2002)
○	NGC 7078 (M15)	no detection	resolved LOS	N-Body models	Baumgardt et al. (2003a)
●	M31 / G1	$2.0^{+1.4}_{-0.8} \times 10^4\,M_\odot$	LOS (integr.)	Orbit superposition	Gebhardt et al. (2002)
○	M31 / G1	no detection	LOS (integr.)	N-Body models	Baumgardt et al. (2003b)
●	M31 / G1	$(1.7 \pm 0.3) \times 10^4\,M_\odot$	LOS (integr.)	Isotropic Jeans Models	Gebhardt et al. (2005)
●	M31 / B023-G078	$9.1^{+2.6}_{-2.8} \times 10^4\,M_\odot$	LOS (integr.)	Anisotrpic Jeans model	Pechetti et al. (2022)

1.4.2.3 Hypervelocity stars

The interactions between a supermassive or intermediate-mass black hole and a stellar binary can lead to the disruption of the binary and the subsequent ejection of a star as a hyper-velocity star via the Hills mechanism (Hills, 1988), a star with a velocity higher than the escape velocity of the Galaxy. While most known hypervelocity stars are attributed to the Galactic Center (Brown, 2015), there are some interesting exceptions: HVS3 has been shown to have a likely origin in the Large Magellanic Cloud (Edelmann et al., 2005; Gualandris & Portegies Zwart, 2007; Erkal et al., 2019), and using a larger statistical sample of hypervelocity stars might even be used to estimate the mass of a potential black hole in the LMC (Han et al., 2025). Another recent discovery is the potential association between a hypervelocity star with the globular cluster M15 (Huang et al., 2024).

1.4.3 Ultraluminous X-ray sources

One last category of IMBH candidates outside of galactic nuclei are “off nuclear” ultraluminous x-ray sources (Kaaret et al., 2017), objects with x-ray fluxes $L_X > 10^{39}\,\mathrm{erg\,s^{-1}}$. Nowadays, most of these sources are interpreted as neutron stars in states of super-Eddington accretion, but some extremely bright objects (with $L_X > 10^{41}\,\mathrm{erg\,s^{-1}}$) remain viable IMBH candidates. The best-studied case is the source HLX-1 (Farrell et al., 2009) in the outskirts of the galaxy ESO 243-49.

2 MASSIVE STAR CLUSTERS

In Section 1.3 we have discussed different formation channels for intermediate-mass black holes, the seeds for massive black holes that form in the early universe. One of the theorized formation channels is by gravitational runaway collisions in dense star clusters, although the efficiency of this channel depends on various assumptions about the retention fraction and the mass loss of very massive stars. To constrain this formation channel observationally, we have to turn to the massive star clusters observable in the local universe. In the following chapter, I give an overview of the different types of massive star clusters, the dynamic processes governing their evolution, and the tools used to model them. Finally, I introduce Omega Centauri (ω Cen), a stripped nucleus and the most massive globular cluster of the Milky Way. The question of whether it hosts a central intermediate-mass black hole has been debated controversially and is also one of the main topics of this thesis (see Chapter 4).

2.1 THE VARIETY OF STAR CLUSTERS

Star clusters are gravitationally bound agglomerations of stars that span a vast range of masses and sizes (Krumholz et al., 2019). It is believed that most stars in the Universe form in either star clusters or stellar associations from giant molecular clouds (e.g. Lada & Lada, 2003). When these gas clouds cool, they become gravitationally unstable and start to fragment and collapse into filaments, the sites of star formation. After the formation of the first stars, stellar feedback in the form of radiation, stellar winds, and supernova explosions starts to expel the gas (e.g. Chevance et al., 2020), ending the active star-formation and leaving behind a star cluster. The future of this star cluster depends on its mass, density, and also its local environment within its host galaxy.

While open star cluster have relatively low masses and lifetimes and are unlikely to retain even stellar-mass black holes, massive star clusters are more promising potential hosts for both stellar-mass and intermediate-mass black holes. We distinguish the following types of massive star clusters:

2.1.1 NUCLEAR STAR CLUSTERS

Nuclear star clusters are the densest ($10^6\,\mathrm{M}_\odot\,\mathrm{pc}^{-3}$) and most massive ($10^5 - 10^8\,\mathrm{M}_\odot$) star clusters in the Universe, and they can be found in the center of galaxies (see Neumayer et al., 2020, for a recent review). The majority of intermediate mass ($M_\mathrm{stellar} \sim 10^9\,\mathrm{M}_\odot$) galaxies host nuclear star clusters, while at lower and higher stellar masses, the fraction of galaxies hosting massive nuclear star clusters decreases (Hoyer et al., 2021). There are two main scenarios for the formation of nuclear star clusters: they could either form through the inspiral and merger of globular clusters (Tremaine et al., 1975) or by in-situ star formation through the (potentially repetitive) accretion of gas towards the galaxy center (Loose et al., 1982). The latter scenario is typically invoked to explain the presence of young stellar populations as found in many galactic nuclei (e.g. Walcher et al., 2006; Kacharov et al., 2018). Likely, both scenarios coexist, with globular cluster accretion dominating the formation of nuclear star clusters in low-mass galaxies ($M<10^9$ $M_\odot$) and in-situ formation dominating in more massive galaxies, see e.g. Fahrion et al. (2021).

Just like the mass of central black holes, the mass of the nuclear star cluster correlates with the mass of their host galaxy (e.g. Ferrarese et al., 2006) and super-massive black holes and nuclear star clusters coexist in many galaxies (Seth et al., 2008). This leads to the question of whether the growth of SMBHs and nuclear star clusters are related. Due to their high masses and densities, both of which increase the chance of stellar interactions and lead to a higher escape velocity (enhancing the retention fraction of black holes), nuclear star clusters are a promising site for IMBH formation through the runaway channel (Stone et al., 2017; Antonini et al., 2019).

2.1.2 Stripped nuclei

In the hierarchical picture of galaxy formation, predicted by the standard ΛCDM model of modern cosmology, massive galaxies grow by accreting lower-mass galaxies. During these mergers, the majority of the accreted dwarf galaxy is tidally disrupted and scattered across the halo of the more massive galaxy (Helmi & White, 2001; Mayer et al., 2002). However, dense and gravitationally bound regions such as globular clusters and nuclear star clusters can survive these events and remain bound (Pfeffer & Baumgardt, 2013; Pfeffer et al., 2014). In the Milky Way, predictions from simulations range between $\sim 1-6$ such objects (Pfeffer et al., 2021), with M54 in the Sagittarius Dwarf Galaxies and ω Cen (see below) being the prime examples. Another candidate is B023-G078, the most massive cluster around M31, it has recently been shown to host a 10^5 $M_\odot$ black hole (Pechetti et al., 2022). Stripped galactic nuclei are also a potential explanation for ultra-compact dwarf galaxies (Drinkwater et al., 2003) and some of them have been shown to host supermassive black holes (Seth et al., 2014).

2.1.3 Globular clusters

The globular clusters observed in the present-day Universe are old ($>$ 10 Gyr), massive (10^4-10^6 $M_\odot$) and relatively compact (half-light radius $r_{\mathrm{HL}} < 10$ pc) spherical star clusters.

For the Milky Way, around 160 globular clusters are known (see e.g. the Harris 1996, 2010 catalog). Due to their brightness, many of them have been known for centuries (e.g. Herschel, 1789), however even in recent years previously unknown globular clusters have been discovered in heavily obscured parts of the Galaxy thanks to infrared surveys (see e.g. Minniti et al. 2011, 2017).

Besides the Milky Way, globular clusters have been found around galaxies of all types, and the properties of the globular cluster system correlate with the properties of the host galaxy (Harris et al., 2013). Therefore, in combination with their luminosity and their long lifetimes, globular clusters can serve as probes for Galaxy assembly (Brodie & Strader, 2006). One important aspect is a bimodality in color, that is observed for the globular cluster systems of many galaxies (e.g. Zepf & Ashman, 1993;

Ostrov et al., 1993; Gebhardt & Kissler-Patig, 1999). Nowadays, this dichotomy is attributed to two different origins of the globular clusters: metal-poor (blue) globular clusters are believed to have formed in low-mass satellite galaxies and have been accreted during galaxy mergers, while metal-rich (red) globular clusters have formed in-situ (e.g. Marín-Franch et al., 2009; Leaman et al., 2013).

The formation of most globular clusters took place at the peak of cosmic star formation ($z \sim 2-3$, Madau & Dickinson 2014) with massive molecular clouds, high gas pressures, and low metallicities leading to very high star formation rates (see reviews by Forbes et al., 2018; Adamo et al., 2020; Kruijssen, 2025). While these conditions are not met in the Milky Way disk today, so-called "young massive clusters" might be the local analogs of the progenitors of the present-day globular clusters (Portegies Zwart et al., 2010; Longmore et al., 2014). They can be found in regions with rapid star formation, e.g., close to the Galactic Center (e.g. Arches, Quintuplet, Westerlund1), in the Magellanic Clouds (e.g. R136 within 30 Doradus, Brandl et al. 1996), and in high numbers in "star-burst galaxies" such as the Antennae Galaxies (Whitmore et al., 1999).

For a long time, globular clusters were believed to be perfect examples of simple stellar populations, where all stars share the same age and chemical compositions. This picture has changed thanks to detailed spectroscopic and photometric observations that revealed multiple populations with chemical abundance variations in almost all globular clusters, see Bastian & Lardo (2018) for a recent review. The observed abundance variations and anti-correlations between specific light elements (e.g. [Na/O], [Mg/Al]) are typically attributed to two generations of star formation, where the first generation formed from primordial gas, while the second generation has been polluted by the nuclearly processed stellar ejecta from the first generation. Even though there are various potential polluters (e.g., asymptotic giant branch stars, fast-rotating massive stars, and very-massive stars formed by runaway collisions), a single scenario that explains all observed abundance variations has not been found yet.

2.2 Dynamics and evolution

2.2.1 Basic properties and timescales

The structure of massive spherical star clusters is typically described by three characteristic radii: The core radius $r_{\rm c}$ marks the radius at which the surface brightness drops to half of its central value; the half-mass radius describes the radius $r_{\rm HL}$, which contains half of the mass of the cluster; and the tidal radius $r_{\rm t}$ marks the border at which the gravitational influence of the Galaxy is stronger than that of the cluster itself. The tidal radius can be considered the outer border of the star cluster.

Massive star clusters are self-gravitating systems in dynamical equilibrium. The gravitational force (pulling inward) is countered by the velocity dispersion of the individual stars, similar to a star that is supported by its gas pressure. Based on the virial theorem, that relates the total kinetic energy T to the gravitational potential energy W with $2T + W = 0$, we can calculate the following expression for the typical velocity dispersion $\sigma_{\rm HL}$ at the half-light radius $r_{\rm HL}$:

$$\sigma_{\rm HL}^2 = \frac{GM_{\rm HL}}{r_{\rm HL}} \tag{2.1}$$

Therefore, the typical crossing time for a star is:

$$t_{\mathrm{cr}} = \frac{r_{\mathrm{HL}}}{\sigma_{\mathrm{HL}}} = \sqrt{\frac{r_{\mathrm{HL}}^3}{GM_{\mathrm{HL}}}} \tag{2.2}$$

Unlike galaxies, which can typically described as collisionless systems, stars in a star cluster interact with each other individually by exchanging energy, leading to so-called "relaxation". Due to their small radii, with respect to the size of the cluster, actual stellar collisions only occur under very extreme circumstances (e.g. core collapse, runaway gravitational mergers). Therefore, most of the interactions are elastic scatterings, which only change the velocity of a star by a small amount. The relaxation time t_{rx} of a cluster is defined as the time by which the cumulative effect of these velocity kicks is equal to the initial velocity dispersion. It is of the order of:

$$t_{\mathrm{rx}} = \frac{N}{8 \ln \Lambda} t_{\mathrm{cr}} = \frac{0.1\, N}{\ln N} t_{\mathrm{cr}} \tag{2.3}$$

where $\ln \Lambda$ is the Coulomb logarithm (see Eq. 1.37 and Eq. 1.38 in Binney & Tremaine 1987). For typical globular clusters in the Milky Way, the relaxation time is on the order of $10^7 - 10^{10}$ yr. So while some globular clusters have already passed several relaxation times, others are still considered "dynamically young".

2.2.2 Evolution

The two-body interactions drive the evolution of the star cluster and lead to several important consequences:

Evaporation: During relaxation, the energy distribution within a cluster approaches a Maxwell-Boltzmann distribution, which has a high-velocity tail. Stars that surpass the escape velocity of the cluster become unbound and leave the cluster, leading to its eventual evaporation. While this is the common fate of less massive, open clusters within the Milky Way, the typical globular cluster has a lifetime of tens to hundreds of Gigayears. However, this process can be accelerated significantly due to tidal interactions with its host Galaxy (e.g. Baumgardt & Makino 2003; see also the spectacular tidal streams of Palomar 5, Odenkirchen et al. 2003).

Energy Equipartition and mass segregation: Two-body relaxation eventually leads to so called energy-equipartition, meaning that all stars share the same average energy (Spitzer, 1969). This means that more massive stars (or their remnants) will have lower average velocities than low-mass stars and, therefore, will sink toward the cluster center, leading to mass segregation.

Core Collapse: The mass segregation and the evaporation lead to an energy transport from the center of the cluster towards the outskirts. The core begins to contract, leading to a higher central velocity dispersion (to maintain dynamical equilibrium), further leading to an even faster energy loss. This runaways process can lead to the collapse of the central regions of a cluster and is referred to as “core collapse” or “gravothermal catastrophe” (Hénon, 1961; Lynden-Bell & Wood, 1968). It is only halted by the formation of hard binaries (i.e. binaries, whose binding energy exceeds the mean kinetic energy of cluster stars), which can serve as a “heat source” for the cluster by adding their binding energy to their surroundings in three-body encounters.

2.2.3 COMPUTATIONAL METHODS FOR STUDYING THE DYNAMICAL EVOLUTION

The study of the dynamical evolution of star clusters requires the precise modeling of various physical processes that take place on different spatial and temporal scales. These processes include tidal interactions, two-body relaxation, stellar and binary evolution, close 3- or 4-body encounters, and even relativistic effects such as the emission of gravitational waves. Each of those processes has to be simulated precisely over the long lifetimes of a cluster, requiring high computational effort. A comprehensive review of the different methods and their development history is given in Spurzem & Kamlah (2023); here I introduce the two most commonly used state-of-the-art methods:

2.2.3.1 DIRECT N-BODY CODES

Direct N-body simulations are conceptually simple: to calculate the change of motion for each star, the gravitational interaction with every other star is calculated at each timestep. In practice, the most efficient and accurate implementations are quite complex, and the development of new, improved simulation codes is an active field of research. The computational complexity of N-Body codes scales with $O(N^2)$ for a single timestep, however, it has to be considered that larger systems also have longer relaxation times, making longer simulation runs necessary. The most commonly used family of codes are the `NBODYx` codes, initially developed by Sverre Aarseth (Aarseth, 2003). The most recent versions (e.g. `NBODY6++GPU`; Wang et al. 2015) are highly parallelized and optimized to run on GPU clusters. Other modern codes include `PETAR` (Wang et al., 2020) and `BIFROST` (Rantala et al., 2023).
The largest current simulations can follow the evolution of $\sim 10^6$ stellar particles over several Gigayears; see e.g. the DRAGON-II simulations (Arca Sedda et al., 2024).

2.2.3.2 MONTE CARLO CODES

Even though direct N-Body models are pushing towards higher and higher particle numbers, they are still too computationally expensive to model massive star clusters over cosmic time. Because of these computational costs, running large studies that vary many parameters is not possible, motivating the development of faster, approximate methods.
The N-body Monte Carlo method is a powerful technique for efficiently simulating the evolution of spherically symmetric systems. The technique was first introduced by Hénon (1971) and uses the following approach (see also Pattabiraman et al. 2013 for a more comprehensive introduction):
Similar to direct N-body models, the simulation follows the evolution of N stellar particles. However, the particles are fully characterized by their orbital properties (energy E and angular momentum J). At the beginning of each simulation step, the cluster’s symmetric potential is calculated. Then for each

star, statistically representative perturbations of E and J are calculated using neighboring stars. At the end of the time step, new positions and velocities for each star particle are determined by randomly sampling a representative orbit.

The main assumptions enabling these approximations are spherical symmetry, a sufficiently large particle number, that the system is dominated by relaxation, and that the relaxation time is significantly larger than the orbital timescales (or crossing time). The computational complexity of the Monte Carlo algorithms scales with $O(N \log N)$.

There are two main modern implementations of this scheme: MOCCA[1] (Giersz et al., 2013, 2015) and CMC[2] (Pattabiraman et al., 2013; Rodriguez et al., 2022), both of which include advanced recipes for the treatment of stellar evolution and binary interactions. Both of these methods have been used to create and follow the evolution of large samples of synthetic star clusters with different parameters such as the CMC Cluster Catalog (Kremer et al., 2020) or the MOCCA-Survey Databases (Askar et al., 2017), where both initial conditions and poorly constrained physical processes can be varied.

2.3 THE ENIGMATIC GLOBULAR CLUSTER ω CEN

2.3.1 OVERALL PROPERTIES

Omega Centauri (ω Cen) is the brightest (m_V=3.68, Harris 2010) and most massive ($M \approx 3.55 \times 10^6$ M$_\odot$, Baumgardt & Hilker, 2018) globular cluster of the Milky Way. Due to its relatively close distance ($d = 5.445$ kpc; see Chapter 5) and its peculiar properties, it has been subject to many observational campaigns over the whole wavelength range, and it may well be the best studied globular cluster. However, the origin of its complex multiple populations, the distribution of its (partially unseen) mass, and the potential connection with its former host galaxy are all unresolved questions under active investigation. In the following, I briefly summarize some of the peculiar properties of ω Cen and introduce the wider context in which the work presented in this thesis was performed. In addition, detailed introductions focusing on specific aspects are given in each individual chapter (Chapter 3: astrometric and photometric studies, Chapter 4: the IMBH case, Chapter 5: the kinematics).

2.3.2 MULTIPLE STELLAR POPULATIONS

The complexity of ω Cen is unique among the globular clusters of the Milky Way: Spectroscopic observations reveal a large spread in metallicity (Freeman & Rodgers, 1975; Johnson & Pilachowski, 2010; Marino et al., 2011; Nitschai et al., 2024) ranging from [Fe/H]~ -2.2 to -0.5. Studies of the age distribution are less conclusive, with results ranging from 0.5 Gyrs (Tailo et al., 2016), 1-2 Gyrs (Joo & Lee, 2013) to 4-5 Gyrs (Villanova et al., 2007). In our recent work based on around 8000 subgiant branch stars we find stellar ages ranging from 10 to 13 Gyrs (Clontz et al., 2024, see also Subsection 8.1.3).

While spectroscopic observations are mostly limited to evolved stars, photometric observations with

---

[1] MOnte Carlo Cluster simulAtor (MOCCA); https://moccacode.net/

[2] The Cluster Monte Carlo Code (CMC); https://clustermontecarlo.github.io/CMC-COSMIC/

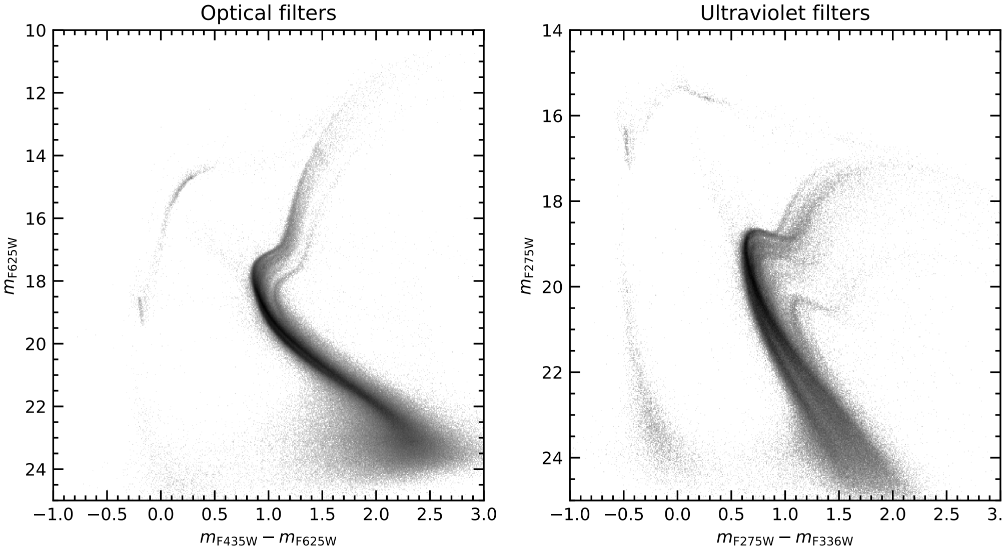

Figure 2.1: Color magnitude-diagrams of ω Cen based on oMEGACat photometry (see Chapter 3). The CMDs are based on observation with optical *(left)* and ultra-violet *(right)* filters. Both CMDs show various stages of stellar evolution (main sequence, sub giants, red giants, horizontal branch, white dwarfs). The complexity of ω Cen's subpopulations causes multiple turn-offs and split-sequences.

the Hubble Space Telescope have also enabled the study of ω Cen's subpopulations on the main sequence revealing even more complexity (Anderson, 1997; Pancino et al., 2000; Bedin et al., 2004; Ferraro et al., 2004; Bellini et al., 2010, 2017c; Milone et al., 2017a). Especially the blue and UV bands (m_{F275W}, m_{F336W}, m_{F435W}) are sensitive to variations in light elements and in Bellini et al. (2017d) at least 15 individual subpopulations were identified. Two color-magnitude diagrams based on the oMEGACat photometry (see Chapter 3) are shown in Figure 2.1.

2.3.3 The accretion scenario

Around 25 years ago, a new scenario for the origin of ω Cen emerged that explains its complexities and the differences with other Milky Way globular clusters: ω Cen could be the stripped nucleus of a dwarf galaxy that has been accreted and disrupted by the Milky Way (Lee et al., 1999; Hilker & Richtler, 2000; Bekki & Freeman, 2003).

Several works used kinematic information from the ESA Gaia mission to link the globular clusters of the Milky Way with different accretion events (Massari et al., 2019; Helmi, 2020; Malhan et al., 2022). In the specific case of ω Cen, both associations with stellar streams (Majewski et al., 2012; Ibata et al., 2019) and with either the Sequoia or the Gaia-Enceladus merger events (Myeong et al., 2019; Massari et al., 2019; Forbes, 2020; Pfeffer et al., 2021; Limberg et al., 2022; Pagnini et al., 2024) were found.

2.3.4 Internal kinematics and IMBH discussions

As a high-mass cluster and potential nucleus of an accreted dwarf galaxy, ω Cen has been the subject of a long debate about the presence of an intermediate-mass black hole in its center. Its kinematics have been studied extensively using both line-of-sight velocity-based measurements (Meylan & Mayor, 1986; Merritt et al., 1997; Pechetti et al., 2024) and proper motions (van Leeuwen et al., 2000a; Bellini et al., 2014; Watkins et al., 2015a,b); see also Chapter 5 and reference therein.

Early works found evidence for a central rise in the velocity dispersion measured with integrated-light spectroscopic observations and used dynamical models to estimate a black hole mass of around 40,000 $M_\odot$ (Noyola et al., 2008, 2010). However, a subsequent analysis of Hubble Space Telescope-based proper motions did not require a black hole (Anderson & van der Marel, 2010; van der Marel & Anderson, 2010), and other works noted the potential influence of stellar-mass black holes on the observed kinematics (Zocchi et al., 2019; Baumgardt et al., 2019b; Bañares-Hernández et al., 2025). With the absence of any accretion signal in both deep radio Tremou et al. (2018) and X-ray (Haggard et al., 2013) searches, the search for an IMBH remained inconclusive. Chapter 4 focuses on identifying fast-moving stars in the center of ω Cen to infer the presence of an IMBH.

2.3.5 The oMEGACat project

Given its special properties discussed above, ω Cen provides a unique opportunity to both study a remnant of an important accretion event in the history of the Milky Way and the nucleus of a dwarf galaxy, whose evolution was halted when it was stripped of its stars and gas. In the oMEGACat collaboration (https://omegacatalog.github.io/), led by Nadine Neumayer[3] and Anil Seth[4], we aim to disentangle both the formation history and the present day dynamics of ω Cen by creating a comprehensive spectroscopic, photometric and astrometric dataset. The spectroscopic catalog of the dataset is based on an extensive VLT MUSE mosaic consisting of both GO (PI: N. Neumayer) and GTO (PIs: Stefan Dreizler, Sebastian Kamann) data. It provides metallicity and line-of-sight velocity measurements for 300,000 stars and has become fully public along with Nitschai et al. (2023).
The complementary astro-photometric catalog is based on hundreds of images taken with the Hubble Space Telescope, that have been obtained from the archive and a dedicated program (GO-16777, PI: A. Seth). The creation and subsequent analysis of the astro-photometric catalog is the main project of this thesis. The data reduction and photometric and astrometric measurements are described in Chapter 3. In Chapter 4 I describe a search for fast-moving stars indicative of an IMBH in ω Cen, and in Chapter 5 I use the combined astrometric and photometric catalogs to study the overall kinematic properties of ω Cen. Several other projects from members of our collaboration use the combined datasets and focus on various aspects of ω Cen, ranging from studies of individual elemental abundances to detailed dynamical models. An overview of the ongoing projects is given in Section 8.1.

---

[3] Max Planck Institute for Astronomy, Heidelberg, Germany
[4] University of Utah, Salt Lake City, USA

II. MAIN SCIENTIFIC RESULTS

3 PHOTOMETRY AND PROPER MOTIONS FOR 1.4 MILLION STARS IN ω CENTAURI AND ITS ROTATION IN THE PLANE OF THE SKY

This chapter has been published in Häberle et al. (2024b). I conducted the described data reduction and analysis and wrote all the text, except for Subsection 3.8.2 which was written by co-author Sebastian Kamann. All co-authors have provided comments on the manuscript and help and advice for the analysis. The formatting has been adapted to match this thesis.

List of co-authors: Nadine Neumayer, Andrea Bellini, Mattia Libralato, Callie Clontz, Anil Seth, Maria Selina Nitschai, Sebastian Kamann, Mayte Alfaro-Cuello, Jay Anderson, Stefan Dreizler, Anja Feldmeier-Krause, Nikolay Kacharov, Marilyn Latour, Antonino Milone, Renuka Pechetti, Glenn van de Ven, Karina Voggel

ABSTRACT

Omega Centauri (ω Cen) is the most massive globular cluster of the Milky Way. It is thought to be the nucleus of an accreted dwarf galaxy because of its high mass and its complex stellar populations. To decipher its formation history and study its dynamics, we created the most comprehensive kinematic catalog for its inner region, by analyzing both archival and new *Hubble Space Telescope (HST)* data. Our catalog contains 1 395 781 proper-motion measurements out to the half-light radius of the cluster ($\sim 5.0'$) and down to $m_{\mathrm{F625}W} \approx 25$ mag. The typical baseline for our proper-motion measurements is 20 years, leading to a median 1D proper motion precision of ~11 µas yr^{-1} for stars with $m_{\mathrm{F625}W} \approx 18$ mag, with even better precision (~6.6 µas yr^{-1}) achieved in the extensively observed centermost ($r < 1.5'$) region. In addition to our astrometric measurements, we also obtained precise *HST* photometry in seven filters spanning from the ultraviolet to the near-infrared. This allows detailed color-magnitude-diagram studies and to separate the multiple stellar populations of the cluster. In this work, we describe the data reduction used to obtain both the photometric and the proper-motion measurements. We also illustrate the creation and the content of our catalog, which is made publicly available. Finally, we present measurements of the plane-of-sky rotation of ω Cen in the previously unprobed inner few arcminutes and a precise measurement of the inclination $i = (43.9 \pm 1.3)^\circ$.

3.1 INTRODUCTION

3.1.1 THE ACCRETION HISTORY OF THE MILKY WAY

In recent years the formation history of the Milky Way has been unraveled, thanks to the *Gaia* satellite (Gaia Collaboration et al., 2016b), which provides 6-D phase space information for millions of stars, in combination with large spectroscopic surveys such as APOGEE (Allende Prieto et al., 2008; Majewski et al., 2017), LAMOST (Deng et al., 2012), and GALAH (De Silva et al., 2015; Buder et al., 2021). These surveys have revealed that our Galaxy has experienced a series of mergers, where smaller dwarf galaxies were accreted by the more massive Milky Way. During those mergers, the dwarf galaxy is disrupted by tidal forces (Helmi & White, 2001; Mayer et al., 2002) and its stars are scattered across the Halo of the Milky Way.

The largest of the recently discovered mergers is the *Gaia Enceladus* event, a merger ~10 Gyrs ago with a satellite galaxy with a stellar mass of 6×10^8 $M_\odot$ (Belokurov et al., 2018; Haywood et al., 2018), similar to the present-day mass of the Small Magellanic Cloud. There are also signs of other smaller accretion events such as *Sequoia* (Myeong et al., 2019),the Helmi-Streams (Helmi et al., 1999) or the Pontus merger Malhan et al. (2022); Malhan (2022). An example, where accretion is still ongoing, is the Sagittarius Dwarf Galaxy (Ibata et al., 1997; Laporte et al., 2018). The central regions of Sagittarius remain bound, including the nuclear star cluster of the galaxy, M54 (Alfaro-Cuello et al., 2019, 2020; Kacharov et al., 2022).

While the field stars of accreted galaxies are scattered across the halo of the Milky Way and can only be identified in action space and via their chemistry, the dense globular clusters of the accreted galaxy can survive the merger (Peñarrubia et al., 2009) and are added to the globular cluster population of the Milky Way (Searle & Zinn, 1978; Kruijssen et al., 2019). Massari et al. (2019) kinematically linked the globular clusters of the Milky Way to different known accretion events, and found that only about 40% of the clusters are likely to have formed in-situ. In addition to globular clusters, most galaxies contain a very dense and massive nuclear star cluster in their center (e.g. Neumayer et al., 2020), which remains intact during accretion. These nuclear star clusters can be fully stripped of their surrounding galaxy (Pfeffer & Baumgardt, 2013) and look very similar to massive globular clusters. Kruijssen et al. (2019) predict 6±1 stripped nuclear star clusters hiding within the Milky Way's globular cluster population.

The most promising stripped nuclear star cluster candidate is Omega Centauri (ω Cen), the most massive ($M \approx 3.55 \times 10^6$ $M_\odot$, Baumgardt & Hilker, 2018) globular cluster in the Milky Way (e.g. Lee et al., 1999; Bekki & Freeman, 2003). ω Cen is relatively close to the Sun ($d_\odot \approx 5.43$ kpc, Baumgardt & Vasiliev, 2021), which allows us to study it in great detail. Decades of observations have shown that ω Cen is unique among the Milky Way's globular clusters in many ways. The first evidence for ω Cen's complex stellar populations was the discovery of a large scatter of the cluster's red giant branch by Cannon & Stobie (1973), followed by spectroscopic observations that revealed a large metallicity spread (Freeman & Rodgers, 1975). Newer spectroscopic catalogs confirmed those early findings and include spectra of thousands (Johnson & Pilachowski, 2010) or most recently even hundreds of thousands of stars (Kamann et al., 2018; Nitschai et al., 2023). These studies found a spread in iron abundance of almost 2 dex, ranging from [Fe/H]~ -2.2 to -0.5, a much larger spread than for other Milky Way globular clusters. In addition to these spectroscopic findings, precise *Hubble Space Telescope (HST)* photometry played a crucial role in highlighting the complexity of the stellar populations for a much larger sample, including fainter stars (Anderson, 1997; Ferraro et al., 2004; Bellini et al., 2010). The detailed color-magnitude diagrams (CMDs) show an amazing complexity of several split sequences and subpopulations. Based on studying various ultra-violet (UV) CMDs, Bellini et al. (2017d) were able to distinguish at least 15 subpopulations along the main sequence. Another very powerful tool to photometrically disentangle the different subpopulations are the so-called chromosome maps based on UV filters (Milone et al., 2017a). The different subpopulations in ω Cen are also believed to have different ages (Hilker et al., 2004; Villanova et al., 2014), although the exact duration of the star formation is still controversial and estimates range from less than 0.5 Gyrs (Tailo et al., 2016), 1-2 Gyrs (Joo & Lee, 2013) to 4-5 Gyrs (Villanova et al., 2007). The determination of relative ages is complicated by differences between the abundances of light elements for the different subpopulations (Marino et al., 2012).

Besides these peculiar stellar populations, there is also kinematic evidence supporting the stripped nucleus scenario: van de Ven et al. (2006) found evidence for the presence of a central stellar disk and a preference for tangential orbits in the outer parts. More recently, both kinematic and chemical associations with stellar streams such as the *Fimbulthul* stream have been found in e.g. Majewski et al. (2012), Ibata et al. (2019), and Limberg et al. (2022). Another approach is taken in Marks et al. (2022), in which a connection between the low retrograde binary fraction in the Milky Way and the star formation conditions in ω Cen's progenitor is studied. Both the Sequoia and the Gaia-Enceladus/Sausage progenitors have been discussed as potential former host-galaxies of ω Cen (Myeong et al., 2019; Massari et al., 2019; Forbes, 2020; Pfeffer et al., 2021).

To summarize, ω Cen is most likely an accreted nuclear star cluster and therefore, both the closest galactic nucleus (even closer than the Galactic Center) and a remnant of an important accretion event in the history of the Milky Way. Studying its formation can reveal both details of the Milky Way's assembly history and nuclear star clusters.

3.1.2 Project overview

The *oMEGACat* project aims to decipher the formation history and dynamics of ω Cen by assembling the largest spectroscopic, photometric, and astrometric data set out to the cluster's half-light radius. The spectroscopic part of this dataset is an extensive study performed with the Very Large Telescope Multi-Unit Spectroscopic Explorer (MUSE, Bacon et al. 2010a) integral field spectrograph. This spectroscopic catalog has recently been published (Nitschai et al., 2023) and contains line-of-sight velocities and metallicity measurements for more than 300 000 stars.

In this paper, we describe the creation of the second part of the dataset, a complementary astro-photometric catalog, based on archival and new *HST* observations.

Both the spectroscopic and the astro-photometric catalogs are made public and therefore provide a legacy dataset for the community.

3.1.3 OUTLINE OF THIS WORK

In Section 3.2 we review other published ground- and space-based astrometric and photometric catalogs for ω Cen. In Section 3.3 we give a brief overview of the dataset that has been used to create our catalog. In Section 3.4 we describe our data reduction, which yields individual astro-photometric measurements from the *HST* images. We explain how we determine proper motions based on those individual data points in Section 3.5. In Section 3.6 we describe how we create a uniform photometric catalog based on the individual measurements. In Section 3.7 we perform several crosschecks and comparisons to other catalogs, which we use to test the quality of our dataset. In Section 3.8 we present the first science results based on our catalog: a redetermination of the plane-of-sky rotation of ω Cen. We conclude the work with a description of the published data products (Section 3.9) and our conclusions in Section 3.10.

3.2 REVIEW OF OTHER ASTROMETRIC AND PHOTOMETRIC CATALOGS FOR ω CEN

3.2.1 OTHER PROPER MOTION CATALOGS

The study of the proper motions within ω Cen has a long history, including several ground- and space-based catalogs. In Table 3.1 we provide a complete overview of all these catalogs along with information on their coverage, depth, and astrometric precision.

Astrometric studies of ω Cen started with photographic plate measurements by Murray et al. (1965) and Woolley (1966) at the Royal Greenwich Observatory. Another large plate-based effort was taken by van Leeuwen et al. (2000b) and reached the impressive precision of 0.1 mas yr^{-1} thanks to the long baseline of more than 50 years. Other plate-based (or hybrid plate / CCD) studies with the goal of constraining the absolute motion of ω Cen were published in Dinescu et al. (1999) and Geffert et al. (2002), although no proper motion catalog was made public along these works. A more recent remarkable wide-field ground-based study was done by Bellini et al. (2009a) with the CCD-imager WFI@ESO/MPG2.2m.

The era of space astrometry was initiated with the Hipparcos Satellite (Perryman et al., 1997), but due to the limited depth, neither the HIPPARCOS catalog, nor the hybrid Tycho-2 catalog (Høg et al., 2000) allowed to study the internal kinematics of ω Cen. Freeman (2001) report only 3 Hipparcos stars and 53 Tycho-2 stars in common with van Leeuwen et al. (2000b).

In comparison, the *Hubble Space Telescope* proved to be the perfect tool for crowded field astrometry. Its high resolution and well-characterized, stable point spread function allow individual astrometric measurements with 0.4 mas precision (Anderson & King, 2006; Bellini et al., 2011). Thanks to its high sensitivity, very faint stars can also be studied. For ω Cen, the main limitation is the comparatively small field of view of its main imaging instruments ($3'.3 \times 3'.3$ for ACS/WFC, $2'.7 \times 2'.7$ for WFC3/UVIS); the existing *HST* proper-motion catalogs cover an area of only one or two *HST* pointings. The first *HST* proper motion study of ω Cen's innermost region was done in Anderson & van der Marel (2010),

Table 3.1: List of all published proper-motion catalogs for Omega Centauri

Catalog	Instrument	Covered Area	Limiting Magnitude	Number of entries	Max. Baseline	Bright Star Proper Motion Error
Murray et al. (1965); Woolley (1966)	Royal Greenwhich Observatory		$B < 16.8$	∼4000	56 yrs	2.0 mas yr^{-1}
Hipparcos (Perryman et al., 1997)	Hipparcos	Allsky		3	3.5 yrs	
Tycho 2 (Høg et al., 2000)	Hipparcos	Allsky		53	3.5 yrs	
van Leeuwen et al. (2000b)	Yale-Columbia 66cm refractor	$r \leq 29'.5$	$B < 16.0 - 16.5$	9847	52 yrs	0.1 mas yr^{-1}
Bellini et al. (2009a)	MPG 2.2m WFI	$33' \times 33'$	$B < 20$	360 000	4 yrs	1.1 mas yr^{-1}
Anderson & van der Marel (2010)	HST	Central Field ($r \leq 2'$) Major Axis field ($r \approx 4'$)	$m_{\mathrm{F625}W} < 23$ $m_{\mathrm{F625}W} < 22.5$	108 507 61 293	4.07 yrs 2.5 yrs	0.1 mas yr^{-1} 0.2 mas yr^{-1}
Bellini et al. (2017a)	HST	$r \leq 2'.5$	$m_{\mathrm{F606}W} < 24$	279 909	10.6 yrs	0.025 mas yr^{-1}
Gaia (E-)DR3 (Gaia Collaboration et al., 2021a)	Gaia	Allsky	*Gaia G* <17 (center)	321 698 (within $r \leq 0.8°$)	2.8 yrs	0.02 mas yr^{-1}
Bellini et al. (2018b)	HST	1 field at $3.5 r_{HL} \approx 17'$	$m_{\mathrm{F606}W} < 27$	5 153	15 yrs	0.01 mas yr^{-1}
Scalco et al. (2021)	HST	2 fields at $2.5 r_{HL} \approx 12'$	$m_{\mathrm{F606}W} < 27$	27 885	2 yrs	0.07 mas yr^{-1}
Gaia FPR (Gaia Collaboration et al., 2023b)	Gaia	$r \leq 0.8°$	*Gaia G* <20.5	526 587	5 yrs	0.3 mas yr^{-1}
oMEGACat (this work)	HST	$10' \times 10'$	$m_{\mathrm{F625}W} < 25$	1 399 455	20.89 yrs	0.007 mas yr^{-1} (center) 0.012 mas yr^{-1} (full field)

with an additional field South-East of the center. The measurements in this area were significantly improved in Bellini et al. (2014) and published along an extensive photometric catalog in Bellini et al. (2017a). This most recent public catalog covers the core region out to a radius of $\sim 2'.7$ and has a maximum temporal baseline of 12 years. One other notable work based on *HST* observations of the center of ω Cen was the detection of astrometric acceleration by dark companions presented in Platais et al. (2023), however the astrometric catalog has not been made public. Other *HST* fields at larger radii have been analyzed in Bellini et al. (2018b) ($r \sim 17' \sim 3.5 r_{\mathrm{HL}}$) and Scalco et al. (2021) ($r \sim 12' \sim 2.5 r_{\mathrm{HL}}$). Due to the lower stellar density at these radii and the long exposure times, those fields mark the deepest observations of ω Cen at the time of writing, reaching magnitudes of $m_{\mathrm{F606}W} \sim 27$.

In addition to *HST*, the *Gaia* astrometry satellite (Gaia Collaboration et al., 2016a) has measured hundreds of thousands of absolute proper motions in the outer regions of ω Cen. However, even in the most recent general data release DR3 (Gaia Collaboration et al., 2023a) (whose astrometric component was already published as Early Data Release 3; Gaia Collaboration et al. 2021a; Lindegren et al. 2021), the *Gaia* measurements are both limited in depth and precision in the center due to the high crowding and the limited resolution of the satellite. One main challenge is the *Gaia* readout window strategy, which runs into processing and downlink limitations for extremely crowded fields such as ω Cen. For this reason, the *Gaia* collaboration has taken dedicated engineering images, the so called Service Interface Function (SIF) images. An extension of the regular *Gaia* catalog for ω Cen has been made public during the *Gaia Focused Product Release (FPR)* (Gaia Collaboration et al., 2023b). Using the engineering images and dedicated on-the-ground data processing, measurements for 526 587 additional stars have been added for a region with a radius of around $\sim 0.8°$ around the center of ω Cen. Especially for the central few arcminutes, this leads to much better completeness than in *Gaia* DR3, however with relatively large astrometric errors (due to the binned nature of the SIF images). In Section 3.7 we present a detailed comparison between the different astrometric datasets.

The new catalog presented in this work represents a significant improvement over previous astrometric catalogs in several ways: In comparison with earlier *HST* catalogs, we cover a much larger field of view out to the half-light radius, with a significantly longer and highly uniform baseline as well as new, state-of-the-art, photometry tools. Our catalog is complementary to the recent *Gaia FPR*: while the strength of the *Gaia FPR* is the uniform completeness out to very large radii and its anchoring in an absolute reference frame, we tackle the crowded inner regions with a higher sensitivity and resolution and much longer temporal baseline, resulting in significantly lower astrometric errors and measurements for fainter stars. Within the half-light radius, the new *HST* measurements probe around 3 magnitudes deeper than the *Gaia FPR* data and have proper motion errors at least one order of magnitude better. In addition, the proper-motion catalog presented in this work is complemented by the uniform 6-band photometry we publish along with it.

3.2.2 OTHER *HST* PHOTOMETRY CATALOGS OF ω CEN

In the past years, several photometric catalogs based on *HST* imaging have been published for ω Cen with various science goals. Some of them were published together with the astrometric catalogs already mentioned in the previous section. The first *HST* based photometric catalog of ω Cen was created as part of the "The ACS Survey of Globular Clusters" and is described in Anderson et al. (2008). A much larger catalog was then published by Anderson & van der Marel (2010), covering a grid of 3×3 ACS/WFC pointings, giving an on-sky extent of $10' \times 10'$ and containing deep photometry for 2×10^6 stars in the F435W and F625W filters. The data used for this study - observed in 2002 - marks the first epoch for most of our proper-motion measurements. With the installation of the WFC3/UVIS instrument, a new range of UV filters became available. They have been used to study multiple populations, for example in Bellini et al. (2010) and Bellini et al. (2013). The deepest photometry for ω Cen has been obtained for a Large Project (Milone et al., 2017b) with the goal of studying the stars at the faint end of the main sequence. Several astrometric and photometric catalogs based on this data have been published (Bellini et al., 2018b; Libralato et al., 2018a; Scalco et al., 2021; Gerasimov et al., 2022). The most recent catalog for the core of ω Cen was published by Bellini et al. (2017a), containing the most comprehensive set of filters (18 WFC3/UVIS filters and 8 WFC3/IR filters) and the same state-of-the-art photometry software as in this work. This catalog is limited to the centermost region of ω Cen with $r \leq 2'.5$.

All the mentioned photometric *HST* catalogs have excellent photometric quality and some of them reach even deeper than the data presented in this work or have a larger set of filters. The unique feature of our catalog is the large field which is uniformly covered with deep photometry in 6 filters while at the same time also adding high-precision astrometry.

3.3 DATASET

ω Cen is one of the individual objects with the largest number of *HST* observations. This is in part due to its interesting properties which have sparked many science programs, but also because it provides an almost ideal calibration target for high-resolution imaging instruments, due to its high and fairly uniform central stellar density. For this reason, it was chosen as the astrometric calibration field for the WFC3/UVIS instrument and is repeatedly observed to monitor the astrometric stability (see e.g. Kozhurina-Platais & Anderson, 2015).

For our study, we used imaging data obtained with the Advanced Camera for Surveys (ACS) Wide Field Channel and the Wide Field Camera 3 UVIS Channel. The data from both of these instruments are similar: both instruments have a mosaic of two 2048×4096 pixel CCD detectors with a narrow chip gap, giving approximately a square footprint on the sky. The ACS/WFC, installed during Service Mission 3B, has a nominal pixel scale of around 50 mas pixel^{-1}, giving a field of view of $3'.3 \times 3'.3$. WFC3/UVIS was installed during Service Mission 4 and has a slightly higher resolution with a pixel scale of around 40 mas pixel^{-1}, resulting in a field of view of $2'.7 \times 2'.7$.

Table 3.2: List of all filters used for the creation of our astro-photometric catalog. In the fourth column we state whether a filter has been used only for photometry (phot.), astrometry (astro.), or both.

Instrument	Filter	$N_{exp.}$	Usage
ACS/WFC	F435W	69	astro. & phot.
ACS/WFC	F475W	7	astro. only
ACS/WFC	F555W	4	astro. only
ACS/WFC	F606W	35	astro. only
ACS/WFC	F625W	40	astro. & phot.
ACS/WFC	F658N	39	phot. only
ACS/WFC	F775W	8	astro. only
ACS/WFC	F814W	33	astro. only
WFC3/UVIS	F275W	85	phot. only
WFC3/UVIS	F336W	106	astro. & phot.
WFC3/UVIS	F390W	15	astro. only
WFC3/UVIS	F438W	49	astro. only
WFC3/UVIS	F555W	25	astro. only
WFC3/UVIS	F606W	184	astro. & phot.
WFC3/UVIS	F775W	18	astro. only
WFC3/UVIS	F814W	79	astro. & phot.

In total, we reduced 236 images taken with the Advanced Camera for Surveys (ACS) Wide Field Channel, and 561 images taken with the Wide Field Camera 3 UVIS Channel, including both archival data and data from a new, dedicated program (GO-16777, PI: A. Seth). However, not all filters are suitable for high-precision astrometry, due to the unavailability of dedicated high-precision geometric distortion corrections. Proper motions are, therefore, based on a subset of the data, including 196 ACS/WFC and 476 WFC3/UVIS exposures. For the photometric catalogs, we restricted ourselves to the six filters with the widest field coverage (WFC3/UVIS F275W, F336W, F814W; ACS/WFC F435W, F625W, F658N). These 6 filters fill the half-light radius with only minimal gaps. In addition, we also included the WFC3/UVIS F606W filter which has only been used in the central region of ω Cen. Due to the large number of calibration observations ($N_{used} = 184$) in this filter it provides excellent photometric quality out to $r \sim 2.5'$. Footprints of the utilized observations can be found in Figure 3.1. Table 3.2 lists all filters and the number of images used for the creation of our catalogs. We note that, while the ACS High Resolution Channel is principally suitable for high-precision astrometry, there are no usable observations within the field covered in this study. Although available in the archive, we also did not make use of any WFC3/IR images, as they are less useful for high-precision astrometry due to their relatively large pixel size (130 mas pixel^{-1}). A state-of-the-art reduction of the WFC3/IR data can be found in Bellini et al. (2017a). A detailed list of all program IDs, filters, and exposure times used for our analysis is shown in Tables 3.6 and 3.7 in Appendix 3.11. In addition, all the HST data used in this paper can be found under the following DOI in the Mikulski Archive for Space Telescopes (MAST): [10.17909/26qj-g090]http://dx.doi.org/10.17909/26qj-g090.

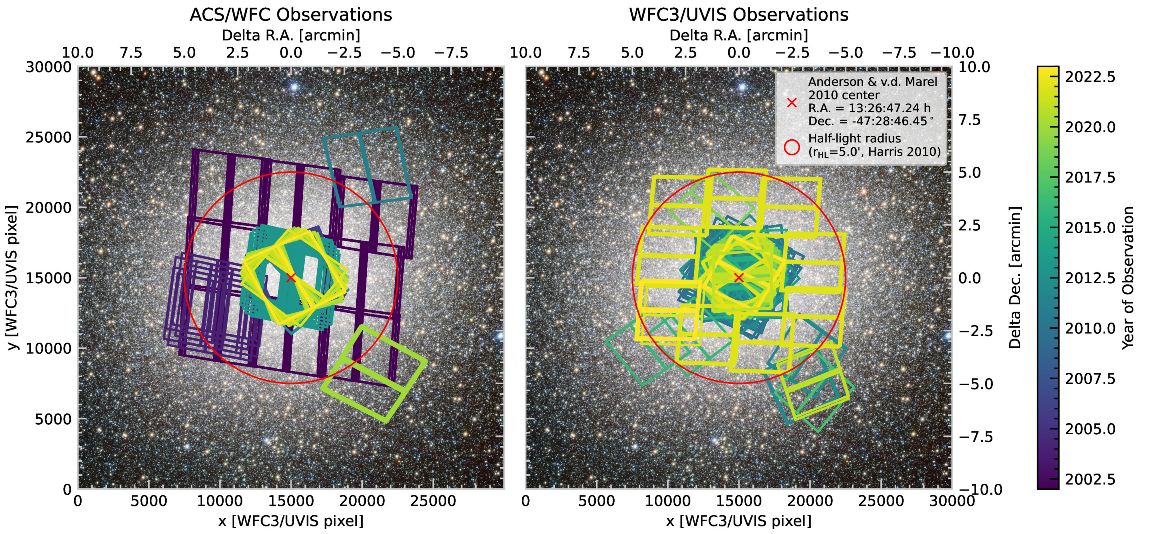

Figure 3.1: The footprint of the *HST* observations used to measure photometry and determine proper motions, color-coded according to the year of observation. The plots are in both our pixel-based coordinate system and in relative angular units. The left panel shows observations with the ACS/WFC instrument, the right panel with the WFC3/UVIS instrument. The background shows a wide field image of ω Cen taken with the ESO/VST telescope (Image Credit: ESO/INAF-VST/OmegaCAM. Acknowledgement: A. Grado, L. Limatola/INAF-Capodimonte Observatory, https://www.eso.org/public/images/eso1119b/)

3.4 ASTROPHOTOMETRIC DATA REDUCTION

In general, our data reduction follows the procedures described in Bellini et al. (2017a), Libralato et al. (2018b), and Libralato et al. (2022). However, we had to adapt the procedures due to the larger field and the large number of epochs.

3.4.1 FIRST PHOTOMETRY ITERATION WITH `hst1pass`

As a first step in our data reduction, we ran the point spread function (PSF) photometry code `hst1pass` (Anderson, 2022) on all individual exposures in our dataset. For all data reduction steps, we used `*_flc.fits` images that are flat-field and charge-transfer-efficiency corrected, but not resampled. This preserves the original astrometric signal we aim to study.

`hst1pass` uses the library effective PSF (ePSF) models described in Anderson & King (2006). When available, we used the state-of-the-art focus-diverse ePSF models described in Bellini et al. (2018a) for ACS/WFC and Anderson (2018) for WFC3/UVIS. `hst1pass` further improves the library ePSF to better match those of each individual image. This is necessary due to the time variability of the *HST* PSF caused by telescope breathing and focus variations. For typical observations, the central values of the PSF change by around 5% (RMS over the full field), although in some rare cases, this change can be up to 25%. We saved these perturbed ePSF models for each image, as we need them later for the second photometry stage.

We used the geometric distortion corrections from Anderson & King (2006); Anderson (2006) for ACS/WFC[1], and from Bellini & Bedin (2009); Bellini et al. (2011) for WFC3/UVIS to correct stellar positions in each `_flc` exposure. For WFC3/UVIS filters with no dedicated high-precision correction available, we used the F606W correction. These filters were not used for the proper motion determination but are only used for photometry.

3.4.2 GROUPING THE DATA INTO EPOCHS

After we obtained single-image catalogs for each exposure, we grouped all these individual exposures in 1-year bins, from 2002 to 2023. If there were multiple sets of non-overlapping exposures (e.g. a set of observations of the center and another one of a different region), we created separate bins for them. In total, this leaves us with 26 groups that we reduced separately. For each of them, we created astrometric master frames (see Section 3.4.3), performed an initial photometric registration (see Section 3.6.1) and finally run the second iteration of the photometry (see Section 3.4.6). This is a compromise between creating very deep image stacks to improve the completeness and having image stacks based on short-time scales to facilitate the detection of fast-moving stars.

3.4.3 REFERENCE FRAME AND ASTROMETRIC IMAGE REGISTRATION

For the second iteration of photometry and the proper-motion determination, we need to set up a common reference frame in which we can precisely anchor each *HST* image. To do so, we use a hybrid *Gaia-HST* reference frame, which is created in the following way:

First, we queried the *Gaia* EDR3 (Gaia Collaboration et al., 2021a; Lindegren et al., 2021) with a search-radius of 10 arcmin around the center of ω Cen. This initial spatial selection gives us 100 170 sources. To them, we applied strict quality selections:

- Successfully measured photometry in both the `RP` and the `BP` bands
- Renormalized Unit Weight Error `RUWE < 1.5`
- Total Position Error `< 1 mas`
- Total proper-motion error `< 0.3 mas/yr`

Many *Gaia* measurements in the center of ω Cen suffer from crowding, and therefore, only 13 520 stars pass our combined selection criteria. These well-measured stars are typically very bright (at $r = 0'$, *Gaia* G mag < 12; at $r = 2.5'$, *Gaia* G mag < 16; and at $r = 5.0'$, *Gaia* G mag < 18). We note that at the time of making this work the *Gaia FPR*, which addresses some of the crowding issues, was not available yet. Regardless, the astrometric precision of the bright stars from *Gaia DR3* used as absolute astrometric reference is higher than the precision of the sources in *Gaia FPR* (see also Section 3.7); therefore, the inclusion of the *Gaia FPR* data would not significantly improve the astrometric registration.

---

[1] For the proper-motion measurements we also applied look-up table corrections to post SM4-*HST* observations, see Section 3.5.2

The *Gaia* proper motions of these reference stars were used to extrapolate their positions from the *Gaia* reference epoch (2016.0) to the epoch of the GO-9442 *HST* observations (∼2002.5), to allow for a more precise astrometric match to the oldest *HST* data. Then, the angular *Gaia* coordinates were converted to a convenient, pixel-based coordinate system using a tangent-plane projection. Our reference frame is defined with North up, East to the left, a pixel scale of 40 mas pixel^{-1} (similar to the UVIS instrument) and the cluster center at $(x, y) = (15000, 15000)$. We used `R.A. = 13:26:47.24h Dec. = -47:28:46.45`° for the cluster center as found by Anderson & van der Marel (2010); these are also the central coordinates provided in the Harris (2010) catalog.

We then crossmatched this *Gaia*-based reference frame with the single-image *HST* catalogs by determining the ideal linear six-parameter transformations to convert our image-based coordinates to the reference frame. At this step we encounter a fundamental challenge: While the well-measured *Gaia* stars are typically very bright, they are saturated in the deep *HST* exposures and therefore unusable for high-precision astrometry.

Therefore, we applied a two-step procedure. In the first step, we only crossmatched the short exposure time ACS observations (12 s-F435W, 8 s-F625W) from the 2002 epoch with the *Gaia* reference stars. For these exposures a sufficiently high number of unsaturated stars was available and we could reliably determine the linear transformations. All the transformed short-exposures were combined to a first short-exposure *HST* master frame. In the second step, we crossmatched all other (long) *HST* exposures with the short-exposure master frame and created, by combining positions measured from all 2002 exposures, our second *HST* astrometric master frame.

For all epochs post-2002 we distinguished between the center and the off-center observations:

- In the central region (where *Gaia* stars are sparse), for each epoch we incrementally crossmatched all exposures with the astrometric master frame of the previous epoch and determined the optimal linear transformations onto this preceding master frame. Then, we averaged the individual measured positions of the new data to create a new master frame (using only filters with a dedicated high-precision geometric distortion correction). This approach is reasonable because the time difference between the central epochs is low (typically just one year) and therefore the spatial displacements between epochs are expected to be small.

- For the non-central regions (where the temporal gaps between *HST* epochs are longer and there are more *Gaia* stars), we updated the *Gaia* based reference frames by propagating the stars to the correct epoch and then using the same hybrid-approach as described above for the 2002 epoch (but also only using exposures with a dedicated geometric distortion correction). When propagating the *Gaia* positions to the correct epoch, we corrected for the absolute motion of ω Cen, as we want all our frames registered to the same cluster-based reference system.

3.4.4 KNOWN-OFFSETS AND MOTION OF THE CENTER

As described above, our astrometric reference system is based on positions from *Gaia* (E-)DR3 and using the center estimate from Anderson & van der Marel (2010) (in the following AvdM10). Although both the AvdM10 center coordinates and the *Gaia* positions are given in the International Celestial Reference System (ICRS), we have to note two caveats here: first of all, the AvdM10 was anchored on the *HST* catalog from Anderson et al. (2008), which itself was anchored on a small number of bright stars from the 2MASS catalog. The 2MASS astrometric reference frame has an absolute astrometric accuracy of 15 mas (Skrutskie et al., 2006), but the errors of individual sources can be significantly larger. Indeed we observe an astrometric offset between the AvdM10 catalog and our new (Gaia-based) absolute astrometry of around 100 mas. Although noticeable, this is still significantly smaller than the uncertainty of 1″ given for the position of the center in AvdM10, therefore, we refrain from correcting the center estimate.

In addition, one has to take into account the absolute proper motion of ω Cen, which leads to a movement of the center over time. As our proper motions are determined in a reference frame co-moving with ω Cen, the center stays fixed at its 2002.5 position in our reference frame. This will lead to a time-dependent offset with respect to other astrometric catalogs. From 2002 (the epoch of our first observations) to 2023 (the epoch of the last observations) the center will have moved by 68 mas (R.A. direction) and 141 mas (Dec. direction). This has to be taken into account when comparing our data with other catalogs (with absolute astrometry) such as the *Gaia* FPR (see also Figure 3.13).

3.4.5 INITIAL PHOTOMETRIC REGISTRATION AND CREATION OF A LIST OF BRIGHT STARS

As there are small photometric zero point variations even between exposures with the same integration time, in this step we determine the relative zero points between them. For each epoch, we then combine all single exposure measurements with the same filter and similar exposure time to a "photometric masterframe". We start by searching for the best linear transformations and relative photometric zero points to crossmatch individual catalogs of a similar exposure time. Then the master frame is created by combining multiple measurements of each single star by calculating the averaged position and photometric measurement. The zero point estimates are iteratively improved, by crossmatching the individual exposure catalogs with the masterframe and then updating the masterframe until convergence. After that, we combine the different exposure master frames of a single filter using the following rules: If a star was measured in multiple master frames, we use the measurement from the longest exposure time master frame in which it was not saturated. If there was no unsaturated measurement, we used the saturated measurement with the shortest exposure time as our best available estimate.

We compile a list of all stars that have an instrumental magnitude[2] brighter than `-9`. This list of bright stars is then used in the next step to mask PSF artifacts around bright stars. The list also contains saturated stars; these are not remeasured in the second photometry iteration and thus the `hst1pass` photometry is the best photometry available for these stars.

---

[2] We define instrumental magnitudes as $m_{inst.} = -2.5\log_{10}(N_{e^-})$ with N_{e^-} being the number of electrons fit with the PSF model.

3.4.6 SECOND PHOTOMETRY ITERATION WITH `KS2`

To obtain our final astro-photometric measurements we used the `KS2` software written by Jay Anderson (for more details, see Bellini et al., 2017a). `KS2` uses the ePSFs tailored to each image in Section 3.4.1, the transformations determined in Section 3.4.3, and the list of bright stars compiled in Section 3.4.5.

The program goes through several iterations of source finding, PSF fitting, and source subtraction. The source detection is based on peak maps from multiple images, which enables the detection of faint sources that do not produce a significant peak in each individual image. A byproduct of this process is the creation of deep stacked images, which we used to create a high-resolution 3-color composite image (see Figure 3.2).

After the finding stage, the program performs photometry on the individual exposures. Before each star is measured, the flux of neighboring stars is subtracted using the ePSF model. KS2 measures photometry with three different methods that are more appropriate for different signal-to-noise regimes. Method 1 fits the ePSF to a 5x5 pixel aperture of the individual exposures with the flux and the (x, y) position being free parameters. This only works if the star is bright enough to produce a significant peak in individual exposures. Method 2 takes the position determined from the peak map in the finding stage and only fits the flux within a 3x3 aperture. Finally, method 3 uses only the 4 brightest pixels and weights them according to their expected flux (based on the ePSF model). For the astrometric measurements, we rely on the method 1 measurements, the only method where position measurements are obtained in each individual image. We still keep the method 2 and method 3 photometry, as they might be useful for some science cases, e.g. when studying the photometry of stars on the faint end of the main sequence or along the white dwarf cooling sequence (e.g., Bellini et al., 2013).

3.5 PROPER MOTIONS

3.5.1 INTER-EPOCH CROSSMATCH

The goal of this step is to identify all stars that appear in multiple epochs, which are the stars for which a proper-motion measurement is possible.

We start by crossmatching each epoch with each of the other epochs. As stars move between epochs (due to their proper motions), to limit the number of miss-identifications we run the crossmatch with increasing matching radii, starting with a search radius of 0.1 UVIS pixel, removing all stars that have been found from both catalogs, and then continuing with increasingly larger search radii up to a maximum radius of 5.0 UVIS pixel. The individual search radii are [0.1, 0.2, 0.3,..., 1.9, 2.0, 2.25, 2.5, 2.75, 3.0, 3.5, 4.0, 4.5, 5.0] UVIS pixels. After all individual epoch pairs have been crossmatched, we combine the results into a single large table. This final table contains 1 482 835 stars measured in at least two epochs, all other (one-epoch-only) detections were discarded from the further analysis. In Figure 3.3 we show how many stars were contributed from each epoch. The epochs with the highest number of contributed stars are, as expected, the ones with the widest field coverage, i.e. the 3×3

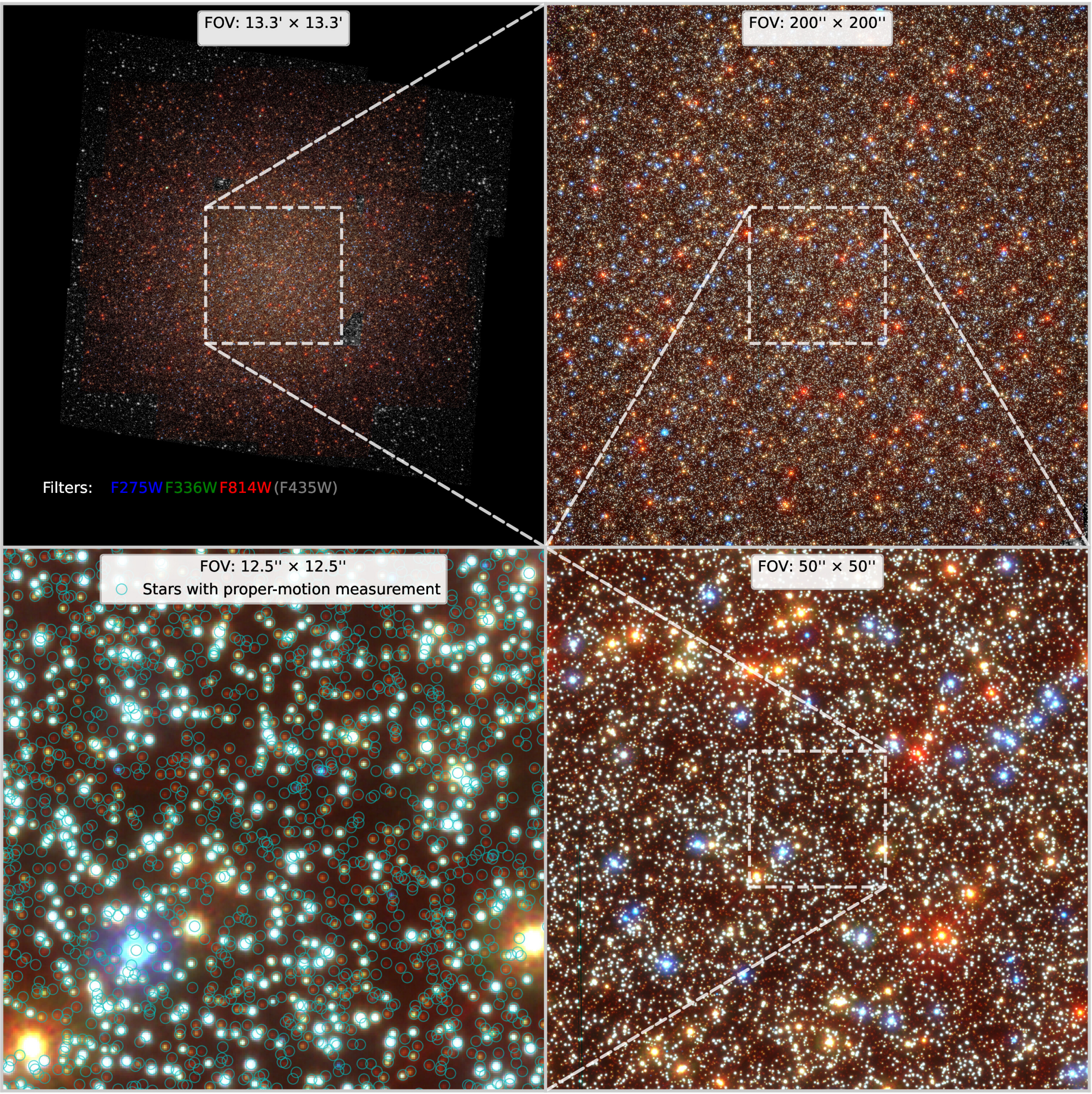

Figure 3.2: Zoom into a three-color composite image based on our stacked images. The red channel is WFC3/UVIS F814W, the green channel is WFC3/UVIS F336W and the blue channel is WFC3/UVIS F275W. Where no three filter coverage was available we used ACS/WFC F435W in gray-scale. Due to the wide color spread blue horizontal branch stars and red giant stars show strong colors and can be easily identified. In the highest magnification panel (lower left) we mark all stars with a successful proper motion measurement with a light-blue circle to demonstrate the depth and completeness of our catalog.

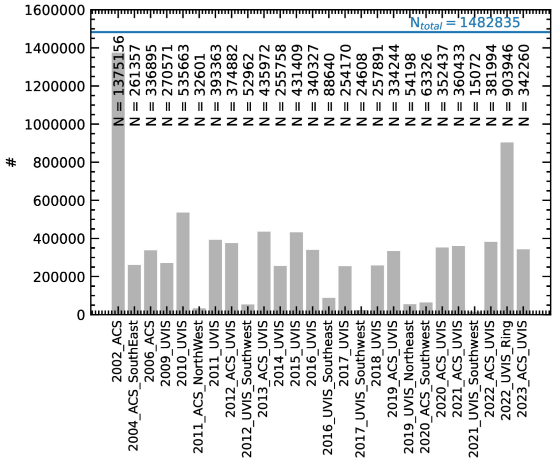

Figure 3.3: Number of stars of each epoch that could be crossmatched with at least one other epoch.

2002 ACS mosaic (GO-9442) with 1 375 156 measurements, and the newly observed ring of 10 UVIS fields contained in the half-light radius (GO-16777) with 903 946. The central epochs contributed typically between 250 000 and 500 000 stars depending on the depth and the dither pattern.

3.5.2 ITERATIVE PROPER MOTION DETERMINATION

Proper motions are measured using the method developed in Bellini et al. (2014) and improved in Bellini et al. (2018b); Libralato et al. (2018b), and we refer to those publications for detailed descriptions of the procedure. Proper motions are measured relative to a subset of well-measured cluster stars. The set of reference stars is iteratively improved. In the first iteration, it is based on photometric-quality indicators and the stars' position in the color-magnitude diagram alone. Once proper motions become available, non-members are also removed based on their position in the vector-point diagram (Figure 3.7) or if they have a spurious proper motion measurement.

The program treats each individual image catalog as a stand-alone epoch. As a first step, all these geometric-distortion-corrected[3] individual-image catalogs are transformed to the reference frame using linear six-parameter transformations. These transformations are determined individually for the 4 amplifiers used to read out the images (i.e. the single image catalogs are split into 4 quadrants, corresponding to the 4 amplifiers reading out the detectors of the instruments) to mitigate potential amplifier-based systematic effects. In the final iteration, the transformations are determined individually for each star using its 100 closest reference stars. The transformed positions of each star are fitted with a straight line in both the x and y directions, to directly fit the two proper-motion components. The fit takes into account the magnitude-dependent astrometric errors and has several stages of outlier rejection.

---

[3] Our software uses the library geometric distortion corrections from Anderson (2003) (ACS), Bellini & Bedin (2009), and Bellini et al. (2011) (UVIS), with an additional look-up table for ACS observations post *HST*-SM4 (2009). We noticed that the ACS/WFC distortion has worsened over time. For this reason, we made additional, time-depend table-of-residuals corrections for the latest observations (epoch $>$ 2018) with the ACS/WFC detector following the prescriptions in Bellini et al. (2011).

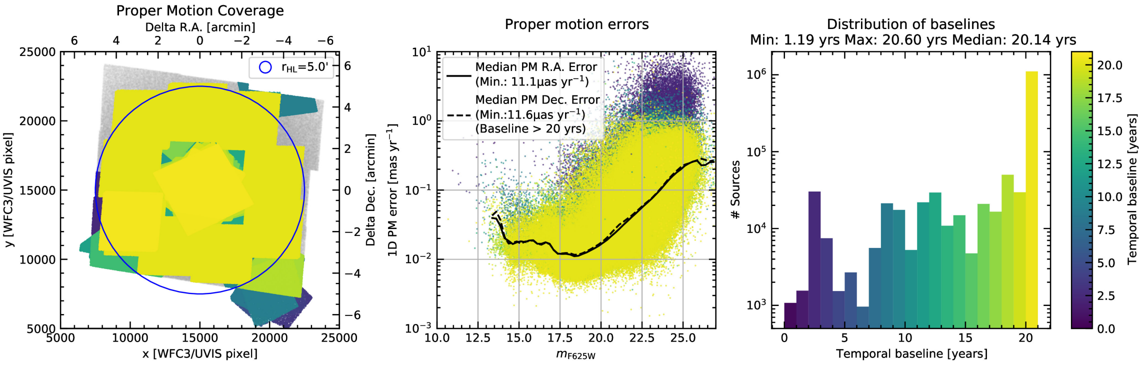

Figure 3.4: This figure shows how the temporal baseline of the astrometric data depends on the position within the observed field and how this affects the proper-motion error. **Left panel:** The colored areas show the parts of the field, where we were able to measure proper motions. The color-coding indicates the maximum temporal baseline used for the measurements. We achieve a highly uniform baseline of typically 20.6 years across most of the field. **Middle Panel:** We plot the proper-motion error as a function of the F625W magnitude and the temporal baseline. A longer baseline leads to a lower proper-motion error. The black line indicates the magnitude-dependent median error. For brighter stars, a better proper-motion error is achieved due to better S/N. This trend is reversed when the star is saturated in an increasing number of exposures (for $m_{\mathrm{F625}W} < 17.5$). **Right Panel:** Here we show the distribution of baselines. The majority (79%) of proper-motion measurements have a baseline longer than 20 years.

In another iterative loop, the crossmatch and the transformations to the master frame positions are improved by using the proper motions to propagate the reference stars to the same epoch as the individual image catalogs. In total, 103 616 339 individual position measurements were used for the proper-motion measurements, making this one of the largest astrometric datasets of all times.

Some detections that appeared as two separate sources during the crossmatch could be reassigned to a single source using the proper motions. Therefore, the final number of entries in our catalog is 1 475 096, slightly lower than the 1 482 835 sources measured at least twice during the crossmatch.

In total, 1 395 781 individual sources pass the iterative process and have a high-precision proper-motion measurement.

The vast majority of our proper motions (1 102 818) have a temporal baseline longer than 20 years. The median number of individual astrometric measurements used for the proper-motion determination is 17, it is lowest in the outskirts of our field of view and quickly increases towards the center. In the very center and in the best-covered magnitude range ($m_{\mathrm{F625}W} = 17.5$ to $m_{\mathrm{F625}W} = 22.0$), many stars have more than 400 individual measurements (with a maximum of 467), leading to a median proper-motion error of only 6.6 μas yr^{-1} ($\sim$0.15 km s^{-1} at the distance of ω Cen) with individual stars reaching as low as 3.3 μas yr^{-1}. The field dependence of the temporal baseline and the number of available measurements and their effect on the proper-motion error are presented in Figures 3.4 and 3.5.

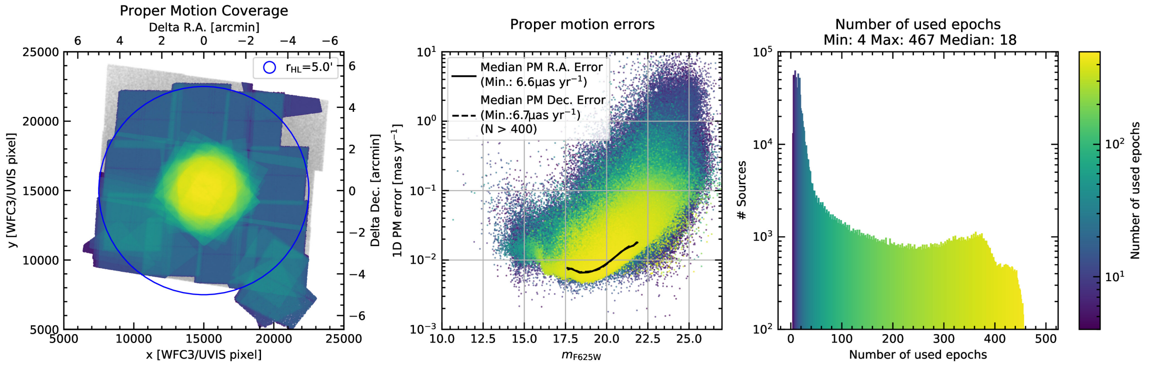

Figure 3.5: Similar to Figure 3.4 but with the number of used epochs as color coding. We can see how the number of astrometric measurements depends on the position within the observed field and how this affects the proper-motion error. **Left panel:** The colored areas show the available number of measurements at different locations in the field. In the center, a very large number of astrometric measurements (up to 467) is available due to the larger amount of data. In the outer parts of the field, there are typically around 10 measurements. **Middle Panel:** We show how the 1D proper-motion error depends on the F625W magnitude and the number of available measurements. The higher the number of measurements, the lower the proper-motion error. The black line indicates the magnitude-dependent median error for stars with more than 400 measurements. These stars are all located close to the center of the cluster and are in an ideal magnitude range from $m_{\mathrm{F625}W} = 17.5$ to $m_{\mathrm{F625}W} = 22.0$. For these stars, a median proper-motion error of only 6.6 μas yr^{-1} is achieved in both directions. **Right Panel:** Here we show a histogram of the number of available measurements. The majority of stars have less than 100 measurements, with a median of 18 measurements.

3.5.3 A-POSTERIORI CORRECTIONS

The resulting (amplifier-based) proper motions are of excellent quality. However, uncorrected charge transfer efficiency effects and residual distortion can lead to small systematic trends in the proper motions that vary both spatially and with the magnitude of the stars. We correct for these with a-posteriori corrections, following the prescriptions from Bellini et al. (2014) and Libralato et al. (2022). For each star, we search for neighboring cluster stars with a similar ($\Delta m < 0.5$) magnitude within a radius of 600 UVIS pixel. If there are less than 50 neighbors matching those criteria, we do not calculate a correction. This is only the case at the edges of the observed field. If there are more than 150 neighboring stars, we use the 150 closest neighbors as reference stars. Using the assumption that the mean motion of those neighboring cluster stars should be zero in both proper-motion directions by construction, we then calculate the 3.5 sigma clipped median of the proper motion of the neighboring stars and use this as correction value. The effectiveness of this method can be seen in Figure 3.6. Applying this correction removes systematic errors, but comes at the cost of adding an additional statistical uncertainty. For a typical 1D velocity dispersion of 0.65 mas yr^{-1} and 150 reference stars, this uncertainty is $\sigma_{correction} = \frac{0.65 \text{ mas yr}^{-1}}{\sqrt{150}} = 0.053$ mas yr^{-1}. As there is no filter for which we have measurements for all stars, we use the following approach to obtain a correction for each star: We calculate the correction in multiple filters, then take the correction from the ACS F625W filter (i.e. the filter with the largest field coverage and the largest number of measurements). If a star has not been measured in that filter, we take the correction from other filters in the order of the number of

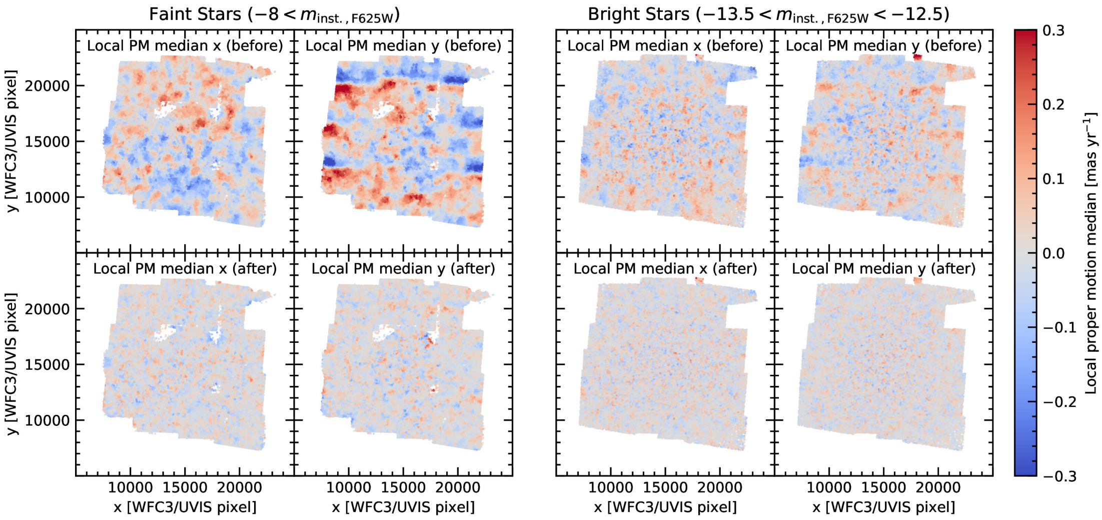

Figure 3.6: The top panels show both locally averaged proper-motion components for faint stars (left sub-figure) and bright stars (right sub-figure) before the a-posteriori corrections are applied. Especially for the faint stars, the imprint of uncorrected charge-transfer-efficiency effects in the y/declination direction becomes clearly visible. The lower panels show the local average of the proper motions after the corrections have been applied. The systematic residuals have disappeared.

measurements (F814W, F435W, F336W, F606W). This approach is reasonable as there is no strong dependence on the filter used for the local corrections, as we search the reference stars in a narrow magnitude interval. In total, we were able to obtain a local correction for 1 384 877 of 1 395 781 stars with a proper-motion measurement.

It is important to note that this local approach to measure proper motions also removes any signature of rotation from the proper motions (as this is a systematic effect on scales larger than the areas used to determine the transformations and local corrections). In Section 3.8 we discuss how the rotation can be recovered.

3.5.4 Vector-point diagram

As a first demonstration of the quality and size of our proper-motion catalog, we show the vector-point diagram of the proper motions in Figure 3.7. In this plot, we only show stars with both well-measured proper motion and well-measured photometry in the F435W and F625W filters, using the exemplary quality cuts described in Section 3.9. These selections leave us with a subset of around 700 000 stars from the sub-giant branch down to white dwarfs and faint main-sequence stars. As expected, most stars are concentrated around the origin $(0, 0)$ and show a normal distribution with $\sigma \approx 0.66$ mas yr^{-1} in both velocity components[4]. In addition to the cluster stars, there are additional over-densities visible corresponding to background galaxies and Galactic field stars in the fore- and background of

---

[4] Please note that this is not a proper measurement of the velocity dispersion of ω Cen yet. For this, we would have to account for the errors on the proper-motion measurements, split the dataset into different radial and mass bins, and perform a more careful selection of cluster stars. A detailed study of the kinematics of ω Cen will be done in a follow-up work.

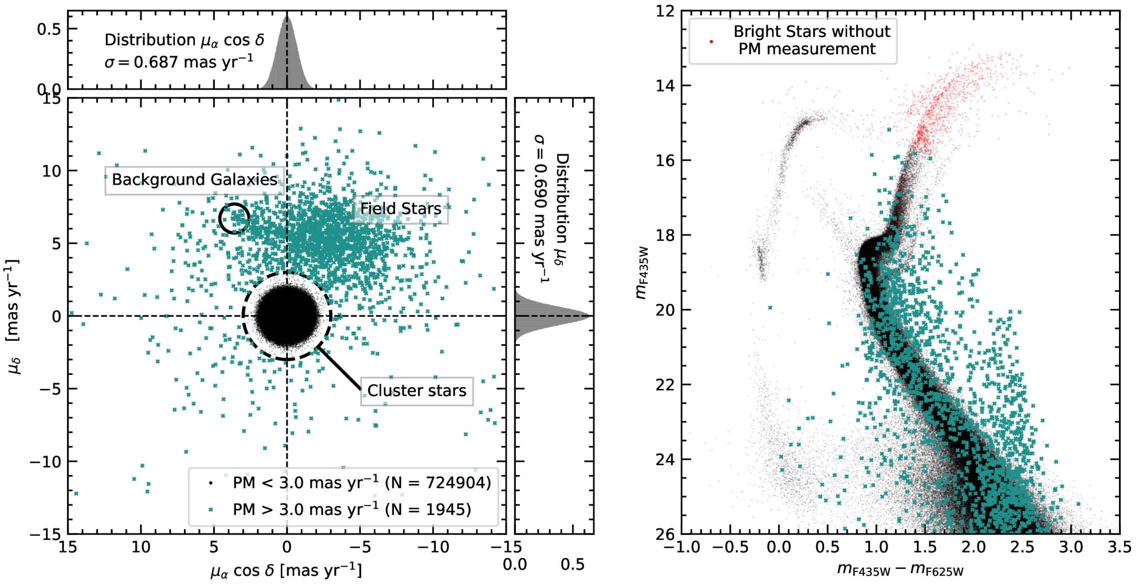

Figure 3.7: **Left panel:** A vector-point diagram of the relative proper motions for a subset of around 700 000 well-measured stars in our catalog. Most stars are distributed around the origin, as expected for ω Cen's member stars and follow a normal distribution in both velocity components (see marginalized histograms at the edge of the plot). A small fraction of stars has a relative proper motion incompatible with the cluster's motion. Those stars lie outside of the 3.0 mas yr^{-1} radius indicated with a dashed circle (corresponding to a 4.5σ deviation from the velocity distribution of the cluster stars) and are marked with turquoise crosses. The non-member stars show substructures that can be attributed to background galaxies (marked with a solid circle) and Galactic foreground/background stars. **Right panel:** A color-magnitude diagram of the same sample. One can see that the stars with a high relative proper motion do not follow the CMD sequences of ω Cen. Our proper motions cover almost the entire CMD, however the brightest stars, indicated with red dots, do not have a proper motion measurement, as they are saturated even in the shortest *HST* exposures.

ω Cen. As shown in the color-magnitude diagram (CMD) in Figure 3.7, a simple total proper motion cut of `PM < 3 mas yr`$^{-1}$ allows an effective separation of cluster stars from field stars.

3.6 CREATION OF THE PHOTOMETRIC CATALOG

After the proper-motion determination, we are left with individual image catalogs that are all matched very precisely with the crossmatched master catalog. However, the photometric information is still based on various different `KS2` runs (see Section 3.4.6) and still in uncalibrated instrumental magnitudes. The goal of this step is to combine all these single-image measurements into a uniform, calibrated, photometric catalog for the 6 filters for which we have coverage over the full field (WFC3/UVIS F275W, F336W, F814W; ACS/WFC F435W, F625W, F658N). In addition, we include the WFC3/UVIS F606W filter, as this is the filter with the most uniform and extensive coverage in the center.

3.6.1 Creation of a photometric reference catalog

The goal of this step is to create calibrated, aperture-photometry-based reference catalogs for all filters that we can then crossmatch with our PSF photometry catalogs to obtain their zero points. The reference catalogs are created similarly to the procedure described in Bellini et al. (2017a), using the current version of the WFC3/UVIS zero points. We perform aperture photometry on a selected subset of exposures for all filters. In contrast to our PSF photometry measurements, we now use the resampled and flux-normalized (to 1 s exposure time) `*drc` type images. For the photometric reference catalog we choose exposures with a representative exposure time for the respective filter and covering the full field of view. For the WFC/ACS filters (F435W, F625W, F658N) we use the full GO-9442 data. For the WFC3/UVIS filters (F275W, F336W, F606W, F814W) we use the full GO-16777 data for the outer fields and the data from GO-11911/12094 for the central field.

We perform aperture photometry with various radii between 2.5 and 10 pixels (and a sky annulus between 12 and 16 pixels). For the ACS data we then add the respective infinite aperture correction from Bohlin (2016) and the date-specific VegaMag zero point from the ACS zero point calculator[5]. For the WFC3/UVIS data these two steps are unified in the python package `stsynphot`[6] including the most recent photometric calibrations (Calamida et al., 2021, 2022). We follow the example notebook[7] to calculate the WFC3/UVIS zero points. Once we have the calibrated, single-exposure, aperture-based photometric catalogs we crossmatch them to our astrometric master catalog and then create a combined reference catalog for each filter. If a star has multiple measurements in the aperture photometry catalogs, we combine them using the median. We remove all stars from the catalog with a brighter neighbor within 20 pixels, as those brighter neighbors contaminate the aperture photometry. Also, we chose the aperture radius that provides the lowest scatter when compared to the PSF photometry. This is 3.5 pixels for the ACS filters (F435W, F625W, F658N), 4.0 pixels for WFC3/UVIS F606W and F814W, and 4.5 pixels for WFC3/UVIS F275W and F336W.

3.6.2 Creation of an error model

Before combining individual measurements, we want to find the dependence of the statistical photometric errors on the instrumental magnitude, to be able to properly weight the individual data points. Therefore, we create an empirical error model for each filter. For each filter, we choose one epoch and collect all stars that have been measured at least 3 times. Then, we determine the 67th percentile of the RMS of the instrumental magnitude of these stars in 0.5 magnitude wide bins. We quadratically interpolate between these values to obtain a smooth error model. The resulting error models are shown in Figure 3.8 and we use these as 1-sigma errors on the individual measurements.

---

[5] https://acszeropoints.stsci.edu/

[6] https://stsynphot.readthedocs.io/en/latest/index.html

[7] https://github.com/spacetelescope/WFC3Library/blob/master/notebooks/zeropoints/zeropoints.ipynb

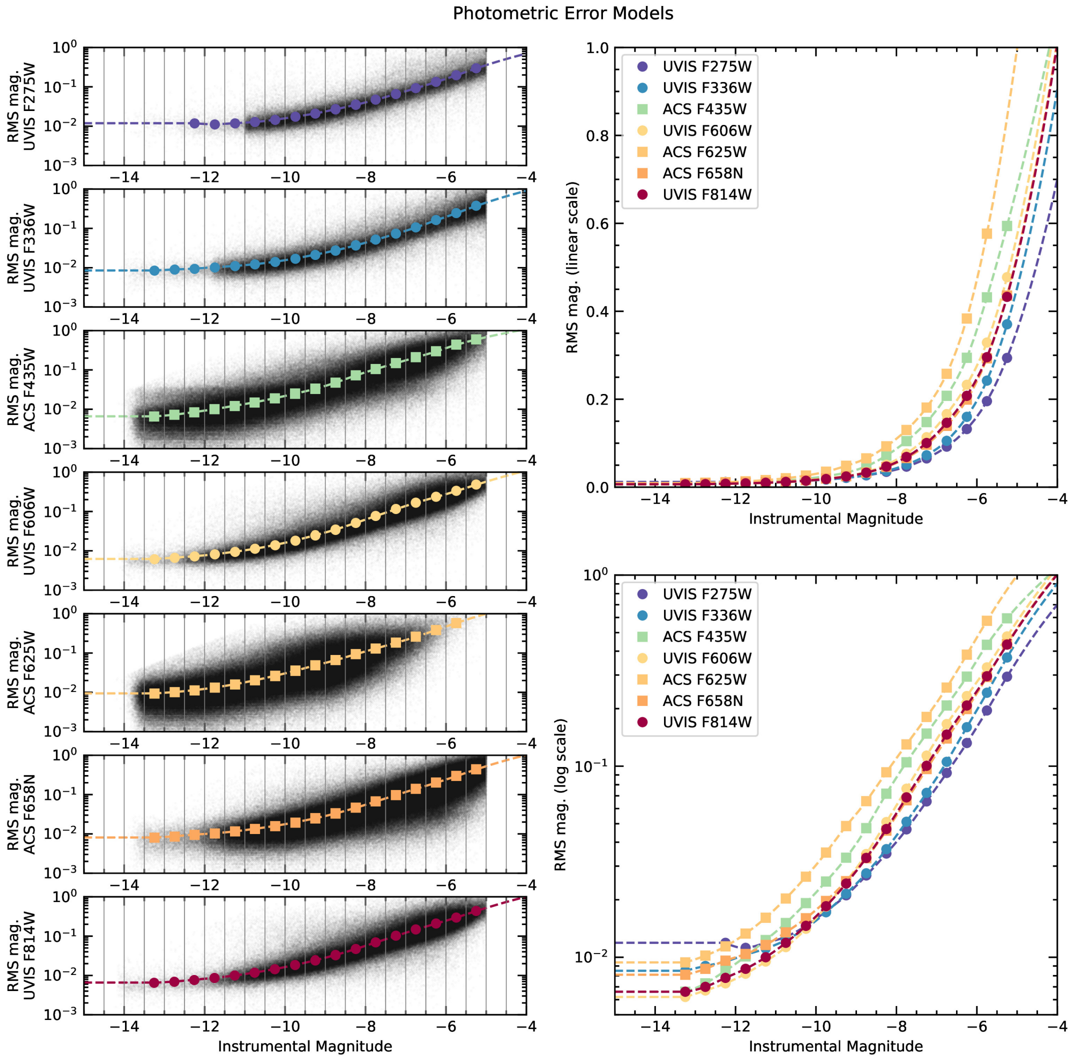

Figure 3.8: Empirical photometric error model for 7 different filters. The plots in the left panel show the RMS of the measured magnitudes of stars that have been detected in at least 3 exposures, plotted against their long-exposure instrumental magnitude (black dots) and the derived error model as colored line. In the two right panels, we compare the error models for the different filters in a linear and a logarithmic plot. All filters show similar curve of rising errors towards fainter magnitudes, but the errors of the two wide ACS filters (F435W, F625W) are higher than the rest. This is due to typically longer exposure times of these filters, which leads to higher crowding.

3.6.3 Creation of a model for CTE effects

As described in Section 3.4.1, we use CTE corrected input images of the `*flc.fits` type. However, the applied CTE correction underpredicts the evolution of the CTE loss for the most recent WFC3/UVIS observations. This leads to noticeable CTE effects in both the astrometry and photometry of observations taken after 2017, especially for images with a low background (i.e. those with a short exposure time and those with a very blue filter). Since the start of this work, `hst1pass` (Anderson, 2022) has been updated with a new and improved CTE correction. However, this correction is meant to be applied to astro-photometry measured on uncorrected `*flt.fits` type images.

Since this improved CTE-correction routine is not currently included in `KS2`, to our `KS2`-based single-exposure catalogs we applied empirical corrections based on the comparison between the `hst1pass` runs on `*flt.fits` and `*flc.fits` images. To derive a model that can transfer the new corrections to our data, we first grouped the data in sets of the same filter and the same exposure time (ensuring the same background level in each such group). After this, we collected the residuals between the hst1pass-flt results and the KS2-flc results. We then modeled these residuals in an instrumental magnitude versus distance-to-amplifier space, to be able to calculate a correction for each measurement in our KS2 based catalogs.

The largest corrections are applied to the UV filters (F275W, F336W) of the GO-16777 program. For the faintest stars ($m_{inst.} \sim -6$) at the largest distances from the amplifier the corrections can reach up to 1 mag, for brighter stars they are much lower.

3.6.4 Combination of measurements

In this step, we combine the photometry from different epochs and KS2 runs and also find the zero points to transform our instrumental magnitudes into the Vega magnitude system.

We follow an iterative approach in which we first crossmatch the individual single-image catalogs with the reference catalogs created in Section 3.6.1 to determine the zero point for each exposure. We determine the zero point by calculating the difference between the instrumental magnitudes and the reference magnitudes. We calculate the 3.5 σ clipped mean of bright ($m_{inst} < -9$), well-measured (`QFIT` > 0.95) stars. Then, we combine measurements of all exposures using the error-weighted mean (with the empirical errors derived in Section 3.6.2):

$$m_{combined} = \frac{\sum_{i=1}^{n} \left(\frac{m_{inst,i} + ZP_i}{\sigma_{m,i}^2} \right)}{\sum_{i=1}^{n} \frac{1}{\sigma_{m,i}^2}} \tag{3.1}$$

The error of this weighted mean is:

$$\Delta m_{combined} = \sqrt{\frac{1}{\sum_{i=1}^{n} \frac{1}{\sigma_{m,i}^2}}} \tag{3.2}$$

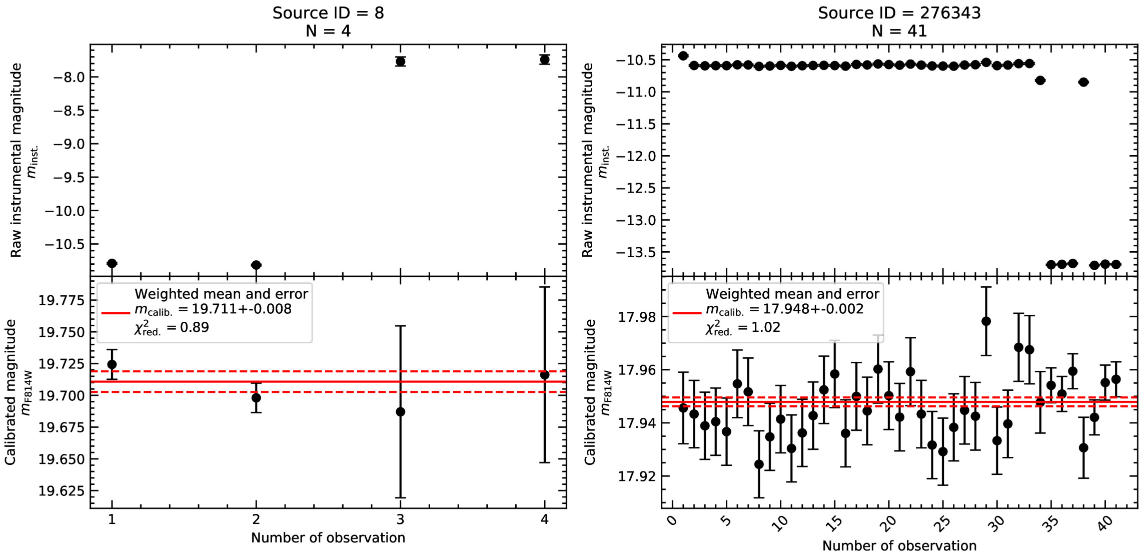

Figure 3.9: This figure shows the individual photometric measurements for two typical sources in the WFC3/UVIS F814W filter. The left panels are for a star measured in the outer regions, where we typically have 4 measurements (2 long and 2 short exposures from program GO-16777). The right panels are for a star in the central region where there is a much higher number of individual exposures and measurements. The upper panels show the raw (uncalibrated) instrumental magnitudes, the lower panels show the individual measurement after the zero point for each exposure is added, and the resulting error-weighted mean magnitude (red line).

After this first iteration is done, we crossmatched the resulting calibrated average catalog again with the individual single-image catalogs and redetermined the zero points. When available, we use the same crossmatch as in the last proper motion iteration (as this crossmatch takes into account the motion of the stars). The new calibrated catalog allows us to also determine the zero point for those pointings for which there is not enough overlap (either spatially or in magnitude) with the initial reference catalog. We repeat this procedure 4 times. After 4 iterations no additional pointings can be added and all zero points have converged. In addition to the weighted mean of the calibrated magnitudes, we also calculate several other statistical quantities based on the distribution of individual measurements (see Table 3.9). An example of the combination of measurements in two typical photometric situations is shown in Figure 3.9.

3.6.5 Empirical photometric corrections

Even though ω Cen is located in a region of the sky with low total extinction ($E(B-V) = 0.12$, Harris 2010) differential reddening of the order of up to ±10% has been reported in Bellini et al. (2017b) for the cluster's core. In addition to these physical effects, there are also small systematic zero point variations over the field caused by instrumental effects such as small variations of the PSF and the detector sensitivity, but also issues caused by the decreasing charge transfer efficiency of *HST*'s ageing detectors.

All these effects broaden the observed CMD sequences of the different subpopulations and limit our ability to separate them. Therefore, we derive an empirical correction for spatially dependent photometry variations.

3.6.5.1 METHOD

The method we developed is adapted from the differential reddening correction described in detail in Bellini et al. (2017b). In contrast to this work and due to the higher complexity of our dataset (two instruments, a larger time-span of the observations, and a much larger field with an irregular mosaic of observations) we could not use the assumption that all spatial photometric variations are caused by true physical extinction that follows a wavelength dependent reddening law. Instead, we determined a spatial photometric correction for each of the 6 filters by studying the behavior of a set of well-measured reference stars that all lie on a single sequence in the CMD.

To define the set of reference stars we only used stars that had a photometric measurement in all of the 6 filters with full field coverage. After an initial quality selection, based on the QFIT and the scatter of the individual measurements, we manually selected a single subpopulation in the $m_{\mathrm{F814}W}$ $vs.$ $m_{\mathrm{F275}W} - m_{\mathrm{F814}W}$ and the $m_{\mathrm{F814}W}$ $vs.$ $m_{\mathrm{F336}W} - m_{\mathrm{F435}W}$ CMD, both with $15 < m_{F814W} < 19.0$. This lower limit is enforced to limit the CTE effects which affect fainter magnitudes more strongly. We intentionally use these two CMDs which, together, allow the clean separation of a single sequence from the other subpopulations, ensuring the spread in the reference stars is only due to instrumental and DR effects. Our initial list of reference stars contains 70 040 entries. It is updated once we perform the selection in differential reddening corrected CMDs. After 3 iterations it contains 59 060 stars.

Once the reference stars were identified, we determined the median color in bins of magnitude, for each of the 15 2-color CMDs that can be created with 6 filters (see Fig. 3.10). These fiducial lines serve as the baseline with respect to which we compare the local distribution of magnitudes in the next step.

We determine the correction for each filter on an evenly spaced on-sky grid with pixel spacing of 100 WFC3/UVIS pixels (4”). For each point in our grid, we identify the 300 closest reference stars with a maximum search radius of 1000 WFC3/UVIS pixel. For gridpoints with fewer than 150 neighbors we do not calculate a correction. Once the local set of reference stars was determined, we optimized the set of 6 photometric corrections by minimizing the squared sum of the deviations from the fiducial lines in each CMD. After the corrections have been determined for the six filters with full field coverage, we also calculated the optimal corrections value for the WFC3/UVIS F606W, which was only used in the central pointing. We interpolate the grid for each filter at every star location to obtain the photometric correction for each star.

To quantify the statistical error of these correction values, we perform 20 bootstrap resamplings on each grid point correction value. This gives us an average error of $\simeq 0.006$ mag for pixels with 300 reference star neighbors. Pixels with fewer than 300 neighbors have increased errors; those with fewer than 150 neighbors do not give us reliable correction estimations which is why we in this case we do not calculate a correction. However, this only affects a small area that the edge of the field.

Table 3.3: Statistical properties of the derived empirical photometric corrections for 7 filters

Instrument	Filter	Min.	Med.	Max.	RMS	Error[8]
WFC3/UVIS	F275W	-0.059	0.007	0.044	0.017	0.0050
WFC3/UVIS	F336W	-0.033	0.003	0.035	0.010	0.0053
ACS/WFC	F435W	-0.037	0.001	0.031	0.009	0.0053
WFC3/UVIS	F606W	-0.027	0.002	0.036	0.010	0.0059
ACS/WFC	F625W	-0.033	0.003	0.041	0.013	0.0056
ACS/WFC	F658N	-0.033	0.004	0.041	0.013	0.0057
WFC3/UVIS	F814W	-0.042	-0.001	0.041	0.015	0.0059

We find a fairly narrow spread and uniform distribution for the error on our photometric corrections and therefore quote one value per filter for the error (see Table 3.3).

3.6.5.2 Results

We show the statistical properties of the correction in Table 3.3 and detailed maps and histograms in Appendix 3.12 (Figure 3.16 and 3.17). The maps show various patterns, that can partially be attributed to physical differential reddening, but also transitions between different pointings. A detailed decomposition into those two components is out of the scope of this work and would not further improve the corrected photometry.

The effectiveness of the correction is demonstrated in various before-/after correction CMDs in Figure 3.11. The corrections lead to narrower CMD sequences and a clearer separation of the different subpopulations in all CMDs.

3.6.6 Treatment of bright stars

The individual photometric measurements discussed in the section above were all performed with the software `KS2`. However, this software is not able to measure saturated stars. This limits our completeness at the bright end, as the brightest red giant stars are saturated even in the shortest exposures of e.g. the F625W and F814W filters. Including precise photometry for these stars is still important, as they have the highest S/N in spectroscopic studies. We substituted the missing KS2 measurements with data from our single-image `hst1pass` catalogs, using the same zero-points as determined in the iterative procedure described in Section 3.6.4.

3.7 Comparison with literature catalogs and validation

To validate our new astro-photometric measurements, we performed a search for residual color and magnitude trends (Appendix 3.13) as well as extensive comparisons with previously published *HST* and *Gaia* based catalogs. These are described in detail in Appendix 3.14. In the following, we limit ourselves to a comparison of the general catalog properties and a summary of the direct astrometric/photometric comparisons.

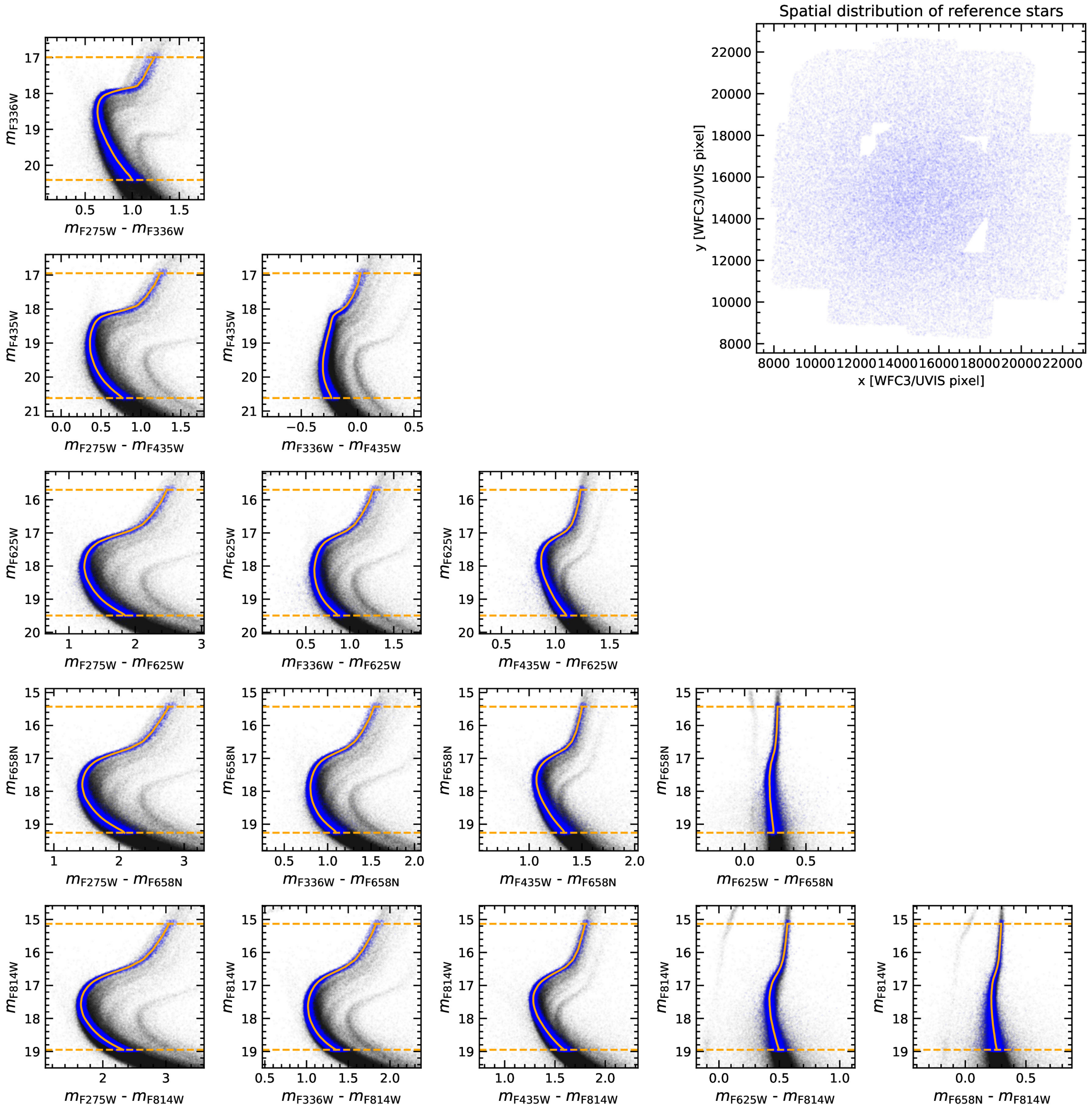

Figure 3.10: The plots in the lower left of this figure illustrate the multi-dimensional space in which we determined the photometric corrections. Each of the 15 smaller panels shows a color-magnitude diagram with a different filter combination. To determine the corrections, we determine the local photometric offsets with respect to fiducial lines (yellow solid lines) based on a single sequence of well-measured reference stars (blue). Yellow dashed lines denote the magnitude limits of the reference stars. The spatial distribution of the reference stars is shown in the upper right.

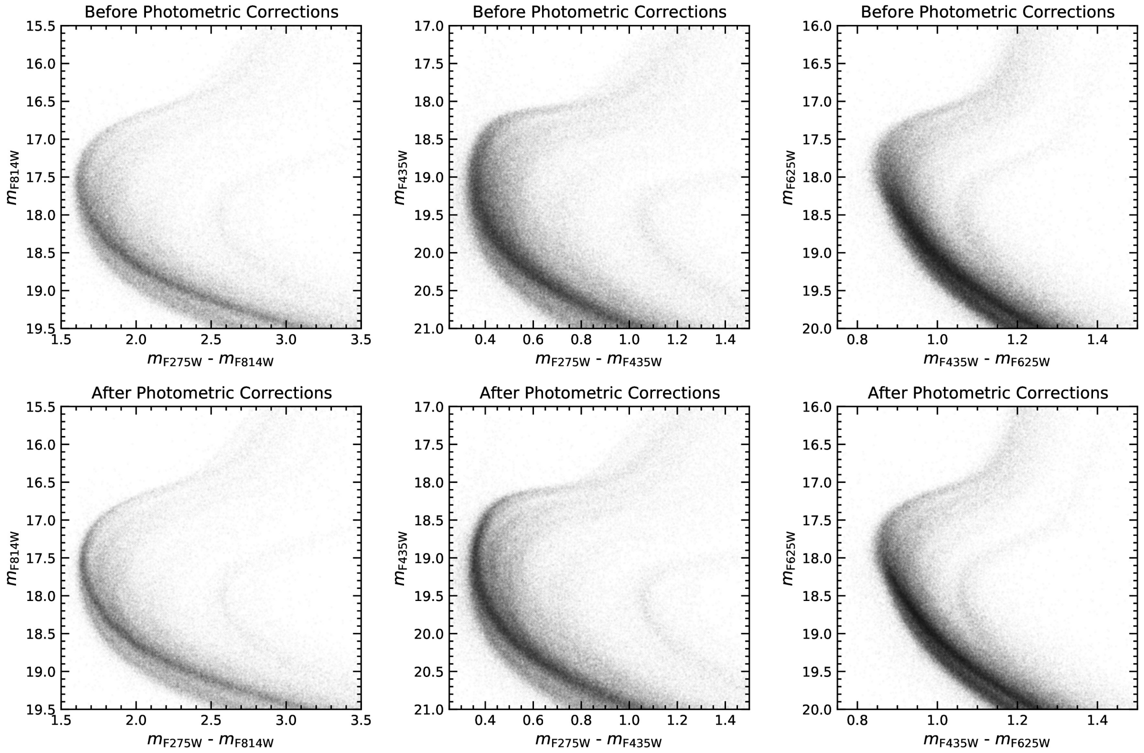

Figure 3.11: Color-magnitude diagrams (CMDs) of the turnoff region using various filter combinations before (top panels) and after (bottom panels) the photometric corrections have been applied. In all CMDs, the corrections lead to narrower sequences and a clearer separation of the different subpopulations.

3.7.1 Comparison of general catalog properties and completeness

We compare our astrometry and our photometry with the two other most recent high-precision catalogs for the central region of ω Cen: The *HST*-based astrophotometric catalog published by Bellini et al. (2017a) and the *Gaia* catalog (combining data from both *DR3* and *FPR*). The two comparison datasets are complementary for our catalog verification: While the Bellini et al. (2017a) catalog probes faint stars in the very center of ω Cen with a similar photometric methodology and a similar approach to measure relative proper motions (although with a significantly shorter temporal baseline), the *Gaia* data is shallower but provides a larger field-of-view and gives us a fully independent comparison with absolute proper motions.

In Figure 3.12, we compare various general properties of the three different datasets: the spatial coverage, the magnitude-dependent proper-motion errors, the source density as a function of radius, and the distribution of magnitudes. We can summarize our findings as follows:

The Bellini et al. (2017a) catalog is limited to a region with only half of the radius of the coverage of our catalog. In this inner region the source density of the photometric catalog is only slightly lower than in our new catalog which is expected, as the Bellini et al. (2017a) catalog is based on a similar dataset and the source detection was performed with the same software. However, if we restrict the comparison to stars where the Bellini et al. (2017a) catalog has proper motion measurements, the density in the literature drops by a factor of around two. This is also expected, as the astrometric part of the Bellini et al. (2017a) catalog is actually based on a previous data reduction (Bellini et al., 2014) with less sensitive photometry software and fewer available data. The proper motion errors of the two *HST* catalogs show a similar dependence on the magnitude, however, the errors in our new catalog are typically lower by a factor of $\sim$2, due to the significantly longer temporal baseline of our catalog. In addition, our proper motion catalog reaches almost 2 magnitudes deeper.

For the comparison with the *Gaia* catalog, we have to differentiate between the measurements published during the general (Early) Data Release 3 (*DR3*), and the measurements published during the Focussed Product Release (*FPR*) on ω Cen. Those two (disjunct) parts of the *Gaia* catalog probe different regions on the sky and different magnitude regimes: While the *Gaia DR3* data has all-sky coverage, the *FPR* data is limited to a region of $r \leq\sim 0.8°$ around the cluster center. This is still significantly wider than the $r \sim 7'$ region covered by our new catalog. The 1D proper motion errors of the *Gaia DR3* reach a precision of $\sim 20\,\mu\mathrm{as\,yr}^{-1}$ for the brightest stars. At fainter magnitudes they are typically around one order of magnitude higher than the errors of our measurements. However, it is known that the nominal *Gaia DR3* errors are underestimated in crowded fields (Vasiliev & Baumgardt, 2021). The two lower panels of Figure 3.12 show that especially in the inner few arcminutes of ω Cen the completeness of *Gaia DR3* is severely affected by crowding. Instead of an increase in the source density, the profile appears flat, and the magnitude distribution shifts towards brighter stars. This is expected: Due to the readout window strategy and its limited processing/downlink capabilities, the *Gaia* satellite is only able to measure the brightest stars during its nominal operations.

The *Gaia FPR* catalog on ω Cen is partially overcoming this crowding limitation, by using dedicated engineering images of the inner region of ω Cen that are processed on the ground. As it can be seen in

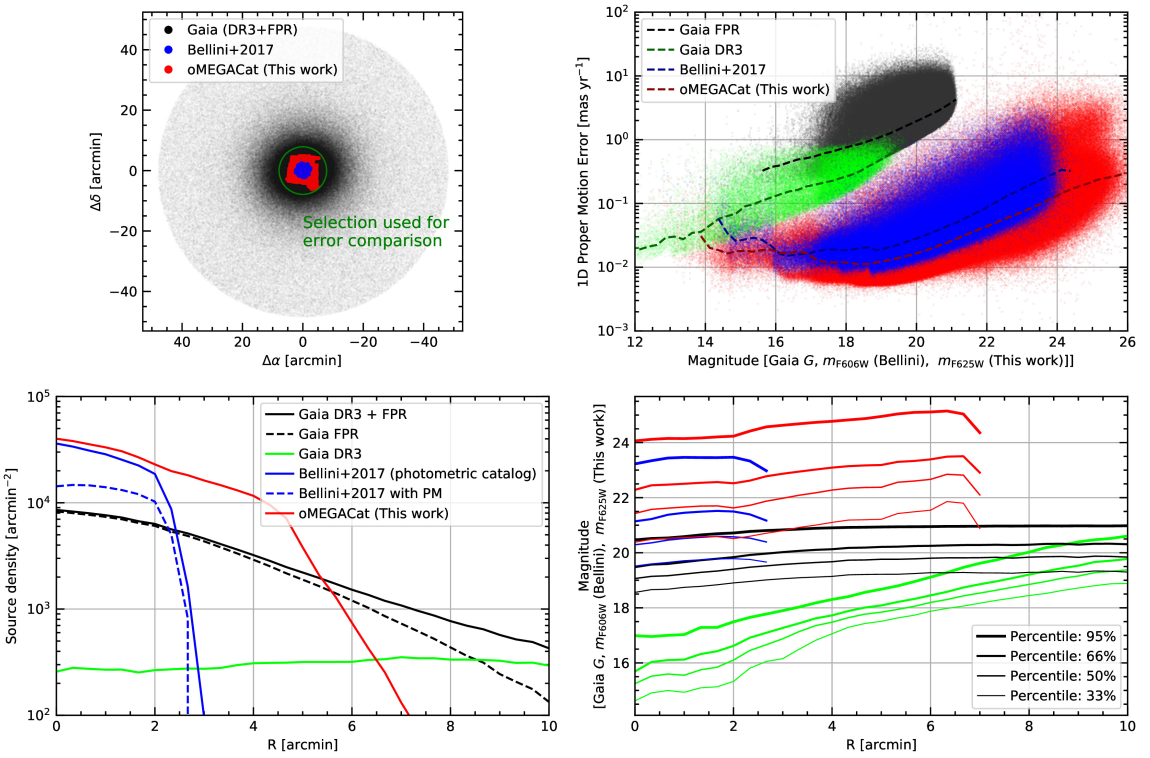

Figure 3.12: In this Figure we compare the general properties of three available high-precision datasets for the core of ω Cen: the new *oMEGAcat* (this work), the astro-photometric catalog by Bellini et al. (2017a), and the combined *Gaia DR3 + FPR* catalog. *Upper left:* Comparison of the on-sky footprint of the different catalogs. *Upper right:* Comparison of proper-motion errors for different magnitudes. *Lower left:* Comparison of the source density of the different catalogs at different radii. *Lower right:* Comparison of different percentiles of the magnitude distribution for the different catalogs.

the figure, the magnitude distribution and the source density profile of the combined catalog indicate a much better completeness towards the center. However, the new *HST* catalog presented in this work still reaches around 3.5 magnitudes deeper, which leads to around 4 times more stars in the centermost region. At all magnitudes, the median proper-motion errors of the *Gaia FPR* measurements are around a factor of ∼50 higher than the ones in our catalog.

3.7.2 Crossmatch and direct comparison of measurements

We crossmatched our new catalog with both the Bellini et al. (2017a) and the *Gaia* literature catalogs to directly compare the measurements. Details of this comparison are described in the Appendix 3.14. To summarize, both catalogs were almost fully included in our new catalogs. With a simple geometric match, we could recover more than 98% of all literature sources, highlighting the completeness of our new catalog, but also the astrometric consistency with the previous works. There is good agreement between both the photometric and the astrometric parts of the Bellini et al. (2017a) catalog.

When comparing our newly measured proper motions with the *Gaia* catalog, more than 99% of the *Gaia* sources within our field of view can be recovered in the *HST* catalog. The differences between

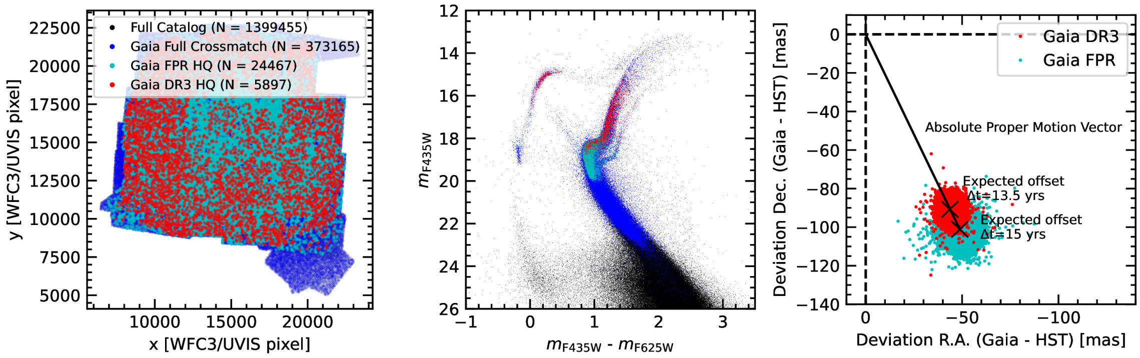

Figure 3.13: **Left panel:** Footprint of our proper-motion catalog and all *Gaia* stars that could be crossmatched (blue). High-quality stars from *Gaia FPR* are marked in cyan, and high-quality stars from *Gaia DR3* are marked in red. **Middle panel:** The same sample of stars, but plotted as a color-magnitude diagram. One can see that all HQ *Gaia DR3* measurements are limited to stars brighter than the main-sequence turn-off, while the *Gaia FPR* sample reaches slightly deeper. **Right panel:** Absolute deviation between the positions from our *HST* catalog and the two HQ *Gaia* subsamples. The shift of the centroid can be explained by the absolute proper motion of ω Cen, while the spread of the distribution is caused by the displacement due to the velocity dispersion.

the measured positions in both catalogs can be explained with the absolute motion of ω Cen, but also the internal dispersion (see Figure 3.13). For the further tests described in Appendix 3.14, we restricted ourselves to a subsample of sources well-measured in both catalogs. This restricts us to relatively bright stars (Figure 3.13, middle) and also highlights the crowding limitations of the *Gaia* catalog in the crowded cluster center (Figure 3.13, left). When comparing the proper motions, one immediately notices the fundamental difference between our *locally measured, relative* proper motions and the *absolute Gaia* measurements. The residuals of the comparison can be explained by bulk motion of ω Cen but also its rotation in the plane of the sky. This is used in the following section to measure the cluster's rotation.

3.8 MEASURING ω CEN'S ROTATION CURVE AND INCLINATION

3.8.1 MEASURING THE ROTATION CURVE

Measurements of the plane-of-sky rotation of globular clusters face a fundamental challenge: The available *HST*-based proper-motion catalogs (including this work) were all created with relative proper motions that were measured with a local approach that determines the stellar motions with respect to other neighboring cluster stars. This erases both the bulk motion and the rotation signature of the cluster from the proper motions. In principle, these quantities can be recovered by searching for extragalactic background sources that show the local bulk motion with a flipped sign (see Anderson & King 2003; Bedin et al. 2003; Bellini et al. 2017d for the introduction of this method and Libralato et al. 2018a for its application to ω Cen). Also in the vector point diagram created with our new catalog, an overdensity of background sources at the inverse absolute proper motion value is visible.

However, due to the low number of these background-objects and their typically faint magnitudes, it is difficult to study a varying velocity field such as that of rotation.

Absolute proper-motion catalogs such as the *Gaia* catalogs do not suffer from these limitations and have been used to measure the rotations of many globular clusters (e.g. Bianchini et al. 2018; Sollima et al. 2019 for *Gaia DR2*, Vasiliev & Baumgardt 2021 for *Gaia EDR3*). However, in the crowded cluster centers only a few stars are measured, and additionally, the rotation signal is hidden by the velocity dispersion of individual stars.

By combining our new relative proper-motion catalog with the absolute measurements from *Gaia DR3 & FPR*, we can overcome the limitations of these past works: By calculating the difference between the absolute *Gaia* proper motion and our relative proper motions, we obtain a direct measurement of the bulk-motion and any local proper motion trends. This works, as the *Gaia* proper motions can be seen as a superposition of the bulk motion of the cluster, locally varying systematic motion such as rotation, and the random motion of individual stars, while our relative proper motions only contain the random motions relative to the bulk motion.

We study these differences for a subset of 30 364 well-measured stars (see Appendix 3.14) both in 2-dimensional maps and radially. To this aim, we used the Voronoi binning code of Cappellari & Copin (2003) to create two-dimensional bins containing $\sim$250 sources each, and manually created radial bins of $0.5'$ width. The results, displayed in Figure 3.14, show a clear rotation pattern with a gradual increase of the rotation in the inner 2 arcminutes flattening out at an amplitude of $\sim$0.3 mas yr^{-1}. At an assumed cluster distance of 5.43 kpc (Baumgardt & Vasiliev, 2021) this corresponds to a rotation of around 7 km s^{-1}, similar to what has been observed using MUSE line-of-sight velocity data (Kamann et al., 2018). We provide the numerical values of the rotation profile in Appendix 3.16; Table 3.10 and in a machine readable format. Other proper motion studies measure a similar rotation amplitude, but were typically limited to regions at larger distances from the center (van Leeuwen et al., 2000b; van Leeuwen & Le Poole, 2002; van de Ven et al., 2006; Bianchini et al., 2018; Vasiliev & Baumgardt, 2021). This also explains the difference between our measurements and the rotation profile derived in Vasiliev & Baumgardt (2021), see Figure 3.14. In the innermost region ($r < 3'$), we see a much steeper increase of the rotation profile than described by Vasiliev & Baumgardt (2021), however, this region was previously unconstrained due to the lack of data at small radii.

3.8.2 MEASUREMENTS OF ω CEN'S INCLINATION

As demonstrated by van de Ven et al. (2006), the availability of both proper motions and line-of-sight velocities enables a direct and nearly model-independent way to measure the inclination i of a stellar system, solely based on the assumption of axisymmetry. This is due to the following relation (eq. 8 in van de Ven et al., 2006) between the mean proper motion along the system's projected semi-minor axis, $\langle \mu_{y'} \rangle$, and the mean line-of-sight velocity, $\langle v_{z'} \rangle$.

$$\langle v_{z'} \rangle (x',\, y') = 4.74\, D\, \tan i\, \langle \mu_{y'} \rangle (x',\, y') \tag{3.3}$$

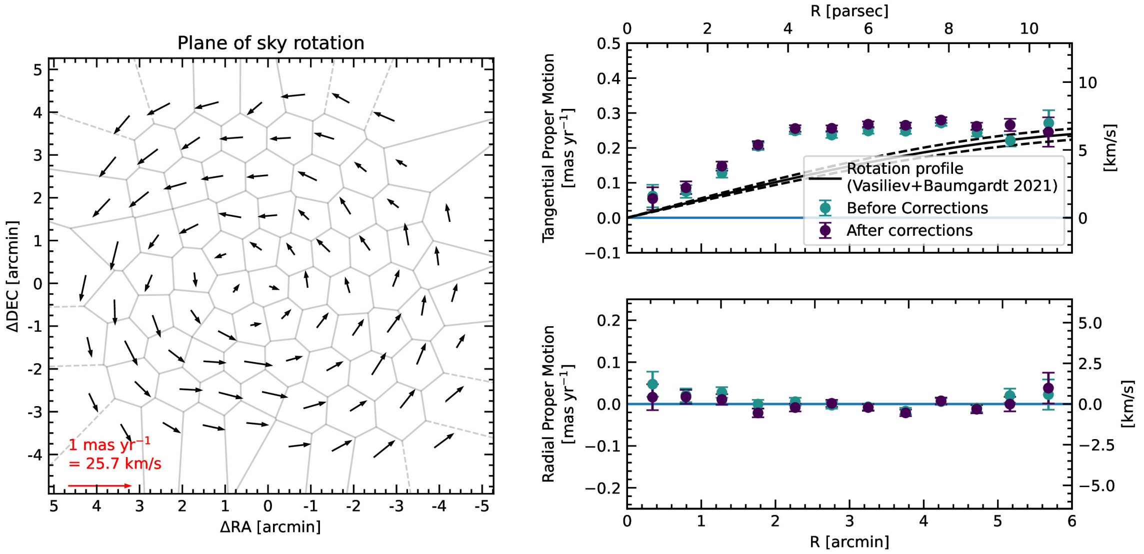

Figure 3.14: Plane of sky rotation determined in 2-dimensional Voronoi bins (*left*) and as radial profiles (*right*). The numerical values of the rotation profile are also listed in Appendix 3.16; Table 3.10. In comparison, the rotation profile from Vasiliev & Baumgardt (2021) shows a significantly shallower increase in the rotation curve. However, it is based on an interpolation of the rotation data towards the center and there were no measurements available to constrain the rotation at smaller radii.

Note that we follow van de Ven et al. (2006) in that x' and y' denote the cluster-centric coordinates along the projected semi-major and semi-minor axes of ω Cen.

To investigate the three-dimensional rotation of ω Cen, we combined the proper motion sample described in Sec. 3.8.1 with the MUSE catalog presented in Nitschai et al. (2023) and kept all stars that appear in all three data sets (i.e., HST, Gaia, and MUSE). We used the same Voronoi bins as shown in Fig. 3.14 to measure mean proper motions and line-of-sight velocities across the face of the cluster.

Inferring the inclination of ω Cen via eq. 3.3 requires an assumption about the orientation of the cluster in the plane of the sky. van de Ven et al. (2006) determined a position angle of the semi-major axis of $PA = 100^\circ$ (measured north to east) by fitting elliptical isophotes to a DSS image of ω Cen. Here, we follow a different approach in that we determine $\langle v_{z'} \rangle$ and $\langle \mu_{y'} \rangle$ in every Voronoi bin for different assumed position angles and fitting a straight line to the relation between the two. Applying eq. 3.3, we adopt the position angle that minimizes the fit residuals between the two. The result of this exercise is shown in the left panel of Fig. 3.15. The fit residuals show a well-defined minimum at a position angle close to the value of $PA = 100^\circ$ obtained by van de Ven et al. (2006). By fitting a quadratic function to the fit residuals within 10° of the minimum, we obtain $PA = 104 \pm 1^\circ$. Note that we adopt our stepsize in position angle as the uncertainty, as the nominal uncertainty of the minimum of the quadratic fit is smaller.

Adopting $PA = 104^\circ$, we show the relation between $\langle v_{z,} \rangle$ and $\langle \mu_{y'} \rangle$ in the right panel of Fig. 3.15. The values and uncertainties for each data point were determined via a maximum likelihood analysis, where each component of the velocity distribution per Voronoi bin was matched to a two-parameter Gaussian model (mean velocity and velocity dispersion) using the Markov-Chain Monte Carlo code

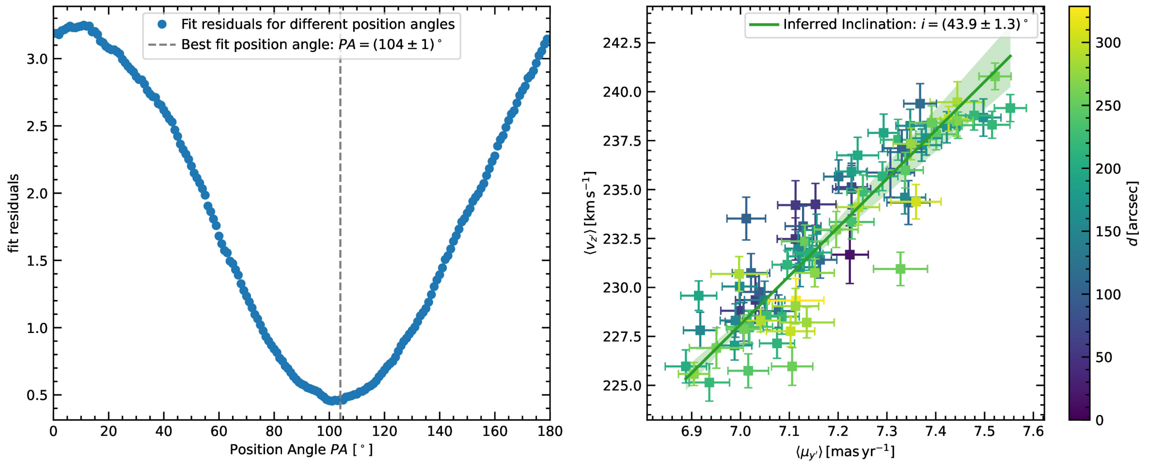

Figure 3.15: Determination of position angle and inclination. The left panel shows the scatter in the relation between mean line-of-sight velocity and mean semi-minor-axis proper motion defined by eq. 3.3, for the different Voronoi bins and for a wide range of assumed position angles of ω Cen. For the position angle yielding the least amount of scatter, the right panel shows the aforementioned relation. The results obtained in the various Voronoi bins are color-coded by the distance of each bin to the cluster center.

emcee (Foreman-Mackey et al., 2013b). We observe a strong correlation between the two quantities, as expected based on eq. 3.3. Nevertheless, it is interesting to note that the individual data points show a larger scatter around the best-fitting linear relation than expected based on their uncertainties. To investigate if this trend is indicative of deviations from axisymmetry, we colour-code the data points by the distances of the corresponding Voronoi bins to the cluster center. However, there is no obvious trend that bins at specific distances show larger deviations.

The linear fit included in the right panel of Fig. 3.15 corresponds to $D \tan i = 5.23 \pm 0.23$ kpc. If we adopt again a distance of $D = (5.43 \pm 0.05)$ kpc (Baumgardt & Vasiliev, 2021), we obtain an inclination of $i = (43.9 \pm 1.3)^\circ$. This value is in good agreement with previous estimates of the inclination of ω Cen. van de Ven et al. (2006) derived a value of $i = 48^\circ\ (+9\ -7)^\circ$, while Sollima et al. (2019) found $i = (39.2 \pm 4.4)^\circ$.

3.9 Released data products and recommended use

We make our catalog public in the form of fits tables and Machine Readable ASCII files in a repository hosted by Zenodo (doi:10.5281/zenodo.11104046). In the following section, we describe the content of the different published files.

3.9.1 Astrometric catalog

We publish a single table that contains the astrometric data including precise positions, proper motions, and several diagnostic parameters. For a description of the different columns see Appendix 3.15; Table 3.8. Our catalogs contains all sources which were recovered in at least two epochs (see Section 3.5.1).

For a small fraction of these sources, no proper motion measurement was possible (either due to saturation or because the proper motion fit did not converge). For these sources we only report the measured position.

3.9.1.1 Exemplary selection of a high-quality subset

Depending on the specific science case one has to restrict the dataset to obtain a subset with the necessary precision and reliability. In the following we discuss how a quality selection combining several diagnostics can be assembled. This exemplary selection is also demonstrated in our example use case notebook and the resulting flag is published with the catalog. The vector-point diagram shown in Figure 3.7 is also using these selctions, demonstrating their effectiveness.

Typically one would start with requiring the formal proper motion error on both components to be below a desired limit (e.g. $\sigma\mu_\delta < 0.2\,\mathrm{mas\,yr^{-1}}$). In addition, it is recommended to use the reduced chi square of the linear fit of both proper motions to limit the sample to stars with a well-behaved measurement, here we adopt a limit of $\chi^2_{red} < 5$.

For our high-quality selection we additionally require a baseline of at least 10 years to obtain a more uniform dataset. The baseline cut is met throughout most of the field of view, however some of the outer regions with partial overlap are lost (see also Fig. 3.4). Finally, to reject stars where a lot of measurements were clipped, we require a fraction of used measurements $N_{used}/N_{found} > 0.8$. The combination of these criteria is met for 1 024 768 of 1 395 781 stars with a proper motion measurement.

3.9.1.2 Recommended use of local corrections

The local astrometric corrections (see Section 3.5.3) use the proper motions of neighbouring stars with similar magnitudes to correct for residual systematic effects. The columns `pmra_corrected` and `pmdec_corrected` contain the proper motions resulting after the local corrections are applied (with the corresponding errors in `pmra_corrected_err` and `pmdec_corrected_err`). We recommend using these corrections for studies including faint stars in the outer fields (where systematic trends caused by CTE are strongest, see Figure 3.6). In the centermost region, where systematic spatial trends are less of an issue due to the higher number of pointings and rotation angles, it is a trade-off between larger statistical errors, due to the error on the correction, and residual spatial trends.

3.9.1.3 Crossmatches with other catalogs

To facilitate future investigations, we include the results of a crossmatch with two literature catalogs in our astrometric table:

The column `Nitschai_ID` contains the ID (Column `MUSE` in the MUSE catalog) of stars that have been matched with *oMEGACat* I MUSE catalog (Nitschai et al., 2023). For the MUSE cross-match we used a matching radius of 40 mas and also required that sources were measured in both the F435W and F625W filter. This allowed us to apply an additional photometric criterion, as the MUSE catalog also contains the photometry from the Anderson & van der Marel (2010) catalog. We required that there were no significant deviations in the photometry between the two catalogs. Finally, if multiple sources from the *HST* catalog lay within matching radius of a MUSE source, we only kept the closest crossmatch. This leads to successful crossmatch for 307 030 of the 342 797 stars in the MUSE catalog.

The column `gaia_id` contains the gaia source ID of stars from a crossmatch with both *Gaia FPR & DR3* (the column `gaia_origin` specifies the data release). Due to the larger astrometric errors in the *Gaia* catalogs, we used a matching radius of 160 mas. We did not apply a photometric cut, however this can be used to further refine the selection. Again we only kept the closest cross-match in the case of multiple sources within the matching radius. In total 373 291 stars match these criteria. To facilitate further comparisons between our dataset and the Gaia measurements we also include several key quantities from the crossmatched *Gaia* catalog in our release data products, including the source positions measured with *Gaia*, the absolute *Gaia* proper motion and the *Gaia G* photometry. The *Gaia* proper motions can be also used to substitute the missing proper motions for stars too bright for *HST* measurements. In that case, the different definitions of the proper motions (oMEGACat: relative; *Gaia*: absolute) have to be taken into account. In addition, we add the flag `gaia_hq_subset` for the high quality subset that has been used for the rotation curve determination.

3.9.2 PHOTOMETRIC CATALOG

3.9.2.1 RECOMMENDED USAGE OF CORRECTIONS AND ERRORS

We publish a table with the photometric information for each of the 3 ACS/WFC filters (F435W, F625W, F658N) and the 4 WFC3/UVIS filters (F275W, F336W, F606W, F814W). For a description of the different columns see Appendix 3.15; Table 3.9. In general, we recommend the use of our empirical photometric corrections (Section 3.6.5.1), although this slighlty reduces the coverage.

Just like for the astrometric catalog, in the following section we explain how to select a sample of well-measured stars, with the caveat that each science case might have different requirements for these selections.

For most photometric use-cases we recommend to use the weighted mean of method 1 (see Section 3.4.6) photometry (`m1_weighted_mean`). The corresponding weighted mean error is saved as column `m1_weighted_mean_error`. This error may be underestimated in cases of crowding, therefore, we recommend scaling it with the square-root of the `chi2_red` whenever $\chi^2_{red.} > 1.0$. When applying the empirical photometric corrections determined in Section 3.6.5.1 (which we also recommend for most cases), one additionally has to add the error on the correction (Table 3.3) in quadrature. For the convenience of the user, we provide the corrected photometry and the combined error in the first two columns `corrected_mag` and `corrected_mag_error` in the published data products. We also note here that the absolute zeropoints have reported uncertainties of ~1% (ACS, Bohlin 2016) and 2-3% (UVIS, Calamida et al. 2022), which corresponds to absolute uncertainties at the 0.02-0.03 mag level. This absolute uncertainty does not affect the internal consistency of our catalog (which is ensured by the corrections), but has to be taken into account when comparing the data e.g. with isochrone models.

3.9.2.2 Caveats about different magnitude regimes

We remind the user, that bright saturated stars were not measured with `KS2`, instead we substituted their `hst1pass` measurement. We mark all stars for which this was the case with the `brightlist_flag`. We also caution the user that brighter stars often only have one short exposure measurement in some of our filters (ACS/WFC F435W, F625W), therefore all photometric selections that require more than one measurement can reduce the coverage and completeness for these otherwise well-measured bright stars.

For faint main-sequence stars ($m_{\mathrm{F275}W} > 22$, $m_{\mathrm{F336}W} > 21$), uncorrected charge-transfer efficiency effects introduce systematic spatial variations in the Filters WFC3/UVIS F275W and F336W. This mostly affects the outer pointings which were taken recently with the aging detectors, while the center is less affected.

Finally we remind the user, that the photometric corrections were derived using reference stars in the magnitude region ($15.0 < m_{F814W} < 19.0$), see also Section 3.5.3. Magnitude independent effects are corrected nevertheless, but the corrections are most effective in this region.

3.9.2.3 Quality criteria

Several quality criteria measure how well the PSF describes the measured flux of the source. This includes the QFIT parameter (the linear correlation coefficient between the PSF and the measured source flux), the RADXS parameter (a measure whether a source is more extended or sharper than expected from the PSF Bedin et al. 2008); and the o value (the ratio between the flux of source and of neighboring stars). These parameters are determined in each individual exposure, when combining measurements with the magnitude-error weighted mean (see Section 3.6), we also calculate a mean of these quality parameter, which is the value we report in the catalogs.

For stars with fainter magnitude, the `QFIT` parameter worsens due to their lower signal-to-noise. Therefore, it is recommended to use magnitude dependent thresholds.

3.9.2.4 Exemplary photometric correction

Our exemplary selection rejects stars below the 10th `QFIT` percentile 0.5 mag wide bins. Stars with `QFIT`> 0.98 are always kept, while stars with `QFIT`< 0.4 are always rejected. The only other criterion we apply is `o`< 0.5 i.e. the stars flux within the fit aperture is at least twice as high as the flux of neighboring sources. The resulting selections is published in column `phot_hq_flag` in the photometric tables.

Table 3.4 lists the number of stars that match the combined photometric criteria in the different filters.

3.9.3 Stacked images

Along our astro-photometric catalog, we publish stacked images for the 7 filters, for which we release photometric information. The stacked images are normalized to the typical exposure time for the

Table 3.4: Number of stars in each filter different that are saturated ($N_{\mathrm{Sat.}}$) or are matching our exemplary quality criterion (N_{HQ}) compared to the total number of measurements available in that filter N_{Total}

Instrument	Filter	$N_{Sat.}$	N_{HQ}	N_{Total}
WFC3/UVIS	F275W	697	599477	825061
WFC3/UVIS	F336W	691	761759	1105255
ACS/WFC	F435W	1383	883083	1355786
WFC3/UVIS	F606W	2088	435618	622052
ACS/WFC	F625W	3944	990139	1395979
ACS/WFC	F658N	4418	953034	1387347
WFC3/UVIS	F814W	2090	1045201	1335929

Table 3.5: Exposure times to which the published stacked images are normalized.

Instrument	Filter	Exposure time
ACS/WFC	F435W	340 s
ACS/WFC	F625W	340 s
ACS/WFC	F658N	440 s
WFC3/UVIS	F275W	773 s
WFC3/UVIS	F336W	475 s
WFC3/UVIS	F606W	40 s
WFC3/UVIS	F814W	250 s

respective filter (see Table 3.5) and combine images from all epochs. Note that the exact flux distribution of sources in the individual images is not preserved in the stacked images, and therefore their main use should be as a high-quality representation of the scene rather than for PSF fitting. The images contain precise WCS information in their header and are also compatible with the pixel coordinates in our astrometric catalog (apart from a shift of [5000, 5000] pixels to allow for a smaller image size). An RGB image based on the filters WFC3/UVIS F275W, F336W and F814W can be found in Figure 3.2.

3.9.4 Public examples on catalog usage

Together with the data products we publish an IPython notebook [9] that can be used as starting point for the usage of our catalog. The notebook includes:

- Selection of high-quality astrometric measurements and plot of a vector-point diagram
- Comparison of *Gaia* and *HST* proper motions
- Selection of high-quality photometric measurements and plot of several CMDs
- An exemplary calculation on how to propagate the stellar motions from the new catalog to any given epoch while properly accounting for the absolute motion of the cluster and the relative motion of the individual stars
- Plots of the stacked images overlaid with data from the catalog

---

[9] Again this notebook is made publicly accessible in a Zenodo repository (doi:10.5281/zenodo.11104046)

3.10 CONCLUSIONS

In this second paper of the *oMEGACat* series we describe the creation of a deep, *HST* based astrometric and photometric catalog covering the cluster ω Cen out to its half-light radius. The full catalog is made public along with this publication.

The catalog contains high-precision proper-motion measurements for around 1.4 million stars, more than any other space- or ground-based catalog of ω Cen. For bright stars ($m_{\mathrm{F625}W} \approx 18$) we reach a median 1D proper-motion error of 0.011 mas yr^{-1}. In the well-covered inner region, this median error decreases down to 0.007 mas yr^{-1}, corresponding to a velocity of only 0.15 km s^{-1} at the distance of ω Cen. We corrected our proper motions from residual systematic effects using an approach that measures the net-motion of neighboring cluster stars.

Our catalog also contains photometry in 6 filter bands (WFC3/UVIS: F275W, F336W, F625W; ACS/WFC: F435W, F625W, F658N) for the full field and an additional filter (F606W) with especially good coverage in the centermost region. This filter set allows the separation of the various, complex stellar subpopulations hosted by ω Cen.

We compare our catalog with the available literature catalogs (Bellini et al., 2017a; *Gaia DR3* Gaia Collaboration et al., 2021a; Lindegren et al., 2021; *Gaia FPR:* Gaia Collaboration et al., 2023b) and can confirm a generally good agreement, with our catalog having a significantly higher proper motion precision and reaching fainter magnitudes than all the previous works.

Our catalog is complementary to the recently published, large spectroscopic catalog (Nitschai et al., 2023), covering the same region on the sky and containing line-of-sight velocity and metallicity measurements for more than 300 000 stars.

As a first science result, we determined the plane-of-sky rotation curve of ω Cen with unprecedented resolution using a combination of our relative proper motions and the absolute proper motions from *Gaia*. In addition, we obtain a precise measurement of ω Cen's inclination of $i = (43.9 \pm 1.3)°$.

The combined *oMEGACat* catalogs are already enabling a broad range of interesting science. Ongoing projects are the study of the Age-Metallicity relation of ω Cen (Clontz et al. in prep.), the automated separation of subpopulations based on photometry and metallicity (Clontz et al. in prep), the discovery of fast-moving stars indicative of an intermediate-mass black hole (Häberle et al., 2024a), the search for spatial differences in the metallicity distribution (Nitschai et al., 2024) and the extraction of individual abundances using stacked spectra (Di Stefano et al. in prep.). The MUSE data of the centermost region is well matched to the depth of our proper motion catalog and has revealed a counter-rotating core in the centermost (Pechetti et al., 2024) region. We plan to use the combined dataset to create a dynamical model of this region (Pechetti et al.) and eventually the whole cluster.

ACKNOWLEDGMENTS

A.B. acknowledges support from STScI grant GO-15857. A.B. C.C.,M.A.C., and A.C.S. acknowledge support from STScI grant GO-16777. Based on archival and new observations with the NASA/ESA Hubble Space Telescope, obtained at the Space Telescope Science Institute, which is operated by

AURA, Inc., under NASA contract NAS 5-26555. SK acknowledges funding from UKRI in the form of a Future Leaders Fellowship (grant no. MR/T022868/1). A.F.K. acknowledges funding from the Austrian Science Fund (FWF) [grant DOI 10.55776/ESP542]. This work has made use of data from the European Space Agency (ESA) mission *Gaia* (https://www.cosmos.esa.int/gaia), processed by the *Gaia* Data Processing and Analysis Consortium (DPAC, https://www.cosmos.esa.int/web/gaia/dpac/consortium). Funding for the DPAC has been provided by national institutions, in particular, the institutions participating in the *Gaia* Multilateral Agreement.

SOFTWARE

astropy (Astropy Collaboration et al., 2022), matplotlib (Hunter, 2007), numpy (Harris et al., 2020), scipy (Virtanen et al., 2020), IPhyon (Perez & Granger, 2007), hst1pass (Anderson, 2022)

3.11 APPENDIX - DATASET

Tables 3.6 and 3.7 show show information on all individual exposures used for the creation of our catalog. A compilation of the full data set is also archived at DOI:10.17909/26qj-g090.

Table 3.6: List of all *HST* WFC3/UVIS observations used for our astrophotometric measurements

GO	PI	Filter	N x Exp. Time	Min. - Max. Epoch (year−2000)	Field
11452	J. Kim Quijano	F275W F336W F438W F606W F814W	1 × 35; 9 × 350; 1 × 35; 9 × 350; 1 × 35; 1 × 35; 1 × 35;	9.53740 - 9.53832	Center
11911	E. Sabbi	F275W F336W F390W F438W F555W F606W F775W F814W	22 × 800; 19 × 350; 15 × 350; 25 × 350; 18 × 40; 27 × 40; 16 × 350; 27 × 40;	10.03462 - 10.50779	Center
12094	L. Petro	F606W	9 × 40;	10.31645 - 10.31699	Center
12339	E. Sabbi	F275W F336W F438W F555W F606W F814W	9 × 800; 9 × 350; 9 × 350; 9 × 40; 9 × 40; 9 × 40;	11.12532 - 11.22895	Center
12353	V. Kozhurina-Platais	F606W	13 × 40;	10.95038 - 11.56642	Center
12580	A. Renzini	F275W F336W F438W	2 × 909; 2 × 914; 2 × 1028; 2 × 1030; 2 × 1267; 2 × 562; 2 × 565; 1 × 945; 1 × 953; 4 × 200; 2 × 210;	12.18821 - 12.32857	Southwest
12694	K. Long	F606W	2 × 350;	12.15906 - 12.32275	Center
12700	A. Riess	F775W	2 × 450;	12.48594 - 12.48620	Center
12714	V. Kozhurina-Platais	F606W	4 × 40;	12.18563 - 12.18574	Center
12802	J. MacKenty	F336W	29 × 10; 8 × 700;	12.56737 - 12.56800	Center
13100	V. Kozhurina-Platais	F606W	3 × 40; 9 × 48;	12.95411 - 13.22892	Center
13570	V. Kozhurina-Platais	F606W	9 × 40;	13.95233 - 14.68451	Center
14031	V. Kozhurina-Platais	F606W	19 × 40; 5 × 60; 1 × 120;	15.02381 - 15.46965	Center
14393	V. Kozhurina-Platais	F606W	19 × 40; 3 × 60;	15.94769 - 16.48538	Center
14550	V. Kozhurina-Platais	F606W	9 × 60;	17.08296 - 17.46694	Center
14759	T. Brown	F275W F336W F438W	3 × 765; 3 × 850; 3 × 630; 3 × 765; 3 × 630; 3 × 1025;	16.94372 - 17.28252	Southeast & Southwest
15000	V. Kozhurina-Platais	F606W	9 × 60;	18.00372 - 18.51208	Center
15593	V. Kozhurina-Platais	F606W	9 × 60;	19.08460 - 19.54426	Center
15594	V. Kozhurina-Platais	F438W F606W F814W	2 × 50; 6 × 697; 2 × 50; 6 × 697; 3 × 50; 9 × 697;	19.15842 - 19.65534	Center
15733	V. Kozhurina-Platais	F606W	6 × 60;	20.08423 - 20.16737	Center
15857	A. Bellini	F275W F336W	1 × 710; 1 × 730; 1 × 497; 1 × 520;	21.15030 - 21.15038	Southwest
16117	M. Reinhart	F606W	4 × 15; 4 × 400;	20.45939 - 20.45956	Center
16413	V. Kozhurina-Platais	F606W	12 × 60;	21.14014 - 21.58543	Center
16441	J. Anderson	F606W	8 × 4; 4 × 800;	21.00757 - 21.00781	Center
16588	V. Kozhurina-Platais	F606W	9 × 60;	22.03211 - 22.48428	Center
16777	A. Seth	F275W F336W F814W	10 × 700; 20 × 773; 20 × 40; 30 × 475; 20 × 15; 20 × 250;	22.62801 - 23.09828	Ring reaching r_{HL} Excluding Center
17023	C. Martlin	F606W	3 × 60;	23.04349 - 23.04357	Center

Table 3.7: List of all *HST* ACS/WFC observations used for our astrophotometric measurements

GO	PI	Filter	N x Exp. Time	Min. - Max. Epoch (year−2000)	Field
9442	A. Cool	F435W	9 × 12; 27 × 340;	2002.48916 - 2002.49745	3x3 grid covering 10′x10′
		F625W	9 × 8; 27 × 340;		
		F658N	36 × 440;		
10252	J. Anderson	F606W	1 × 15; 5 × 340;	2004.94612 - 2004.94636	South East
		F814W	1 × 15; 5 × 340;		
10775	A. Sarajedini	F606W	2 × 4; 8 × 80;	2006.16055 - 2006.55718	Center
		F814W	2 × 4; 8 × 90;		
12193	J. Lee	F606W	1 × 200; 1 × 500;	2011.53248 - 2011.53254	North West
		F814W	1 × 400;		
13066	L. Smith	F435W	9 × 6; 9 × 339;	2012.63115 - 2012.63150	Center
		F606W	1 × 339;		
13606	J. Anderson	F435W	4 × 339;	2013.95179 - 2013.95223	Center
		F606W	4 × 80;		
		F814W	4 × 90;		
15594	V. Kozhurina-Platais	F435W	2 × 42; 6 × 647;	2019.15842 - 2019.65534	Center
		F606W	2 × 42; 6 × 656;		
		F814W	2 × 42; 6 × 656;		
15764	N. Hathi	F435W	2 × 339;	2020.10328 - 2020.54298	Center
		F475W	2 × 339;		
		F555W	1 × 339;		
		F606W	2 × 339;		
		F625W	1 × 339;		
		F658N	1 × 339;		
		F775W	2 × 339;		
		F814W	2 × 339;		
15857	A. Bellini	F606W	2 × 417; 2 × 668; 1 × 671; 2 × 700; 3 × 757;	2020.70743 - 2021.15038	South West
		F814W	3 × 337; 3 × 379;		
16380	M. Chiaberge	F606W	6 × 40; 6 × 150; 6 × 400;	2021.54871 - 2021.55220	Center
16384	Y. Cohen	F435W	2 × 337;	2021.14867 - 2021.65577	Center
		F475W	2 × 337;		
		F555W	2 × 337;		
		F606W	3 × 337;		
		F625W	2 × 337;		
		F658N	1 × 350;		
		F775W	3 × 337;		
		F814W	2 × 337;		
16520	N. Hathi	F435W	2 × 337;	2022.19657 - 2022.61983	Center
		F475W	2 × 337;		
		F555W	1 × 337;		
		F606W	2 × 337;		
		F625W	1 × 337;		
		F658N	1 × 350;		
		F775W	2 × 337;		
		F814W	2 × 337;		
16968	N. Hathi	F435W	1 × 337;	2023.08588 - 2023.08596	Center
		F475W	1 × 337;		
		F606W	1 × 337;		
		F775W	1 × 337;		
		F814W	1 × 337;		

3.12 Appendix - Photometric corrections

Figures 3.16 and 3.17 show maps of the spatially variable photometric corrections derived in Section 3.6.5. These corrections are a superposition of differential reddening, which has a physical origin, and instrumental effects and zero-point variations.

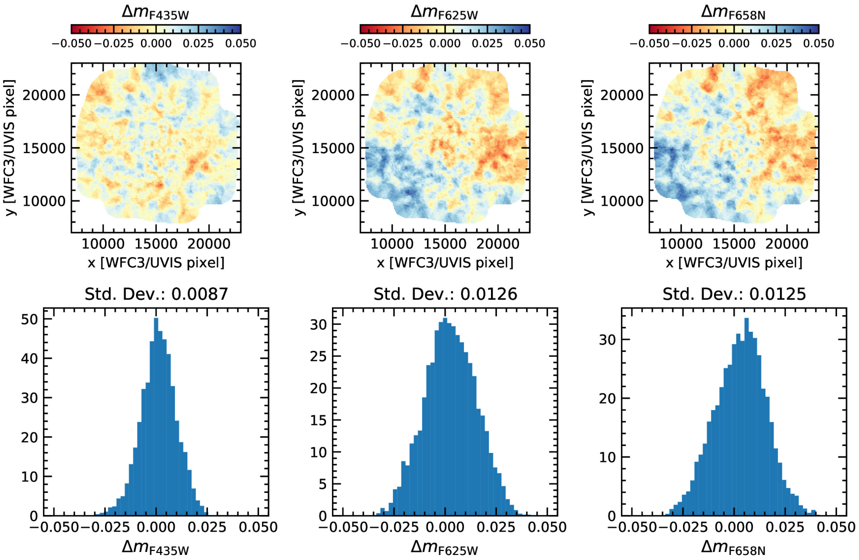

Figure 3.16: The upper row in this figure shows maps of the empirical photometric corrections (see Section 3.5.3) for each of the 3 ACS/WFC filters in our dataset. They are a combination of physical differential reddening and instrumental/calibration effects. The lower panel shows histograms of the distribution of correction values.

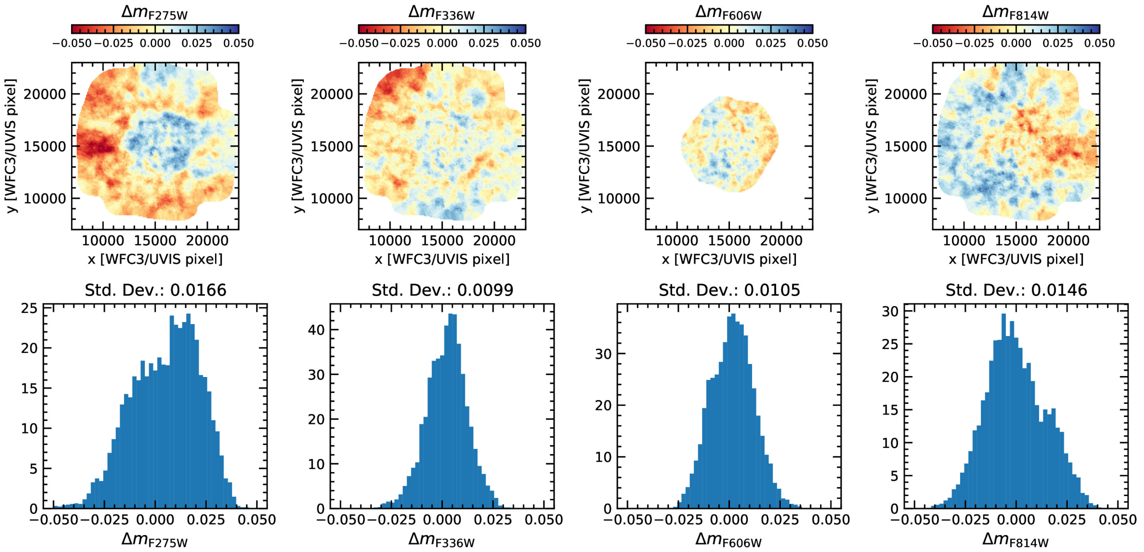

Figure 3.17: The upper row in this figure shows maps of the empirical photometric corrections (see Section 3.5.3) for each of the 4 WFC3/UVIS filters in our dataset. They are a combination of physical differential reddening and instrumental/calibration effects. The lower panel shows histograms of the distribution of correction values.

3.13 APPENDIX - CATALOG VALIDATION: SEARCH FOR SYSTEMATIC EFFECTS IN MAGNITUDE AND COLOR

By construction, the a-posteriori corrections described in Section 3.5.3 identify any systematic spatial trends within certain magnitude ranges and remove them. Figure 3.6 shows that these trends were strongest for faint magnitudes and that the a-posteriori corrections could remove them efficiently.

In addition to the local trends in magnitude, we also searched for global trends in magnitude and color, by dividing the proper motions in $m_{\mathrm{F625}W}$-magnitude, or $m_{\mathrm{F625}W} - m_{\mathrm{F814}W}$ color bins (see Figure 3.18). We calculated the median of the two proper-motion components in each bin and did not see any significant deviation from zero, neither for the raw nor for the a-posteriori corrected proper motions (see Figure 3.18).

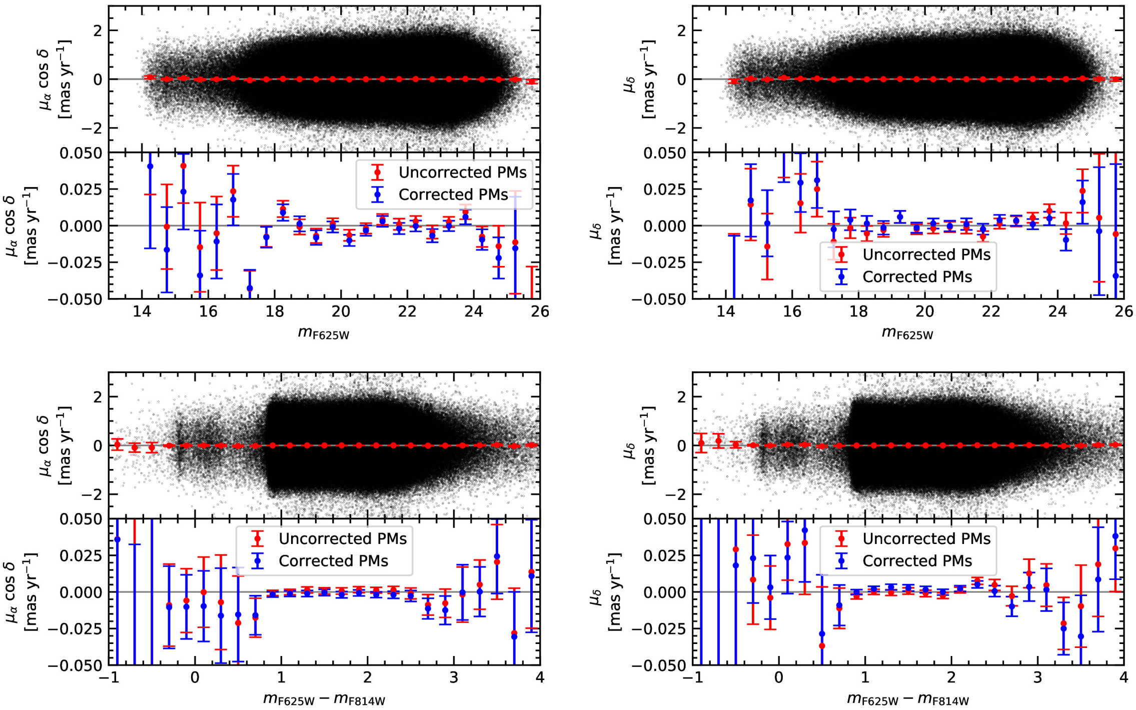

Figure 3.18: Illustration of our search for global systematic effects as a function of magnitude and color. The first row shows the proper-motion measurements plotted against the magnitude for the right ascension (left) and declination (right) components. The individual measurements are shown as black dots, the median proper motion in 0.5 mag wide bins with red error bars. As the median proper motion is very close to zero, we show a more detailed view in the second row. Neither a-posteriori corrected nor uncorrected proper motions show any significant systematic trend. Similarly in rows 3 and 4 we show the two proper-motion components plotted against their $m_{\mathrm{F625}W} - m_{\mathrm{F814}W}$ color index. Also here, there are no significant trends visible.

3.14 APPENDIX - COMPARISONS WITH LITERATURE CATALOGS

3.14.1 CROSSMATCH AND DIRECT COMPARISON WITH BELLINI ET AL. (2017A)

The deepest and most precise photometric and astrometric catalog of the central region of ω Cen beside this work was published by Bellini et al. (2017a). The authors published `KS2` (see Section 3.4.6) photometry for 26 filters of WFC3/UVIS and WFC3/IR. In addition, they crossmatched and published the proper-motion catalog from Bellini et al. (2014) along with the photometric catalogs. In our catalog we include 9 years of additional data and use improved analysis tools, (Bellini et al., 2014 do not use second-pass photometry for the proper-motion measurements, no focus variable PSF models were available at that time) and therefore, we expect significantly smaller astrometric errors in our new catalog. We crossmatched both catalogs to see whether the photometry and astrometry results are consistent, at least in the core region included in both catalogs.

We transformed the pixel-based coordinate system of Bellini et al. (2017a) to our own reference system using 6 parameter linear transformations. After that, we used a matching radius of 1 WFC/UVIS pixel (40 mas) to crossmatch stars. This radius is large enough, as the reference epochs of the two catalogs are similar (Bellini et al.: 2007.0; This work: 2012.0). In 5 years the stars will have an RMS displacement of just 0.08 pixel. As it can be seen in Figure 3.19, the Bellini et al. catalog is fully contained within our larger field and most stars can be crossmatched (465 362/478 477 for the photometric and 242934/245443 for the astrometric catalog).

While the Bellini et al. catalog contains photometry for 26 filters, the focus of our study was on the 6 (3 ACS/WFC, 3 WFC3/UVIS) filters for which we have full coverage out to the half-light radius and the WFC3/UVIS F606W filter for which we have the largest number of photometric measurements in the center. Therefore, there are only 4 filters that we can compare. We show the difference of the method 1 (see Section 3.4.6) photometry for these 4 filters in Figure 3.19. The overall agreement is good and only very small systematic shifts of the zero point can be observed (F275W: -0.007; F336W: 0.014; F606W: 0.027; F814W: 0.006). We attribute those differences to the updated instrumental zero point values (see Section 3.6.1) and the slightly different radii used to create the aperture-photometry-based reference systems. They are of the same order of magnitude as the reported uncertainties on the absolute flux calibration (Calamida et al., 2022).

To directly compare the proper motions, we restrict our analysis to stars brighter than $m_{\mathrm{F606}W} = 18$, as their statistical errors are lower and potential systematic effects are easier to detect. Figure 3.20 shows the comparison of the raw proper motions. While the overall agreement is good (RMS of difference $\sim$0.09 mas yr^{-1} in both components), one can see some low spatial frequency effects with amplitudes of up to $\sim$0.1 mas yr^{-1}. These systematic deviations cannot be explained using the individual proper-motion errors alone (the error distributions are 2.31/2.56 times wider than what would be expected from the proper motions errors alone). This is not unexpected for the raw proper motions and can be attributed to CTE effects and residual distortion and is also why we employed the local a-posteriori corrections (see Section 3.5.3).

In Figure 3.21, we compare the proper motions after the local a-posteriori corrections have been applied in both catalogs. As expected, the low spatial frequency pattern has disappeared. Instead, we now can see some granularity which is most likely caused by the spatial scale of the local corrections and the limited number of available reference stars. The errors of the corrected proper motions do account for this additional uncertainty and, therefore, the distribution of the residuals is now much more compatible with the errors in the proper-motion catalogs (1.36 / 1.33 times wider than what would be expected from the proper motions errors). The magnitude dependence of the deviations between the proper-motions from the two catalogs is compared in Figure 3.22, as expected the deviations increase for fainter stars.

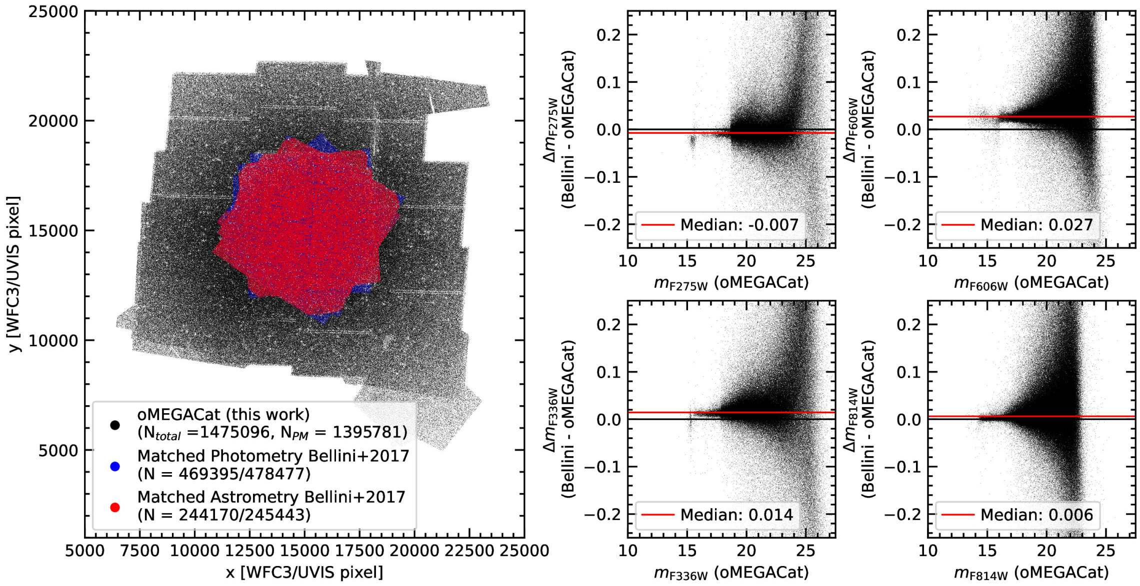

Figure 3.19: *Left:* Footprint of our proper-motion catalog (black) and the photometric (blue) and astrometric (red) catalogs published in Bellini et al. (2017a). *Right:* Comparison of calibrated photometry between this work and the Bellini et al. (2017a) photometric catalog for 4 WFC3/UVIS filters (F275W, F336W, F606W, F814W)

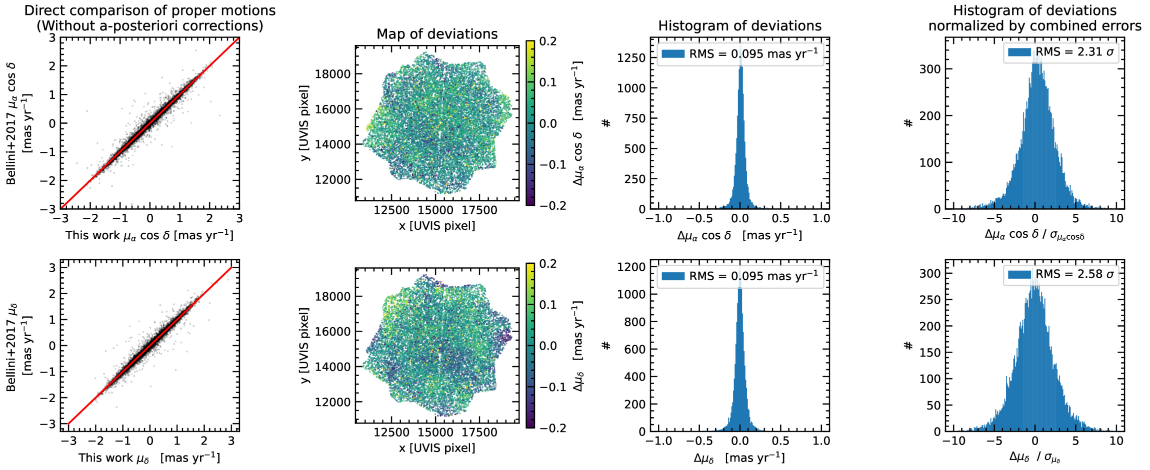

Figure 3.20: Comparison of uncorrected proper motions with Bellini et al. (2017a) for the right-ascension (upper row) and the declination proper-motion component (lower row). The panels first-from-the-left show a direct comparison of the proper-motion components. The red line is the plane-bisector and not a fit to the data. The second-from-the-left panels show how the proper motion difference between the two datasets varies over the field. Some mild systematic trends are visible, as expected for the uncorrected, amplifier-based, proper motions. The third-from-the-left panels show a histogram of the differences between the measurements, the fourth-from-the-left panels show the same differences but divided by the combined proper-motion error.

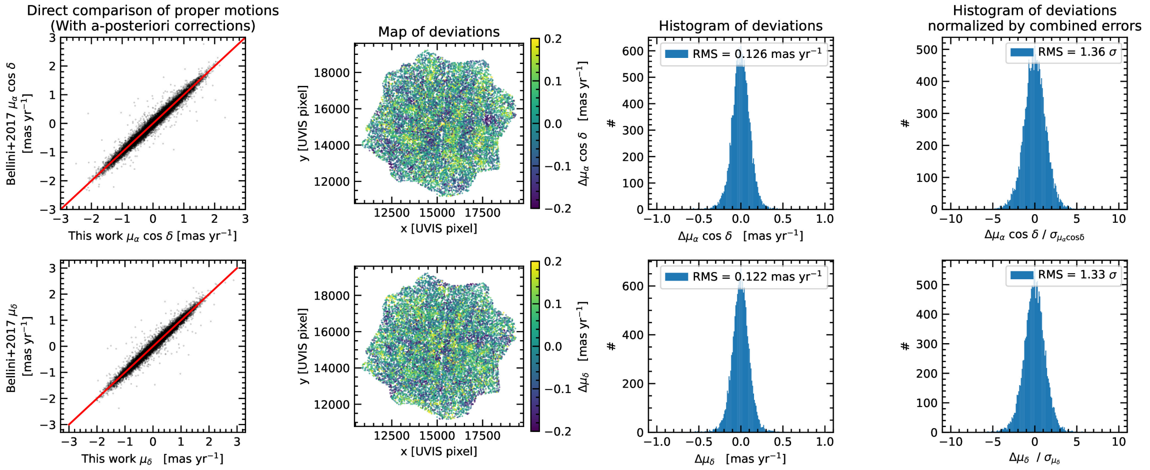

Figure 3.21: Similar to Figure 3.20, but instead of the amplifier-based proper motions, we apply the local a-posteriori corrections in both catalogs before the comparison. Note how the spatial variation of the deviations (second-from-left panels) and the normalized distribution of deviations (rightmost panels) change with respect to Figure 3.20.

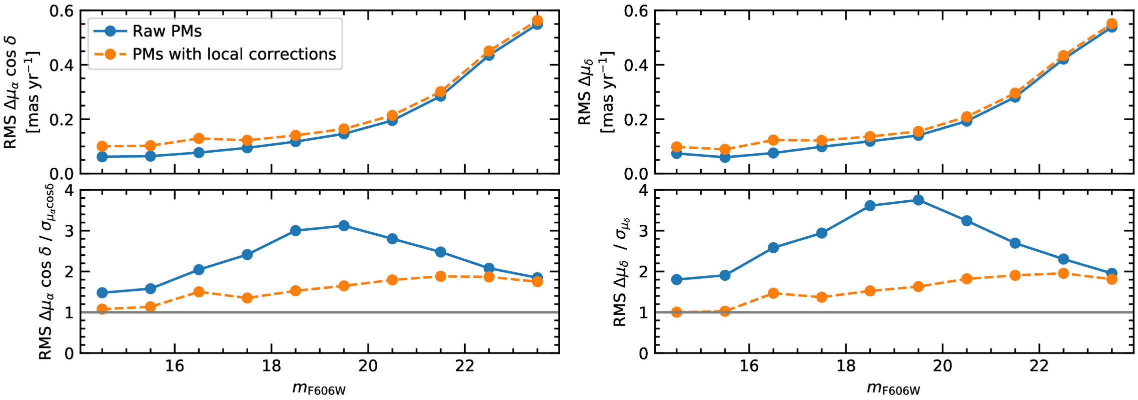

Figure 3.22: Analysis of how the dependence of the RMS of the deviation between this work and the Bellini et al. (2017a) catalogs changes with magnitude. The upper panels show the RMS of the absolute deviation of the two proper-motion components, and the lower panels show the RMS of the relative (i.e. scaled by the combined error) proper-motion components.

3.14.2 CROSSMATCH AND DIRECT COMPARISON WITH *GAIA* DR3 & FPR

As already described above, the *Gaia DR3* is affected by crowding and has been extended by the *Gaia FPR*. Here, we crossmatch the combined *DR3 + FPR Gaia* catalog with our new *HST* catalog. Using a simple geometric cutoff of 160 mas, we find 373 291 stars in common with our catalog (27 123 from *DR3* and 346 168 from the *FPR*). When comparing the completeness of the two catalogs with respect to each other, see Figure 3.23, one can see very good agreement. When using our new *HST* catalog as reference, the combined *Gaia DR3 + FPR* catalog shows good completeness for magnitudes brighter than $m_{\mathrm{F625}W} \sim 19$, for fainter stars the *Gaia* completeness drops sharply. On the other hand, if one uses the *Gaia* catalog as a reference and restricts it to the region covered by our *HST* catalog, almost all ($> 99\%$) *Gaia* sources can be recovered in the *HST* catalog over the full magnitude range. However, the sources brighter than *Gaia G* 14.5 typically have no *HST* proper motion measurements, due to saturation in the *HST* data.

As many of the crossmatched *Gaia* sources have limited accuracy and are affected by crowding, for the following analysis we limited ourselves to a subset of well-measured stars. We used a simple proper motion error cut of 0.6 mas yr^{-1} in both components and both datasets. In addition, we restrict the matching radius to 40 mas (1 WFC3/UVIS pixel) for the high-quality subset and only use stars with a minimum proper-motion baseline of 10 years. This high-quality (HQ) subset of crossmatched stars contains 5 897 entries from *DR3* and 24 467 from the *FPR*. In Figure 3.13 (left), it can be seen that, while the actual stellar density increases towards the center, the number of well-measured Gaia stars decreases. Also, it can be seen in the color-magnitude diagram in Figure 3.13 (middle panel) that the overlap between the catalogs is limited to a relatively small magnitude range of mostly evolved stars. In the right panel of Figure 3.13, we study the positional residuals between our catalog and well-measured stars from the *Gaia* catalogs. Given the different reference epochs of the catalogs (our catalog: 2012.0, *Gaia DR3*: 2016.0; *Gaia FPR:* 2017.5), and the fact that we anchored our (co-moving) astrometric reference system on observations from 2002.5, we expect both a systematic shift (based on the absolute cluster motion with respect to 2002.5), and random deviations (caused by the individual stars random motion). As it can be seen in the figure, the absolute deviation is around 101 mas for *DR3*, and 112 mas for *FPR*, which is compatible with what we expect from the known absolute cluster motion from our initial 2002.5 epoch towards the respective *Gaia* reference epochs. The random position deviation has an RMS of ~ 3 mas (*DR3*) and 4 mas (*FPR*), also compatible with the displacement expected from the velocity dispersion of the cluster.

Figure 3.24 (*DR3*) and 3.25 (*FPR*) show the direct comparison and the differences between the proper motion components between the *Gaia* datasets and our new catalog. While there is an overall good agreement in terms of pure proper-motion values after the absolute proper motion of ω Cen is accounted for, there is one large-scale systematic trend that leads to differences of up to $\sim$0.3 mas yr^{-1}. The reason for these systematic differences lies in the different approaches used to measure proper motions: While *Gaia* measures absolute proper motions anchored to a fixed reference frame, we measure our *HST* proper motions relative to the bulk motion of cluster stars. We further discuss these systematic differences between the two catalogs in the following Section 3.8, where we use them to obtain a new, accurate measurement of ω Cen's rotation curve.

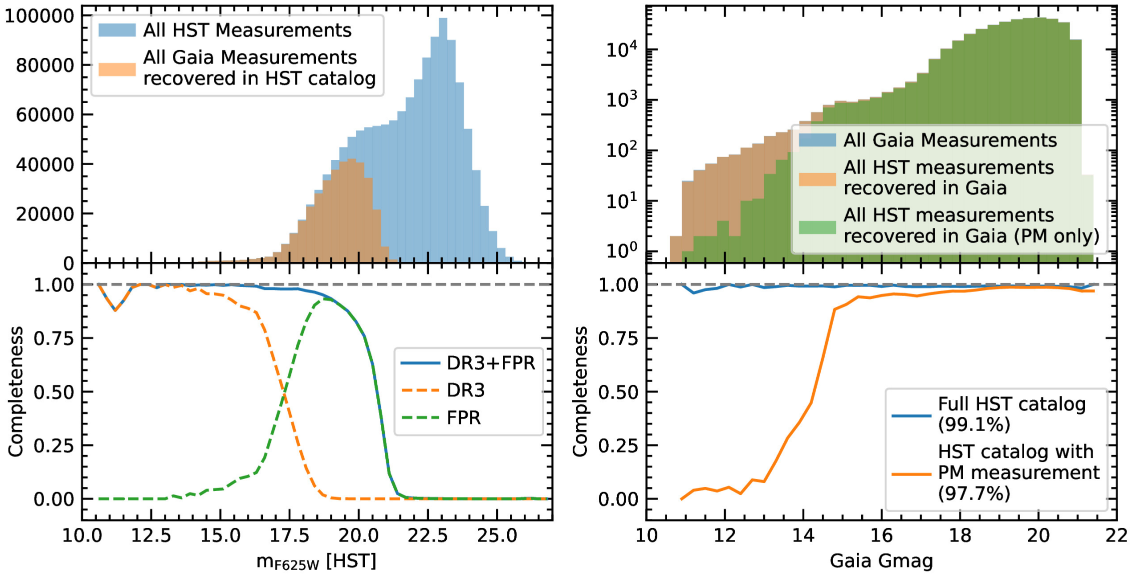

Figure 3.23: The upper panels show histograms of the magnitude distribution of both our new *oMEGACat HST* catalog and the combined *Gaia DR3+FPR* catalog, and the respective cross-matches between them. The ratio of recovered stars over all stars gives us the relative completeness between the catalogs, which is shown in the lower panels. The combined *Gaia* catalog shows high completeness ($> 90\%$) with respect to *HST* until it sharply drops at faint magnitudes. A 50% level of completeness is reached around $m_{\mathrm{F625}W} \sim 21$. The *HST* catalog is complete ($> 99\%$) with respect to *Gaia* over the full *Gaia* magnitude range, however at bright magnitudes (*Gaia* Gmag < 14.5) typically no *HST* proper motions are available due to saturation in the *HST* images.

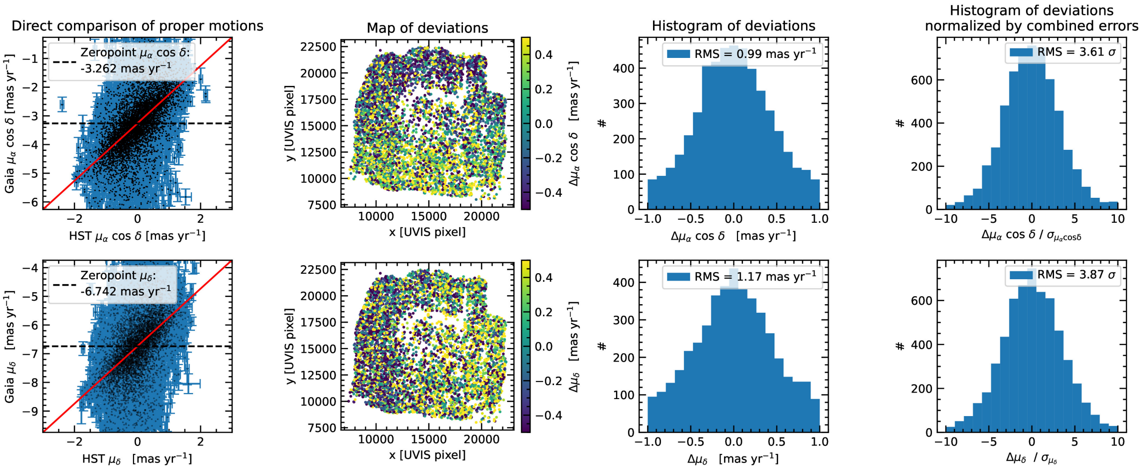

Figure 3.24: Similar to Figures 3.20 and 3.21, but in this figure we compare the corrected relative proper motions from this work with the absolute proper motions from the *Gaia DR3*. In the second-from-left panel one can see the dearth of *Gaia DR3* stars in the center of ω Cen, but also some completeness issues of our *oMEGACat* at very bright magnitudes. The visible systematic trends are the clear imprint of the cluster's rotation, which is further studied in Section 3.8 and Figure 3.14.

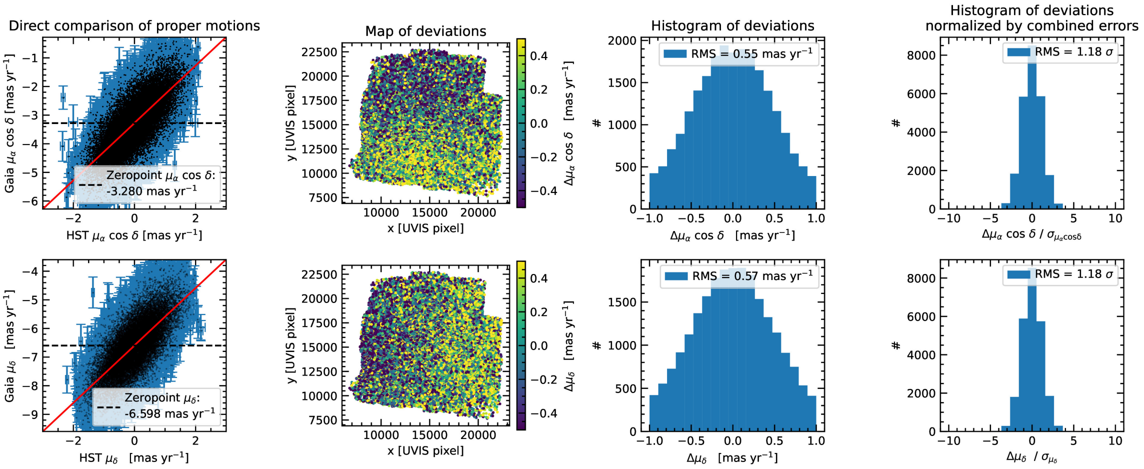

Figure 3.25: Similar to Figure 3.24, but in this figure we compare the corrected relative proper motions from this work with the absolute proper motions from the *Gaia FPR*. In comparison with *Gaia DR3* the completeness in the center is much better and astrometric residuals are lower. Just as in Figure 3.24 one can see the clear imprint of the cluster's rotation, which is further studied in Section 3.8 and Figure 3.14.

3.15 APPENDIX - DESCRIPTION OF COLUMNS IN THE DATA PRODUCT TABLES

Table 3.8 shows the content of the astrometric catalog with explanations for each individual column (see also Section 3.9.1). Table 3.9 shows the content of each of our seven photometric catalogs with explanations for each column (see also Section 3.9.2). The tables can be downloaded from Zenodo: doi:10.5281/zenodo.11104046.

Table 3.8: Content of the astrometric catalog.

Column	Description	Unit
`ID`	oMEGACat II Identifier	-
`RA`	Right Ascension α	degree
`DEC`	Declination δ	degree
`x`	x coordinate in pixel based coordinate system	40 mas (∼1 WFC3/UVIS pixel)
`y`	y coordinate in pixel based coordinate system	40 mas (∼1 WFC3/UVIS pixel)
`pmra`	Proper motion in R.A. direction $\mu_\alpha \cos\delta$	mas yr^{-1}
`pmdec`	Proper motion in Dec. direction μ_δ	mas yr^{-1}
`pmra_err`	Proper motion error in R.A. direction $\sigma\mu_\alpha \cos\delta$	mas yr^{-1}
`pmdec_err`	Proper motion error in Dec. direction $\sigma\mu_\delta\delta$	mas yr^{-1}
`ra_err_measured`	Error on R.A. position measurement	mas
`dec_err_measured`	Error on Dec. position measurement	mas
`chi2x`	Reduced χ^2 for PM fit in R.A. direction	-
`chi2y`	Reduced χ^2 for PM fit in Dec. direction	-
`uuu`	Flag indicating whether a star was used as reference star	-
`nfound`	Number of astrometric measurements available for PM Fit	-
`nused`	Number of astrometric measurements actually used for PM Fit	-
`baseline`	Temporal baseline of the PM Fit	years
`pmra_corrected`	Locally corrected proper motion in R.A. direction	mas yr^{-1}
`pmdec_corrected`	Locally corrected proper motion in Dec. direction	mas yr^{-1}
`pmra_corrected_err`	Error on locally corrected proper motion in R.A. direction	mas yr^{-1}
`pmdec_corrected_err`	Error on locally corrected proper motion in Dec. direction	mas yr^{-1}
`n_correction_stars`	Number of stars used for local a posteriori correction	-
`rmax_correction_stars`	Maximum distance to reference stars used for local a posteriori correction	40 mas (∼1 WFC3/UVIS pixel)
`nitschai_id`	ID in *oMEGACat I* MUSE spectroscopic catalog (Nitschai et al., 2023)	-
`gaia_id`	Gaia Source Identifier	-
`gaia_origin`	Gaia Data Release in which crossmatched sources were published	-
`gaia_ref_epoch`	Gaia reference epoch (2016.0 for DR3, 2017.5 for FPR)	years
`gaia_ra`	Gaia Right Ascension	degree
`gaia_ra_err`	Gaia Right Ascension Error	mas
`gaia_dec`	Gaia Declination	degree
`gaia_dec_err`	Gaia Declination Error	mas
`gaia_pmra`	Gaia proper motion in R.A. direction (absolute)	mas yr^{-1}
`gaia_pmra_err`	Gaia proper motion error in R.A. direction	mas yr^{-1}
`gaia_pmdec`	Gaia proper motion in Declination direction (absolute)	mas yr^{-1}
`gaia_pmdec_err`	Gaia proper motion error in Dec. direction	mas yr^{-1}
`gaia_phot_g_mean_mag`	Gaia G band mean magnitude	mag
`gaia_hq_flag`	Flag indicating whether a star was considered reliable in both Gaia and HST and used for rotation measurements	-
`hst_pm_hq_flag`	Flag indicating whether a star passed the exemplary combined quality criterion	-

Table 3.9: Content of each photometric catalog.

Column	Description	Unit
`ID`	oMEGACat II Identifier	-
`corrected_mag`	Photometry with empirical local corrections	mag
`corrected_mag_err`	$Red.\chi^2$ scaled error including error on corrections	mag
`m1_weighted_mean`	Weighted mean of the calibrated method 1 photometry	mag
`m1_weighted_mean_error`	Standard error of the weighted mean of the method 1 photometry	mag
`m1_weighted_rms`	Weighted RMS of the calibrated method 1 photometry	mag
`m1_median`	Median of the calibrated method 1 photometry	mag
`m1_mad`	Median absolute deviation of the calibrated method 1 photometry	mag
`m1_mean`	Standard mean of the calibrated method 1 photometry	mag
`m1_rms`	RMS of the calibrated method 1 photometry	mag
`n_measurements`	Number of measurements used to determine the combined photometric results for this filter	-
`chi2`	χ^2 value of the combined calibrated magnitude	-
`chi2_red`	reduced χ^2 value of the combined calibrated magnitude	-
`qfit_weighted_mean`	Weighted mean of the QFIT parameter of all individual measurements	-
`o_weighted_mean`	Weighted mean of the o value (ratio $f_{Source}/f_{Neighbors}$) of all individual measurements	-
`rx_weighted_mean`	Weighted mean of the radial excess parameter of all individual measurements	-
`m2_weighted_mean`	Weighted mean of the calibrated method 2 photometry	mag
`m3_weighted_mean`	Weighted mean of the calibrated method 3 photometry	mag
`iter_00_flag`	Flag indicating whether initial (non PM) crossmatch was used	-
`brightlist_flag`	Flag indicating whether photometry had to substituted from `hst1pass` due to saturation	-
`phot_hq_flag`	Flag indicating whether star passed exemplary photometric criteria	-

3.16 APPENDIX - NUMERICAL VALUES OF ROTATION PROFILE

Table 3.10 shows the numerical values for the plane-of-sky rotation profile determined in Section 3.8.1. It is also available in machine-readable form in the Zenodo Repository: DOI:10.5281/zenodo.11104046

Table 3.10: Numerical values of the rotation profile from Fig. 3.14

Lower limit of bin [arcsec]	Median radius of stars in bin [arcsec]	Upper limit of bin [arcsec]	Number of Stars -	Median tangential proper motion [mas yr^{-1}]	Inferred Rotation Velocity [km s^{-1}]
0.0	20.66	30.0	270	0.0548±0.0324	1.41±0.83
30.0	47.6	60.0	1020	0.086±0.0181	2.21±0.47
60.0	76.65	90.0	1620	0.1478±0.0131	3.8±0.34
90.0	105.91	120.0	2423	0.2088±0.0105	5.38±0.27
120.0	135.99	150.0	3031	0.2556±0.0093	6.58±0.24
150.0	165.6	180.0	3882	0.2562±0.0083	6.59±0.21
180.0	195.11	210.0	4361	0.2678±0.008	6.89±0.21
210.0	225.38	240.0	4470	0.2648±0.0078	6.82±0.20
240.0	254.06	270.0	4186	0.2797±0.0083	7.2±0.21
270.0	282.86	300.0	3020	0.2619±0.0103	6.74±0.27
300.0	309.92	330.0	985	0.2658±0.0176	6.84±0.45
330.0	340.91	360.0	246	0.2455±0.0421	6.32±1.08

4 FAST-MOVING STARS AROUND AN INTERMEDIATE-MASS BLACK HOLE IN ω CENTAURI

This chapter has been published in Häberle et al. (2024a). I conducted the data analysis and wrote all the text, except for Subsection 4.2.2 and Subsection 4.2.7 (written by co-author Anil Seth), Subsection 4.2.14 (written by co-author Holger Baumgardt), and Subsection 4.2.13 (written by co-author Matthew Whittaker). All co-authors have provided comments on the manuscript and help and advice for the analysis. The formatting has been adapted to match this thesis.

List of co-authors: Nadine Neumayer, Anil Seth, Andrea Bellini, Mattia Libralato, Holger Baumgardt, Matthew Whitaker, Antoine Dumont, Mayte Alfaro-Cuello, Jay Anderson, Callie Clontz, Nikolay Kacharov, Sebastian Kamann, Anja Feldmeier-Krause, Antonino Milone, Maria Selina Nitschai, Renuka Pechetti, Glenn van de Ven

ABSTRACT

Black holes have been found over a wide range of masses, from stellar remnants with masses of 5–150 solar masses ($M_\odot$), to those found at the centers of galaxies with $M > 10^5\ M_\odot$. However, only a few debated candidate black holes exist between 150 and $10^5\ M_\odot$. Determining the population of these intermediate-mass black holes is an important step towards understanding supermassive black hole formation in the early universe (Greene et al., 2020; Inayoshi et al., 2020). Several studies have claimed the detection of a central black hole in ω Centauri, the Milky Way's most massive globular cluster (Noyola et al., 2008, 2010; Baumgardt, 2017). However, these studies have been questioned due to the possible mass contribution of stellar mass black holes, their sensitivity to the cluster center, and the lack of fast-moving stars above the escape velocity (Anderson & van der Marel, 2010; van der Marel & Anderson, 2010; Zocchi et al., 2019; Baumgardt et al., 2019b). Here we report observations of seven fast-moving stars in the central 3 arcseconds (0.08 pc) of ω Centauri. The velocities of the fast-moving stars are significantly higher than the expected central escape velocity of the star cluster, so their presence can only be explained by being bound to a massive black hole. From the velocities alone, we can infer a firm lower limit of the black hole mass of $\sim$8,200 $M_\odot$, making this a compelling candidate for an intermediate-mass black hole in the local universe.

4.1 MAIN TEXT

ω Centauri (ω Cen) is a special case among the globular clusters of the Milky Way. Due to its high mass, complex stellar populations, and kinematics, ω Cen is widely accepted to be the stripped nucleus of an accreted dwarf galaxy (Hilker & Richtler, 2000; Ibata et al., 2019). These factors combined with its proximity (D=5.43 kpc, Baumgardt & Vasiliev 2021) have made it a prime target for searching for an IMBH. As part of the *oMEGACat* project (Nitschai et al., 2023; Häberle et al., 2024b), we recently constructed an updated proper-motion catalog of the inner regions of ω Cen, based on more than 500 *Hubble Space Telescope* archival images taken over a timespan of 20 years. The unprecedented depth and precision of this catalog have allowed us to make the remarkable discovery of a significant overdensity of fast-moving stars in the center of the cluster (Figure 4.1 & Figure 4.4). In total, we find 7 stars with a total proper motion higher than 2.41 mas yr^{-1} within 3" of the center determined in Anderson & van der Marel (2010); Goldsbury et al. (2010), hereafter AvdM10 center. At a cluster distance of 5.43 kpc (Baumgardt & Vasiliev, 2021), this corresponds to projected 2D velocities higher than the escape velocity of the cluster if no IMBH is present ($v_{\mathrm{esc.}}$ = 62 km s^{-1}, Baumgardt & Hilker 2018; see Methods).

We show in this paper that the presence of these stars strongly indicates a massive black hole, similar to the S-stars in the Galactic center (Gillessen et al., 2017). A list of the fast-moving stars is shown in Table 4.1 and we label the fast-moving stars with letters from A–G, sorted by their proximity to the AvdM10 center. All these stars lie along the cluster main sequence in the color-magnitude diagram (Figure 4.2). The fastest and centermost star (Star A in Figure 4.1) has a 2D proper motion of 4.41±0.08 mas yr^{-1} (113.0±1.1 km s^{-1}). The motion of this star was measured over 286 epochs and a full 20.6 year time baseline (see Figure 4.3). We run extensive quality checks to ensure that the astrometry of the discovered fast stars is reliable. To ensure the cleanest possible dataset, we limit our analysis to stars whose velocity is at least 3σ above the escape velocity. This leads to the exclusion of Stars B and G, however, this has negligible influence on the determined IMBH constraints.

Four of the fast stars, including the 3 fastest in the sample, are found within the centermost arcsecond ($r_{\mathrm{projected}} < 0.03$ pc or < 0.09 ly). Surprisingly, these four innermost stars are all fainter than $m_{\mathrm{F606W}} > 22.7$, which is unlikely ($p = 0.013$) to be a random occurrence given the overall distribution of stellar magnitudes in ω Cen's center. In addition, all of them lie towards the blue side of the main-sequence. Both these properties could have interesting physical implications for the mechanism involved in capturing these stars or on their tidal interactions with the IMBH.

We expect a certain number of Milky Way stars in our field of view and because they have a large proper motion with respect to ω Cen, they can mimic fast-moving cluster stars. Based on the number density of fast stars at larger radii (Extended Data Figure 4.4), we estimate the rate of contaminants to be 0.0026 arcsec^{-2}, which is consistent with expectations from the Besançon Milky Way model (Robin et al., 2003). This number density gives an expected average value of only 0.074 foreground stars in the inner 3-arcsecond radius. A detection of 5 such stars by a pure coincidence can therefore strongly be ruled out by simple Poisson statistics ($p = 1.7 \times 10^{-8}$, Gehrels 1986). Having 2 or more random contaminants within our 5-star sample can also be ruled out at the 3σ level ($p = 0.0026$). We also show in the Methods section that these stars cannot be explained by objects bound to stellar mass ($\lesssim$100 $M_\odot$) BHs, and that ejections from three-body interactions or an IMBH are not plausible.

Therefore, the presence of the seven central stars moving faster than the escape velocity of the cluster can only be explained if they are bound to a compact massive object near the center, raising the local escape velocity. If no massive object was present, their velocities would cause them to leave the central region in less than 1,000 years, and then eventually escape the cluster. These fast stars are a predicted consequence of an IMBH, but are not expected from mass-segregated stellar-mass black holes (Baumgardt et al., 2019b).

We do not know several parameters of the system including the mass and exact location of this massive object, the relative line-of-sight distance between it and the stars, and the line-of-sight velocity of the stars. Despite this, we can calculate a lower limit on the mass of the dark object using the fast-moving stars' 2D velocities, assuming only that they are bound to it. The combined constraint from the 5 robustly measured fast stars' velocities is $\sim 8,200$ $M_\odot$, thus making an IMBH the only plausible solution. The position of the IMBH requiring the lowest mass is only 0.3 arcsec away from the AvdM10 (Anderson & van der Marel, 2010) center, in excellent agreement with the $\pm$1" error on the AvdM10 center. Further details of this calculation can be found in the Methods.

While the linear motion and the velocity of the stars can be measured with great precision, the expected acceleration signal from an IMBH is considerably weaker and harder to detect. However, even a non-detection of acceleration could provide useful constraints on the mass and location of the IMBH. The accelerations of all stars are consistent with zero within 3σ, but two stars do have $>2\sigma$ acceleration measurements. We model both the velocity and acceleration measurements to further constrain the IMBH properties (see Methods); this calculation increases the lower limit on the black hole mass to 21,100 $M_\odot$ (99% confidence) and gives a preferred position for the IMBH 0.77" Northeast of the AvdM10 center.

In addition to these constraints that are purely based on the assumed escape velocity and our astrometric data of the 5 robustly measured fast-moving stars, we also compared the full velocity distribution observed in the inner 10" of ω Cen to already existing state-of-the-art N-Body models (Baumgardt, 2017) with various IMBH masses. Models with no IMBH, a stellar mass black hole cluster, or with an IMBH with a mass greater than 50,000 $M_\odot$ are all strongly ruled out, while models with an IMBH mass of 39,000 and 47,000 $M_\odot$ are most consistent with the fraction of fast stars and the observed velocity distribution. However, we caution that our comparisons show that low number statistics limit these comparisons, and mismatches with the overall velocity distribution suggest a need for improved modeling (see Methods for more details).

The detection of fast-moving stars in ω Cen's center strengthens the evidence for an IMBH in this cluster. Due to ω Cen's likely origin as the nucleus of the Gaia-Enceladus-Sausage dwarf galaxy (Massari et al., 2019; Pfeffer et al., 2021) this black hole provides an important data point in the study of black hole demographics in low-mass galaxies, along with other black holes that have been detected in more massive globular clusters and stripped nuclei around M31 such as G1 ($M \sim 20,000$ $M_\odot$; Gebhardt et al. 2002, 2005) or B023-G078 ($M \sim 100,000$ $M_\odot$; Pechetti et al. 2022). In addition, this black hole provides the closest massive black hole and only the second after Sgr A* for which we can study the motion of multiple individual bound stellar companions. A comparison with the motion of the stars in the Galactic center is shown in the Methods and Figure 4.11.

A more precise estimate of the black hole mass requires dynamical modeling of all newly available kinematic data using models that include the impact of both an IMBH and mass-segregated dark remnants. The exact properties of the orbits of the fast stars have to be determined by deep, pinpointed follow-up observational studies. Spectroscopic observations with integral-field-unit instruments such as VLT MUSE (Bacon et al., 2010a) or JWST NIRSpec IFU (Böker et al., 2022) could yield line-of-sight velocities for the fast-moving stars. Even more precise and deeper astrometric measurements with existing (VLTI GRAVITY+, GRAVITY Collaboration et al. 2017; JWST NIRCam, Rieke et al. 2023) or future (ELT MICADO, Davies et al. 2021; VLT MAVIS, Rigaut et al. 2021) instruments could enable the detection of additional tightly bound stars, and the measurements of accelerations, key for obtaining direct measurements of the black hole mass. Our result also motivates revisiting the other likely accreted nuclear star clusters of the Milky Way (Pfeffer et al., 2021), with M54 being the clearest case. For the search for IMBHs in other globular clusters, our results imply that it may be necessary to extend kinematic studies to the faintest stars, which is observationally challenging for clusters at larger distances and with high central densities.

4.1.1 FIGURES FOR MAIN PART

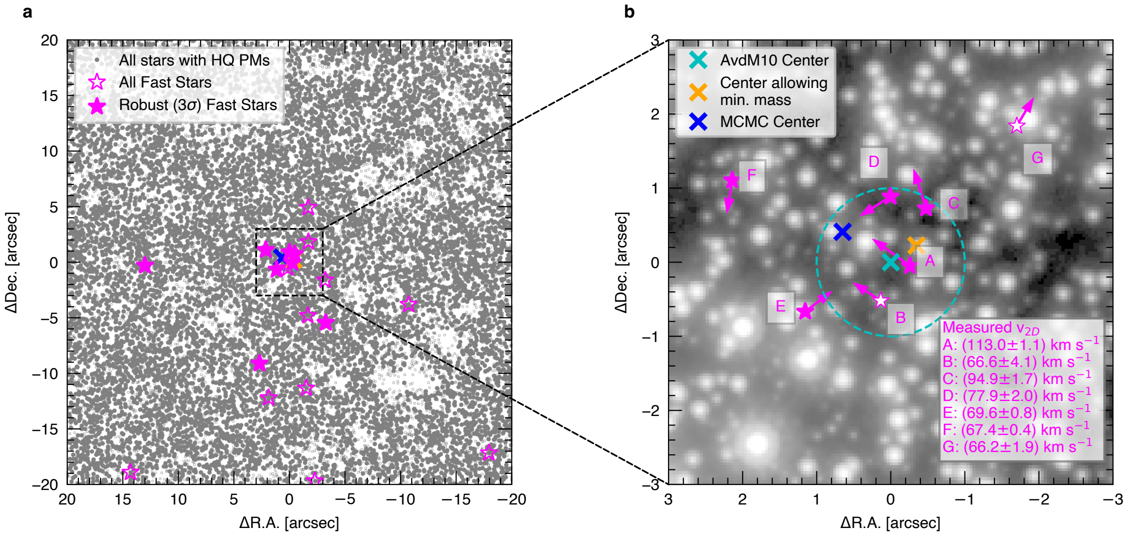

Figure 4.1: **Location of fast-moving stars.** **a**, This plot shows all stars we detected in our new proper motion catalog within a $40'' \times 40''$ region centered on the AvdM10 center (Anderson & van der Marel, 2010). Well-measured stars with velocities higher than the cluster escape velocity (62 $\mathrm{km\,s^{-1}}$) and lying on the cluster main sequence in the color-magnitude diagram (Fig. 4.2) are marked in pink. We use filled markers for stars that are at least 3σ over the escape velocity. **b**, Stacked image of the innermost region of ω Cen using all observations in the WFC3/UVIS F606W filter. The fast-moving stars and their proper motion vectors are shown in pink. The arrows indicate the stellar motion over 100 years. We also list the individual measured velocities in the lower right. The cyan cross indicates the photometric center of ω Cen measured by Anderson & van der Marel (2010) with the dashed circle indicating the 1" error reported for this center, the orange cross marks the center allowing for the lowest IMBH mass and the blue cross marks the most likely position of an IMBH given the MCMC analysis of the acceleration limits of the fast stars.

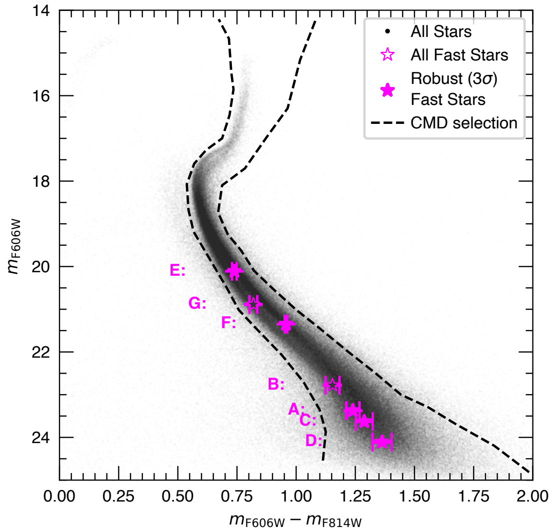

Figure 4.2: **Hubble Space Telescope based color magnitude diagram (CMD) of ω Cen.** The CMD locations of all fast-moving stars are marked with a pink symbol with their photometric 1σ errors marked with error-bars. All of them lie on the main sequence, showing they are likely members of ω Cen. The stars are labeled from A-G sorted by their distance from the AvdM10 center.

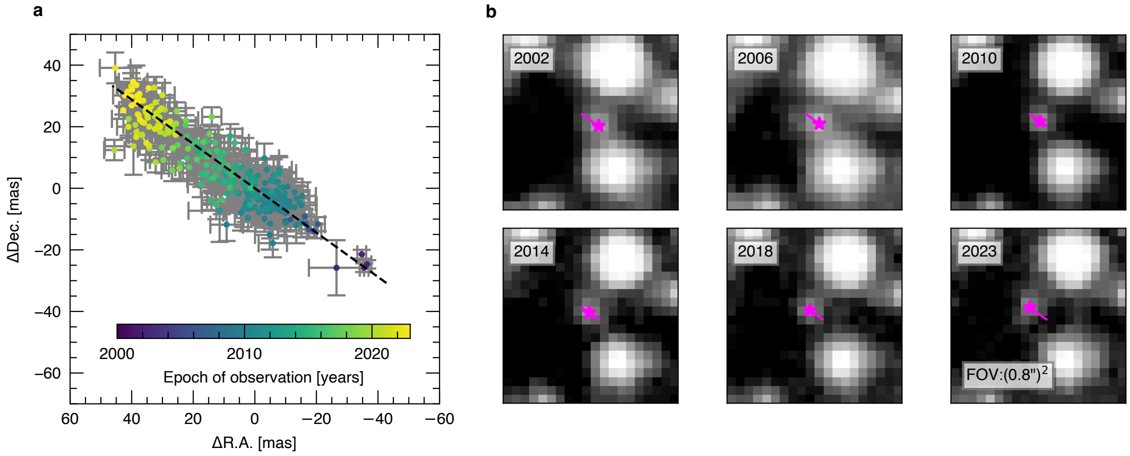

Figure 4.3: **Motion of the fastest star.** **a** Individual measured positions with 1σ error-bars and **b** multi-epoch HST imaging for Star A, the fastest ($v_{\text{proj.}} = 113.0 \pm 1.1\ \text{km s}^{-1}$) and centermost of the 7 newly discovered fast-moving stars in ω Cen's center. The star is indicated with a pink marker on the images and its motion over 21 years with a line. This plot shows the excellent astrometric quality and the long temporal baseline we have in our unique dataset. Similar plots for all other stars are shown in Figure 4.5.

4.2 METHODS

4.2.1 DISCUSSION OF PREVIOUS IMBH DETECTIONS IN ω CENTAURI

The debate about an IMBH in ω Cen dates back almost two decades but has remained controversial. Early dynamical modeling based on line-of-sight integrated-light velocity dispersion measurements suggested an IMBH of $M_{\rm IMBH} = (4.0^{+0.75}_{-1.0}) \times 10^4\,{\rm M}_\odot$ (Noyola et al., 2008). These results were challenged with a precise redetermination of the center of the cluster (Anderson & van der Marel, 2010) and dynamical modeling of proper motions (van der Marel & Anderson, 2010) measured from multi-epoch *Hubble Space Telescope (HST)* imaging observations that placed an upper limit of $1.2 \times 10^4\,{\rm M}_\odot$ on the IMBH. Using additional integrated light observations and a center based on the maximum LOS velocity dispersion, (Noyola et al., 2010) obtained a best fit IMBH mass of $M_{\rm IMBH} = (4.7 \pm 1.0) \times 10^4\,{\rm M}_\odot$. When assuming the AvdM10 center, the IMBH mass was slightly lower, $M_{\rm IMBH} = (3.0 \pm 0.4) \times 10^4\,{\rm M}_\odot$.

Subsequent comparisons of both proper motions and line-of-sight velocities to N-Body simulations continued to show evidence for a $\sim 4.0 \times 10^4\,{\rm M}_\odot$ IMBH (Jalali et al., 2012; Bellini et al., 2017a). However, these observations were shown to also be fully consistent with a dark cluster of stellar mass black holes in the central region of $\omega\,Cen$ (Zocchi et al., 2019). The lack of fast-moving stars in previous proper motion catalogs supported this scenario over an IMBH (Baumgardt et al., 2019b). Other works noted the influence of radial velocity anisotropy on dynamical mass estimates (Zocchi et al., 2017; Aros et al., 2020).

Most recently, the discovery of a counter-rotating core using VLT MUSE line-of-sight velocity measurements of individual stars (Pechetti et al., 2024) highlighted once again the kinematic complexity of the centermost region of ω Cen. The center of this counter-rotation coincides with the AvdM10 center within ~5", but is incompatible with the centers used in Noyola et al. (2008, 2010).

4.2.2 PREVIOUS ACCRETION CONSTRAINTS IN CONTEXT

With the detection of a $10^{4-5}\,{\rm M}_\odot$ IMBH, the upper limits on any accretion signal in the X-ray (Haggard et al., 2013) and radio (Tremou et al., 2018) wavelengths make this the most weakly accreting black hole known. Deep ~291 ksec Chandra observations place an upper limit of 0.5-7 keV luminosity of $\sim 10^{30}$ ergs s^{-1} (Haggard et al., 2013), roughly 12 orders of magnitude below the Eddington limit. The radio upper limit implies an even fainter source, with the 5 GHz upper limit of 1.3×10^{27} ergs s^{-1} (Tremou et al., 2018) corresponding to an implied X-ray luminosity via the fundamental plane of $\sim 10^{29}$ ergs s^{-1} (Plotkin et al., 2012). Assuming standard bolometric corrections of ~10 (Duras et al., 2020), this X-ray luminosity upper limit suggests an Eddington ratio $\log(L_{bol}/L_{edd}) < -12$, far fainter than that for Sgr A* (Event Horizon Telescope Collaboration et al., 2022b) or any other known black hole. This faint signal could be due to a combination of low surrounding gas density, a low accretion rate of that gas, and/or a low radiative efficiency (Tremou et al., 2018). Low-luminosity active galactic nuclei including Sgr A* are brightest at IR and sub-mm wavelengths due most likely to synchrotron emission from compact jets (GRAVITY Collaboration et al., 2020b; Fernández-Ontiveros et al., 2023).

Therefore, future observations with the James Webb Space Telescope or the Atacama Large Millimeter array would provide the highest sensitivity to any emission from ω Cen's IMBH. Any detection would reveal the location of the IMBH as well as provide valuable constraints on the black hole accretion in this extremely faint source.

4.2.3 Proper motion measurements and sample selection

Our proper motion measurements are based on the reduction of archival *Hubble Space Telescope* data of the central region of ω Cen, taken over a time span of more than 20 years. We used the state-of-the-art photometry tool KS2 (Bellini et al., 2017a) for the source detection and the astro-photometric measurements, and the established procedure described by Bellini et al. (2014, 2018b); Libralato et al. (2018b, 2022) to measure proper motions relative to the bulk motion of the cluster. The result of this extensive study is a proper motion catalog with high-precision measurements for 1.4 million stars out to ω Cen's half-light radius with a typical temporal baseline of more than 20 years. Thanks to the large number of observations (in total we reduced over 500 images and some stars in the central region have up to 467 individual astrometric measurements) the catalog reaches unprecedented depth and precision. The highest precision is achieved in the well-covered center of the cluster, where our proper motions have a median error of only $\sim$6.6 μas yr^{-1} (0.17 km s^{-1}) per component for bright stars.

The catalog is larger than any other kinematic catalog published for a globular cluster and significantly extends previous proper motion catalogs for ω Cen (Anderson & van der Marel, 2010; Bellini et al., 2017a; Gaia Collaboration et al., 2023c). A detailed comparison with other proper motion datasets is published along with the catalog (Häberle et al., 2024b). In a following section and in Figure 4.6 we compare the completeness of the different catalogs to show that it is plausible that the fast-moving stars have been missed in previous searches.

We use a high-quality subset of the proper motion catalog to search for real fast-moving stars and limit spurious astrometric measurements (e.g. two sources that are falsely identified as one) that can have apparent high proper motion measurements. Our criteria for this subset are based on the amount of available data for the measurements. Specifically, we used only sources that had at least 20 astrometric measurements covering a temporal baseline of at least 20 years, and a fraction of rejected measurements (based on sigma clipping) of less than 15%. We also made cuts on the quality of the proper motion fit requiring both a proper motion error less than 0.194 mas yr^{-1} $\approx$5 km s^{-1} and a reduced $\chi^2 < 10$ for the linear proper motion fit for both the R.A. and Dec. measurements. In addition to these quality selections, we also required the star to lie on the CMD sequence in an *HST* based color-magnitude diagram (Figure 4.2). These cuts all help to drastically reduce the number of contaminants. These criteria are met uniformly out to a radius of $\sim$90 arcsec, at larger radii they lead to selection effects due to reduced observational coverage. A total of 157,320 out of 241,133 (65.2%) entries of the proper motion catalog within $r <$90" match the combined criteria. Table 4.1, b, shows the individual measured proper motion components for the 7 fast-moving stars. We note that for this analysis we have not applied the local a-posteriori proper motion corrections provided with the catalog (Häberle et al., 2024b), as we are studying the central region which is well dithered and observed with various rotation angles. We verified that applying these corrections would neither change our fast star sample nor our conclusions.

4.2.4 DETAILS ON VERIFICATION FOR FAST-MOVING STARS

The criteria detailed above should lead to a clean data set with very few spurious proper motion measurements. To ensure that the measurements for the fast-moving stars are reliable, we inspected each of them carefully.

As a first step, we tested the quality of the raw astrometric measurements by studying several goodness-of-fit parameters and photometric quality indicators for the point-spread-function fits used to measure stellar positions (see Figure 4.6). We performed this analysis for the WFC3/UVIS F606W filter as it is the most used filter in the center of ω Cen and each star has at least 195 measurements in this filter. To verify the goodness-of-fit, we used the mean of the so-called "quality-of-fit" flag (QFIT) and the radial excess value, both of which take into account the residuals of the point-spread-function fit. In addition we looked at the mean of the ratio of source flux with respect to the flux of neighboring sources within its fit aperture. All five stars used for our analysis behave typically for well-measured stars of their magnitude and none of them show extreme values that would indicate problems with the photometry. It is noteworthy that the two stars excluded from our analysis based on their velocities being $<3\sigma$ above the escape velocity show some deviations: Star B has a relatively low mean QFIT value and high radial excess. Star G is the only one in the sample where the Flux Neighbour over Flux Star ratio is larger than one.

As a second step, we looked at the stars in several stacked *HST* images taken at various epochs ranging from 2002 to 2023. The extensive multi-epoch imaging is demonstrated in Extended Data Fig 4.5. The proper motion of a star at the escape velocity (62 km s^{-1}) is 2.41 mas yr^{-1}. Therefore, we expect to see a motion of at least 50 mas over 21 years, which corresponds to 1.25 WFC3/UVIS pixels. Indeed this motion can be seen by eye for all seven stars in the multi-epoch images. Again the excluded stars B and G stick out in the sense that they are partially blended with neighboring stars, thus explaining their larger astrometric errors.

Finally, we tested the reliability of our proper motion measurements by limiting the raw position measurements to different subsets and redoing both the linear and quadratic fits to the motion of the stars. The first test run included only high S/N measurements. The second test run included only measurements taken with the WFC3/UVIS F606W filter. By using only one filter, we are immune to color-induced effects such as a partially resolved blend between two differently colored stars. The proper motions of all fast stars are consistent within the measurement uncertainties using both methods.

4.2.5 COMPARISON WITH OTHER PROPER MOTION DATASETS

Before our analysis, two other high-precision proper motion catalogs based on *HST* data have been published (Anderson & van der Marel, 2010; Bellini et al., 2017a) covering the center of ω Cen. Both datasets were searched for central high proper motion stars, but none of the stars in our sample have been reported before. To understand why this is the case, we compare the completeness of the different catalogs. Extended Data Figure 4.6, **a** shows histograms of the magnitudes of stars with measured proper motions. In the inner 20", our new catalog contains more than 3 times the number of stars of the literature catalogs and extends to significantly fainter magnitudes. The newly detected fast-moving stars all lie at faint magnitudes, where the completeness of the older catalogs is significantly lower than in the new proper motion catalog. This is due to larger amount of data and the updated source-finding algorithms in the new catalog, and explains the previous non-detection of the fast-moving stars.

4.2.6 Discussion of photometric errors

Beside the astrometric reliability we also studied the quality of the photometric measurements used to locate the stars in the color-magnitude diagram. Even though the innermost stars are faint, their statistical photometric errors are small due to the large number of individual photometric measurements combined to a weighted mean value. The statistical errors range from 0.004 to 0.037 mag and are given in Extended Data Table 4.1c. However, especially for faint stars, this statistical error is not able to capture systematic issues caused e.g. by the influence of brighter neighboring stars. Those can only be identified by verifying the quality of the PSF fit used to determine the individual photometric measurements. We report the mean quality-of-fit, radial excess, and "neighbour flux / source flux" flags for both filters in Table 4.1c and compare them with those of stars at similar ($\Delta m < 0.5$) magnitudes in Extended Data Figure 4.6. All stars in the robustly measured sample show typical quality-of-fit for their respective magnitude. We note that stars B and G (which were excluded from the analysis) show comparatively poor QFIT. Star E and G show a possible flux contribution from a neighboring source (indicated by a high radial excess value and a high "neighbor flux / source flux"). This can be confirmed by the stacked images shown in Figure 4.5, where these stars show a close neighbor. Due to the relatively bright magnitude of star E and the low astrometric scatter we still consider its measurement valid.

4.2.7 Comparing the density of Milky Way contaminants to the background

To quantify our expected level of contamination from Milky Way foreground and background stars, we compared our results to those of a Besançon model (Robin et al., 2003). Using the 'm1612' model, we simulate a 1 square degree patch centered on ω Cen retrieving Johnson colors and kinematics. We then transform the model Johnson V and I magnitudes into F606W and F814W magnitudes using linear relations fitted to Padova models (Bressan et al., 2012) between $V - I$ of 0 and 2. We use the same color cuts and consider stars between F606W of 16 to 24. Then we count the number of stars with a total proper motion above 2.41 mas yr^{-1} (equivalent to our velocity cutoff at the escape velocity $v_{\mathrm{esc.}}$ =62 km s^{-1}). These would appear as contaminants in our fast star sample. We find a density of 0.0039 stars arcsec^{-2}. This is somewhat higher than the 0.0026$\pm$0.0003 stars arcsec^{-2} found as the background level in our observations; this discrepancy is alleviated by considering only 65.2% of all stars within our catalog meet the high-quality criteria used for our fast star selection (see above). Correcting for this factor, we get an expected background of 0.0025 stars arcsec^{-2}, perfectly matching the observed background density (Figure 4.4). This suggests that our background level is consistent with being predominantly Milky Way contaminants. Relaxing our requirement that stars be more than 3σ above the escape velocity results in a higher observed background level of 0.0042 stars arcsec^{-2}, no longer consistent with the Milky Way background. This suggests that our stricter definition of a fast-moving star reduces contamination from poorly measured stars in ω Cen to a negligible level.

4.2.8 Discussion of other scenarios that could explain the fast-moving stars

A complete contamination of our sample by Milky Way foreground/background stars that are non-members of ω Cen can be ruled out statistically. We now explore and rule out alternative scenarios to the fast stars being bound to an IMBH. One alternative explanation for stars with a high velocity is to have them bound in a close orbit with a stellar-mass black hole. This scenario can be ruled out for BHs <100 $M_\odot$, as the periods required to reach the observed velocities are <10 years, well within the 20-year span over which we have observed linear motions.

Another scenario could be that the stars are actually unbound from the cluster, and have been recently accelerated by three-body interactions, either with stellar-mass black hole binaries or an IMBH. Ejection by an IMBH in the center of the cluster can be ruled out by the very high rate of ejections necessary to sustain the observed number of fast stars within the center and the absence of observed fast-moving stars at larger radii. To sustain a density of 0.18 fast stars arcsec^{-2} in the inner 3 arcseconds (equivalent to our conservative sample of 5 stars) moving with at least 2.4 mas yr^{-1}, would require ejections with a rate of 0.004 stars yr^{-1}. This would lead to $\sim$117 additional fast-moving stars at larger radii (20”$< r <$90”), in addition to $\sim$60 foreground stars expected from the (completeness corrected) Besançon Milky Way model. In our dataset we find 61 fast-moving stars between 20”$< r <$90”, consistent with the expected Milky Way background but not consistent with a significant number of additional ejected stars. In addition, a high hypothetical ejection rate of 0.004 stars yr^{-1} would deplete all of ω Cen’s $\sim$10 million stars in just 2.5 Gyr. If no IMBH is present, accelerations of stars above the escape velocity are still possible by 3- or 4- body interactions between stellar or compact object binaries (see e.g. (Weatherford et al., 2023)). However, these interactions would not be limited to the innermost few arcseconds of the cluster, due to the slowly varying stellar density in ω Cen’s core. In addition, the expected rate of these ejection events is of the order of less than one ejection per one million years, $\sim$1,000 times lower than needed to explain the observed number of fast stars in the center of ω Cen (Weatherford et al., 2023; Cabrera & Rodriguez, 2023).

4.2.9 Search for the fast-moving stars in recent line-of-sight velocity data

Line-of-sight velocities of the fast-moving stars could help to exclude contaminants and provide additional constraints on the orbits of the stars and the mass and position of the IMBH. The deepest and most extensive spectroscopic catalog of stars in ω Cen is Part I of our recently published *oMEGA-Cat* (Nitschai et al., 2023). This catalog was created using a large mosaic of observations with the

VLT MUSE integral field spectrograph and contains both line-of-sight velocity measurements and metallicities for over 300,000 stars within the half-light radius of ω Cen. While we could successfully cross-match 5 of the 7 fast-moving stars, their signal-to-noise ratio is typically too low for reliable velocity measurements, in particular for the 4 fastest, innermost stars ($S/N \sim 2$).

We could, however, obtain a line-of-sight velocity value for star E ($v_{\rm LOS} = 261.7 \pm 2.7\,{\rm km\,s^{-1}}$) and star F ($v_{\rm LOS} = 232.5 \pm 4.0\,{\rm km\,s^{-1}}$). These velocities are very close to the systemic line-of-sight velocity of ω Cen ($232.99 \pm 0.06\,{\rm km\,s^{-1}}$, Nitschai et al. 2023), confirming their membership in the cluster, as the Milky Way foreground is centered at $v_{\rm LOS} \sim 0$ with a dispersion of $70\,{\rm km\,s^{-1}}$ (Robin et al., 2003). However, as the relative line-of-sight velocity with respect to the cluster is low and we only have those two velocities for these outer stars, the line-of-sight velocities do not add stronger constraints on the IMBH. For this reason, we did not include them into the rest of our analysis.

4.2.10 TESTING THE ROBUSTNESS OF THE ASSUMED ESCAPE VELOCITY

Varying the parameters of the N-Body models: Because we use the escape velocity of ω Cen (assuming no IMBH is present) as the threshold for determining whether a stars is considered "fast" or not, it is important to verify the robustness of the escape velocity value. We adopt an escape velocity $v_{\rm esc.} = 62\,{\rm km\,s^{-1}}$ (Baumgardt & Hilker, 2018); we have verified this value based on fitting similar N-Body models to several state of the art datasets including MUSE LOS velocity dispersion measurements (Kamann et al., 2018) and *HST* proper motion based dispersion measurements (Watkins et al., 2015a) for the central kinematics and Gaia DR3 (Gaia Collaboration et al., 2023a) measurements at larger radii using an assumed distance of 5.43 kpc. We varied both the assumed initial stellar mass function (using either the canonical Kroupa IMF (Kroupa, 2001) or the bottom-light IMF derived in Baumgardt et al. 2023) and the black hole retention fraction (assuming values of 10%, 30%, 50%, or 100%). Despite changes to the central M/L between models, the central escape velocity changes only minimally, with a range of values of from $61.1\,{\rm km\,s^{-1}}$ to $64.8\,{\rm km\,s^{-1}}$. Adopting any of these values leaves our sample of seven central stars above the escape velocity unchanged.

An independent test using surface-brightness profiles: As a second test, independent of the N-Body models, we calculated a surface brightness profile based escape velocity profile using various literature surface brightness profiles and dynamical models. We started by parameterizing the surface brightness profile using Multi-Gaussian Expansion (MGE) (Emsellem et al., 1994) models. Then we converted the surface brightness to a mass density using several literature mass-to-light ratios and distances. From the mass density we can derive the gravitational potential ($\Phi(r)$). The escape velocity profile is then given by $v_{\rm esc.}(r) = \sqrt{2(\Phi(r_{tidal}, 0) - \Phi(r, 0))}$ (with the tidal radius $r_{tidal} = 48.6' \approx 74.6$pc from Harris (1996, 2010)).

These tests showed, that the central escape velocity does not depend strongly on the stellar mass distribution in the centermost region, instead it is dominated by the global M/L ratio and the assumed distance. The early dynamical models in the IMBH debate both assumed a distance of 4.8 kpc (van de Ven et al., 2006) and a M/L of 2.6 (vdMA10, van der Marel & Anderson 2010) or 2.7 (N08, Noyola et al. 2008, 2010). With these values our tests give a central escape velocity of $55.4\,{\rm km\,s^{-1}}$ (vdMA10) and 56.9 km s^{-1} (N08). If we would also use the 4.8 kpc distance to scale the proper-motions, this gives a cutoff of 2.43 mas yr^{-1} (vdMA10) and 2.48 mas yr^{-1} (N08), close to the adopted cut-off at 2.41 mas yr^{-1} and not changing the sample of seven detected fast stars. Thanks to the parallax measurements of the Gaia satellite and updated kinematic distance measurements, the distance to ω Cen was robustly redetermined and larger values have been found (5.24±0.11 kpc, Soltis et al. 2021; 5.43±0.05 kpc, Baumgardt & Vasiliev 2021). A dynamical model using the same surface brightness profile as Noyola et al. (2008) but a larger distance of $5.14^{+0.25}_{-0.24}$ kpc was presented in Zocchi et al. (2019); this study found a M/L of $2.55^{+0.35}_{-0.28}$. Using these values, the central escape velocity derived from the surface brightness profile is 61.1 km s^{-1} (equivalent to a proper motion of 2.51 mas yr^{-1}); again not changing our fast stars sample. Finally, varying the distance of any model by 0.2 kpc while holding the M/L constant results in a ∼3 km/s variation in escape velocity. These results show that our fast star limit ($v_{\mathrm{esc.}}$ = 62 km s^{-1} at a distance of 5.43 kpc) is consistent with escape velocity values directly derived from surface-brightness profiles and several dynamically estimated M/L ratios. To visualize the escape velocity we calculated the escape velocity using the surface-brightness profile of Noyola et al. (2008), a M/L ratio of 2.4, and a distance of 5.43 kpc as found from the N-Body models with a cluster of stellar mass black holes. The resulting profile is shown in Figure 4.8f. The predicted escape velocity is flat out to ∼50”, a property shared by all of the calculated escape velocity profiles. This makes the detection of the fast-stars only in the central few arcseconds more compelling.

An empirical confirmation of the central escape velocity: We make one final, and relatively model-independent, empirical confirmation of the central escape velocity based on the distribution of 2D velocities in the innermost region of ω Cen (see Figure 4.7). As we have seen in the analysis above, the escape velocity only varies slightly within the inner ∼ 50” of the core of ω Cen. In addition, the velocity dispersion profile is relatively flat in the innermost 10”, with a value of ∼20 km/s (Anderson & van der Marel, 2010; Watkins et al., 2015a; Pechetti et al., 2024). Therefore, one would expect rather similar distributions of stellar velocities in both the very center ($0'' < r < 3''$) and an outer ring at ($3'' < r < 10''$). While we observe a clear excess of fast-moving stars in the inner 3 arcseconds, there is a sharp cutoff very close to the adopted escape velocity in the ($3'' < r < 10''$) bin. Even though there is a total of 2090 stars there is only one star with a velocity significantly faster than the escape velocity (instead of 17 stars expected from a 2D Maxwell-Boltzmann distribution with $\sigma_{1D} = 20\,\mathrm{km\,s^{-1}}$). This suggests the stars with these velocities have escaped the central region. This one outer fast star has a 2D velocity of 75.8 km s^{-1} and is at a radius of $r = 9.5''$. From the density of Milky Way contaminants with apparent velocities above the escape velocity we would expect ∼0.7 foreground stars in the ($3'' < r < 10''$) region, therefore this fast star is consistent with being a Milky Way foreground star.

4.2.11 THE ESCAPE VELOCITY PROVIDES A MINIMUM BLACK HOLE MASS

The escape velocity for an isolated black hole is given by

$$v_{\text{esc., BH}} = \sqrt{\frac{2GM_{\text{BH}}}{r_{3\text{D}}}}. \tag{4.1}$$

In ω Cen we have to take into account the potential of the globular cluster as well. If we assume this to be constant over the very small region in which we found the fast-moving stars (an assumption that agrees with published surface brightness profiles, see Figure 4.8,**f**), we obtain:

$$v_{\text{esc.,total}} = \sqrt{v^2_{\text{esc.,BH}} + v^2_{\text{esc.,cluster}}} \tag{4.2}$$

If a star at the distance of $r_{3\text{D}}$ with a velocity $v_{3\text{D}}$ is bound to the black hole, we can calculate the following lower limit on the black hole mass[1]:

$$M_{\text{BH}} > \frac{\left(v^2_{3\text{D}} - v^2_{\text{esc., cluster}}\right) r_{3\text{D}}}{2G} \geq \frac{\left(v^2_{2\text{D}} - v^2_{\text{esc., cluster}}\right) r_{2\text{D}}}{2G} \tag{4.3}$$

A lower limit can also be calculated if the line-of-sight velocity and distance are not known, as $v_{3\text{D}} \geq v_{2\text{D}}$ and $r_{3\text{D}} \geq r_{2\text{D}}$. Since we do not know the exact 2D position of the black hole relative to the fast-moving stars, we calculated this lower limit for all stars and a grid of assumed 2D locations around the AvdM10 center (Anderson & van der Marel, 2010). Each individual star alone would allow for a very low mass, as the location of the black hole could coincide with the star (Figure 4.8, a-d). However, combining these limits for all stars gives a higher minimum black hole mass (Figure 4.8, e). If we assume that all 5 robustly detected stars are bound to the black hole, the lower limit is $\sim 8,200\,\text{M}_\odot$ and the minimum mass location is only 0.3" away from the AvdM10 (Anderson & van der Marel, 2010) center at the location R.A.: 201.6966908°[2] Dec.:-47.4795066°. If we assume that the 2 most constraining stars are just random foreground contaminants, which is ruled out at the 3σ level ($p = 0.0026$), this limit drops to $\sim 4\,100\,\text{M}_\odot$, still well within the IMBH range.

4.2.12 ACCELERATION MEASUREMENTS

The astrometric analysis in the catalog (Häberle et al., 2024b) considered only linear motions of the stars. If there is a massive black hole present near the center, we might also be able to measure accelerated motion of the closest stars, allowing for a direct mass measurement of the black hole. With an IMBH mass of $40,000\,\text{M}_\odot$ and at a radius of 0.026 pc (1" on the sky), the acceleration of a star would be $0.25\,\text{km}\,\text{s}^{-1}\,\text{yr}^{-1}$ (or $0.01\,\text{mas}\,\text{yr}^{-2}$). This is at the limit of the precision of our current dataset: With a 20 year baseline, we only expect a deviation of 0.05 pixel from a linear motion. For

---

[1] The original published version of this equation contained a typographical error. We have since issued a correction, see DOI:10.1038/s41586-024-08017-4. The version presented in this thesis is the corrected one.

[2] This value has been corrected for an error that occurred during the conversion from relative to absolute coordinates. See also DOI:10.1038/s41586-024-08017-4

bright stars the astrometric uncertainty can be as low as 0.01 pixel, however for the faint fast-moving stars we have detected, the errors are significantly larger.

To constrain these possible accelerations, we repeated the fit of the motion of each star allowing the addition of a quadratic component. The results for this fit are shown in Table 4.1. All of the stars' accelerations are consistent with zero within 3σ, but two stars have $>2\sigma$ acceleration measurements. The errors on our acceleration measurements lie between 0.004 and 0.03 mas yr^{-2} and are, therefore, of a magnitude similar to the expected acceleration signal. The strongest acceleration is shown by Star B, which has been excluded from the robust subset of fast-moving stars because its proper motion is not 3σ above the escape velocity. Due to the proximity of a bright neighbor star, we do not deem this acceleration measurement to be reliable.

As the line-of-sight distances to the fast stars are unknown, it is not possible to place direct constraints on the IMBH mass using the upper limits on accelerations. If no acceleration is detected, as is the case for the centermost star A, this could mean that either the black hole is not very massive or that the line-of-sight distance of star A to the black hole is large. Combining the measurements for the ensemble of fast-moving stars, and making some assumptions on their spatial distribution still allows us to use the acceleration limits to place additional constraints on the black hole mass and its location. This is described in the next section.

4.2.13 Details about MCMC fitting of the acceleration data

Assuming the fast-moving stars are bound to the IMBH, we can model the stars as being on Keplerian orbits around the IMBH. We used Bayesian analysis to sample the posterior distribution for the unknown mass and position of the black hole. In this analysis, there were 8 free parameters: black hole mass, its on-sky x- and y-position, and 5 line-of-sight distances between the black hole and each fast-moving star. This analysis makes use of the available astrometric observations but stops short of modeling individual stellar orbits which would introduce additional free parameters.

We use a likelihood function with these 8 free parameters and give the likelihood based on the observed on-sky x- and y- acceleration, proper motion, and position of the 5 robustly measured fast-moving stars. For each star, we calculated a first likelihood term based on the modeled acceleration a_{modeled} using a Gaussian distribution with mean a_{observed} and width equal to the acceleration uncertainty. The second term in the likelihood accounts for the escape velocity constraints and is kept constant if the observed 2D velocity of the star is below the modeled escape velocity. For stars with 2D velocities above the modeled escape velocity, the likelihood is a Gaussian distribution with mean $v_{2\mathrm{D}} - v_{\mathrm{esc.\ total}}$ and width equal to the uncertainty in observed proper motion.

We make these prior assumptions about the model: 1) The black hole mass is between $1\,\mathrm{M}_{\odot}$ and $100,000\,\mathrm{M}_{\odot}$, since a black hole mass beyond this upper limit is ruled out by our N-Body models. 2) The black hole is located within the distribution of the fast-moving stars. We use a Gaussian prior in the black hole x- and y- positions with a mean equal to the mean position of the fast-moving stars and width equal to their 1-dimensional positional standard deviation, $\sigma_{\mathrm{stars}} = 0.0221$ pc; we also use a cutoff at ± 0.16 pc. 3) The stellar positions are isotropically distributed around the black hole. We model the line-of-sight positions of the stars relative to the black hole using a Gaussian distribution with mean 0 and width σ_{stars}.

The posterior was sampled using a Markov chain Monte Carlo (MCMC) ensemble sampler implemented using the package *emcee* (Foreman-Mackey et al., 2013b) using recommended burn-in and autocorrelation corrections. We show the posterior distribution for the black hole mass in Figure 4.9, a. The 99% confidence lower limit (21,100 $M_\odot$) is significantly higher than that derived from escape velocity constraints alone, while the upper limit on the mass is not well constrained. We also find a position for the black hole east of the AvdM10 center, with $\Delta x = -0.017\,^{+0.017}_{-0.031}$ pc and $\Delta y = 0.011\,^{+0.011}_{-0.025}$ pc (Figure 4.9), b. The coordinates of the MCMC based center estimate are R.A: 201.6970988°[3] Dec.: -47.4794533°. We note that the black hole location estimate is dominated by the marginal 2σ acceleration signal of Star D which is the faintest star in the sample; follow-up studies are required to obtain more precise acceleration measurements.

4.2.14 N-BODY MODELS

In addition to the analysis of stars with velocities above the escape velocity, we also used a set of existing N-body models with and without central IMBHs to get additional constraints on the IMBH mass. We compared the simulations to the full velocity dispersion and surface density profile of ω Cen to determine the best-fitting model and the mass of a central IMBH. The set of models and the details of the fitting procedure are described in detail in Baumgardt (2017); Baumgardt et al. (2019b). We note that these models have been presented already in the literature, but the fits to these models have been updated to incorporate the most recent Gaia DR3 data.

In short, the models started from King profiles (King, 1962) with central concentrations between $c = 0.2$ and $c = 2.5$ and initial half-mass radii between $r_h = 2$ pc and $r_h = 35$ pc. In the models with an IMBH, we varied the mass of the IMBH so that it contains either 0.5%, 1%, 2% or 5% of the cluster mass at $T = 12$ Gyr when the simulations were stopped. The models with an IMBH assumed a retention fraction of stellar-mass black holes of 10% while in the models without an IMBH we varied the assumed retention fraction of stellar-mass black holes between 10% to 100%. At the end of the simulations, we calculated surface density and velocity dispersion profiles for each N-body model and then determined the best-fitting model by interpolation in our grid of models and using χ^2 minimization against the observed velocity and surface density profile of ω Cen.

The velocity distributions from observations and the models are shown in Figure 4.10. We compare the distribution of measured 2D stellar velocities in the inner 10" of ω Cen with the various models using a Kolmogorov–Smirnov test. In addition, we compare the fraction of fast-moving stars in the innermost 3 arcseconds (see Table 4.2). Models without an IMBH and with a 20,000 $M_\odot$ IMBH are both strongly excluded both by the overall velocity distribution and the complete lack of fast-moving stars. The overall velocity distribution is in best agreement with the 47,000 $M_\odot$ distribution, while the fraction of fast stars is best matched by the 39,000 $M_\odot$ simulation. This tension might be alleviated

---

[3] This value has been corrected for an error that occurred during the conversion from relative to absolute coordinates. See also DOI:10.1038/s41586-024-08017-4

in future models, that contain both an IMBH and a cluster of stellar mass black holes. We caution that these simulations have smaller numbers of stars than observed, and that there can be significant variations in the distribution of central stars due to strong encounters with remnants and binaries. Nonetheless, the simulations suggest black holes with masses of $M \lesssim 50{,}000\ \mathrm{M}_\odot$ are consistent with the observed distribution of central velocities and fast-moving stars, while the no-IMBH case and significantly more massive black holes are disfavored due to an overprediction of fast stars. Updated N-Body models fit to the oMEGACat kinematic data and dynamical modeling of these same datasets with Jeans models are currently underway.

4.2.15 COMPARISON WITH S-STARS IN THE GALACTIC CENTER

The black hole indicated by our fast star detection is only the second after Sgr A*, for which we can study the motion of multiple individual bound stellar companions. Therefore, the extensively measured stars around Sgr A* provide a unique comparison point to our fast-moving star sample. We compare the motions of the stars in the S-Star catalog from Gillessen et al. (2017) with our ω Cen fast star sample in Figure 4.11. When taking into account the different distances and the approximate black hole mass ratio of 100, the motions indeed show similar amplitudes. However, the density of tracers in ω Cen is significantly lower, despite the greater depth of the observations.

ACKNOWLEDGMENTS

Based on observations with the NASA/ESA Hubble Space Telescope, obtained at the Space Telescope Science Institute, which is operated by AURA, Inc., under NASA contract NAS 5-26555. SK acknowledges funding from UKRI in the form of a Future Leaders Fellowship (grant no. MR/T022868/1). AS, MAC, MW, and AB acknowledge support from HST grant GO-16777. AB acknowledges support from STScI grants GO-15857 and AR-17033. AFK acknowledges funding from the Austrian Science Fund (FWF) [grant DOI 10.55776/ESP542]

DECLARATIONS

DATA AVAILABILITY

The data used in this paper are based on archival observations taken with the *Hubble Space Telescope* which are freely available in the Mikulski Archive for Space Telescopes. All used observations have been grouped under a DOI (DOI:10.17909/26qj-g090). In addition, the full proper-motion catalog is made public along with the respective publication (Häberle et al., 2024b).

CODE AVAILABILITY

We used the following python packages to perform the analysis:
`matplotlib` (Hunter, 2007), `scipy` (Virtanen et al., 2020), `numpy` (Harris et al., 2020), `astropy` (Astropy Collaboration et al., 2022), `emcee` (Foreman-Mackey et al., 2013b). The N-Body simulations were run with the publicly available `NBODY6` code (Nitadori & Aarseth, 2012). We can share the code used in the data analysis upon request.

AUTHOR'S CONTRIBUTIONS

All authors helped with interpretation of the data and provided comments on the manuscript. MH has led the analysis of the data and is the main author of the text. AS and NN designed the overall project with significant contributions from AB, GvdV, and SK. AS, NN, HB, MW, and AD contributed text. AS determined the expected density of Milky Way contaminants. AB, ML and JA provided their expertise on astrometric measurements with the *HST*. HB provided and fitted the N-Body models for the analysis. MW ran the Bayesian Analysis used to constrain the IMBH mass and position. AD performed the surface-brightness-profile based calculations. SK and MSN helped to find available LOS data for the stars.

Competing interests

The authors declare no competing interests.

EXTENDED DATA

Table 4.1: **Detailed astrometric and photometric information of the fast-moving stars.** The table in **a** shows the position, the number of astrometric measurmements N_{used}, and the projected distance from the AvdM10 center for each of the fast-moving stars. **b** lists the individual proper motion components, the total proper motion, the inferred 2D velocity and the measurements of the acceleration for the seven fast-moving stars. All shown errors correspond to the 1σ errors, which were estimated by scaling the formal errors on the parameters by $\sqrt{\chi^2_{red.}}$ of the respective fit. The strongest accelerations are shown by Star B, however, this star has been discarded from the set of robustly measured stars due to large astrometric errors. All robust stars show an acceleration consistent with zero to within 2 σ. Finally, Table **c** lists several photometric properties of the fast-moving stars in two filters, including the measured brightness and several photometric diagnostics (the quality of fit (QFIT) parameter, the radial excess (RADX) parameter and the flux ratio between the flux of each source and the flux of neighboring sources). Together with the photometric diagnostic values we show their percentile with respect to stars with a similar magnitude (p).

a

		General Properties			
Star	**Catalog ID**	**R.A. [degree]**	**Dec. [degree]**	**$r_{\text{proj.}}$ ["]**	**N_{used}**
A	532867	201.6967263	-47.4795835	0.265	308
B	475236	201.6968888	-47.4797138	0.537	353
C	1422379	201.6966378	-47.4793672	0.870	262
D	476492	201.6968346	-47.4793233	0.886	195
E	509644	201.6973080	-47.4797545	1.333	430
F	476467	201.6977125	-47.4792625	2.408	427
G	510061	201.6961340	-47.4790585	2.506	338

b

			Velocity and Acceleration Measurements			
Star	**PM R.A. $\mu_\alpha\cos\delta$ [mas yr^{-1}]**	**PM Dec. μ_δ [mas yr^{-1}]**	**Total PM [mas yr^{-1}]**	**v_{2D} [km s^{-1}]**	**Acceleration R.A. [mas yr^{-2}]**	**Acceleration Dec. [mas yr^{-2}]**
A	3.563±0.038	2.564±0.055	4.390±0.044	113.0±1.1	-0.0069±0.0083 (0.8σ)	0.0085±0.0098 (0.9σ)
B	2.167±0.182	1.415±0.081	2.588±0.159	66.6±4.1	0.0702±0.0239 (2.9σ)	0.0228±0.0157 (1.5σ)
C	1.117±0.127	3.514±0.056	3.687±0.066	94.9±1.7	0.0028±0.0333 (0.1σ)	-0.0060±0.0123 (0.5σ)
D	2.559±0.082	-1.617±0.061	3.027±0.076	77.9±2.0	0.0357±0.0177 (2.0σ)	-0.0194±0.0162 (1.2σ)
E	-2.149±0.025	1.638±0.037	2.702±0.030	69.6±0.8	0.0072±0.0042 (1.7σ)	-0.0009±0.0075 (0.1σ)
F	0.436±0.017	-2.584±0.016	2.620±0.016	67.4±0.4	0.0052±0.0038 (1.4σ)	-0.0015±0.0038 (0.4σ)
G	-1.317±0.098	2.207±0.062	2.571±0.073	66.2±1.9	-0.0197±0.0267 (0.7σ)	0.0173±0.0170 (1.0σ)

c

				Photometric Properties				
Star	**m_{F606W}**	**QFIT_{F606W}**	**RADX $_{F606W}$**	**$f_N/f_\star$ $_{F606W}$**	**m_{F814W}**	**QFIT_{F814W}**	**RADX $_{F814W}$**	**$f_N/f_\star$ $_{F814W}$**
A	23.373±0.009	0.976 (p =0.716)	-0.006 (p =0.192)	0.366 (p =0.532)	22.134±0.027	0.945 (p =0.170)	-0.004 (p =0.249)	0.363 (p =0.537)
B	22.778±0.014	0.940 (p =0.096)	0.082 (p =0.981)	0.122 (p =0.322)	21.625±0.026	0.956 (p =0.128)	0.072 (p =0.964)	0.494 (p =0.639)
C	23.630±0.009	0.940 (p =0.283)	0.050 (p =0.8249	0.147 (p =0.320)	22.342±0.034	0.916 (p =0.109)	-0.014 (p =0.136)	0.327 (p =0.514)
D	24.108±0.017	0.952 (p =0.585)	-0.008 (p =0.216)	0.064 (p =0.180)	22.745±0.037	0.952 (p =0.291)	-0.056 (p =0.022)	0.079 (p =0.198)
E	20.112±0.004	0.996 (p =0.131)	0.014 (p =0.950)	0.424 (p =0.923)	19.373±0.009	0.995 (p =0.109)	0.018 (p =0.938)	0.622 (p =0.975)
F	21.348±0.004	0.997 (p =0.635)	-0.002 (p =0.340)	0.028 (p =0.253)	20.391±0.004	0.998 (p =0.799)	0.004 (p =0.587)	0.032 (p =0.232)
G	20.888±0.009	0.980 (p =0.031)	-0.003 (p =0.219)	2.049 (p =0.997)	20.069±0.014	0.983 (p =0.053)	0.007 (p =0.730)	0.971 (p =0.984)

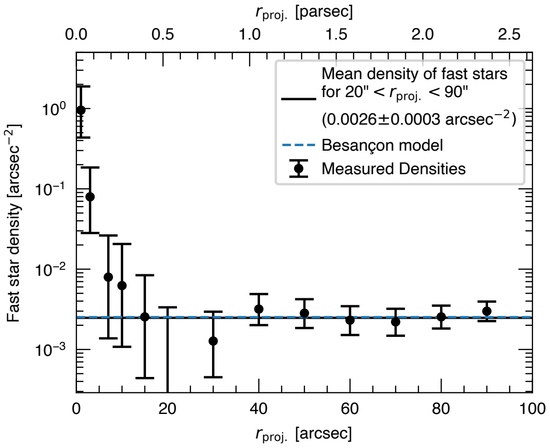

Figure 4.4: **Number density of fast-moving stars.** The black markers with errorbars (1σ; based on Poisson statistics) show the measured number density of robustly detected fast-moving stars determined in radial bins with respect to ω Cen's center. A constant density of Galactic fore-/background stars is expected, but we see a strong and statistically significant rise of the density towards the AvdM10 (Anderson & van der Marel, 2010) center. Based on the number density of fast-moving stars at large radii (which is consistent with predictions from a Besançon Milky Way model, dashed line) only ~0.073 fast-moving stars are expected within the central 3” compared to the 5 observed stars.

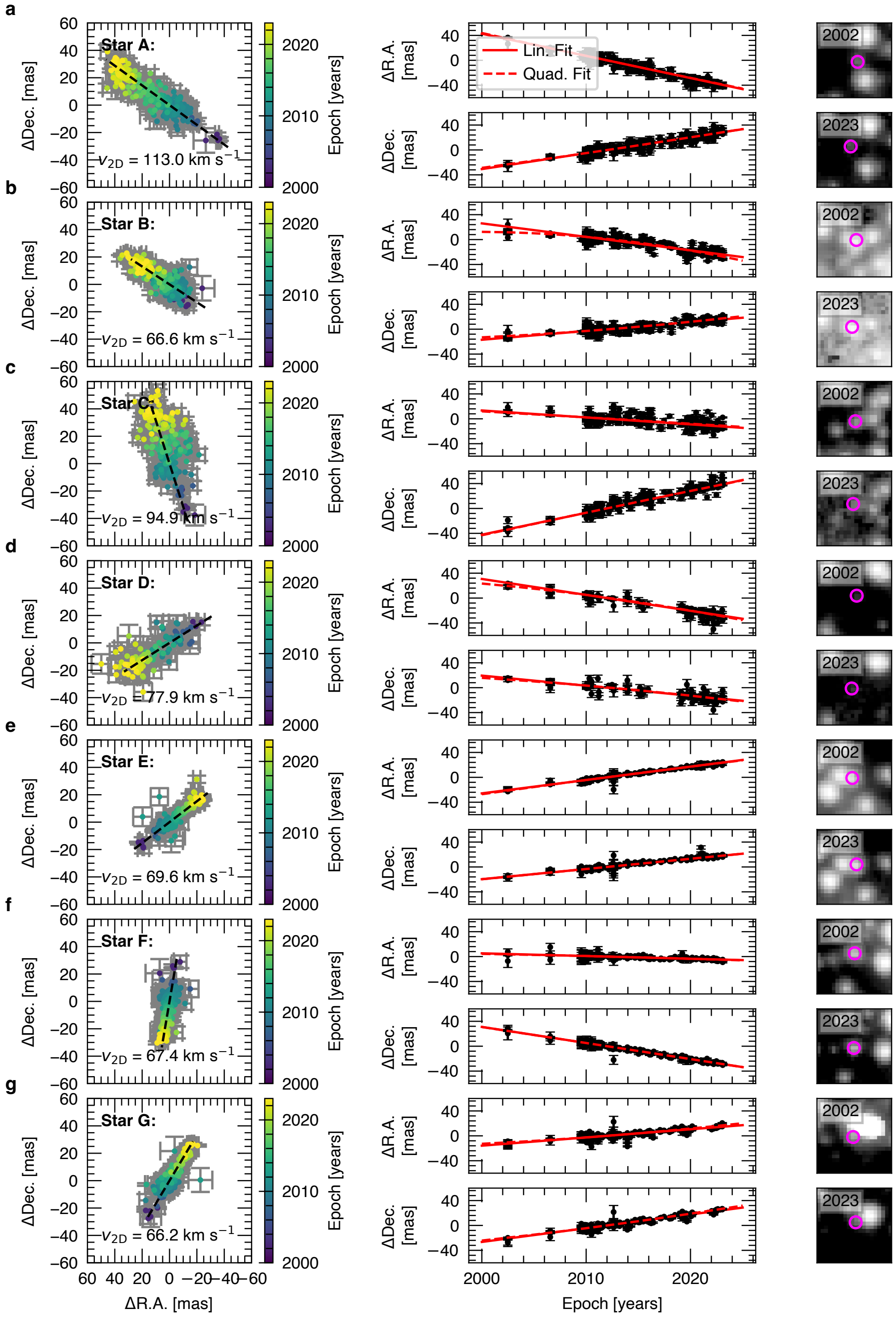

Figure 4.5: **Astrometry and multi epoch imaging for all fast-moving stars.** Each row (**a-g**) shows the astrometry and imaging for one of the 7 fast-moving stars. The left column shows the raw astrometric measurements used to determine the proper motions, color-coded by the epoch of their observation. The center column shows the linear and quadratic fits to both the R.A. and Dec. position change of the stars. Errorbars correspond to the 1σ error on the individual position measurements. The right column shows stacked images from 2002 (ACS/WFC F625W) and 2023 (WFC3/UVIS F606W), the positions of the fast stars are marked with a pink open circle.

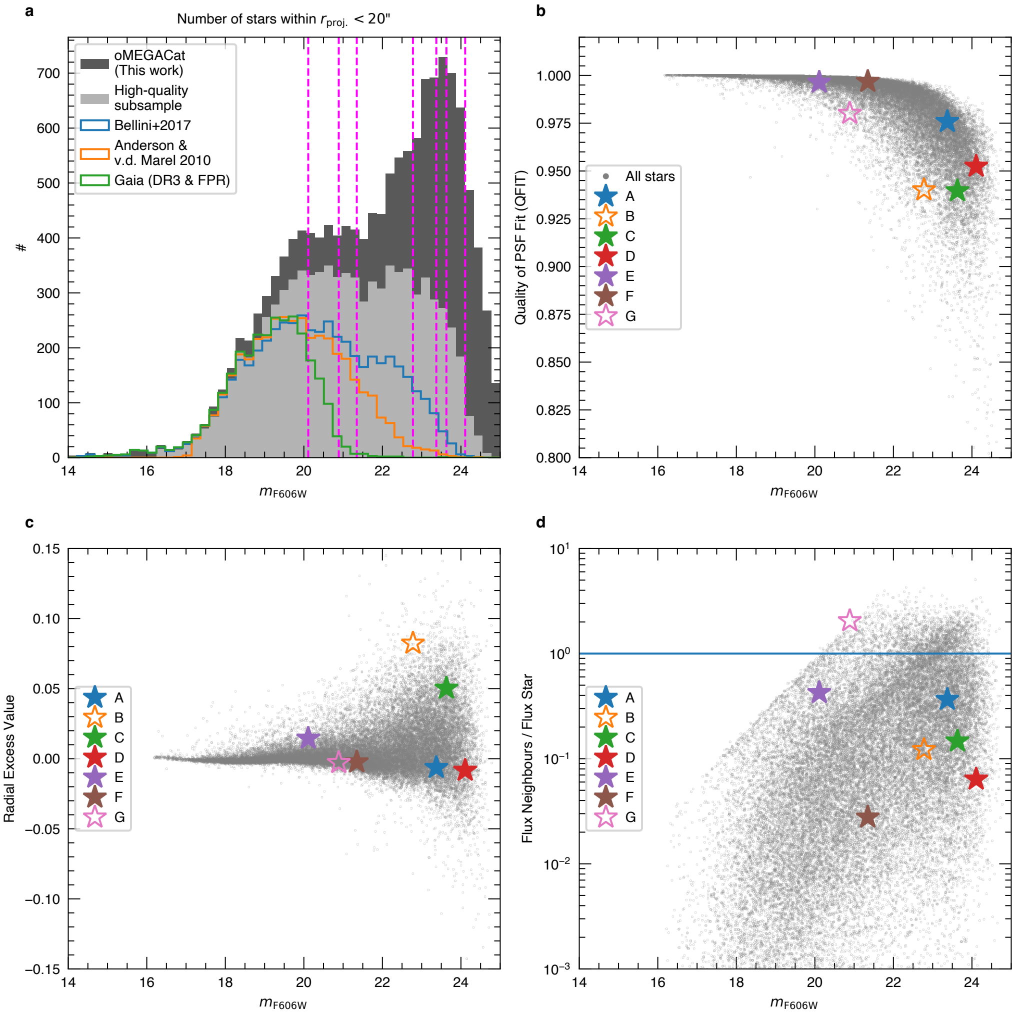

Figure 4.6: **Completeness of the catalog and photometric diagnostics.** Panel **a** compares the completeness of the various available proper motion datasets for the core of ω Cen using histograms of the magnitude distribution. The new oMEGACat (Häberle et al., 2024b) has significantly higher completeness and reaches fainter magnitudes than the literature catalogs even if we apply the strict quality criteria used in this work. This explains why previous catalogs have not found the faint fast-moving stars (marked with vertical lines) we detect here.

The grey dots in **b**, **c**, and **d** show the mean of photometric diagnostics for the raw PSF photometry measurements for the fast-moving stars compared with the bulk of stars in the catalog. The first panel shows the QFIT parameter, given by the linear correlation function between the PSF and the pixel values in the image. The second panel shows the radial excess parameter, a parameter that compares the residual flux inside versus outside of the fit aperture. The third panel shows the flux ratio between the flux of a star itself and its neighboring sources. All 5 robustly measured stars show typical behavior for their magnitude, while the excluded fast-moving stars (B, G) are influenced by bright neighboring sources.

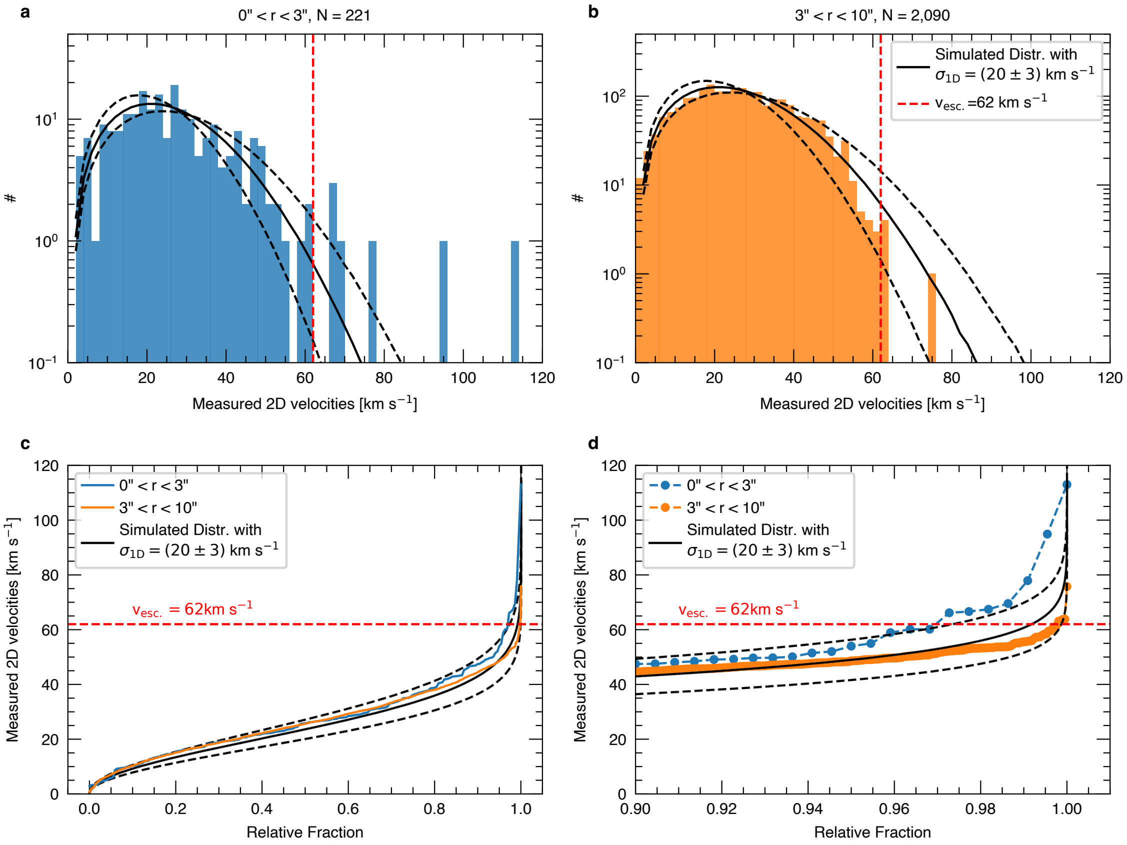

Figure 4.7: **Empirical verification of the escape velocity.** Panels **a** and **b** show histograms of the observed 2D velocity distribution in the very center ($0'' < r < 3''$; **c**) and in an outer ring ($3'' < r < 10''$; **d**). While the lower velocities are well described by £a 2D Maxwell-Boltzmann distribution with $\sigma_{1D} = 20\ \mathrm{km\,s^{-1}}$ (marked with a solid black line, the dashed black lines refer to alternative distributions with $\sigma_{1D} = 17\ \mathrm{km\,s^{-1}}$ and $\sigma_{1D} = 23\ \mathrm{km\,s^{-1}}$), there are clearly notable differences at higher velocities. Those become especially visible in the cumulative normalized histogram shown in Panel **d** and the zoom-in in Panel **e**: While the distribution between ($0'' < r < 3''$, blue line) shows an excess of fast-moving stars, the distribution at larger radii ($3'' < r < 10''$, orange line) shows a clear deficit of stars at velocities larger than the escape velocity, making the used escape velocity threshold very plausible. Even though the sample is 10 times larger, there is only a single star with a velocity significantly larger than $v_{\mathrm{esc.}}$. This star has a 2D velocity of $75.8\ \mathrm{km\,s^{-1}}$ and is at a radius of $r = 9.5''$. It is consistent with being a Milky Way foreground star.

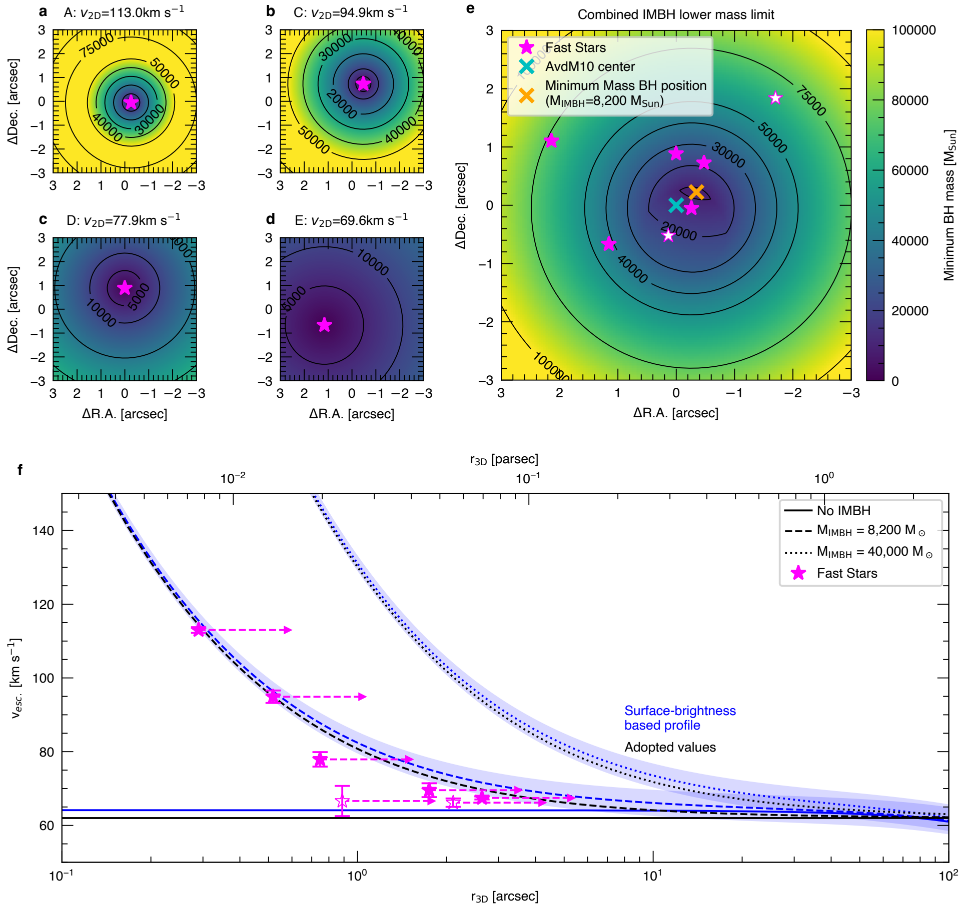

Figure 4.8: **Determination of a lower limit on the IMBH mass using the escape velocity.** The presence of stars with velocities above the escape velocity of the cluster indicates that they are bound to a massive object. Since we neither know the mass nor the exact position of the object, we can only infer a lower mass limit for each possible 2D location. The 4 left plots (**a-d**) show the contours of the minimum black hole mass indicated by the 4 centermost robustly measured fast-moving stars. By combining the minimum black hole mass constraints from each of the fast-moving stars we can find the position that allows for the lowest IMBH mass (**e**). This analysis indicates a firm lower limit of around 8,200 $M_\odot$. Our minimum mass location only differs by $\sim$0.3 arcsec from the AvdM10 (Anderson & van der Marel, 2010) center. This result does not significantly change if we assume some of the fast-moving stars are contaminants and remove them from the analysis.
Panel **f** shows the results for a surface brightness profile based escape velocity profile in blue, using the surface brightness profile from Noyola et al. (2008) and the dynamical distance (5.43 kpc) and M/L ratio (2.4) derived from N-Body models, either without any IMBH, with a 8,200 $M_\odot$ IMBH, or a 40,000 $M_\odot$ IMBH. The radii are measured with respect to the minimum mass center shown in **e**. The shaded regions indicate the uncertainty introduced by an assumed error of ±0.2 kpc on the distance. The surface-brightness profile based escape velocity is compatible with the adopted value of $v_{esc.}$ =62 km s^{-1}. The profile without an IMBH is also nearly flat in the inner $\sim$50”, justifying the assumption of a flat profile in the innermost region.

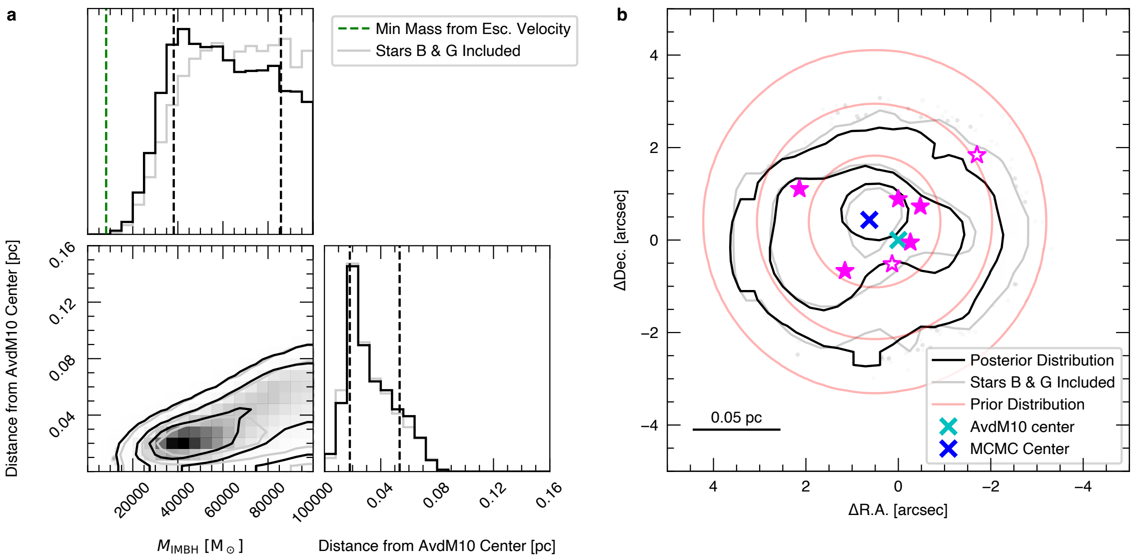

Figure 4.9: **Constraints on the IMBH using the acceleration measurements.** Taking into account the limits on the accelerations gives us additional constraints on black hole mass (**a**) and on-sky position (**b**). The contours shown correspond to the 1-, 2-, and 3-sigma levels of the distribution. This analysis using both escape velocity and acceleration measurements from the 5 robustly measured fast stars constrains the minimum IMBH mass stronger than escape velocity constraints alone. Both plots also show the distribution from an MCMC run including stars B and G.

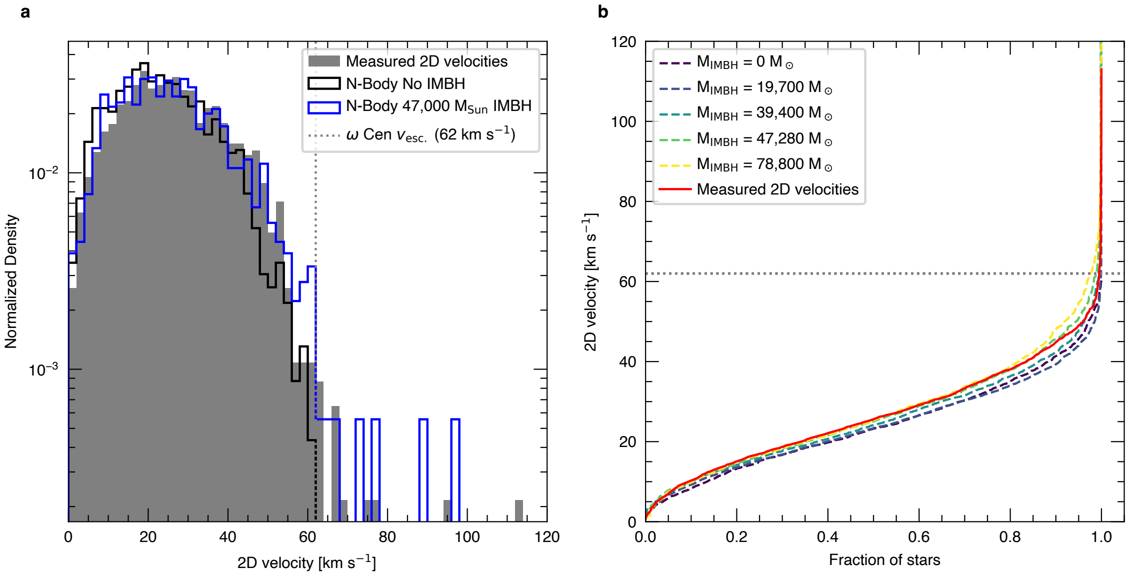

Figure 4.10: **Comparison of the observed velocity distribution with N-Body models.** **a**, 2D velocity distribution for the stars in the inner 10 arcseconds of ω Cen. We show the observed data in gray, the results for an N-Body model without an IMBH in black and the results for a model with an 47,000 M$_\odot$ IMBH in blue (based on the models of Baumgardt et al. 2019b). The N-Body model without an IMBH predicts no stars above the escape velocity, the 47,000 M$_\odot$ model predicts a number close to our observations. **b**, Comparison of the normalized, cumulative distribution of stellar velocities for our data and five different N-Body models.

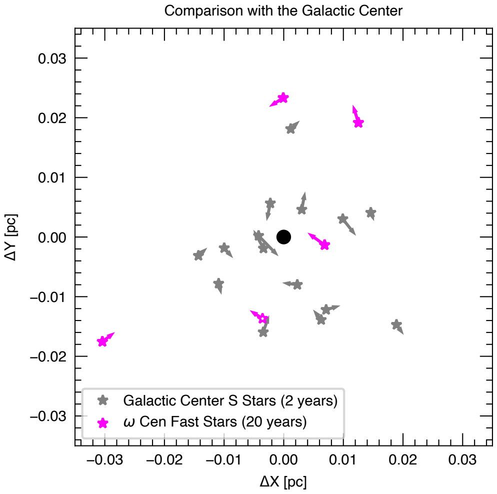

Figure 4.11: **Comparison with the Galactic Center:** In this figure we compare the observed physical motion of our fast star sample with the stars orbiting the black hole Sgr A* in the Galactic Center (Gillessen et al., 2017). The physical scale probed by the fast-moving stars is similar to that probed by the S stars in the Milky Way center, however, the density of these tracers is lower. Due to the approximately ∼100 times higher black hole mass of Sgr A*, we expect the motions to be ∼10 times faster and periods of the stars to be ∼10 times shorter, and thus show the motion for 2 years for the S stars to compare to the 20 year time span we observe the stars in ω Cen.

Table 4.2: **Comparison of the observed velocity distribution with N-Body models.** In this table we report results of the comparison of the observed distribution of 2D velocities with different N-Body models (see also Figure 4.10). The first two columns indicate the relative and absolute mass of the IMBH in the N-Body models. The third column shows the total number of stars within 10” of the cluster center. In the fourth column, we show the results of a Kolmogorov-Smirnov test comparing the measured velocity distribution with the different N-Body models. Finally, the last three columns compare the absolute number and the fraction of fast-moving stars in the centermost 3 arcseconds.

IMBH mass fraction in model	**M_{IMBH} [$M_\odot$]**	**$N_{10''\mathrm{total}}$**	**KS test p-Value**	**$N_{3'',\mathrm{fast}}$**	**$N_{3'',\mathrm{total}}$**	**$N_{3'',\mathrm{fast}}$/ $N_{3''\mathrm{total}}$**
Observed	Data	2,324	-	7	218	3.2%
0	0	1,148	6.21e-7	0	113	0%
0.5%	20,000	1,342	8.60e-10	0	113	0%
1.0%	39,000	868	0.0027	3	89	3.4%
1.2%	47,000	901	0.27	7	85	8.3%
2.0%	78,800	843	0.18	7	70	10.0%

5 ANALYSIS OF THE OVERALL KINEMATICS OF OMEGA CENTAURI IN 3D: VELOCITY DISPERSION, KINEMATIC DISTANCE, ANISOTROPY, AND ENERGY EQUIPARTITION

This chapter has been submitted to The Astrophysical Journal on January 16th, 2025 and has already received a positive referee report requesting only minor revisions. I conducted the data analysis and wrote all the text. All co-authors have provided comments on the manuscript and help and advice for the analysis. The formatting has been adapted to match this thesis.

List of co-authors: Nadine Neumayer, Callie Clontz, Anil Seth, Peter Smith, Sebastian Kamann, Renuka Pechetti, Maria Selina Nitschai, Mayte Alfaro-Cuello, Holger Baumgardt, Andrea Bellini, Anja Feldmeier-Krause, Nikolay Kacharov, Mattia Libralato, Antonino Milone, Stefano Souza, Glenn van de Ven, Zixian Wang

ABSTRACT

Omega Centauri (ω Cen) is the Milky Way's most massive globular cluster and is likely the stripped nucleus of an accreted dwarf galaxy. In this paper, we analyze ω Cen's kinematics using data from oMEGACat, a comprehensive catalog of ω Cen's central regions, including 1.4 million proper motion measurements and 300,000 spectroscopic radial velocities. Our velocity dispersion profiles and kinematic maps are consistent with previous work but improve on their resolution, precision, and spatial coverage. The cluster's 3D dispersion is isotropic in the core, with increasing radial anisotropy at larger radii. The 2D kinematic maps show an elongation of the velocity dispersion field comparable to the flattening observed photometrically. We find good agreement between proper motions and line-of-sight velocity dispersion and measure a kinematic distance of 5445 ± 41 pc, the most precise distance to ω Cen available. The subset of data with precise metallicity measurements shows no correlation between metallicity and kinematics, supporting the picture of well-mixed stellar populations within the half-light radius of ω Cen. Finally, we study the degree of energy equipartition using a large range of stellar masses. We find partial energy equipartition in the center that decreases towards large radii. The spatial dependence of the radial energy equipartition is stronger than the tangential energy equipartition. Our kinematic observations can serve as a new reference for future dynamical modeling efforts that will help to further disentangle the complex mass distribution within ω Cen.

5.1 INTRODUCTION

5.1.1 INTRODUCING OMEGA CENTAURI

Omega Centauri (ω Cen, NGC 5139) is the most massive ($M \approx 3.55 \times 10^6$ $M_\odot$, Baumgardt & Hilker, 2018) globular cluster of our Milky Way. The stellar populations within ω Cen are complex and include an unusually wide spread in age (Hilker et al., 2004; Villanova et al., 2007; Joo & Lee, 2013; Villanova et al., 2014; Tailo et al., 2016; Clontz et al., 2024) and metallicity (Freeman & Rodgers, 1975; Johnson & Pilachowski, 2010; Marino et al., 2011; Nitschai et al., 2024). These complexities are also apparent in the color-magnitude diagram, which shows a multitude of different splits and sequences (Anderson, 1997; Pancino et al., 2000; Bedin et al., 2004; Ferraro et al., 2004; Bellini et al., 2010, 2017c; Milone et al., 2017a; Clontz et al., 2025). For these reasons, ω Cen is now widely accepted to be the stripped nucleus of a dwarf galaxy that has been accreted and disrupted by the Milky Way (e.g. Lee et al., 1999; Bekki & Freeman, 2003). Other evidence for this accretion scenario has been found by associating ω Cen with stellar streams in the Milky Way Halo (Majewski et al., 2012; Ibata et al., 2019) and by finding potential connections with either the Sequoia or the Gaia-Enceladus merger events (Myeong et al., 2019; Massari et al., 2019; Forbes, 2020; Pfeffer et al., 2021; Limberg et al., 2022; Pagnini et al., 2024).

This makes ω Cen the closest nuclear star cluster and an important witness to the formation history of the Milky Way.

Besides its peculiar stellar populations and its likely accreted origin, the internal kinematics of ω Cen have also intrigued astronomers for many years as a way to understand its mass distribution and its formation history. Traditionally, the stellar motions in ω Cen have been studied using line-of-sight velocities, limiting the observable sample to a relatively small number of a few hundred bright, evolved stars (Suntzeff & Kraft, 1996; Mayor et al., 1997; Reijns et al., 2006). Early ground-based proper motion studies (van Leeuwen et al., 2000a) were similarly limited to bright stars, although thousands of individual proper motions could already be measured.

The number of stars for which kinematic measurements are available has changed dramatically with the availability of multi-epoch Hubble Space Telescope (HST) data that has enabled the measurement of proper motions for hundreds of thousands of stars (Anderson & van der Marel, 2010; Bellini et al., 2014, 2018b) down to very faint main sequence stars. More recently, the MUSE integral field spectrograph (Bacon et al., 2010b) at the ESO Very Large Telescope has been used to obtain spectra for hundreds of thousands of stars (Kamann et al., 2018; Nitschai et al., 2023; Pechetti et al., 2024).

Previous kinematic studies of ω Cen have focused on various aspects of its kinematics including its velocity dispersion (Watkins et al., 2015a), kinematic distance (van de Ven et al., 2006; Watkins et al., 2015b; Baumgardt & Vasiliev, 2021), rotation (Meylan & Mayor, 1986; Merritt et al., 1997; Kamann et al., 2018; Pechetti et al., 2024; Häberle et al., 2024b), and the energy equipartition both in the center (Watkins et al., 2022) and at larger radii (Bellini et al., 2018b). These studies showed that ω Cen is rotating with relatively high $\frac{v}{\sigma}$ leading to significant flattening. In addition, the stellar motions show partial energy equipartition and increasing radial anisotropy at larger radii.

The kinematic measurements have also served as the basis for various dynamical modeling efforts using numerous techniques to constrain the mass distribution in ω Cen which has proved to be a very complex and sometimes inconclusive task. Based on modeling of the inner region, there has been a long debate about the presence of a central, intermediate-mass black hole (Noyola et al., 2008, 2010; Anderson & van der Marel, 2010; van der Marel & Anderson, 2010; Zocchi et al., 2017, 2019; Baumgardt et al., 2019b; Bañares-Hernández et al., 2025). The recent discovery of several high-proper motion stars near ω Cen's center (Häberle et al., 2024a) provides the latest piece in this puzzle and was used to estimate a lower limit for the mass of an intermediate-mass black hole of $M_{\mathrm{IMBH}} > 8,200\,\mathrm{M}_{\odot}$.

5.1.2 The oMEGACat project

In the oMEGACat project, we have created the most comprehensive spectroscopic and astro-photometric data set for ω Cen to date. The basis for this project is two large data sets that cover the half-light radius ($r_{\mathrm{HL}} = 287''$, Baumgardt & Hilker 2018) of ω Cen: first, an extensive mosaic with VLT MUSE integral field observations. Based on these observations, Nitschai et al. (2023), hereafter Paper I, provided a spectroscopic catalog with metallicities and line-of-sight (LOS) velocities for over 300 000 stars within the half-light radius of ω Cen. The second component of the project is a large astrometric and photometric catalog (see Häberle et al. 2024b, hereafter Paper II), which includes high-precision proper motions and multi-band photometry for around 1.4 million sources based on hundreds of new and archival HST observations.

The combined data set enables a broad range of science cases, including studies of the metallicity distribution of various subpopulations (Nitschai et al., 2024), the age-metallicity relation (Clontz et al., 2024), the abundances of Helium (Clontz et al., 2025) and other individual elements.

5.1.3 This work: Overall kinematics of ω Cen in 3D

In this work we revisit several of the key kinematic properties of ω Cen using the new combined oMEGACat catalogs, significantly extending the spatial coverage, precision, and depth of existing kinematic studies. We describe the data selection in Section 5.2. Section 5.3 describes the determination of velocity dispersion, anisotropy and rotation profiles using all three velocity dimensions and the derivation of a new kinematic distance estimate. Section 5.4 describes the creation of 2-dimensional kinematic maps. In Section 5.5 we search for potential variations of the kinematics with metallicity and in Section 5.6 we provide new detailed measurements of the state of energy equipartition. Finally, Section 5.7 contains a summary and conclusions.

Our paper stops short of studying the kinematic differences between different subpopulations and fitting dynamical models, both of which will be the content of future work. We make all products of this analysis available in electronic form to facilitate future modeling efforts. The data products released with this paper are described in Section 5.8.

5.2 DATA AND QUALITY SELECTIONS

The spectroscopic catalog and its creation are described in detail in Paper I; the HST-based astro-photometric catalog is described in Paper II. Here we only give a brief overview of the catalog content and describe the various quality selections used to restrict the data set to a reliable sub-sample of cluster member stars.

The spectroscopic catalog is based on observations with the VLT MUSE integral field spectrograph (Bacon et al., 2010b) with a total of 103 pointings. The observations were obtained for "The MUSE Survey of Galactic Globular Clusters" (PI: S. Dreizler, S. Kamann, see also Kamann et al. 2018) and for GO Program 105.20CG.001 (PI: N. Neumayer). Both data sets were partially observed with and without adaptive optics mode.

The astro-photometric catalog is based on around 800 individual exposures taken with the two Hubble Space Telescope instruments ACS/WFC and WFC3/UVIS and in various different filters. The data were taken from the Archive or the dedicated Program GO-16777 (PI: A. Seth). The complete underlying data set has been collected under the following DOI: [DOI:10.17909/26qj-g090]http://dx.doi.org/10.17909/26qj-g090.

We photometrically reduced the data using the KS2 software (see e.g. Bellini et al., 2017a) and measured relative proper motions using the technique introduced in Bellini et al. (2014). The typical temporal baseline of the proper motion measurements is around 20.6 yrs leading to high proper motion precision. The final catalog contains 1,395,781 sources with a proper motion measurement. On the faint end, the catalog reaches $m_{\mathrm{F625W}} \approx 25$, while stars brighter than $m_{\mathrm{F625W}} < 13.9$ are typically saturated.

5.2.1 SELECTIONS WITHIN THE HST CATALOG

5.2.1.1 ASTROMETRIC AND PHOTOMETRIC QUALITY SELECTIONS

When studying the velocity dispersion, it is important to restrict the data to measurements with reliable proper motions and errors. This is especially true for energy equipartition studies, where a large range of stellar masses and, therefore, magnitudes has to be probed. In this study, we use the corrected proper motions from Paper II. These proper motions have been corrected for residual spatial and magnitude-dependent effects; the assumed proper motion errors are the quadratic sum of the errors of the linear proper motion fit (determined using the actual residuals) and the statistical error on the empirical correction.

We start the selection process with several global cuts on some properties of the astrometric measurements. For all stars we require the following conditions to be met (see also Figure 5.18, Appendix, for histograms of these selections):

- Temporal Baseline longer than 10 years
- $N_{\mathrm{used}}/N_{\mathrm{found}}$ fraction > 0.75
  This parameter gives the ratio of data points that were used for the proper motion fit with

respect to the total number of available measurements. A low value indicates that many data points were removed during the clipping stage, indicating unreliable astrometry.

- Reduced Chi-Square < 5 for the proper motions fits in both components

In addometric criteria, we require reliable photometry in the two reddest broad-band filters in the data set: ACS/WFC F625W and WFC3/UVIS F814W. The reason for these photometric quality cuts is two-fold: First, reliable photometry is needed to assess the cluster membership using color-magnitude diagrams and to estimate the mass of individual stars via isochrone fitting. Second, accurate photometry also indicates good astrometric quality, and by using two filters for which the typical time baseline is long (F625W: 2002, F814W: 2022) we can ensure that the astrometric measurements are of good quality throughout the whole monitored temporal baseline, leading to reliable proper motions.

Our photometric selections are similar to the exemplary ones described in Paper II and provided in the catalog, but slightly stricter. For both filters (F625W, F814W) we require:

- No saturation (this leads to the exclusion of all red-giant branch stars with $m_{\mathrm{F625W}} < 13.8$)
- A quality-of-fit (QFIT) value higher than the 85th percentile of 0.5 mag wide intervals (using m_{F625W}). Stars with a QFIT higher than 0.99 are always included, and stars with a QFIT lower than 0.9 are always excluded. The QFIT parameter describes how well the used point-spread-function model describes the flux distribution of each source. A value close to 1 indicates good agreement.
- A ratio of flux from neighboring stars within the fit aperture over the flux of the star smaller than 0.5

The combined cuts above already provide us with a reliable subsample. To ensure high and consistent quality throughout the whole magnitude range, we add one last, magnitude-dependent criterion: For both proper motion components, we require the proper motion error to be within the lower 95% of the error distribution in 0.5 mag wide intervals (see Figure 5.1, left). As can be seen in Figure 5.1, this selection tracks the magnitude dependence of the bulk of all well-measured stars, while excluding outliers with unusually high errors. One can also see that at a magnitude of $m_{\mathrm{F625W}} = 24$ the errors reach an order of magnitude of 0.3 mas yr^{-1} ($\sim$7.7 km s^{-1}). As this is similar to half of the typical velocity dispersion in the outer regions of our studied field, we exclude stars fainter than this magnitude limit. Including stars with errors similar to the actual velocity dispersion would complicate the determination of the velocity dispersion and make it quite sensitive to the modeling of the proper motion errors.

5.2.2 Spectroscopic quality selections

For the spectroscopic catalog we defined the following criteria to create a well-measured subset of the data:

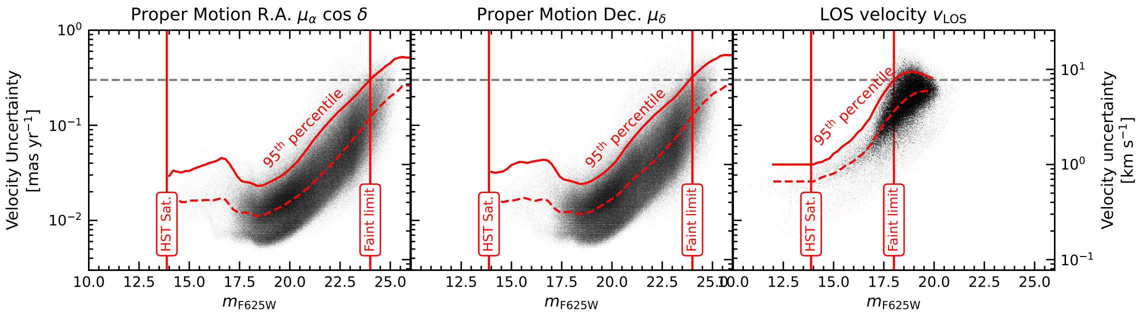

Figure 5.1: The three panels show the uncertainty of the individual velocity measurements for both the two proper motion directions and the line-of-sight direction plotted against the magnitude in the m_{F625W}. The red line marks the 95th percentile of the error distribution determined in 0.5 mag wide bins and is used to reject stars with unusually large proper motion errors. The dashed line marks the median of the error distribution. To facilitate comparisons between the proper motion and the line-of-sight uncertainties all three panels have the same y scale, the left axis shows astrometric units, the right axis shows physical units at an assumed distance of 5445 pc (this leads to a conversion of 1 mas yr^{-1} =25.83 km s^{-1}).

- We require that each star matches the standard quality criterion defined in Paper I. This combined criterion contains cuts in the quality and reliability of the spectral fit, the accuracy of the recovered magnitude, the average signal-to-noise ratio, and the cluster membership. We further restrict the kinematic subsample to measurements with a relative mag accuracy `mag_rel`>0.9 and a reliability parameter `rel`>0.9. This helps to remove stars that are influenced by neighboring sources and may bias the kinematic measurements.

- Similar to the HST-based proper motions, we rejected measurements whose line-of-sight velocity error was larger than the 95th percentile in 0.5 mag wide bins (see Figure 5.1, *right*).

- We set an overall magnitude cutoff at $m_{\mathrm{F625W}} > 18$. At this magnitude our magnitude-dependent error cutoff reaches a level of ~ 7.7 km s^{-1} (equivalent to the 0.3 mas yr^{-1} cutoff of $m_{\mathrm{F625W}} = 24$ for the proper motion measurements).

- We also require a successful crossmatch with the HST-based catalog (this was achieved for 307,030 of 342,797 stars from the MUSE catalog; see Paper II) and a high-quality HST-based measurement. This effectively makes the MUSE sample a subset of the HST sample and allows us to apply the same membership selections. In addition, it makes the MUSE subset a true 3D sample allowing us to compare the results for both proper motion and line-of-sight based measurements. The final MUSE sample contains 32,092 stars with a high-quality LOS measurement.

5.2.3 Cluster membership selection

To restrict our sample to likely cluster members and exclude fore- and background sources, we use both a photometric and a proper-motion-based criterion. First, we require that the stars lie on the

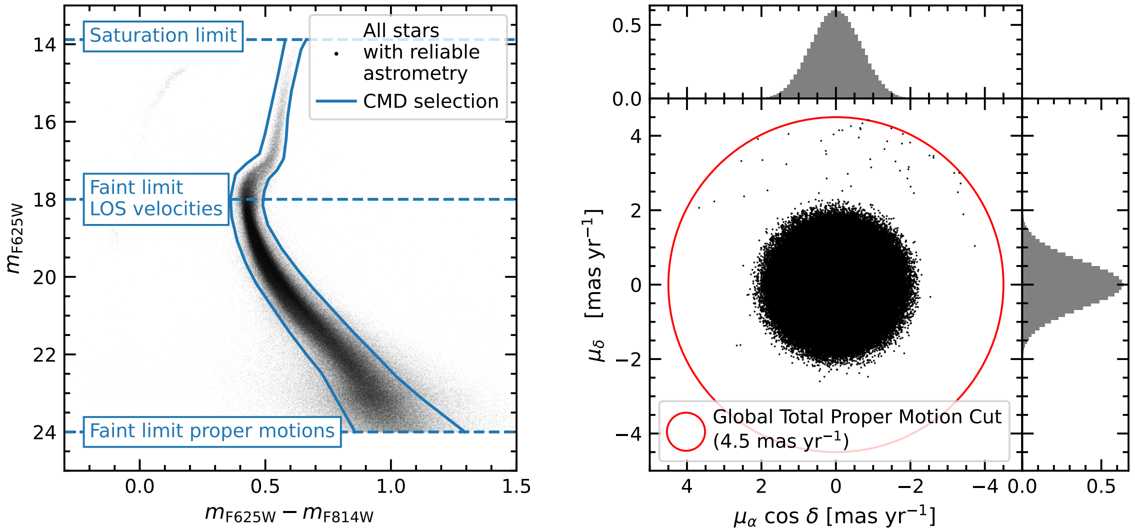

Figure 5.2: *Left:* A color-magnitude diagram based on photometry in the m_{F625W} and the m_{F814W} filter for all stars that pass the basic quality selections for the subsample used for the kinematic analysis. The blue solid lines mark our selection of main sequence and red-giant branch stars that are members of ω Cen. The dashed lines mark the bright and faint limits of the subsample used for the kinematic analysis. *Right:* A vector-point diagram of the stars in the high-quality subsample. The red circle marks the global proper motion cutoff of 4.5 mas yr^{-1}. Stars with a total proper motion higher than this value are excluded from the kinematic analysis as they are likely fore- or background stars. The histograms in the side panels show the marginalized distributions of the two proper motion components.

red-giant branch or the main sequence in the F625W-F814W color-magnitude-diagram using two manually defined fiducial lines (see Figure 5.2, *left*). This excludes cluster stars on the horizontal branch, however, their numbers are comparatively low and no MUSE line-of-sight velocities were measured for them. The other criterion is a global cut-off in total proper motion of 4.5 mas yr^{-1}. This corresponds to around 115 km s^{-1}, around 5.5 times higher than the typical velocity dispersion for main-sequence stars in the center of ω Cen. There is a small number of stars that pass this criterion but are likely non-members (see stars in upper-right of the vector-point diagram in Figure 5.2). These sources are removed with an additional sigma-clipping step when determining the actual kinematic properties.

5.2.4 SUMMARY OF SELECTIONS

From an initial number of 1,395,781 stars with a proper motion measurement, 669,975 pass our combined quality selection criteria, of which 610,846 then pass the subsequent membership cuts, constituting our proper motion sample.

From 342,797 stars with a line-of-sight velocity, 307,030 were successfully crossmatched with the HST catalog, of which 32,092 passed all spectroscopic quality criteria. Finally, 24,928 stars have both a high-quality astrometric and photometric measurement. The full 3D sample of velocities is shown in a 3-dimensional version of a vector point diagram in Figure 5.3. This Figure shows that all 3 velocity components show a similar distribution when assuming a distance of $d = 5445$ pc (our best fit kinematic distance, see Subsection 5.3.5).

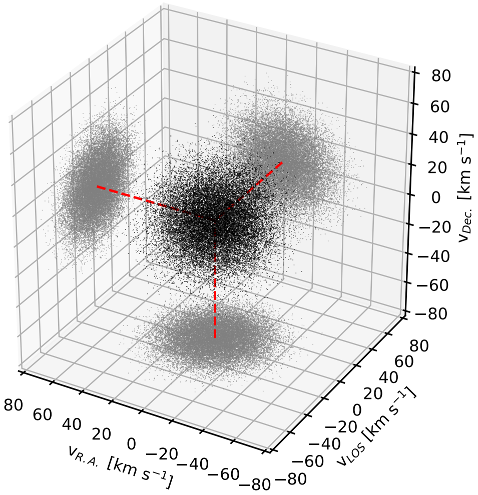

Figure 5.3: 3D vector point diagram for the 24,928 stars that match both our proper motion and line-of-sight velocity quality criteria. Proper motions have been converted to physical velocities using our new kinematic distance of d =5445 pc.

5.3 1D PROFILES OF THE KINEMATIC PARAMETERS

5.3.1 DETERMINATION OF THE VELOCITY DISPERSION

The observed velocity distribution for both proper motions and LOS velocity is a superposition of the true velocity distribution and the measurement errors. To measure the underlying velocity dispersion we used the log-likelihood function for a Gaussian distribution with heterogeneous errors in the form presented by Pryor & Meylan (1993):

$$LL = -\frac{1}{2}\sum_i \left(\frac{(v_i - \bar{v})^2}{(\sigma^2 + \sigma_i^2)} + \log(2\pi(\sigma^2 + \sigma_i^2)) \right) \tag{5.1}$$

with $\bar{v}$ being the mean velocity in a certain subsample, σ being the true velocity dispersion, and v_i and σ_i being the individual stellar velocity measurements with their uncertainties. We sampled the likelihood function using the Markov-Chain Monte-Carlo code `emcee` (Foreman-Mackey et al., 2013b), using flat priors and 12 walkers with 500 steps each. We use the median of the posterior distribution as our best estimate for the velocity dispersion and use the 16th and 84th percentile as measures of the uncertainty.

5.3.2 PROPER MOTION BASED 1D PROFILES OF THE VELOCITY DISPERSION.

To measure spatial variations of the velocity dispersion the data is typically split into radial bins. Several binning schemes are possible, and there is a trade-off between spatial resolution, stochastic noise, and ease of presentation. We compare several binning schemes in Section 5.11 but choose an adaptive logarithmic binning scheme as our standard. The radii of successive bins are increased by a factor of at least $10^{0.05} \approx 1.122$, while maintaining a minimum number of 100 stars per bin.

For the overall (combined) proper motion dispersion $\sigma_{\mathrm{PM,c}}$ we treat the radial and tangential components of the proper motion as separate samples from the velocity distribution, which doubles the number of measurements. The resulting profile is shown in Figure 5.4, and the individual numerical values can be found in Table 5.2 (Section 5.8). The velocity dispersion rises steadily from 0.52 mas yr^{-1} (13.4 km s^{-1}) at large radii to the central 10 arcseconds, where it reaches a mean value of $\sim$0.81 mas yr^{-1} (20.9 km s^{-1}). The error bars at large radii are as small as 0.001 mas yr^{-1} but are higher near the center due to the smaller number of stars per bin.

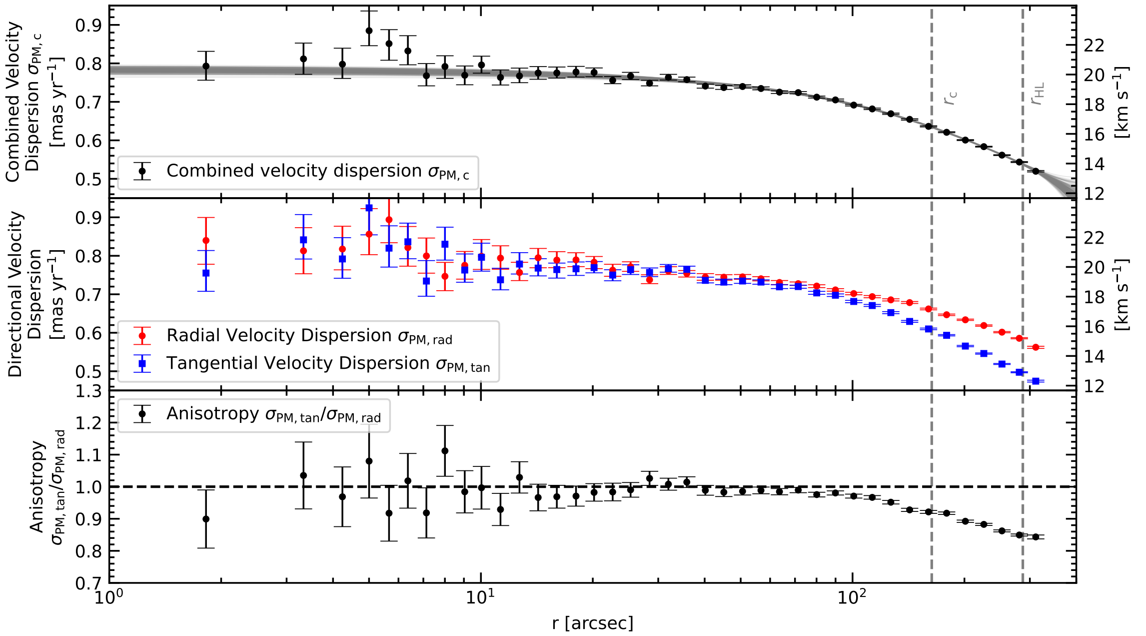

Figure 5.4: Proper motion dispersion profiles determined using the new oMEGACat data using the full magnitude range. The profiles were determined using an adaptive logarithmic binning scheme with a stepsize of $\Delta\log r = 0.05$ and a minimum number of 100 stars per bin. The dashed vertical lines indicate the core and the half-light radii as reported in Baumgardt & Hilker (2018) *Top:* Overall dispersion, for which measurements of the tangential and the radial component of the proper motion were combined. The grey line shows the result of 100 4th-order polynomial fits to the dispersion profile and is meant for visualization purposes only. *Center:* Individual components of the proper motion dispersion in which the tangential and the radial components were treated separately. *Bottom:* Anisotropy profile calculated as the ratio between the tangential and the radial proper motion dispersion component.

5.3.2.1 COMPARISON WITH LITERATURE PROFILES

The previous most widely used profile of the proper motion dispersion in the inner region of ω Cen has been published in Watkins et al. (2015a) (thereafter Watkins15). In Figure 5.5 we compare the literature profile with our new profile. For the comparison, we have to take into account that the Watkins15 profile is based on a subset of bright stars. Due to the partial energy equipartition in the core of ω Cen, we expect a higher dispersion measured from our catalog, as we include lower mass stars in the analysis. To allow for a consistent comparison, we also calculated a profile using only stars brighter than $m_{\mathrm{F625W}} = 19$, a threshold similar to the one used in Watkins15 and using a similar binning scheme.

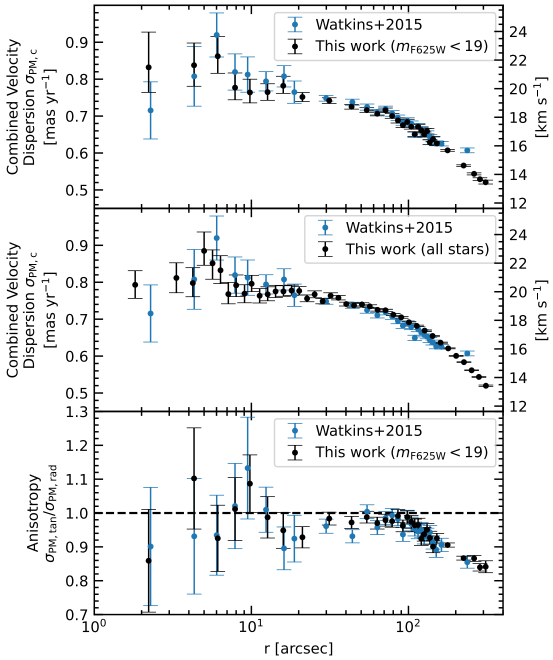

Figure 5.5: Proper motion dispersion profiles determined using the new oMEGACat (black markers). We compare the new dispersion measurements with the literature profile by Watkins15 (blue markers). For better comparability, in the *top panel* we restrict our data set to bright stars and use a binning scheme similar to the literature. In the *center panel* we use logarithmic radial bins and the full high-quality subset. In the *bottom panel* we compare the anisotropy, again using the bright sample only.

The comparison of the profiles (Figure 5.5, *middle panel*) matches our expectations: Due to the significantly larger number of included measurements both the spatial resolution and the individual errors in the new dispersion profile are improved when all well-measured stars from the new proper motion catalog are used. Our profile shows less scatter and extends to larger radii. At larger radii, it shows slightly larger dispersion values as expected from energy equipartition arguments.

When comparing a similar sample of bright stars (Figure 5.5, *top panel*) we see similar errors in the dispersion measurements (as these errors are dominated by the limited number of available stars in each bin and not on the individual proper motion measurement errors) and overall agreement between the two profiles. However, we notice an overall smaller dispersion in all but the two innermost bins. One potential explanation could be a small underestimation of the proper motion errors in the literature work, leading to an overestimation of the velocity dispersion.

5.3.3 VELOCITY ANISOTROPY PROFILES

To study the velocity dispersion anisotropy, we decompose the proper motion measurements into their radial and tangential components (with respect to the cluster center). We then calculate the dispersion profile for the two components separately (Figure 5.4, middle panel). While there are no apparent differences in the central regions, at larger radii, the radial velocity dispersion ($\sigma_{\mathrm{PM,rad}}$) is significantly higher than the tangential velocity dispersion ($\sigma_{\mathrm{PM,tan}}$). To quantify this we also calculate the ratio between the two dispersion values $\sigma_{\mathrm{PM,tan}}/\sigma_{\mathrm{PM,rad}}$, see bottom panel in Fig. 5.4. We find no significant anisotropy within $r < 30''$; after that, the velocity distributions become increasingly radially anisotropic, reaching $\sigma_{\mathrm{PM,tan}}/\sigma_{\mathrm{PM,rad}} = 0.0849 \pm 0.003$ at $281''$ close to the half-light radius.

There is good agreement between our new measurements and the anisotropy profiles derived in Watkins15, see bottom panel of Figure 5.5. However, the new measurements reach significantly larger radii.

5.3.3.1 COMPARISON WITH OTHER CLUSTERS

Libralato et al. (2022) derived detailed kinematics for a large sample of Milky Way globular clusters and related the velocity dispersion anisotropy at the half-light radius with the half-light radius relaxation time (see their Figure 6). With an anisotropy value of $\sigma_{\mathrm{PM,tan}}/\sigma_{\mathrm{PM,rad}} = 0.0849 \pm 0.003$, the half-light anisotropy in ω Cen is significantly lower than for most other Milky Way globular clusters. Due to its young dynamical age (half-mass relaxation time $\sim$ 21 Gyr; Baumgardt & Hilker 2018) it still follows the trends presented in Libralato et al. (2022).

5.3.4 DISPERSION AND ROTATION PROFILES BASED ON THE LOS DATA

Unlike the proper motions, which have been measured relative to the bulk motion of the cluster and therefore do not contain any rotation signal, the line-of-sight velocity measurements are absolute and do show the rotation. Thus, the velocity dispersion and the rotation profile have to be determined simultaneously. We do this using the method developed in Kamann et al. (2018), which simultaneously fits for the velocity dispersion σ_{LOS}, the rotation v_{LOS} and the position angle of the rotation axis θ_0 in each bin.

Again we use an adaptive logarithmic binning scheme ($\Delta \log r = 0.05$, $N_{\mathrm{min}} = 50$) to split the data into circular bins. The resulting dispersion and rotation curves of the LOS velocities are shown in Figure 5.6 and in Table 5.3 (Section 5.8).

The measured rotation curve starts with relatively high values in the innermost bins (although with uncertainties as large as $\sim$5 km s^{-1} due to the small number of measurements) before reaching a minimum at around r =30". Afterwards it increases monotonically until reaching a plateau with

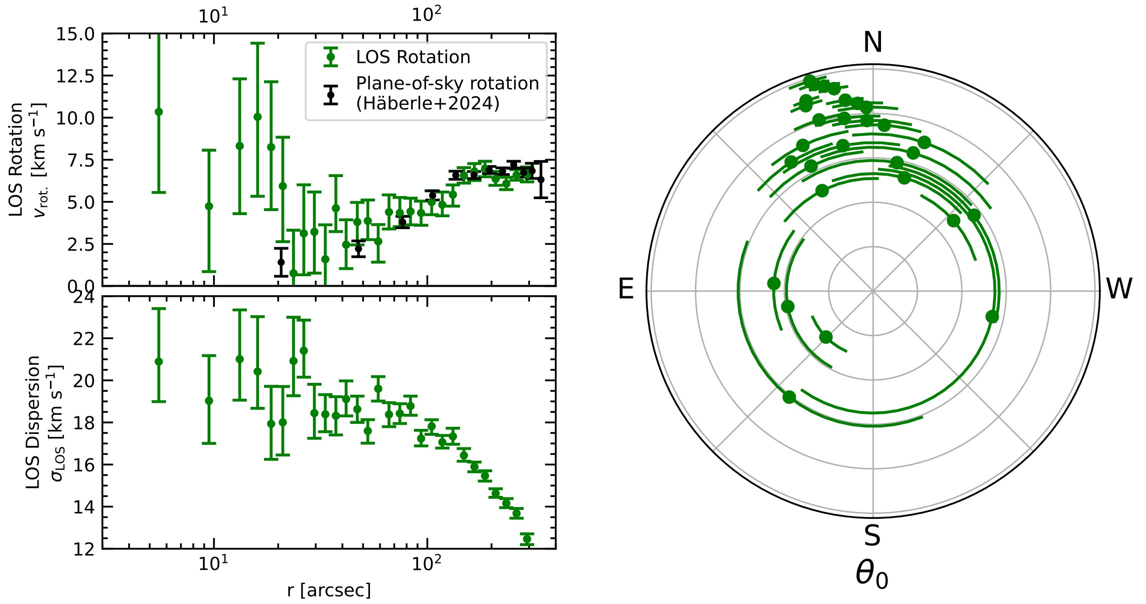

Figure 5.6: *Top left:* Rotation profile determined using the line-of-sight velocities. We compare our new LOS rotation profile with the plane-of-sky rotation curve presented in Häberle et al. (2024b) and find good agreement. *Bottom left:* Line-of-sight velocity dispersion profile. *Right:* Result for the position angle of the determined rotation axis.

$v_{\text{rot}} = 7\,\text{km}\,\text{s}^{-1}$ at around r =150”. The mean value of the position angle of the rotation axis for $r > 30''$ is $\theta_{\text{LOS}} = (104.3 \pm 1.4)^{\circ}$.

The initial decrease of the rotational velocity is likely related to the counter-rotating structure discovered in Pechetti et al. (2024) as also indicated by the flip of the rotation angle (see Figure 5.6, *right*). The constant rotation velocity at radii larger than r =150” is also observed in the plane-of-sky rotation (see Häberle et al. 2024b), as shown by the comparison in Figure 5.6. The similar rotation amplitudes of the different spatial components are expected due to the inclination of $i = (43.9 \pm 1.3)^{\circ}$ as determined in Häberle et al. (2024b).

5.3.5 COMPARISON BETWEEN PROPER-MOTION AND LINE-OF-SIGHT DISPERSION PROFILES AND KINEMATIC DISTANCE

As the kinematic LOS sample is a subset of the proper motion sample, we can also calculate the proper motion profile using the same stars for all dimensions. This allows us to determine the kinematic distance of ω Cen, but also to capture potential systematic effects in either data set.

We use the following equation to obtain a kinematic distance estimate for each individual bin of the line-of-sight velocity dispersion profile, assuming that the proper motion dispersion and the line-of-sight velocity dispersion are the same:

$$d\,[\text{pc}] = (210.51\,[\text{pc}\,\text{km}^{-1}\,\text{s}\,\text{yr}^{-1}]) \cdot \frac{\sigma_{\text{LOS}}\,[\text{km}\,\text{s}^{-1}]}{\sigma_{\text{PM,c}}\,[\text{mas}\,\text{yr}^{-1}]} \tag{5.2}$$

The upper panel of Figure 5.7 shows a comparison between the proper motion dispersion ($\sigma_{\mathrm{PM,c}}$) and the line-of-sight velocity dispersion (σ_{LOS}) using a distance of 5445 pc, the best fit distance described below. The two profiles show good agreement within their error bars for most of the bins. In the lower panel of Figure 5.7 we compare the line-of-sight profile with the radial and tangential components of the proper motion dispersion. At larger radii, where the velocity anisotropy is more pronounced, one can see that the line-of-sight dispersion falls in between the radial and tangential proper motion dispersion profile. This can be explained geometrically: the LOS velocities contain both a radial and a tangential component, depending on the (unknown) LOS position of the star.

The results for the kinematic distance are shown in Figure 5.8. The variance weighted mean of all individual kinematic distance estimates is (5445 ± 41) pc in excellent agreement with the value of $(5{,}430 \pm 50)$ pc determined in Baumgardt & Vasiliev (2021) by averaging several different distance estimation methods (see their paper for a detailed comparison of various other literature distance estimates). As our estimate is based on a consistent dataset (with the same large sample of stars with both well-measured proper motions and LOS velocities) we consider it the most reliable available kinematic distance value, in addition to being the most precise distance measurement of any kind available for ω Cen. An overview of various other distance estimates including Gaia parallaxes is given in Table 5.4 in the Appendix.

We note that our simple method of estimating the kinematic distance assumes isotropy between the proper motion and the line-of-sight velocity components. While this holds true in the central region and has also been assumed for other previous kinematic distance estimates, we expect some bias at larger radii due to anisotropy and flattening of the velocity field (see also van de Ven et al., 2006). The lower kinematic distance values for the bins at larger radii might be caused by this effect. The Gaia kinematic distance estimate from Baumgardt & Vasiliev (2021) of (5359 ± 141) pc is derived from data at predominantly larger radii than our estimate; its consistency despite the larger expected anisotropy suggests that the systematic effects of anisotropy are minimal. This suggests our kinematic distance is reliable, however, modeling of the oMEGACat data based on an accurate anisotropic, rotating, and flattened model fit to the data could result in an improved estimate.

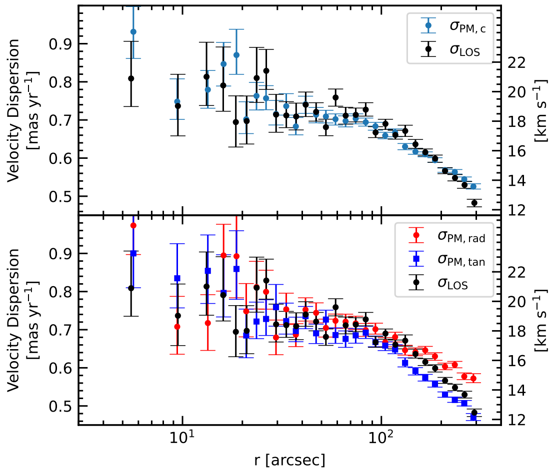

Figure 5.7: *Top:* A comparison between the line-of-sight velocity dispersion profile and the overall proper motion dispersion. A distance of 5445 pc was assumed to convert between proper motions and physical velocities. The two profiles show good agreement. *Bottom:* A comparison between the line-of-sight velocity dispersion and the individual (radial and tangential) components of the proper motion dispersion. At larger radii, where the proper motion field turns increasingly radially anisotropic, the line-of-sight velocity dispersion lies in between the two different proper motion profiles.

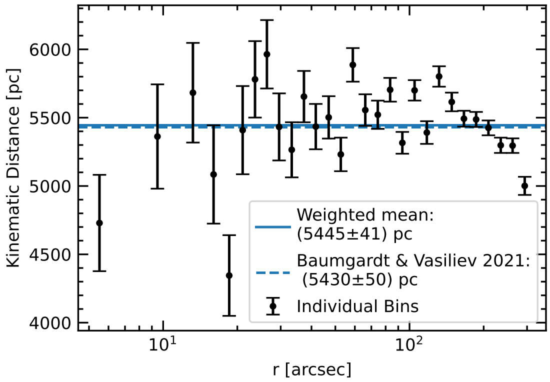

Figure 5.8: Kinematic distance of ω Cen derived by calculating the ratio between line-of-sight and proper motion dispersion in different circular bins (see also Figure 5.7, *top*). The weighted mean value is in good agreement with the literature distance value derived in Baumgardt & Vasiliev (2021).

5.4 KINEMATIC MAPS

The large number of stellar measurements in the new oMEGACat catalogs allows us to derive kinematic maps with fine spatial resolution and large spatial coverage.

5.4.1 MAPS OF THE TOTAL PROPER MOTION DISPERSION

To create velocity dispersion maps of the proper motion we use the Python Voronoi binning package `vorbin` (Cappellari & Copin, 2003) to separate the field into approximately equally populated 2-dimensional bins. We set a target number of 250 stars per bin, which yields a median uncertainty of approximately 0.02 mas yr^{-1} (≈ 0.5 km s^{-1}) per bin and a total number of 2,434 bins. Figure 5.9 shows the resulting map of the combined velocity dispersion $\sigma_{\mathrm{PM,c}}$ with a zoom into the innermost arcminute. The map shows the overall decrease of the velocity dispersion towards larger radii and has an overall symmetric and smooth appearance, indicative of the large number and high quality of the underlying velocity measurements.

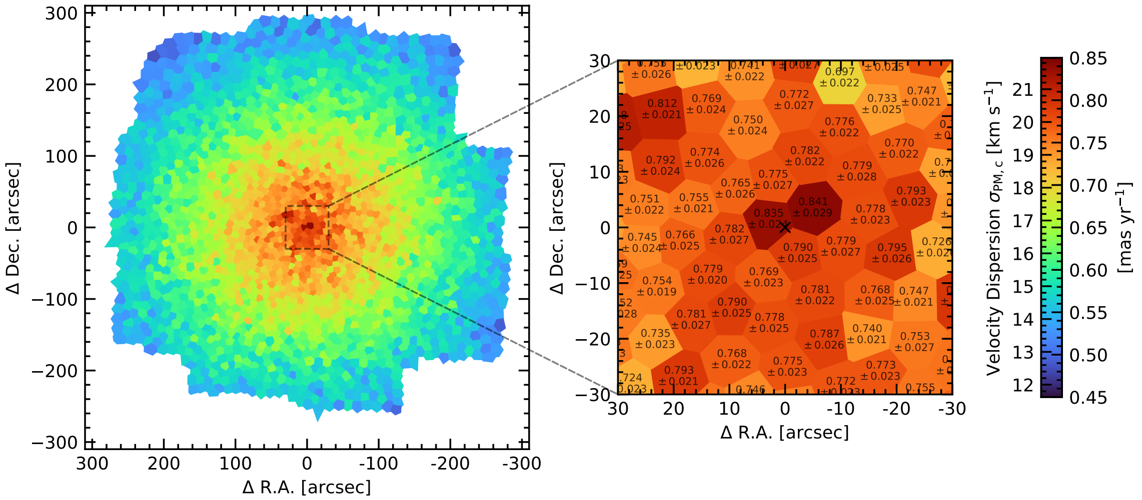

Figure 5.9: Dispersion map combining both proper motion components and determined using $N = 250$ Voronoi bins. The right panel shows a zoom into the centermost arcminute with the numerical values (in mas yr^{-1}) for the individual bins shown in black letters.

5.4.2 EMPIRICAL FITS OF A SMOOTH MODEL

To determine the general geometric properties of the velocity dispersion map and a kinematic estimate for the cluster center, we fit a 2D Gaussian function to velocity dispersion values determined in the Voronoi bins. A single 2D Gaussian provides a decent fit (see Figure 5.10) with a reduced $\chi^2 = 0.99$ and independently recovers the cluster center (ΔR.A. $= -1.31'' \pm 0.72''$, ΔDec. $= 1.44 \pm 0.66''$) with respect to the photometric center determined in Anderson & van der Marel 2010). The best-fit position angle is $\Theta = (101.4 \pm 2.4)^\circ$ (counterclockwise offset of the major axis with respect to North), and the dispersion distribution is flattened along the minor axis of the cluster with $1 - \sigma_y/\sigma_x = 0.09$.

The flattening of the velocity field is similar to the photometric flattening, where the mean ellipticity $\epsilon = 1 - \frac{b}{a} = 0.010$ (Geyer et al., 1983; Pancino et al., 2003; Calamida et al., 2020), see also Section 5.11. The position angle also is in agreement with the photometric value (e.g. 100°, van de Ven et al. 2006) and with the rotation axis value found using LOS velocities ($\Theta_{0,\mathrm{LOS}} = (104.3 \pm 1.4)^\circ$, see above).

Even though the global properties are well described by a single Gaussian, the residuals show that there is a significant rise of the velocity dispersion within $r < 10''$. Future dynamical models are necessary to interpret this further, but the size of this feature is comparable to the radius of influence of a ∼20,000 $\mathrm{M}_\odot$ intermediate-mass black hole using the equation of Peebles (1972). Allowing a second Gaussian component (with the same center as the first component) in the fit model (see Figure 5.10, *lower row*) allows to describe this central rise in velocity dispersion and to further reduce the reduced χ^2 to 0.91. The kinematic center, the position angle, and the flattening of the outer component are still successfully recovered.

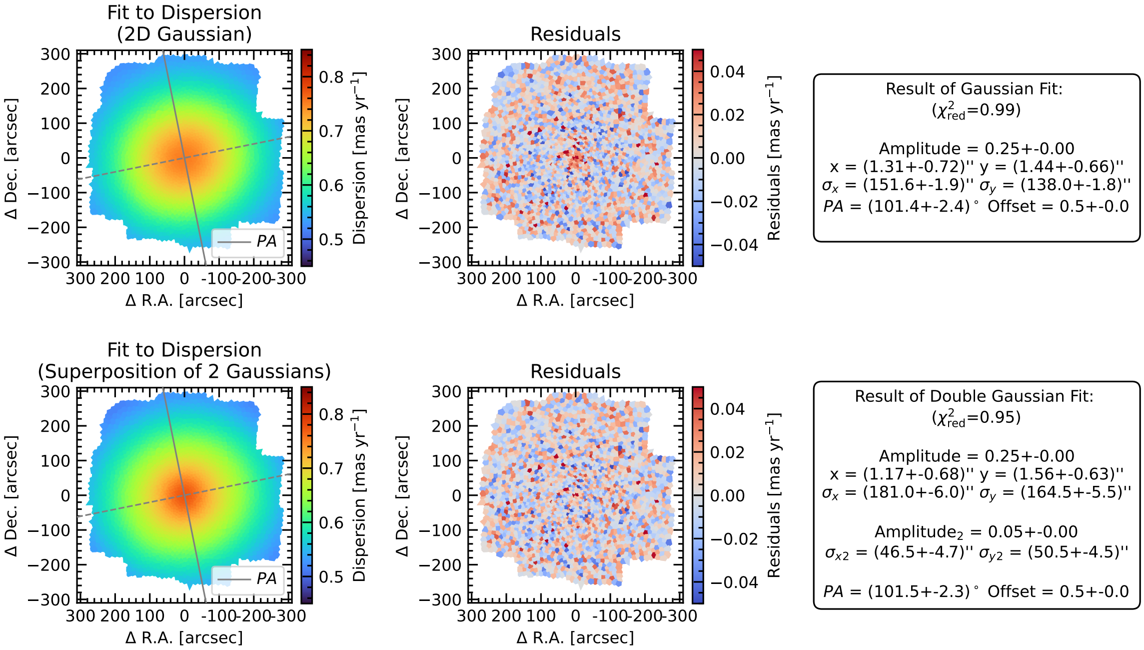

Figure 5.10: *Top:* Result of a single component 2D Gaussian fit to the 2D proper motion dispersion field shown from Figure 5.9. The *left* shows the result, the *center* shows the residuals, which are in good agreement besides an underestimation of the cusp of the velocity dispersion in the centermost region, and the *right* shows the parameters of the Gaussian fit. *Bottom:* Results for a 2-component 2D Gaussian fit. This 2-component model is able to also describe the velocity dispersion in the innermost region as can be seen from the residuals. Both models successfully recover the ellipticity and the position angle of the dispersion field.

5.4.3 Maps of the proper motion anisotropy

To study the 2-dimensional variation of the velocity anisotropy we use the same binning scheme as in the previous section, but now calculate the two dispersion components ($\sigma_{\mathrm{PM,rad}}$ and $\sigma_{\mathrm{PM,tan}}$) separately, see Figure 5.11. While the overall velocity dispersion distribution shows only mild ellipticity, the radial velocity dispersion appears highly flattened with respect to the rotation axis of the cluster and the tangential velocity dispersion appears to be elongated along the rotation axis. The 2D map of the anisotropy ($\sigma_{\text{tan}}/\sigma_{\text{rad}}$) shows the overall trend to radial anisotropy at larger radii, but also two "tangentially anisotropic" plumes along the rotation axis. This 2D structure can be naturally explained as a superposition of the actual physical anisotropy in the velocity dispersion and a geometric projection effect of the rotation of the cluster: In a 2-dimensional projection, stars that are close to the rotation axis preferentially move orthogonally to the axis resulting in an apparent increase in the observed tangential velocity dispersion.

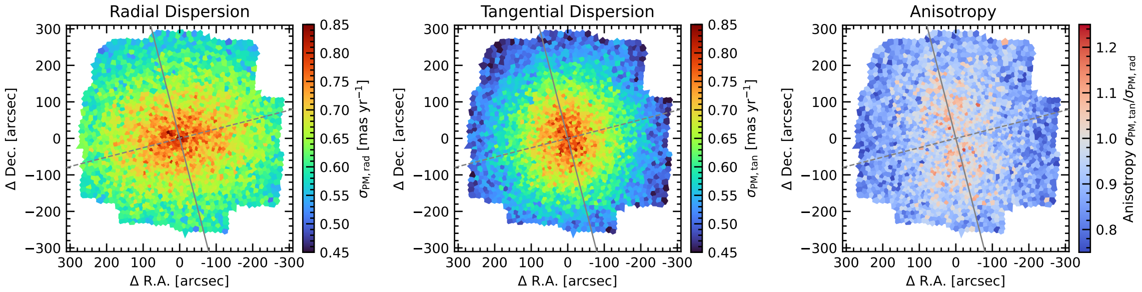

Figure 5.11: Proper motion dispersion maps determined separately for the radial (*left*) and the tangential (*center*) proper motion component. These individual-component velocity fields show strong flattening/elongation along the rotation axis (solid grey line) of the cluster, which is likely a geometric effect. The ratio of the two components (*right*) gives a measure for the anisotropy of the velocity fields. At larger radii, the field becomes increasingly radially anisotropic. In addition, there are two tangentially anisotropic plumes along the rotation axis.

5.4.4 MAPS OF THE LINE-OF-SIGHT MEAN VELOCITY AND DISPERSION

In Figure 5.12 we derive Voronoi binned kinematic maps based on the line-of-sight velocity measurements. Due to the significantly smaller size of the LOS sample (24,928 sources compared to 610,846 sources in the proper motion sample) we resorted to a smaller target bin size of $N = 100$ stars per bin. This still leads to larger bins compared to Figure 5.9.

Opposite to the proper motion measurements (which by construction have a zero mean motion) the line-of-sight velocities contain the rotation signal of the cluster. Therefore we show both the mean line-of-sight velocity per bin (Figure 5.12, *left*) and the derived velocity dispersion σ_{LOS}(Figure 5.12, *right*).

The mean velocity map nicely shows the line-of-sight rotation pattern. The dispersion map looks similar to the maps derived with the proper motions, however, it shows larger scatter (as expected due to the smaller sample size). We performed a 2D Gaussian fit to the dispersion field (Figure 5.13), which showed a similar reduced χ^2 value to the proper motion maps. This fit again recovered the cluster center and the position angle (compare with Figure 5.10) albeit with larger statistical errors. Contrary to the velocity dispersion map, a second Gaussian component did not improve the fit (likely due to the larger bin sizes and statistical uncertainties).

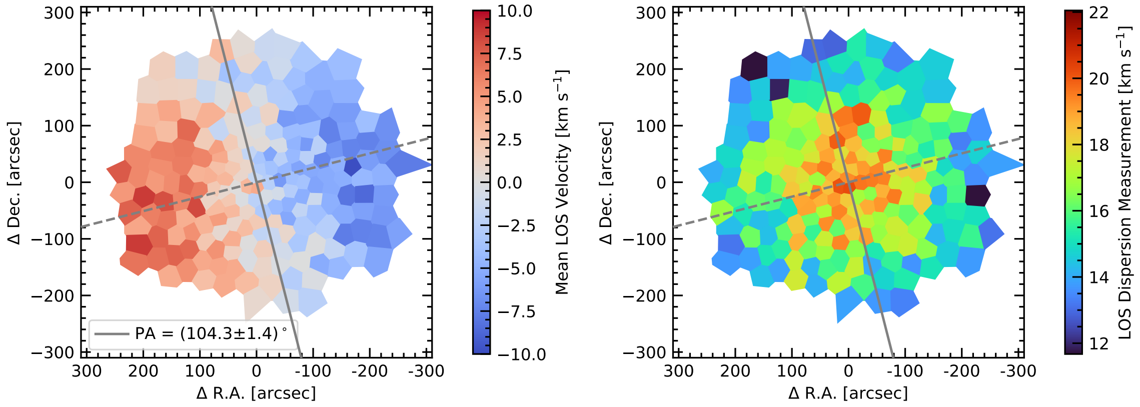

Figure 5.12: *Left:* Mean line-of-sight velocity determined in $N = 100$ Voronoi bins. The global rotation of ω Cen is clearly visible. *Right:* Line-of-sight velocity dispersion determined in Voronoi bins.

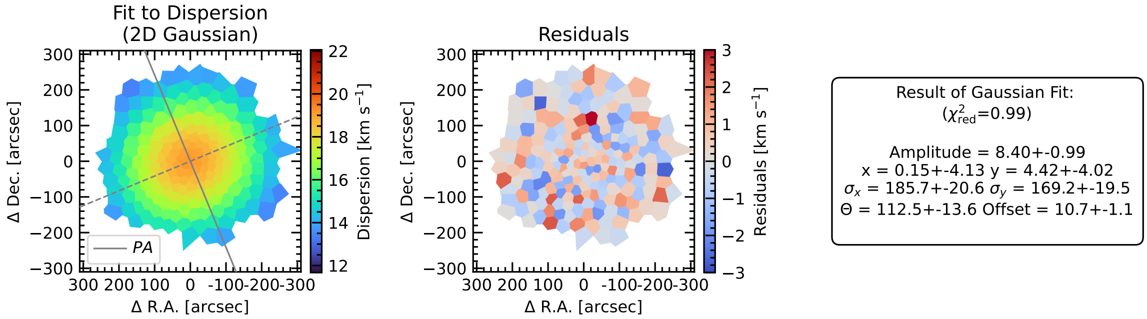

Result of Gaussian Fit:
(χ^2_{red}=0.99)

Amplitude = 8.40+-0.99
x = 0.15+-4.13 y = 4.42+-4.02
σ_x = 185.7+-20.6 σ_y = 169.2+-19.5
Θ = 112.5+-13.6 Offset = 10.7+-1.1

Figure 5.13: Result of a 2D Gaussian model fit to the line-of-sight velocity dispersion map (compare with Figure 5.10). *Left:* Best fit Gaussian model *Center:* Residuals *Right:* Parameters of the fit.

5.5 SEARCH FOR METALLICITY DEPENDENT KINEMATICS

It is well known that ω Cen hosts multiple stellar populations with a wide spread in metallicity (see introduction). Differences in the spatial distribution and the kinematics of the different subpopulations can help to constrain their origin (see Alfaro-Cuello et al., 2019, 2020; Kacharov et al., 2022, for the case of M54). Various papers have studied the spatial distribution of the different subpopulations in ω Cen. Early works using ground-based data (Sollima et al., 2007; Bellini et al., 2009b) found an increase in the concentration of the helium-enhanced blue main sequence within the inner region of the cluster, while at larger radii ($r > 10'$) the ratio of the different helium abundance subpopulations remains approximately constant (however Calamida et al. 2017 and Calamida et al. 2020 found evidence for a more extended distribution of the blue main-sequence stars). Most recently, Nitschai et al. (2024) found no radial variation of the stellar distribution with MUSE-based metallicity measurements within the half-light radius, while Scalco et al. (2024) confirmed the trend of a more centrally concentrated blue main sequence from Bellini et al. (2009b) with precise space-based photometry at larger radii ($\sim 1 - 3r_{\mathrm{HL}}$).

The kinematics of the different subpopulations have been subject to several investigations: E.g. Anderson & van der Marel (2010) found no kinematic differences between the blue and red-main-sequence populations in the inner region of ω Cen. At larger radii ($\sim 3.5\,r_{\mathrm{HL}}$), Bellini et al. (2018b) found significant differences between the anisotropy, the systemic rotation, and the state of energy equipartition for the different populations.

In this work, we focus on the bright end of the sample, where precise line-of-sight velocities and metallicity measurements are available. To do so, we further restrict the sample of 24,928 stars with a full 3D velocity measurement to $m_{\mathrm{F625W}} < 17$ (this limit is necessary to obtain reliable and bias-free metallicity, see Nitschai et al. 2024), which leaves us with a subset of 6,193 stars. The metallicity distribution for this sample is shown in Figure 5.14 (*upper panel*). We then further split the data set into 4 quartiles in metallicity and search for differences in the velocity dispersion in different radial bins (again we used an adaptive logarithmic binning scheme with $\mathrm{N}_{min} = 100$ and $\Delta\mathrm{Log}r = 0.15$) and for all 3 velocity components (LOS velocity, radial proper motion, tangential proper motion), see Figure 5.14 (*lower grid of plots*). In each radial bin and for each velocity component we run a Kolmogorov–Smirnov (KS) and a k-sample Anderson-Darling test to see whether the distribution of an individual metallicity quartile differed significantly from the total distribution. The p-values for the null hypothesis (i.e. that the samples are drawn from the same distribution) for both tests are shown in Figure 5.14. We do not find significant ($p < 0.05$) deviations between the distributions in any of the velocity components (radial and tangential proper motion, LOS velocity) and in any of our radial bins.

This is consistent with the picture of well-mixed populations within the half-light radius of ω Cen, see also Nitschai et al. (2024). More subtle kinematic differences between the subpopulations may still be discovered when using the full proper motion sample instead of the sample limited to bright stars with a reliable spectroscopic metallicity measurement. This is the subject of a planned future project.

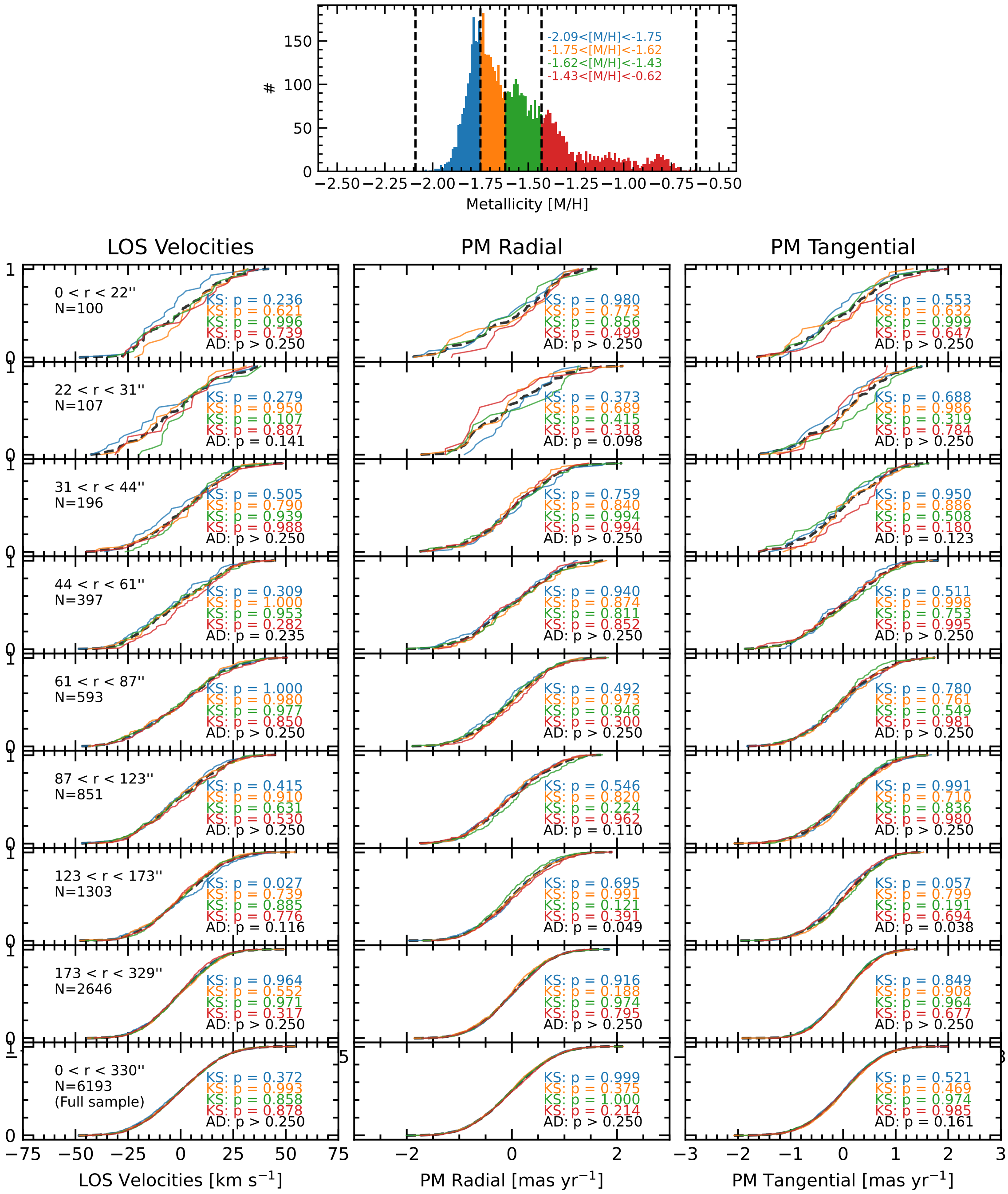

Figure 5.14: *Top:* Metallicity distribution for bright ($m_{\mathrm{F625W}} < 17$), well-measured stars in the catalog. We split the sample into metallicity quartiles indicated with different colors. *Bottom:* Normalized cumulative distribution functions for the 3 velocity components and for 8 different radial bins. We compared the velocity distribution for each metallicity quartile with the overall velocity distribution (black dashed line) using a Kolmogorov–Smirnov (KS) and a k-sample Anderson Darling (AD) test but found no significant differences. The p values for the null hypothesis are shown in each panel.

5.6 ENERGY EQUIPARTITION

Due to two-body relaxation processes, globular clusters evolve towards a state of energy equipartition, in which lower-mass stars show higher velocity dispersion than stars with higher masses (Spitzer, 1969). Traditionally, the state of energy equipartition has been parametrized by fitting the parameter η, where the velocity dispersion σ shows the following dependence on the mass m:

$$\sigma \propto m^{-\eta}. \tag{5.3}$$

A value of $\eta = 0.5$ would mean full energy equipartition, however, N-body simulations show that globular clusters only reach partial energy equipartition (Baumgardt & Makino, 2003; Trenti & van der Marel, 2013).

A different parametrization of the state of energy equipartition using the so-called equipartition mass (m_{eq}) was introduced in Bianchini et al. (2016) with the equation:

$$\sigma(m) = \begin{cases} \sigma_0 \exp(-\frac{1}{2}\frac{m}{m_{\mathrm{eq}}}) & \text{if } m \leq m_{\mathrm{eq}} \\ \sigma_{\mathrm{eq}}\,(\frac{m}{m_{\mathrm{eq}}})^{-1/2} & \text{if } m > m_{\mathrm{eq}} \end{cases} \tag{5.4}$$

where σ_0 indicates the velocity dispersion for massless particles and σ_{eq} corresponds to the value of velocity dispersion for $m = m_{\mathrm{eq}}$. The m_{eq} mass is a proxy for the level of partial energy equipartition reached by the system, such that for $m > m_{\mathrm{eq}}$ the system is in full energy equipartition.

The state of energy equipartition is a measure for the overall evolutionary state of the cluster (Baldwin et al., 2016) and other underlying properties such as the presence of black holes, which can reduce the level of energy equipartition in the luminous stars in the cluster (Weatherford et al., 2018; Aros & Vesperini, 2023; Dickson et al., 2024). Initial anisotropy in the velocity distribution of a stellar cluster has been shown to influence how fast the system evolved towards energy equipartition (Pavlík & Vesperini, 2021; Pavlík et al., 2024), with tangentially anisotropic systems showing a more rapid evolution. Pavlík & Vesperini (2022) further predict differences in the evolution towards energy equipartition for the radial and the tangential components of the velocity also in the 2D projected quantities that can be measured via proper motions.

Observationally, the energy equipartition can be studied by comparing the velocity dispersion measured for stars in different mass bins. However, this is challenging due to the need for velocity measurements with reliable uncertainties over a wide range of stellar masses and magnitudes. While spectroscopic LOS velocity measurements are typically limited to bright evolved stars that have similar masses, HST-based proper motion catalogs have recently enabled the study of energy equipartition in a variety of globular clusters (e.g. Libralato et al., 2018b, 2022) including ω Cen (Anderson & van der Marel, 2010; Bellini et al., 2018b; Watkins et al., 2022). Due to its high precision and depth, the oMEGACat proper motion catalog is perfectly suited to extend these existing studies to lower masses and wider radial coverage.

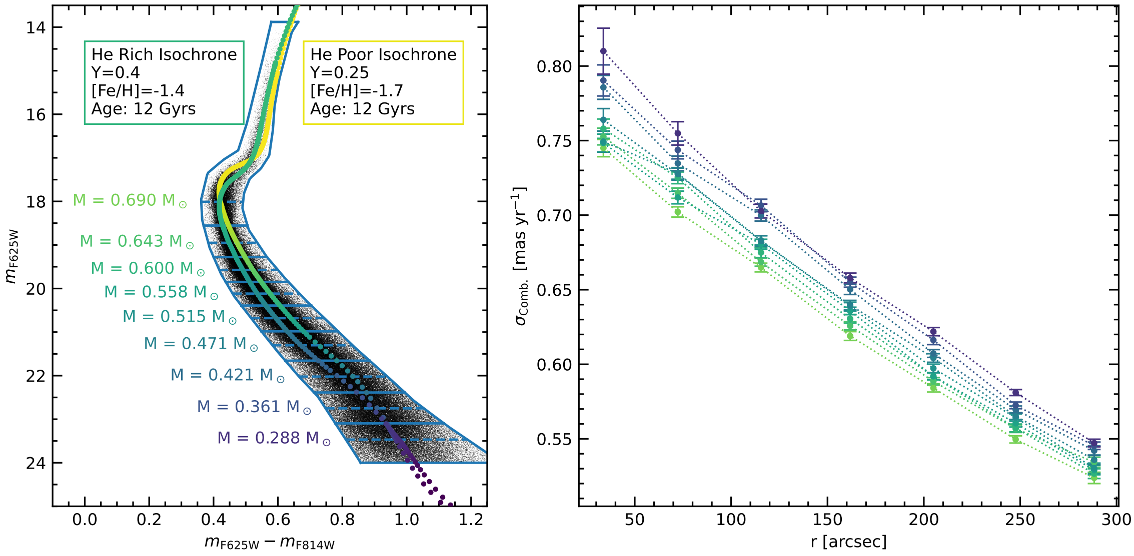

Figure 5.15: *Left:* m_{F625W}, m_{F814W} color-magnitude diagram used to split the data set in 10 equally populated m_{F625W} bins. For each bin, a weighted mean mass is estimated using two isochrones to account for both the helium-rich and helium-poor populations in ω Cen. *Right:* Combined velocity dispersion profile determined for the different mass bins and for 7 different radial bins.

5.6.1 ESTIMATION OF STELLAR MASSES

As a first step for our energy equipartition studies, we split our high-quality proper-motion subset into 10 equally number bins in magnitude (see Figure 5.15). Due to the complex stellar populations in ω Cen, it is not straightforward to directly infer stellar masses from their color-magnitude-diagram position. As we focus on the overall kinematics (and do not yet aim to study each subpopulation separately) we use the following approximation (adapted from Bellini et al. 2018b, but with different weights for the different stellar populations) to determine the mean stellar mass in each magnitude bin: We use two different 12 Gyr isochrones representing the helium-rich and the helium-poor population of the main sequence to infer the mean mass for the different magnitude bins (see Figure 5.15, *left*). For each magnitude bin, we calculated the mean magnitude and interpolated the two isochrones to infer the corresponding stellar mass. We then combined the two different mass estimates, giving them an equal weight (due to their similar fraction within the half-light radius, see Bellini et al. 2009b). The isochrones were obtained using the Dartmouth Stellar Evolution Database (Dotter et al., 2007, 2008). We used the following parameters:

- Helium Rich Isochrone: Y=0.4, [Fe/H] = -1.4 Weight: 50%
- Helium Poor Isochrone: Y=0.25, [Fe/H] = -1.7 Weight: 50%
- Reddening: E(B-V)=0.16

The mean masses per bin in our sample extend from 0.288 $M_\odot$ to 0.690 $M_\odot$, a large range that was previously not accessible in the inner regions of ω Cen.

5.6.2 VARIATION OF THE ENERGY EQUIPARTITION WITH RADIUS

Besides splitting our data set into different mass bins, we also split it into 7 different annular radial bins (each with a width of 45”). This allows us to probe the state of energy equipartition at different radii of the cluster. For each magnitude and radial bin we determine the proper-motion dispersion both for the combined proper motion, but also the radial and tangential components individually. A plot showing the different dispersion profiles is shown in Figure 5.15 *(right)*. Already in this plot, it can be seen, that the high-mass stars show lower velocity dispersion than stars with lower masses, indicative of at least some level of energy equipartition. In the next step, we fit the mass dependency of the velocity dispersion in each radial bin using either the classical η or the Bianchini m_{eq} parametrization. The results are shown in Figure 5.16 and Figure 5.17.

We can make the following general observations: At all radii and for both proper motion directions we can observe at least some degree of energy equipartition. The energy equipartition is highest in the innermost bin ($\eta = 0.088 \pm 0.017$; m_{eq}=(2.97±0.69) $\mathrm{M}_{\odot}$) and decreases towards larger radii (at the half-light radius: $\eta = 0.049 \pm 0.009$; m_{eq}=(4.51±0.70) $\mathrm{M}_{\odot}$). This trend is consistent with measurements at significantly larger radii ($\eta = 0.030 \pm 0.019$; $r \sim 3.5\, r_{\mathrm{HL}} \sim 975''$), see Bellini et al. (2018b).

5.6.3 ANISOTROPY IN THE ENERGY EQUIPARTITION

The overall trends measured for the combined velocity dispersion also hold for the individual radial and tangential directions. However, we can find the following differences between the two directions: While the degree of energy equipartition of the radial component quickly decreases with radius (and the radial velocity dispersion almost does not vary with mass at $r \approx r_{HL}$, see Figure 5.16), the tangential component shows an overall higher degree of energy equipartition and a weaker dependence with radius. This is tentatively in line with recent simulation results (Pfeffer et al., 2021; Pavlík & Vesperini, 2022; Pavlík et al., 2024) that find a faster evolution towards energy equipartition for the tangential component of the velocity.

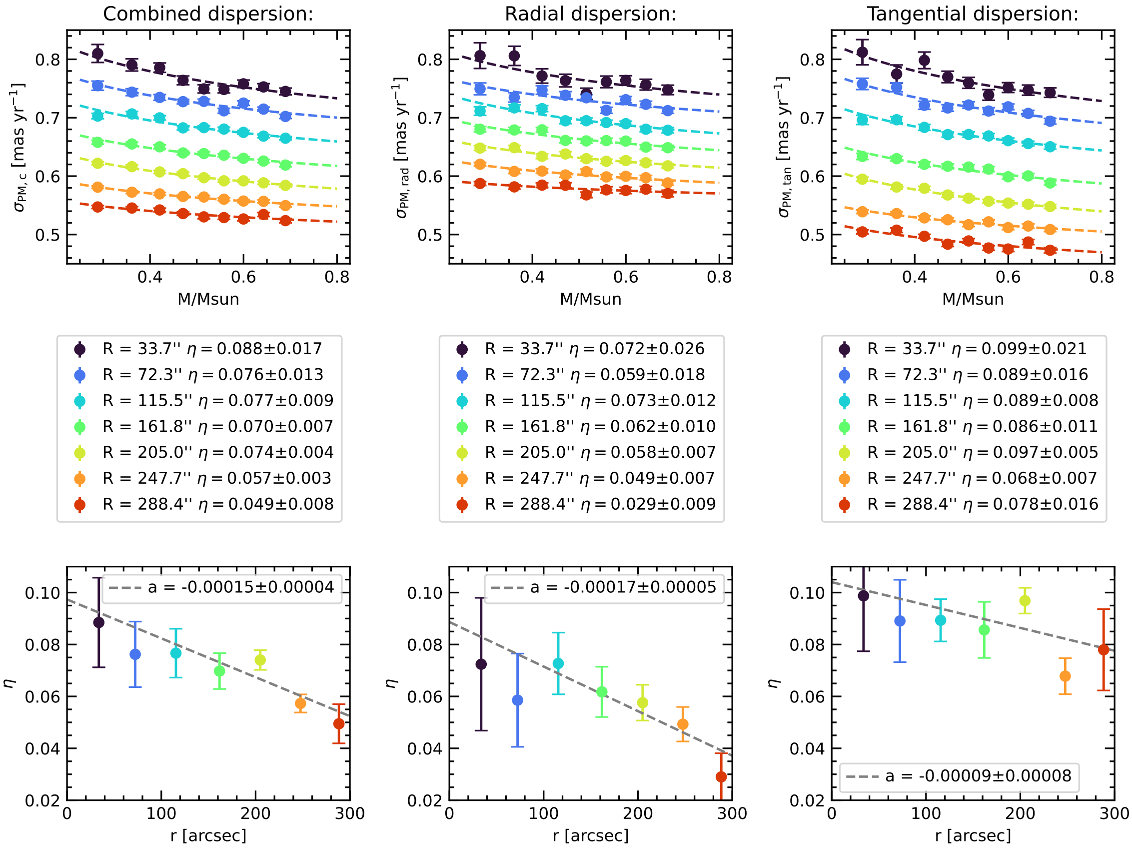
Combined dispersion:

Radial dispersion:

Tangential dispersion:

Figure 5.16: *Top:* Variation of the velocity dispersion with stellar mass. We compare the behavior of the combined velocity dispersion with the individual spatial components (*left:* combined velocity dispersion, *middle:* radial velocity dispersion, *right:* tangential velocity dispersion). The different colors show the measurements in 7 different radial bins. The dashed line shows the best fit of the mass dependence using the classical η parametrization. In the middle row, we show the numerical values of the fit results and in the bottom row, we show the radial behavior of the energy equipartition parameter. For both spatial directions, we can observe a decrease in the degree of energy equipartition with radius, indicated by a lower value of the parameter η. This trend is stronger for the radial component than for the tangential component.

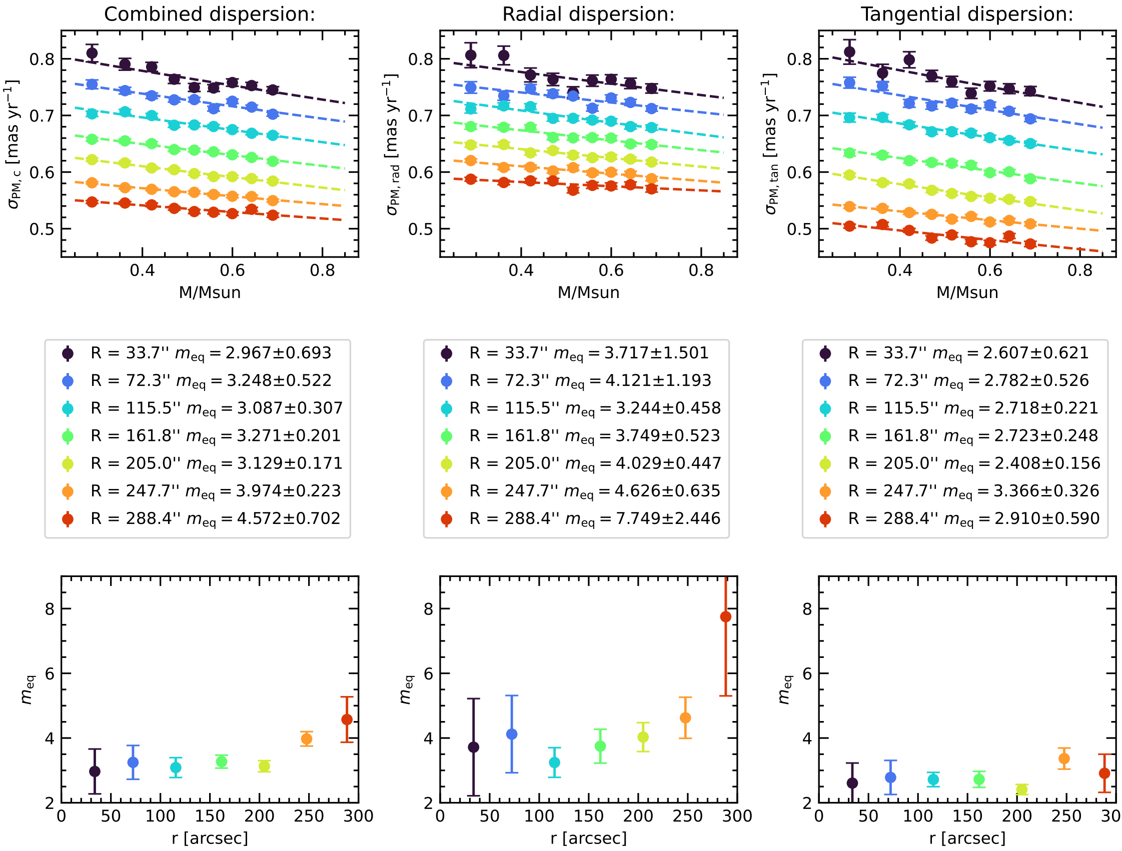

Figure 5.17: This Figure is equivalent to Figure 5.16 and compares the spatial variability of the degree of energy equipartition for the different components of the proper motion. Instead of the η parameter, we use the energy equipartition mass ($m_{\rm eq}$) parametrization (Bianchini et al., 2016) to quantify the degree of energy equipartition. A lower value of $m_{\rm eq}$ indicates a higher degree of energy equipartition.

5.7 SUMMARY AND CONCLUSIONS

We present a study of several basic kinematic properties of the massive globular cluster ω Cen based on the new spectroscopic and astro-photometric oMEGACat catalogs (Paper I; Paper II). Due to the enhanced radial coverage and precision of these catalogs and the unique 3-dimensional combination of plane-of-sky proper motions and spectroscopically measured line-of-sight velocities, our analysis significantly improves the kinematic picture of ω Cen and can serve as input for future modeling efforts. We can summarize our analysis as follows:

- We determine dispersion profiles with better errors and higher resolution and a range covering 1”- 300”, reaching the half-light radius of the cluster. The dispersion profiles show a smooth behavior, with a moderate increase towards the centermost region. We also study the anisotropy of the velocity dispersion field. In the inner region ($r < 30''$), the velocity distribution is isotropic; at larger radii, it starts to become increasingly radially anisotropic, reaching $\sigma_{\mathrm{PM,tan}}/\sigma_{\mathrm{PM,rad}} = 0.0849 \pm 0.003$ at the half-light radius.

- Beside the 1-dimensional profiles, we also calculate 2-dimensional velocity dispersion maps. Fitting these maps with a smooth Gaussian model allows us to recover the ellipticity of the velocity field, the position angle, and the kinematic center (which is in agreement with the photometric center derived in Anderson & van der Marel 2010).

- The line-of-sight velocities cover a smaller range in magnitudes but allow us to directly study the rotation curve of the cluster. At small radii ($r \leq$30”) we can recover the counter-rotating signal described in Pechetti et al. 2024 (however, with lower significance, as our spectroscopic sample is limited to brighter magnitudes). Outside this region, there is a continuous increase of the rotation curve until it converges to a value of around 7 km s^{-1} at $r \approx$150”. This is consistent with findings from the plane of sky rotation (Häberle et al., 2024b). The line-of-sight velocity dispersion profile shows a monotonic increase towards the center. A comparison with the proper motion dispersion profile yields consistent results. By calculating the ratio between the two, we can obtain a kinematic distance estimate of (5445±41) pc, the most precise distance estimate derived for ω Cen and in good agreement with previous results in Baumgardt & Vasiliev (2021).

- We split our sample into four metallicity quartiles and searched for variations of the kinematics with metallicity. We do not find metallicity-dependent variations in any of our velocity directions (radial proper motions, tangential proper motions, line-of-sight velocities.). We note, however, that we had to significantly restrict the data set to a smaller subset of 6,193 stars. In principle, the large number of stars with proper motions and precise photometry should enable the search for more subtle variations that were not detectable with the used subset.

- The precise proper motion measurements down to faint magnitudes allow us to study the state of energy equipartition of the cluster for stars with a wide range of masses (0.288 $M_\odot$ to 0.690 $M_\odot$). We measure a low degree of energy equipartition in the cluster center ($\eta = 0.088 \pm 0.017$)

that decreases further towards larger radii. Interestingly, the radial component of the energy equipartition shows a much quicker decrease with radius than the tangential component, whose profile is relatively shallow.

- Our kinematic profiles and maps are made public along with the paper in the following archive: https://www.dropbox.com/scl/fo/xwea9e65oowd71qx6grmf/AOAJEeg45zkDChyR3l6D2EE?rlkey=kdhkvrjxfbg8xla1ytzdi207j&st=m2l6y8tz&dl=0
  Note: This is just a preliminary link, once the paper has been accepted for publication I will save the final version of the data products in a permanent Zenodo repository
  A description of the data products and tabular versions of the kinematic profiles are given in Section 5.8.

The next step for a better understanding of the dynamics of ω Cen will be to fit dynamical models to the kinematic data (Pechetti et al. in prep.; Smith et al. in prep.). Our rich data set, which allowed us to accurately measure many peculiar features of ω Cen such as rotation, flattening, anisotropy, partial energy equipartition, and fast-moving central stars, poses both a challenge and an opportunity for all future modeling efforts. While our data covers the region within the half-light radius, it can be complemented with proper motion measurements obtained with the HST at larger distances from the cluster center (Bellini et al., 2018b; Scalco et al., 2024) and data from the ESA Gaia mission (Gaia Collaboration et al., 2023c), in addition, there are collections of individual radial velocities at large radii obtained with multi-object spectrographs (see Baumgardt & Hilker, 2018).

SOFTWARE

astropy (Astropy Collaboration et al., 2022), matplotlib (Hunter, 2007), numpy (Harris et al., 2020), scipy (Virtanen et al., 2020), IPython (Perez & Granger, 2007), emcee (Foreman-Mackey et al., 2013a), VorBin (Cappellari & Copin, 2003)

ACKNOWLEDGEMENTS

ACS acknowledges support from Hubble Space Telescope grant GO-16777. MH thanks Francisco Aros for useful suggestions that improved the manuscript. AFK acknowledges funding from the Austrian Science Fund (FWF) [grant DOI 10.55776/ESP542].

5.8 APPENDIX: DATA PRODUCTS

One of the main purposes of this work is to provide the community with a state-of-the-art kinematic analysis of the inner regions of ω Cen using the novel oMEGACat data, that can be used to dynamically model the cluster. Therefore, we publish the following data-products along with the paper. The data can be accessed using the following link:
https://www.dropbox.com/scl/fo/xwea9e65oowd71qx6grmf/AOAJEeg45zkDChyR3l6D2EE?rlkey=kdhkvrjxfbg8xla1ytzdi207j&st=m2l6y8tz&dl=0
Note: This is just a preliminary link, once the paper has been accepted for publication I will save the final version of the data products in a permanent Zenodo repository. All files are provided both as fits tables (file ending: `*.fits`) and as machine-readable textfiles (file ending: `*.dat`). The following files are contained in the archive:

- IPython Notebook containing examples on how to read and plot the different data products
  - `data_products_demonstration_and_test.ipynb`
- Proper Motion dispersion profiles (combined, radial, tangential) using different binning schemes
  - Adaptive logarithmic bins: `proper_motion_dispersion_log_bins.fits` (see also Table 5.2)
  - Linear bins: `proper_motion_dispersion_lin_bins.fits`
  - Equal number bins: `proper_motion_dispersion_equaln_bins.fits`
- LOS profiles (rotation, dispersion, position angle)
  - `los_profile.fits` (see also Table 5.3)
- Kinematic maps
  - Proper motion dispersion measurements: `proper_motion_dispersion_voronoi_bins.fits`
  - Line-of-sight mean velocity and disperison measurements: `los_dispersion_and_rotation_voronoi_bins.fits`
- A set of selections that can be applied to the catalog to obtain the high quality subsample that we have used for our analysis:
  - `catalog_and_selections.fits`
    This file contains the selections and for convenience also various other columns taken from the oMEGACat catalogs. A description of the content is given in Table 5.1.

Table 5.1: Content of the catalog and selection file

Column	Description	Unit
`ID`	oMEGACat II Identifier; same as in Paper II (Häberle et al., 2024b)	-
`RA`	Right Ascension α; Paper II	degree
`DEC`	Declination δ; Paper II	degree
`x`	x coordinate in pixel based coordinate system; Paper II	40 mas ($\sim$ 1 WFC3/UVIS pixel)
`y`	y coordinate in pixel based coordinate system; Paper II	40 mas ($\sim$ 1 WFC3/UVIS pixel)
`pmra_corrected`	Locally corrected proper motion in R.A. direction; Paper II	mas yr^{-1}
`pmdec_corrected`	Locally corrected proper motion in Dec. direction; Paper II	mas yr^{-1}
`pmra_corrected_err`	Error on locally corrected proper motion in R.A. direction; Paper II	mas yr^{-1}
`pmdec_corrected_err`	Error on locally corrected proper motion in Dec. direction; Paper II	mas yr^{-1}
`vlos`	Line-of-sight velocity; Paper I	km s^{-1}
`vlos_err`	Error on line-of-sight velocity; Paper I	km s^{-1}
`f625w`	Magnitude in the F625W filter (diff. red. corrected); Paper II	-
`f814w`	Magnitude in the F814W filter (diff. red. corrected); Paper II	-
`nitschai_id`	ID in *oMEGACat I* MUSE spectroscopic catalog (Nitschai et al., 2023)	-
`voronoi_bin_ids_pm`	Attribution to Voronoi bins in proper motion based kinematic maps	-
`voronoi_bin_ids_los`	Attribution to Voronoi bins in line-of-sight based kinematic maps	-
`selection_hq_f625w`	High quality flag for F625W photometry	-
`selection_hq_f814w`	High quality flag for F814W photometry	-
`selection_hq_astrometry`	High quality flag for astrometry	-
`selection_hq_astrometry_and_membership`	Combined criteria for proper motion quality and cluster membership (CMD and vector-point diagram selections). This is the sample used for the proper motion-based analysis.	-
`selection_hq_los`	High quality flag for line-of-sight velocity measurements	-
`selection_hq_pm_and_los`	Combined proper motion and line-of-sight velocity flag. This is the sample used for the line-of-sight velocity based analysis.	-

5.9 APPENDIX: PLOTS DESCRIBING THE SELECTIONS

Several cuts in astrometric and photometric quality parameters were used to restrict the full oMEGACat II catalog to a subsample of reliable proper motion measurements (see also Section 5.2). Figure 5.18 shows the overall distributions and thresholds for the parameters used for the astrometric selection. Figure 5.19 shows magnitude-dependent photometric quantities (quality-of-fit parameter QFIT, relative flux value of neighboring sources) and the spatial distribution of photometrically well-measured sources.

5.10 APPENDIX: COMPARISON OF KINEMATIC DISTANCE ESTIMATES

Our new kinematic distance estimate for ω Cen is $d = (5445 \pm 41)$ pc. In Table 5.4 we compare it with several other recent distance estimates, for which there is overall good agreement. We refer to Baumgardt & Vasiliev (2021) for a more extensive discussion of previous distance measurements to ω Cen.

Table 5.2: Tabular version of proper motion dispersion profile. We also show physical velocity values, converted using our kinematic distance estimate of 5445 pc.

r_{lower}	r_{median}	r_{upper}	N_{Stars}	$\sigma_{\mathrm{PM,c}}$	$\sigma_{\mathrm{PM,rad}}$	$\sigma_{\mathrm{PM,tan}}$	$\sigma_{\mathrm{PM,c}}$	$\sigma_{\mathrm{PM,rad}}$	$\sigma_{\mathrm{PM,tan}}$	Anisotropy $\sigma_{\mathrm{rad}}/\sigma_{\mathrm{tan}}$
[arcsec]	[arcsec]	[arcsec]	-	[$\mathrm{mas\,yr^{-1}}$]	[$\mathrm{mas\,yr^{-1}}$]	[$\mathrm{mas\,yr^{-1}}$]	[$\mathrm{km\,s^{-1}}$]	[$\mathrm{km\,s^{-1}}$]	[$\mathrm{km\,s^{-1}}$]	-
0.00	1.82	2.68	100	$0.793^{+0.038}_{-0.037}$	$0.840^{+0.060}_{-0.062}$	$0.755^{+0.059}_{-0.048}$	$20.48^{+0.99}_{-0.95}$	$21.69^{+1.54}_{-1.60}$	$19.51^{+1.51}_{-1.23}$	0.899±0.091
2.68	3.33	3.78	100	$0.812^{+0.041}_{-0.040}$	$0.813^{+0.060}_{-0.060}$	$0.841^{+0.066}_{-0.050}$	$20.97^{+1.06}_{-1.04}$	$21.00^{+1.55}_{-1.54}$	$21.73^{+1.70}_{-1.29}$	1.035±0.104
3.78	4.24	4.67	101	$0.798^{+0.042}_{-0.037}$	$0.818^{+0.059}_{-0.054}$	$0.792^{+0.055}_{-0.050}$	$20.61^{+1.08}_{-0.96}$	$21.12^{+1.53}_{-1.40}$	$20.45^{+1.43}_{-1.30}$	0.969±0.093
4.67	5.00	5.34	101	$0.885^{+0.051}_{-0.039}$	$0.856^{+0.066}_{-0.053}$	$0.925^{+0.079}_{-0.070}$	$22.86^{+1.32}_{-1.01}$	$22.12^{+1.71}_{-1.38}$	$23.88^{+2.03}_{-1.81}$	1.080±0.115
5.34	5.66	5.99	109	$0.851^{+0.036}_{-0.043}$	$0.894^{+0.063}_{-0.060}$	$0.820^{+0.058}_{-0.049}$	$21.99^{+0.94}_{-1.11}$	$23.09^{+1.63}_{-1.55}$	$21.18^{+1.50}_{-1.27}$	0.917±0.087
5.99	6.36	6.72	137	$0.832^{+0.040}_{-0.036}$	$0.821^{+0.055}_{-0.048}$	$0.836^{+0.049}_{-0.044}$	$21.50^{+1.02}_{-0.93}$	$21.21^{+1.42}_{-1.25}$	$21.60^{+1.25}_{-1.14}$	1.018±0.085
6.72	7.13	7.54	147	$0.768^{+0.032}_{-0.026}$	$0.800^{+0.046}_{-0.045}$	$0.734^{+0.053}_{-0.040}$	$19.83^{+0.82}_{-0.68}$	$20.66^{+1.20}_{-1.16}$	$18.97^{+1.37}_{-1.02}$	0.918±0.078
7.54	8.00	8.46	204	$0.792^{+0.028}_{-0.031}$	$0.747^{+0.036}_{-0.037}$	$0.830^{+0.044}_{-0.041}$	$20.45^{+0.72}_{-0.80}$	$19.29^{+0.93}_{-0.96}$	$21.44^{+1.14}_{-1.07}$	1.112±0.079
8.46	9.05	9.50	227	$0.769^{+0.024}_{-0.025}$	$0.775^{+0.036}_{-0.036}$	$0.763^{+0.042}_{-0.032}$	$19.87^{+0.62}_{-0.64}$	$20.03^{+0.93}_{-0.93}$	$19.71^{+1.08}_{-0.82}$	0.984±0.066
9.50	10.04	10.65	271	$0.796^{+0.023}_{-0.021}$	$0.799^{+0.043}_{-0.034}$	$0.796^{+0.037}_{-0.036}$	$20.56^{+0.59}_{-0.55}$	$20.63^{+1.12}_{-0.88}$	$20.56^{+0.95}_{-0.93}$	0.997±0.066
10.65	11.29	11.95	363	$0.763^{+0.019}_{-0.020}$	$0.794^{+0.032}_{-0.029}$	$0.738^{+0.030}_{-0.026}$	$19.72^{+0.50}_{-0.51}$	$20.51^{+0.83}_{-0.75}$	$19.05^{+0.77}_{-0.67}$	0.929±0.050
11.95	12.70	13.41	419	$0.767^{+0.020}_{-0.018}$	$0.757^{+0.026}_{-0.021}$	$0.779^{+0.030}_{-0.026}$	$19.82^{+0.53}_{-0.45}$	$19.54^{+0.68}_{-0.54}$	$20.11^{+0.77}_{-0.67}$	1.029±0.049
13.41	14.26	15.05	540	$0.775^{+0.016}_{-0.016}$	$0.795^{+0.024}_{-0.026}$	$0.768^{+0.024}_{-0.020}$	$20.02^{+0.43}_{-0.43}$	$20.53^{+0.63}_{-0.67}$	$19.84^{+0.63}_{-0.52}$	0.966±0.041
15.05	16.00	16.88	720	$0.775^{+0.015}_{-0.013}$	$0.789^{+0.022}_{-0.020}$	$0.764^{+0.017}_{-0.022}$	$20.02^{+0.40}_{-0.34}$	$20.38^{+0.56}_{-0.51}$	$19.74^{+0.43}_{-0.57}$	0.969±0.036
16.88	18.03	18.94	821	$0.778^{+0.015}_{-0.013}$	$0.789^{+0.018}_{-0.017}$	$0.766^{+0.018}_{-0.017}$	$20.09^{+0.38}_{-0.34}$	$20.39^{+0.48}_{-0.45}$	$19.79^{+0.46}_{-0.45}$	0.971±0.031
18.94	20.16	21.25	1099	$0.776^{+0.012}_{-0.011}$	$0.783^{+0.015}_{-0.017}$	$0.769^{+0.016}_{-0.014}$	$20.06^{+0.30}_{-0.29}$	$20.23^{+0.39}_{-0.43}$	$19.87^{+0.41}_{-0.35}$	0.982±0.027
21.25	22.62	23.85	1426	$0.756^{+0.010}_{-0.009}$	$0.763^{+0.015}_{-0.016}$	$0.750^{+0.014}_{-0.015}$	$19.52^{+0.25}_{-0.23}$	$19.70^{+0.40}_{-0.41}$	$19.37^{+0.35}_{-0.38}$	0.983±0.028
23.85	25.28	26.76	1779	$0.767^{+0.010}_{-0.009}$	$0.771^{+0.013}_{-0.012}$	$0.764^{+0.013}_{-0.012}$	$19.82^{+0.25}_{-0.24}$	$19.93^{+0.33}_{-0.31}$	$19.73^{+0.33}_{-0.32}$	0.990±0.023
26.76	28.43	30.02	2299	$0.748^{+0.008}_{-0.007}$	$0.738^{+0.013}_{-0.010}$	$0.757^{+0.012}_{-0.011}$	$19.33^{+0.20}_{-0.18}$	$19.05^{+0.34}_{-0.25}$	$19.55^{+0.30}_{-0.28}$	1.026±0.022
30.02	31.95	33.68	2912	$0.764^{+0.008}_{-0.007}$	$0.761^{+0.011}_{-0.009}$	$0.767^{+0.011}_{-0.009}$	$19.72^{+0.21}_{-0.18}$	$19.65^{+0.29}_{-0.23}$	$19.80^{+0.28}_{-0.23}$	1.008±0.019
33.68	35.81	37.79	3587	$0.758^{+0.006}_{-0.006}$	$0.754^{+0.008}_{-0.009}$	$0.765^{+0.008}_{-0.010}$	$19.57^{+0.17}_{-0.15}$	$19.47^{+0.20}_{-0.24}$	$19.75^{+0.22}_{-0.26}$	1.014±0.017
37.79	40.17	42.40	4709	$0.741^{+0.005}_{-0.005}$	$0.745^{+0.009}_{-0.008}$	$0.736^{+0.008}_{-0.007}$	$19.14^{+0.13}_{-0.14}$	$19.23^{+0.24}_{-0.21}$	$19.01^{+0.22}_{-0.17}$	0.989±0.015
42.40	45.04	47.58	5591	$0.737^{+0.005}_{-0.005}$	$0.744^{+0.006}_{-0.008}$	$0.732^{+0.008}_{-0.007}$	$19.04^{+0.14}_{-0.12}$	$19.23^{+0.17}_{-0.20}$	$18.90^{+0.20}_{-0.17}$	0.983±0.013
47.58	50.58	53.38	6940	$0.740^{+0.005}_{-0.004}$	$0.745^{+0.006}_{-0.006}$	$0.735^{+0.006}_{-0.006}$	$19.11^{+0.12}_{-0.11}$	$19.25^{+0.16}_{-0.16}$	$18.97^{+0.16}_{-0.16}$	0.986±0.012
53.38	56.70	59.89	9066	$0.735^{+0.004}_{-0.003}$	$0.740^{+0.005}_{-0.005}$	$0.732^{+0.006}_{-0.006}$	$18.98^{+0.11}_{-0.09}$	$19.12^{+0.14}_{-0.14}$	$18.90^{+0.15}_{-0.14}$	0.988±0.010
59.89	63.58	67.20	10920	$0.725^{+0.003}_{-0.003}$	$0.731^{+0.005}_{-0.005}$	$0.719^{+0.005}_{-0.005}$	$18.73^{+0.09}_{-0.09}$	$18.87^{+0.13}_{-0.14}$	$18.58^{+0.14}_{-0.12}$	0.985±0.010
67.20	71.42	75.40	13445	$0.724^{+0.003}_{-0.003}$	$0.728^{+0.004}_{-0.005}$	$0.720^{+0.004}_{-0.004}$	$18.70^{+0.07}_{-0.08}$	$18.79^{+0.11}_{-0.12}$	$18.60^{+0.09}_{-0.11}$	0.990±0.008
75.40	80.09	84.60	16942	$0.712^{+0.003}_{-0.002}$	$0.721^{+0.003}_{-0.004}$	$0.704^{+0.004}_{-0.004}$	$18.40^{+0.07}_{-0.06}$	$18.63^{+0.09}_{-0.10}$	$18.17^{+0.10}_{-0.10}$	0.975±0.007
84.60	89.93	94.93	20309	$0.705^{+0.002}_{-0.003}$	$0.711^{+0.003}_{-0.003}$	$0.698^{+0.003}_{-0.003}$	$18.21^{+0.06}_{-0.07}$	$18.37^{+0.08}_{-0.08}$	$18.02^{+0.09}_{-0.08}$	0.981±0.006
94.93	100.73	106.51	23917	$0.692^{+0.002}_{-0.002}$	$0.702^{+0.003}_{-0.003}$	$0.681^{+0.003}_{-0.003}$	$17.86^{+0.05}_{-0.06}$	$18.13^{+0.08}_{-0.08}$	$17.60^{+0.07}_{-0.08}$	0.971±0.006
106.51	112.97	119.50	27379	$0.682^{+0.002}_{-0.002}$	$0.694^{+0.003}_{-0.003}$	$0.671^{+0.003}_{-0.002}$	$17.61^{+0.06}_{-0.04}$	$17.92^{+0.07}_{-0.08}$	$17.33^{+0.07}_{-0.06}$	0.967±0.006
119.50	126.76	134.09	30196	$0.669^{+0.002}_{-0.002}$	$0.686^{+0.003}_{-0.003}$	$0.652^{+0.003}_{-0.003}$	$17.28^{+0.05}_{-0.04}$	$17.71^{+0.07}_{-0.07}$	$16.85^{+0.07}_{-0.07}$	0.952±0.005
134.09	142.43	150.45	34236	$0.655^{+0.002}_{-0.002}$	$0.678^{+0.003}_{-0.002}$	$0.629^{+0.003}_{-0.002}$	$16.91^{+0.04}_{-0.05}$	$17.52^{+0.07}_{-0.06}$	$16.26^{+0.07}_{-0.06}$	0.928±0.005
150.45	160.11	168.80	43889	$0.636^{+0.001}_{-0.001}$	$0.662^{+0.002}_{-0.002}$	$0.610^{+0.002}_{-0.002}$	$16.44^{+0.04}_{-0.04}$	$17.10^{+0.06}_{-0.06}$	$15.75^{+0.06}_{-0.05}$	0.921±0.004
168.80	179.11	189.40	54408	$0.621^{+0.001}_{-0.001}$	$0.647^{+0.002}_{-0.002}$	$0.593^{+0.002}_{-0.002}$	$16.04^{+0.04}_{-0.03}$	$16.71^{+0.05}_{-0.05}$	$15.33^{+0.05}_{-0.04}$	0.917±0.004
189.40	201.15	212.51	61707	$0.601^{+0.001}_{-0.001}$	$0.634^{+0.002}_{-0.002}$	$0.565^{+0.002}_{-0.002}$	$15.52^{+0.03}_{-0.03}$	$16.37^{+0.05}_{-0.04}$	$14.60^{+0.05}_{-0.04}$	0.892±0.004
212.51	225.54	238.44	71611	$0.584^{+0.001}_{-0.001}$	$0.619^{+0.002}_{-0.002}$	$0.546^{+0.001}_{-0.002}$	$15.07^{+0.03}_{-0.03}$	$15.98^{+0.04}_{-0.04}$	$14.11^{+0.04}_{-0.04}$	0.882±0.003
238.44	252.36	267.54	78997	$0.562^{+0.001}_{-0.001}$	$0.602^{+0.002}_{-0.002}$	$0.519^{+0.001}_{-0.001}$	$14.51^{+0.02}_{-0.03}$	$15.54^{+0.04}_{-0.04}$	$13.40^{+0.04}_{-0.03}$	0.862±0.003
267.54	280.94	300.18	60637	$0.544^{+0.001}_{-0.001}$	$0.586^{+0.002}_{-0.001}$	$0.497^{+0.001}_{-0.001}$	$14.04^{+0.03}_{-0.03}$	$15.13^{+0.04}_{-0.04}$	$12.85^{+0.03}_{-0.04}$	0.849±0.003
300.18	311.12	346.07	18485	$0.520^{+0.002}_{-0.002}$	$0.562^{+0.003}_{-0.003}$	$0.474^{+0.003}_{-0.002}$	$13.42^{+0.05}_{-0.05}$	$14.53^{+0.07}_{-0.08}$	$12.25^{+0.07}_{-0.06}$	0.843±0.006

Table 5.3: Tabular version of line-of-sight (LOS) dispersion profile.

r_{lower} [arcsec]	r_{median} [arcsec]	r_{upper} [arcsec]	N_{Stars} -	v_{LOS} [km s^{-1}]	σ_{LOS} [km s^{-1}]	θ_0 [degree]
0.00	5.66	7.90	50	$10.3^{+5.1}_{-4.8}$	$20.9^{+2.5}_{-1.9}$	$-135.8^{+21.2}_{-20.9}$
7.90	9.41	11.35	50	$4.7^{+3.3}_{-3.9}$	$19.0^{+2.1}_{-2.0}$	$-169.7^{+50.5}_{-46.4}$
11.35	13.41	14.51	50	$8.3^{+4.0}_{-4.0}$	$21.0^{+2.3}_{-1.9}$	$175.6^{+26.9}_{-32.4}$
14.51	16.09	17.08	51	$10.0^{+4.4}_{-4.7}$	$20.4^{+2.6}_{-1.7}$	$41.2^{+21.7}_{-23.9}$
17.08	18.68	19.68	51	$8.2^{+3.9}_{-3.7}$	$17.9^{+1.8}_{-1.7}$	$116.9^{+24.4}_{-29.1}$
19.68	20.91	22.09	64	$5.9^{+2.9}_{-3.3}$	$18.0^{+1.7}_{-1.6}$	$74.6^{+35.2}_{-32.6}$
22.09	23.55	24.78	92	$0.8^{+2.6}_{-3.1}$	$20.9^{+2.1}_{-1.7}$	$-12.1^{+99.1}_{-113.5}$
24.78	26.31	27.79	137	$3.1^{+2.9}_{-2.5}$	$21.4^{+1.5}_{-1.3}$	$36.9^{+45.3}_{-50.7}$
27.79	29.52	31.17	119	$3.2^{+2.4}_{-2.5}$	$18.4^{+1.4}_{-1.2}$	$79.5^{+42.9}_{-37.9}$
31.17	33.24	34.98	179	$1.6^{+2.0}_{-1.9}$	$18.4^{+0.9}_{-0.8}$	$-128.4^{+59.4}_{-72.9}$
34.98	37.15	39.26	224	$4.6^{+1.9}_{-1.4}$	$18.3^{+0.9}_{-0.9}$	$116.4^{+20.7}_{-21.8}$
39.26	41.55	44.05	282	$2.5^{+1.5}_{-1.4}$	$19.1^{+0.9}_{-0.8}$	$73.8^{+37.1}_{-38.4}$
44.05	46.97	49.43	359	$3.8^{+1.2}_{-1.4}$	$18.6^{+0.6}_{-0.6}$	$101.7^{+25.0}_{-21.7}$
49.43	52.60	55.47	457	$3.9^{+1.2}_{-1.1}$	$17.6^{+0.5}_{-0.6}$	$122.4^{+16.1}_{-16.5}$
55.47	58.79	62.26	590	$2.6^{+1.0}_{-1.2}$	$19.6^{+0.6}_{-0.6}$	$71.0^{+26.2}_{-27.7}$
62.26	66.08	69.86	591	$4.4^{+1.0}_{-1.0}$	$18.4^{+0.6}_{-0.6}$	$115.8^{+12.6}_{-16.5}$
69.86	74.29	78.39	766	$4.3^{+0.9}_{-0.8}$	$18.4^{+0.5}_{-0.5}$	$86.1^{+13.2}_{-12.5}$
78.39	83.43	87.95	903	$4.4^{+0.8}_{-0.8}$	$18.8^{+0.5}_{-0.4}$	$92.1^{+11.3}_{-14.7}$
87.95	93.34	98.68	1107	$4.3^{+0.7}_{-0.7}$	$17.2^{+0.4}_{-0.3}$	$99.5^{+9.4}_{-11.4}$
98.68	104.57	110.72	1291	$5.0^{+0.7}_{-0.8}$	$17.8^{+0.3}_{-0.4}$	$107.6^{+8.1}_{-8.8}$
110.72	117.26	124.24	1239	$4.8^{+0.8}_{-0.7}$	$17.1^{+0.3}_{-0.3}$	$92.1^{+8.5}_{-9.5}$
124.24	131.59	139.40	1274	$5.4^{+0.6}_{-0.7}$	$17.3^{+0.4}_{-0.4}$	$94.8^{+7.4}_{-7.3}$
139.40	148.36	156.42	1755	$6.6^{+0.5}_{-0.4}$	$16.4^{+0.3}_{-0.3}$	$98.3^{+5.4}_{-5.1}$
156.42	166.17	175.50	2098	$6.8^{+0.5}_{-0.5}$	$15.9^{+0.2}_{-0.2}$	$110.0^{+4.3}_{-4.6}$
175.50	186.00	196.92	2358	$7.0^{+0.5}_{-0.5}$	$15.5^{+0.2}_{-0.3}$	$109.4^{+3.4}_{-3.5}$
196.92	208.94	220.95	2453	$6.4^{+0.4}_{-0.4}$	$14.6^{+0.2}_{-0.2}$	$100.9^{+4.0}_{-3.6}$
220.95	234.05	247.90	2662	$6.1^{+0.4}_{-0.4}$	$14.2^{+0.2}_{-0.2}$	$103.4^{+3.9}_{-4.0}$
247.90	261.11	278.14	2401	$6.6^{+0.3}_{-0.3}$	$13.7^{+0.2}_{-0.2}$	$105.9^{+3.8}_{-3.7}$
278.14	290.28	332.28	1275	$6.6^{+0.5}_{-0.4}$	$12.5^{+0.2}_{-0.3}$	$106.8^{+5.4}_{-4.1}$

Table 5.4: Comparison of our new kinematic distance estimate with various recent literature estimates.

Distance	Data and Method	Reference
(5445±41) pc	**oMEGACat, kin. dist.**	**This work**
(5240±110) pc	Gaia EDR3, parallax	Soltis et al. (2021)
(5480±240) pc	Gaia EDR3, parallax	Baumgardt & Vasiliev (2021)
(5359±141) pc	Gaia EDR3, kin. dist.	Baumgardt & Vasiliev (2021)
(5260±120) pc	HST, kin. dist.	Baumgardt & Vasiliev (2021)

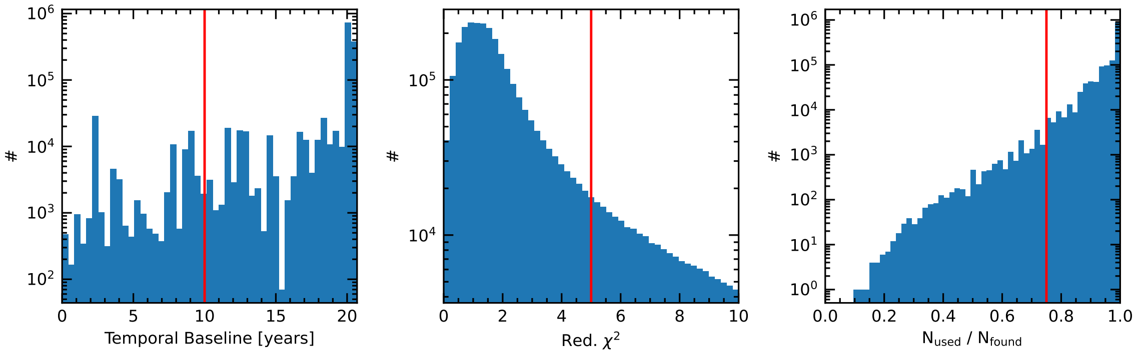

Figure 5.18: Histograms and thresholds of the astrometric quality parameters used to define the high-quality subsample of reliable proper motion measurements. *Left:* Temporal baseline used for proper motion determination, *Center:* Reduced χ^2 value of the linear fit to the astrometric data used to determine the proper motions. *Right:* Fraction of used measurements for the proper motion fit. A low value indicates unreliable astrometry.

5.11 APPENDIX: VARIATION OF BINNING SCHEMES

5.11.1 RADII OF CIRCULAR BINS

Traditionally, the velocity dispersion has been measured in circular radial bins. The choice of the bin radii is ultimately arbitrary, and with more than 600,000 individual stellar measurements and a large radial range of around 350” several binning schemes are feasible. In Figure 5.21 we explore three different binning options: our first binning choice is an adaptive, logarithmic binning scheme. The stepsize is $\Delta \log r = 0.05$, but we require a minimum number of at least 100 stars per bin. This binning choice has a high resolution in the centermost region while being more coarse in the outer regions. The second explored binning scheme is a simple linear scheme with a bin size of $\Delta r = 2.5''$, naturally maintaining a uniform resolution in both the inner and outer regions. Finally, we explored equally populated bins with a number of $N = 250$ stars per bin. The advantage of this scheme is the uniform uncertainties in all bins. However, the resolution in the center is comparatively low, while the bin density is very large at larger radii. The three binning schemes agree with each other within their uncertainties and we make all profiles publicly available so that the user can choose the scheme most appropriate to their science case. For our further discussions, we use the first adaptive logarithmic binning scheme.

5.11.2 TESTING ELLIPTICAL INSTEAD OF CIRCULAR BINS

The stellar density and the surface-brightness of ω Cen show significant flattening with variable ellipticity that reaches a maximum of $\epsilon = 1 - \frac{b}{a} = 0.16$ at $r = 8'$ and a mean value of $\epsilon = 0.10$ (Geyer et al., 1983; Pancino et al., 2003; Calamida et al., 2020). Therefore, the choice of circular bins might not fully capture the nature of the dispersion profile of the cluster. To determine the ellipticity of the 2D velocity dispersion field we first calculated a dispersion map on a regular grid with a bin size of $5'' \times 5''$. We then symmetrized the map using the photometric Anderson & van der Marel

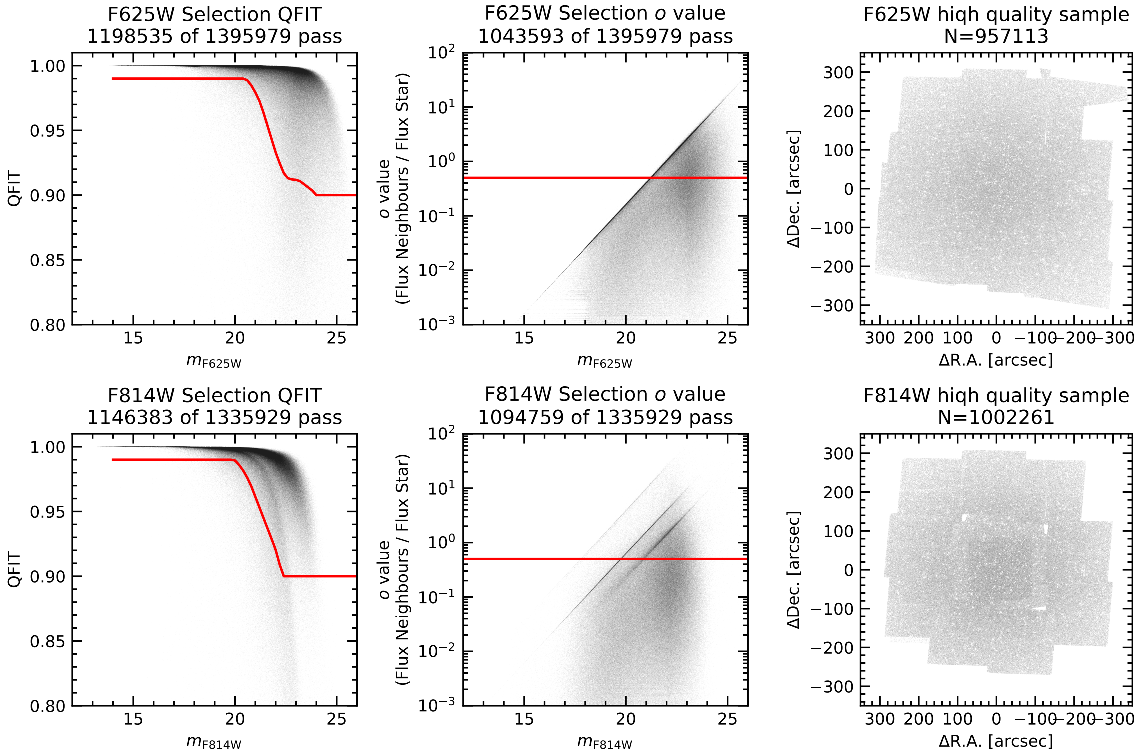

Figure 5.19: Photometric quality selections used to determine a high-quality subset of the data for both the ACS WFC F625W filter (*top*) and the WFC3/UVIS F814W filter (*bottom*). *Left:* Magnitude dependent threshold on the QFIT value that characterizes how well the point-spread-function could be fit to the data. *Center:* o value that characterized the fraction of flux from neighboring sources for each photometric measurement. *Right:* Spatial distribution of well-measured stars. The measurements in the F625W are quite uniformly distributed. The F814W measurements show some spatial dependences and minor gaps, due to the distribution of pointings.

(2010) center as a pivot point to fill in the gaps in the data set (see Figure 5.20, *left*). Then we used the `photutils.isophot` function to fit elliptical “isophots” (or isodispersion contours) to the map. At smaller radii ($r \leq 2'$), the ellipticity and position angle are poorly constrained and show large scatter. At larger radii, the ellipticity converges to a median value of $\epsilon_{\mathrm{disp.}} = 0.12$ with a median position angle of $PA = 108°$ in good agreement with the light distribution and the results of the Gaussian fits (see Figure 5.10). Using these values we calculated the dispersion profile using elliptical bins instead of circular bins but did not find significant differences when comparing bins with the same mean radii.

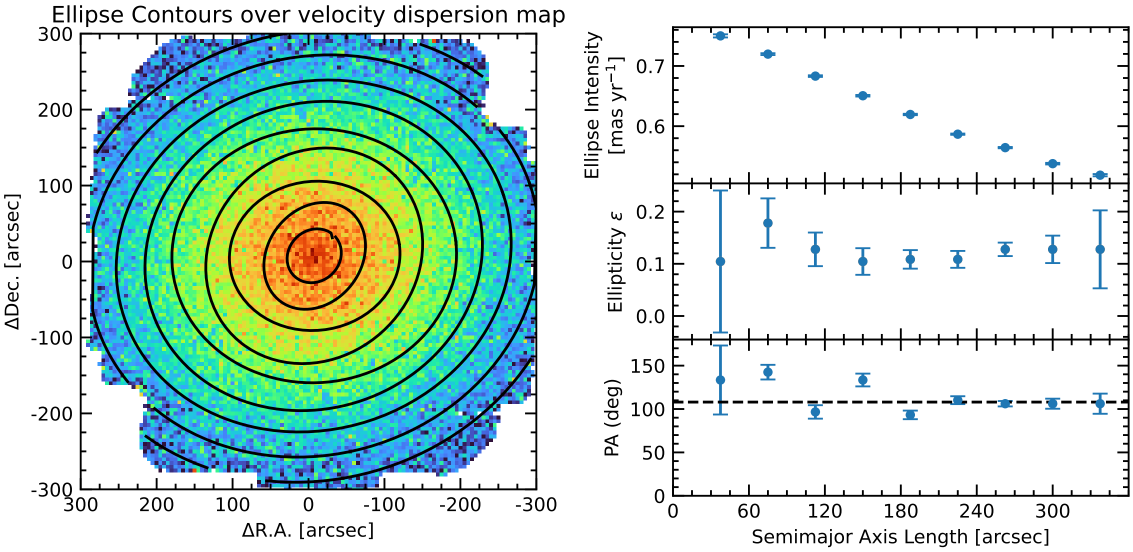

Figure 5.20: Determination of the ellipticity of the velocity field. *Left:* A symmetrized map of the proper motion dispersion determined in $5'' \times 5''$ grid cells. The black ellipses show the isodispersion contours fit with `photutils.isophote`. *Right:* Profiles of the determined ellipse parameters of the isodisperion contours (*top:* dispersion, *middle:* ellipticty, *bottom:* position angle). The median ellipticity is $\epsilon_{\text{disp.}} = 0.12$, the position angle $PA = 108°$.

5.11.2.1 DETERMINATION OF THE ELLIPTICITY OF THE DISPERSION FIELD - FIGURE 5.20

5.11.2.2 COMPARISON OF BINNING SCHEMES - FIGURE 5.21

5.11.3 2D

5.11.3.1 COMPARISON OF VORONOI BINNING SCHEMES WITH DIFFERENT N - FIGURE 5.22

5.11.3.2 COMPARISON BETWEEN VORONOI BINNING AND NEAREST NEIGHBOR SCHEMES

For our kinematic maps, we used a Voronoi binning scheme to separate the data into 2D bins. This offers the advantage of splitting the data into fully independent bins that each contain a similar number of stars and, therefore, yield a similar statistical noise level. Another commonly used method (see, e.g., Pechetti et al. 2024; Nitschai et al. 2024) to derive 2D binned maps in stellar fields is to use a nearest-neighbor scheme to group the stars. In Figure 5.23 we used this scheme to create a kinematic map with the same properties as in Figure 5.9. Overall there is good agreement between the two spatial binning methods. The KNN map shows granularity with a feature size comparable to the size of the Voronoi bins in Figure 5.9, which is set by the search radius necessary to find the required number of neighbors. At small scales, the KNN map has a smoother appearance (as neighboring points share a large part of their star sample); however, this should not be mistaken as better precision. It just means that the uncertainties are correlated on scales smaller than the neighbor search radius.

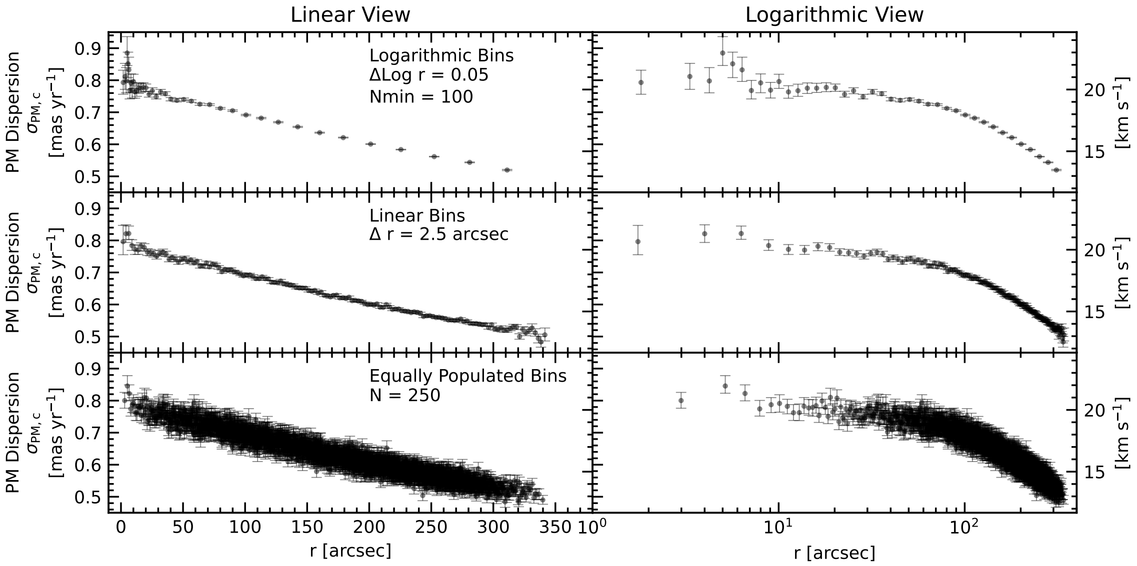

Figure 5.21: Comparison of the total proper motion dispersion profile determined with various binning schemes (*top:* adaptive logarithmic, *middle:* linear/equal radius, *bottom:* equi-populated). The profiles are shown in both linear (*left*) and logarithmic (*right*) scale. The different profiles show overall agreement but differ in resolution and scatter.

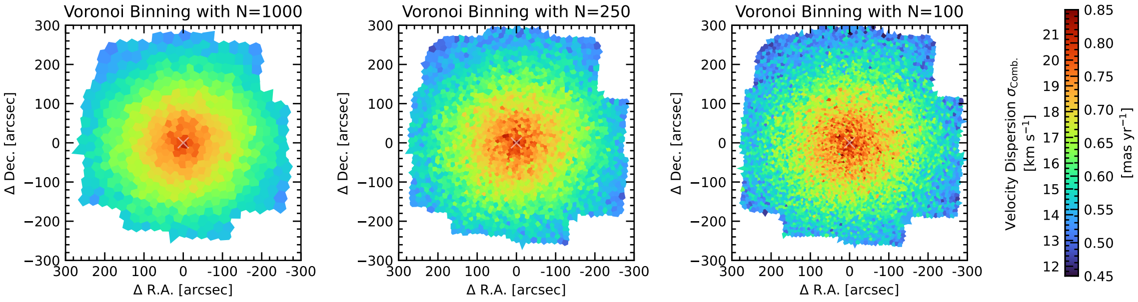

Figure 5.22: Comparison of proper motion dispersion maps using three different Voronoi binning schemes with a different number of measurements per bin. *Left:* $N = 1000$, *Center:* $N = 250$, *Right:* $N = 100$

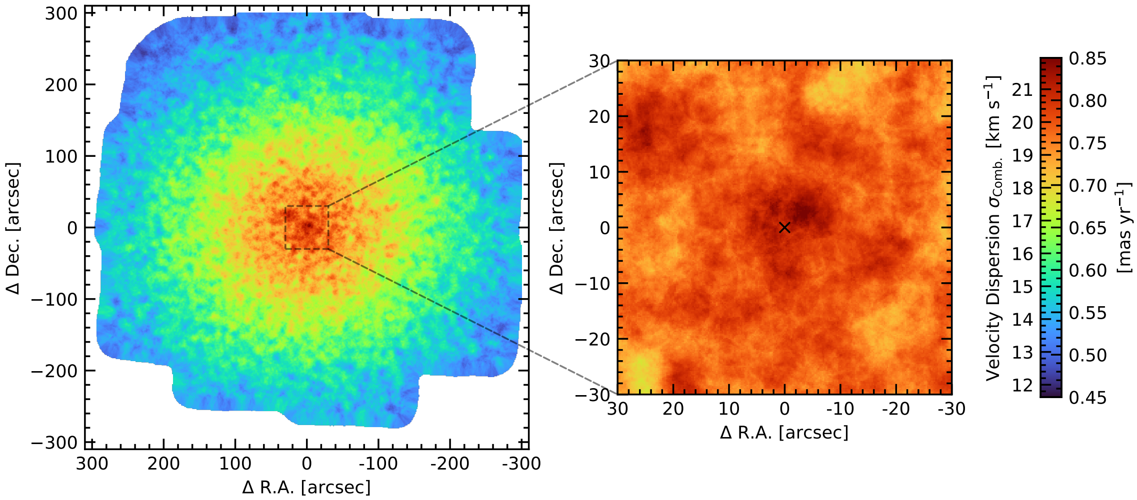

Figure 5.23: A proper motion dispersion map based on a nearest neighbor binning scheme with $N = 250$. This Figure allows to compare the KNN scheme with the Vornoi binning scheme used in Figure 5.9.

6 VALIDATING THE LOCAL VOLUME MAPPER ACQUISITION AND GUIDING HARDWARE

This chapter has been published in Häberle et al. (2022). I built the laboratory setup, conducted the measurements (except the gain and read-noise measurements; these were done by co-author Tom Herbst), and wrote all the text. All co-authors have provided comments on the manuscript and help and advice for the analysis. The formatting has been adapted to match this thesis.

List of co-authors: Thomas M. Herbst, Peter Bizenberger, Guillermo Blanc, Florian Briegel, Niv Drory, Wolfgang Gässler, Nick Konidaris, Kathryn Kreckel, Markus Kuhlberg, Lars Mohr, Eric Pellegrini, Solange Ramirez, Christopher Ritz, Ralf-Rainer Rohloff, Paula Stepień

ABSTRACT

The Local Volume Mapper (LVM) project is one of three surveys that form the Sloan Digital Sky Survey V. It will map the interstellar gas emission in a large fraction of the southern sky using wide-field integral field spectroscopy. Four 16-cm telescopes in siderostat configuration feed the integral field units (IFUs). A reliable acquisition and guiding (A&G) strategy will help ensure that we meet our science goals. Each of the telescopes hosts commercial CMOS cameras used for A&G. In this work, we present our validation of the camera performance. Our tests show that the cameras have a readout noise of around 5.6 e- and a dark current of 21 e-/s, when operated at the ideal gain setting and at an ambient temperature of 20 °C. To ensure their performance at a high-altitude observing site, such as the Las Campanas Observatory, we studied the thermal behaviour of the cameras at different ambient pressures and with different passive cooling solutions. Using the measured properties, we calculated the brightness limit for guiding exposures. With a 5 s exposure time, we reach a depth of $\sim$16.5 Gaia gmag with a signal-to-noise ratio (SNR) > 5. Using Gaia Early Data Release 3, we verified that there are sufficient guide stars for each of the $\sim$25 000 survey pointings. For accurate acquisition, we also need to know the focal plane geometry. We present an approach that combines on-chip astrometry and using a point source microscope to measure the relative positions of the IFU lenslets and the individual CMOS pixels to around 2 µm accuracy.

6.1 INTRODUCTION

The Sloan Digital Sky Survey V (SDSS-V) is an all-sky spectroscopic survey of $<$ 6 million objects, designed to decode the history of the Milky Way, reveal the inner workings of stars, investigate the origin of solar systems, and track the growth of supermassive black holes across the Universe (Kollmeier et al., 2017). The three individual programs within the SDSS-V are the Milky Way Mapper, the Black Hole Mapper, and the Local Volume Mapper (LVM) (Konidaris et al., 2020).

The goal of the LVM project is to map the interstellar gas emission in a large fraction of the southern sky using wide-field integral field spectroscopy. During the $\sim$4.5 years of the survey around 2500 deg^2 of sky will be mapped with a spectral resolution of around R$\sim$ 4000.

To achieve these goals, an entirely new facility is currently under construction at Las Campanas Observatory in Northern Chile. The LVM instrument consists of four 16-cm telescopes (Herbst et al., 2020) in siderostat configuration. Each of the telescopes is equipped with an integral field unit (IFU) that is connected to DESI like spectrographs (Perruchot et al., 2018), that have a spectral resolution of R$\sim$4000 and a wavelength range from 365 nm to 980 nm. One telescope conducts the scientific observations, while two telescopes will observe sky fields for sky-emission calibration, and the final telescope will observe multiple spectro-photometric calibration stars. Herbst et al. (2022) gives an up-to-date overview of the telescope construction and commissioning phase.

6.2 GUIDING AND ACQUISITION CAMERAS

6.2.1 OPTICAL SETUP

The siderostats feed the light to a stable, table-mounted, optical setup (see Figure 6.1). On the optical tables, the light is focused by a d $\sim$16.1 cm, f/11.42 triplet lens[1]. After the lens, the beam is de-rotated by a K-mirror[2], before it reaches the IFU and the guiding system in the focal plane.

6.2.2 FOCAL PLANE DESIGN

There are three slightly different focal plane layouts for the different telescopes. The Science and the Sky telescopes are equipped with 2 A&G-sensors and an IFU in the centre of the focal plane. The science IFU has a hexagonal shape with 1801 microlenses, while the sky IFUs of the Sky telescopes are smaller with 59 and 60 microlenses. The microlenses have a diameter of 315 µm and a spacing of 330 µm.

The Spectrophotometric telescope is equipped with a single A&G sensor and hosts a rotation mask shutter mechanism, that allows illumination of individual fibres. Instead of a fully populated IFU, only 24 fibres are mounted. A schematic of the different layouts appears in Figure 6.2.

---

[1] Lanz et al. (paper 12184-218, this conference) provide a complete description of the objective lens design, manufacturing, and testing.

[2] See Kuhlberg et al. (paper 12184-261, this conference) for details on the K-mirror.

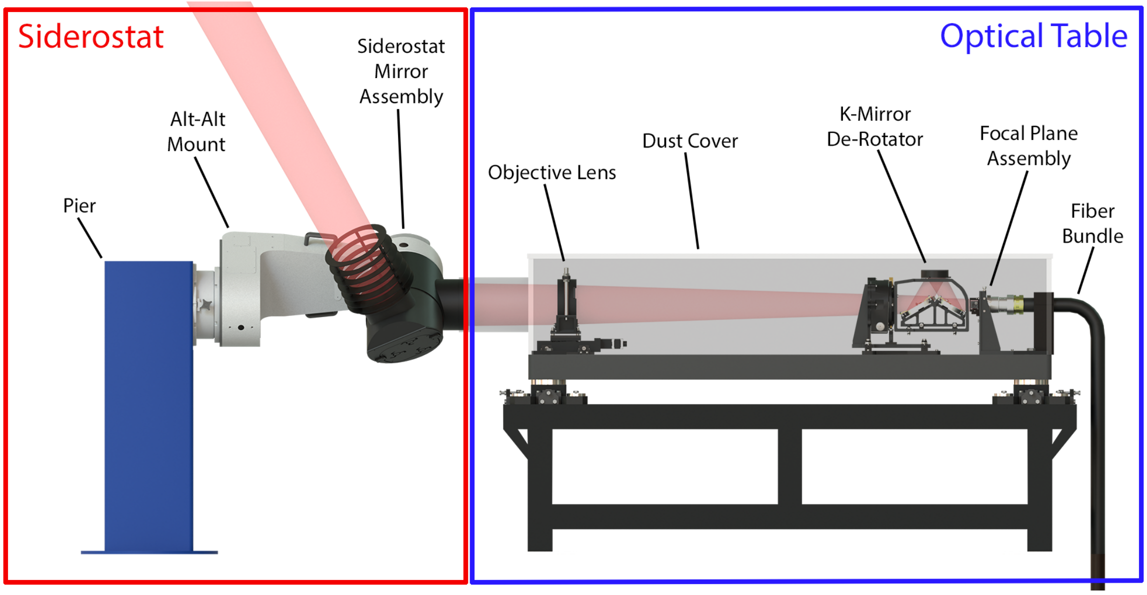

Figure 6.1: Schematic of the table mounted optical setup.

In all cases, the sensors of the A&G cameras are mounted orthogonal to the plane of the fibers, and a 45° mirror reflects the light to the sensors. A test setup that is very similar to the final design appears in Figure 6.2.

6.2.3 Characterisation of the noise properties and the thermal performance of the acquisition and guiding cameras

6.2.3.1 The cameras

In the past, active pixel complementary metal-oxide semiconductor (CMOS) sensors have not been a viable alternative to charge-coupled device (CCD) sensors for astronomical applications, due to higher read-out noise and low quantum efficiency. However, in recent years, new developments and technology improvements have changed this (Janesick et al., 2006, 2013; Jorden et al., 2017) and there are various CMOS high performance devices commercially available.

We use commercial FLIR Blackfly S BFS-PGE-16S7M cameras as A&G cameras. These compact cameras have a GigE interface and use power over Ethernet, which means only a single cable per camera is needed. The cameras are equipped with the *Sony IMX432* CMOS sensor[3]. This monochrome sensor has an effective pixel count of 1608x1104 and a physical size of 14.4 mm x 9.9 mm. The pixel pitch is 9 µm. As these CMOS devices are typically used in non-astronomical applications (such as high-frame rate machine vision), the relevant quantities for photometric applications (read noise, dark current, gain) are not stated on the datasheet. We therefore characterised them in the laboratory.

---

[3] Datasheet: https://www.sony-semicon.co.jp/products/common/pdf/IMX432LLJ_LQJ_Flyer.pdf

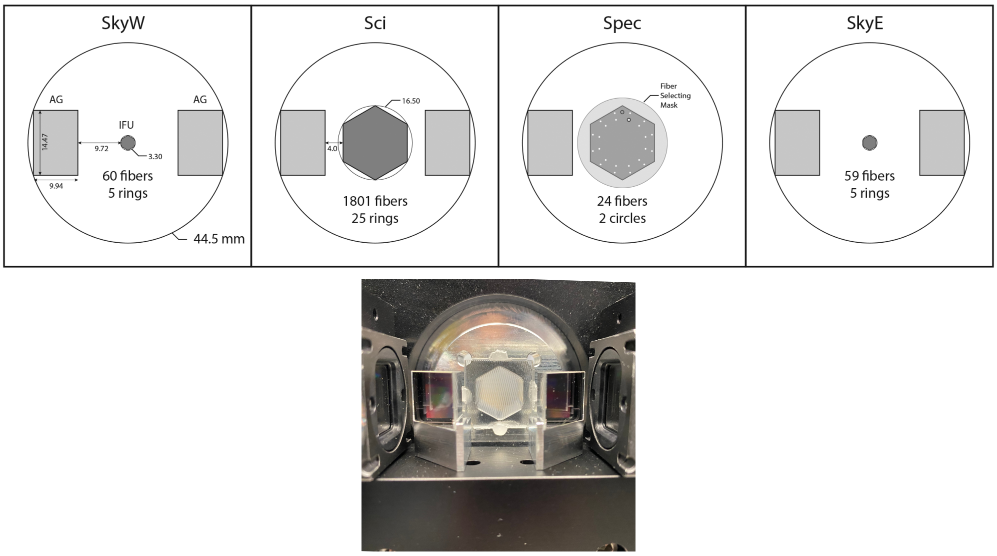

Figure 6.2: On the left, we show a schematic of the different focal plane layouts of the 4 LVM telescopes. Note that for the A&G sensors the positions shown are after the light is reflected by the 45° mirrors. The photo on the right shows a test setup for the focal plane metrology. The full Science IFU is substituted by a dummy microlens array.

6.2.3.2 GAIN AND READ NOISE MEASUREMENTS

The photons hitting the detector generate electrons, but the cameras deliver values in analog-digital-converter units (ADUs). The gain is the (adjustable) conversion factor between the number of measured electrons and the ADUs.

The classical method to determine the gain value is to do a so called mean-variance test: As photons (and the generated electrons) obey Poisson statistics, the standard deviation of measured electrons is related to their count by $\sigma_e = \sqrt{N_e}$. This leads to a linear relation between the variance in ADU (σ^2_{ADU}) and the signal:

$$\sigma_e^2 = (Gain \cdot \sigma_{ADU})^2 = N_e = Gain \cdot N_{ADU} \tag{6.1}$$

The slope of the linear relation between mean (ADU-)counts per pixel and the variance gives the gain. To make the measurment, we linearly increased exposure time with constant illumination until the sensors reached saturation. For each exposure time/signal level, we saved 20 images, allowing us to determine the variance per pixel (which unlike the total of the image is not affected by pixel to pixel variations). After that, we performed a linear fit function to the mean-variance points. An example for such a measurement is shown in Figure 6.3.

At the same time, the zero-signal variance (or Y-intercept of the linear fit to the mean-variance relation) gives a measure of the read noise.

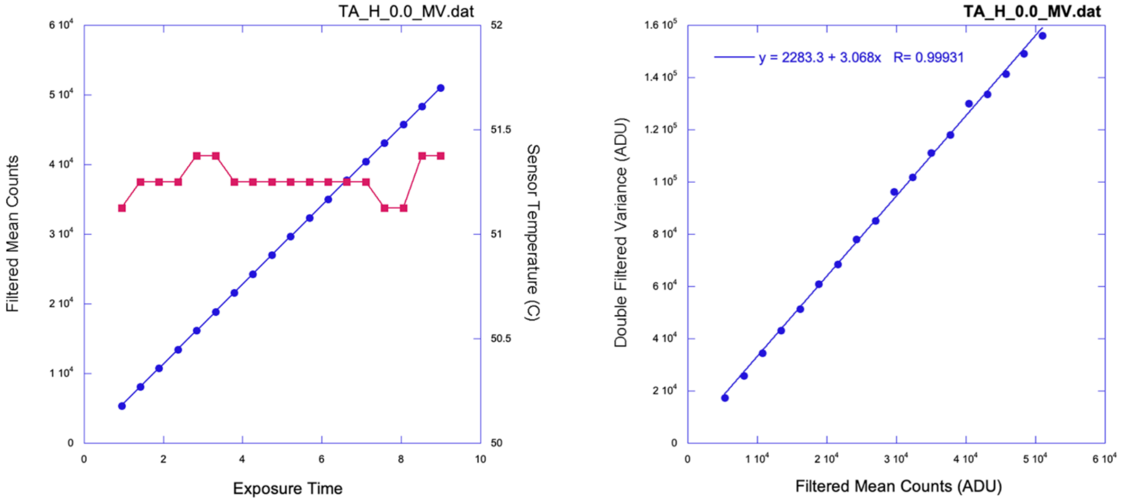

Figure 6.3: The left plot shows how the mean signal increases linearly with the exposure time. As the sensor temperature also affects the performance, we logged it during the measurement. The right plot shows the variance plotted against the mean counts.

6.2.3.3 Results and determination of the optimal gain

The cameras offer various gain settings, separated into *High Conversion Gain (HCG)* and *Low Conversion Gain (LCG)* modes and with an adjustable gain value between 0 and 48. We performed the mean-variance test for seven gain values in the two modes. The results for the different settings appear in Table 6.1. The gain setting LCG 48 produced questionable results and is excluded from the table. In general, the *HCG* modes show significantly lower read noise, and increasing the gain of the camera leads to lower read noise. For our LVM use case, a gain setting of 5 in the *HCG* mode is a good compromise between dynamic range (with a gain of 0.177e^-/ADU we reach saturation at ∼12 000e^-) and read noise ($\sigma_R = 5.6\, e^-$), and we use this as the baseline for our guide star brightness calculations (6.3.3).

Table 6.1: Results for gain and read noise for different gain settings of the cameras. All measurements were made with a sensor temperature of ∼51° C.

High conversion gain:							
Gain Setting	0	5	15	25	35	45	48
Gain [e-/ADU]	0.326	0.177	0.0562	0.0180	0.00575	0.00178	0.00125
Read Noise [e-]	15.6	5.62	3.79	2.29	2.98	2.67	2.59

Low conversion gain:							
Gain Setting	0	5	15	25	35	45	48
Gain [e-/ADU]	1.59	0.878	0.289	0.0918	0.0294	0.00889	-
Read Noise [e-]	24.5	12.0	13.6	12.9	12.9	11.8	-

6.2.3.4 Dark current measurements

The dark current was measured by taking so-called dark-frames. We kept the sensor in complete darkness by dimming the lights in the laboratory and sealing the sensor with a plastic cap. The dark frames were determined while the cameras were warming up, using a 10 s exposure time. In this way, we also measure the temperature dependence of the dark current (see next section and Figure 6.4). We determined the median image value and used the measured gain and the exposure time to convert the image counts to electrons/second.

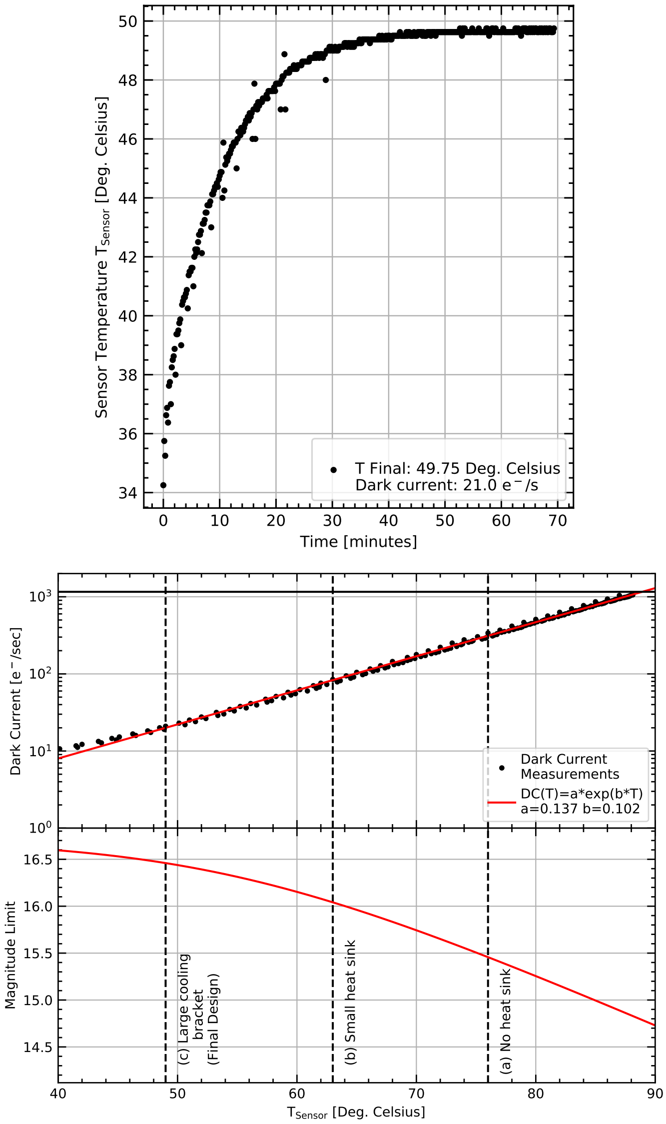

Figure 6.4: The left panel shows how one of the A&G cameras heats up under laboratory conditions and reaches its equilibrium temperature after around 45 minutes. The right panel shows the exponential dependence of the dark current on the temperature (top) and its effect on the magnitude limit (bottom, see also section 6.3.3).

6.2.3.5 Temperature behaviour and optimisation of passive cooling

The dark current of a silicon detector shows a strong dependence on temperature. Even though the average power consumption of each of the cameras is just 3 W (including the Ethernet interface), the sensors themselves reach a much higher temperature than their surroundings, due to their small physical size and therefore heat dissipation. Our camera model has an onboard-temperature sensor close to the imaging sensor. In addition to this, we also measured the surface temperature of the camera housing using a thermal infrared camera (see Figure 6.6).

Under laboratory conditions (ambient temperature around 20° C), a bare camera reached a sensor temperature of around $75^\circ\ C$, leading to a dark current of around 300 e^-/s. These conditions would affect the sensitivity of the guide images in a very negative way (see Figure 6.4. The details of the signal-to-noise ratio (SNR) calculation are explained in 6.3.3). For this reason, many cameras used for astronomical applications are actively cooled (either using thermoelectric cooling with Peltier devices, or if even lower temperatures are required, cryogenics such as liquid nitrogen). Due to the limited space in the focal plane, and to avoid additional complexity, we aimed to reduce the temperature of the cameras to an acceptable level using only passive cooling. We started with a small commercial (25 mm)^2 heatsink which led to a decrease of the sensor temperature of 12° C (to around 63° C). To further reduce the temperature we experimented with custom cooling brackets with additional heatsinks and fins. Beside the heat dissipation, the cooling brackets also serve as the adaptor to mount the cameras to the Focal Plane Assembly. An overview off the different tested setups appears in Figure 6.6. With the final cooling brackets, the equilibrium temperature of the sensors is ∼49° C, giving a dark current of 21 e^-/s (a factor of ∼15 lower than the initial setup). This is of the same order as the sky-brightness in a full-moon-night; further reducing the dark current would therefore only have a small influence on the SNR of the stars (see 6.3.3).

6.2.3.6 Influence of ambient pressure

As air convection plays is an important mechanism for heat dissipation, we expect a worse cooling performance for the A&G cameras at high-altitude observing sites where the ambient pressure is lower than in our close-to-sea-level laboratory. To ensure a sufficient cooling performance also at the observatory, we simulated a lower ambient pressure by placing the camera inside a vacuum vessel. We lowered the pressure to a minimum of around 600 mbar, similar to what would be expected at Mauna Kea at 4200 m elevation, one of the highest astronomical observing sites. Las Campanas observatory is situated at 2380 m elevation, with a typical pressure of 760 mbar. We waited until the sensor temperature of the camera reached its equilibrium and studied how the final temperature changes with pressure. The results are shown in Figure 6.5. As predicted, we see higher temperatures at lower pressures, but the difference is small: between our laboratory and LCO, we only expect a difference of around 1° C. Please note that these tests were performed with only a small heat-sink and not the final large cooling-bracket, but we expect a similar trend for the final cooling solution.

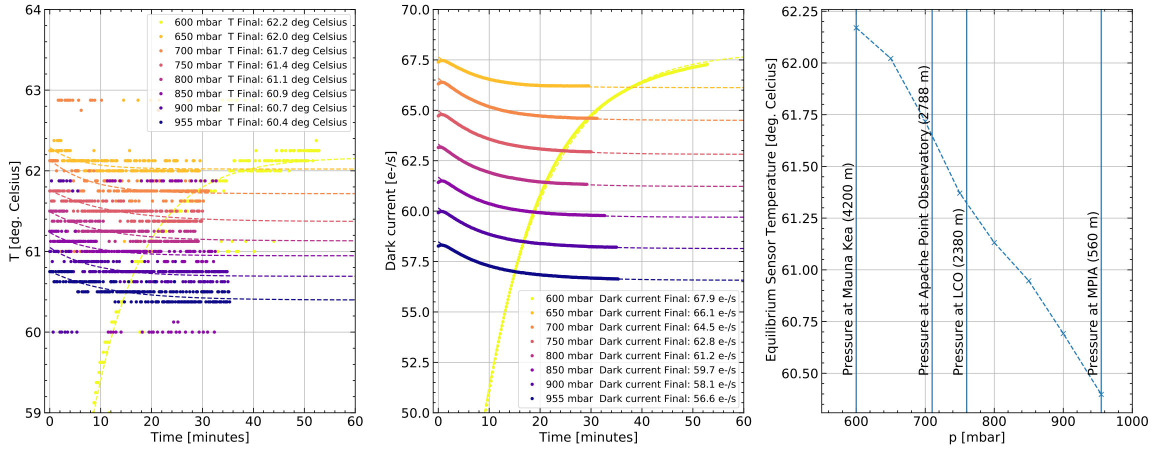

Figure 6.5: The left plot shows a time series of how the camera sensor temperature reaches its equilibrium for different simulated ambient pressures. The middle plot shows the corresponding dark current. The plot on the right shows the equilibrium temperature plotted against the pressure. The vertical lines mark the pressure at a few representative observing locations.

6.3 Verifying the number of guide stars for each survey pointing

6.3.1 Introduction

The LVM Survey aims to map the entire Galaxy - from the crowded inner regions to the relatively empty zones at higher Galactic latitudes. The stellar density in these different fields varies by orders of magnitude, and we have to ensure a sufficient number of guide stars for each of the ~25 000 planned survey pointings.

Note that the symmetry of the focal plane (Figure 6.2) allows us to rotate the field of view by $+60^\circ$ or -60°, in case a pointing would not have a sufficient number of guide stars. Figure 6.9 demonstrates the three different possible field rotation angles for an example pointing.

6.3.2 Throughput calculations

To determine the systems sensitivity, we have to take the full system throughput into account. To do so, we multiply the reflectivity of all reflective surfaces by the throughput of the lens and the quantum efficiency of the detector. The resulting wavelength dependent throughput function appears in Figure 6.7. We used the pyphot-package[4] to calculate the flux of Vega given our throughput. The resulting flux of Vega is $2.17 \cdot 10^6\ e^- s^{-1} cm^{-2}$. With a telescope area of $\sim$ 206 cm^2, this gives us a total electron rate of $4.47 \cdot 10^8\ e^- s^{-1}$ and a zeropoint of -21.6.

---

[4] https://mfouesneau.github.io/pyphot/index.html

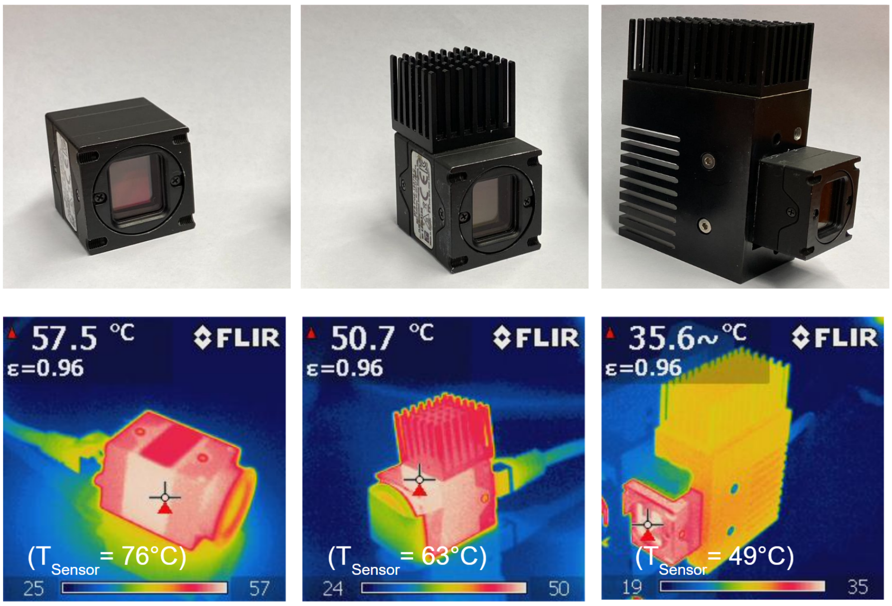

Figure 6.6: The upper row shows photos of the different heatsink configurations which we tested. The lower row shows corresponding thermal images, which we used to verify, whether the heatsinks are working efficiently.

6.3.3 Estimating the signal-to-noise ratio for guide stars

To calculate the signal-to-noise ratio (SNR) for the guide stars, we assume a $N_{Pixel} = (7\text{ pixel})^2 = 49$ pixel guide window. This should capture all of the light, as the combined (seeing+diffraction+optical) requirement on full-width half maximum (FWHM) of the point-spread-function (PSF) size is 3.5 arcsec which is around 3.5 pixel.

The individual components entering the SNR calculation are:

Signal level We calculate the flux of electrons expected from a source with a specific magnitude using the zero point calculated in 6.3.2. The resulting number of electrons then is: $N_e = t_{exp} \cdot f_\star$.

Shot noise of source The number of electrons is Poisson distributed with the standard deviation of the number electrons being: $\sigma_e = \sqrt{N_e}$.

Dark current As measured in the laboratory, we use a dark current of $f_{Dark} = 21\, e^-/s/pixel$. This occurs for an A&G sensor temperature of 49° C.

Sky Background We calculate the sky background using the LVM exposure time calculator[5]. In a full moon night (i.e. the worst case), we have a sky background of $f_{Sky} = 28\, e^-/s/pixel$.

Readout noise As measured in the laboratory for our preferred gain setting (see 6.2.3.3), we use a read noise of $\sigma_R = 5.6e^-$.

---

[5] https://github.com/sdss/lvmetc_lco_script

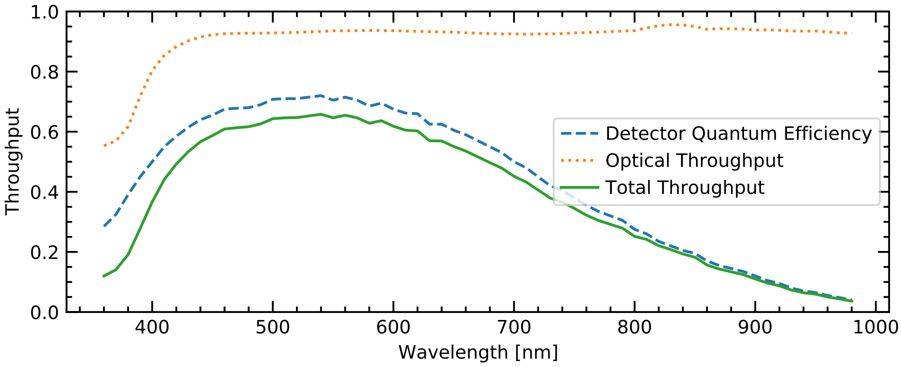

Figure 6.7: The wavelength dependence of the LVM guiding system throughput for the science and sky telescopes.

We calculate the total noise by quadratically adding the different contributions. This leads us to the following expression:

$$SNR = \frac{t_{exp} \cdot f_\star}{\sqrt{N_{Pixel} \cdot (\sigma_R^2 + t_{exp} \cdot (\frac{f_\star}{N_{Pixel}} + f_{Dark} + f_{Sky}))}} \tag{6.2}$$

Figure 6.8 shows how the calculated SNR depends on the guide stars magnitude and on the exposure time. With the baseline exposure time of 5 s, we reach a SNR of at least 5 for stars with gmag<16.5.

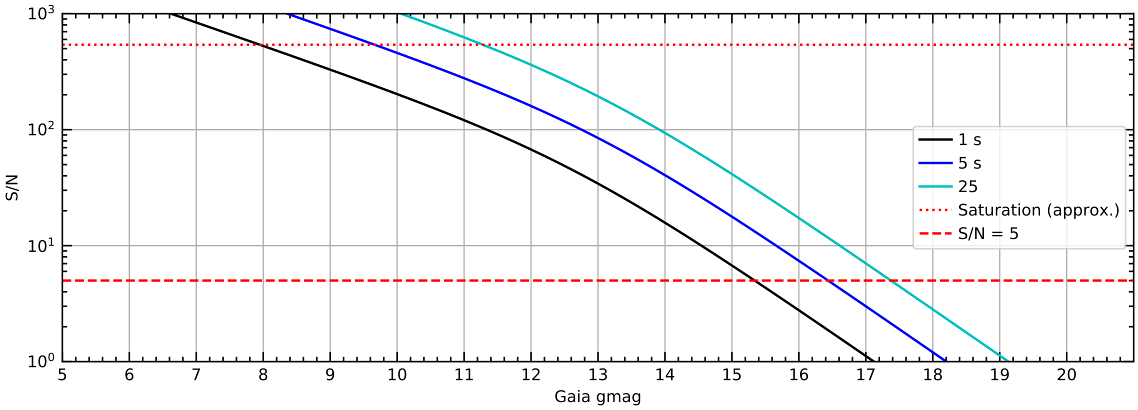

Figure 6.8: SNR estimates for different guide star magnitudes and exposure times. Those plots assume the as-measured read-out noise and the dark current with the passively cooled camera and a full moon night sky brightness

6.3.4 QUERYING THE NUMBER OF GUIDE STARS USING GAIA EDR3

We create a list of the planned survey pointings using the survey simulation tools[6]. In the relevant magnitude range for our small telescopes, the Gaia Early Data Release 3 (EDR3) (Gaia Collaboration et al., 2021b) offers an essentially complete (Fabricius et al., 2021) all-sky catalogue of stars. To determine a list of potential guide stars we performed the following steps:

1. Determine the pointing coordinates from the Survey Planning Tools
2. Query 0.69 deg around pointing coordinates using a local copy of the Gaia catalogue. This query (which in principle has to choose from almost two billion Gaia stars) is made efficient by splitting the Gaia catalogue into 50 000 HEALPix tiles (Zonca et al., 2019; Górski et al., 2005)[7] (Order 6).
3. Convert angular coordinates into metric focal plane coordinates using an image scale of 8.92 µm/arcsec.
4. Test which stars fall into the rectangular region of the two A&G sensors for the three possible position angles (See Figure 6.9).

After the potential guide stars have been identified, we simply count the number of stars per sensor for different magnitude cutoffs.

6.3.5 RESULTS

The minimum, maximum and median number of guide-stars for various magnitude limits appears in Table 6.2. Figure 6.9 shows a full-sky map, color-coded with the number of available guide stars brighter and a histogram of the number of available guide stars for the representative magnitude limit of gmag<16.

Based on the SNR calculations (Figure 6.8) we can assume a magnitude limit of 16.5 mag in the brightest (full moon) nights. Even when adding more than a full magnitude as reserve, the minimum number of stars brighter than gmag = 15 on a single camera chip is 6. Therefore, we can conclude that our guiding strategy will work for all planned survey pointings, and that no further mitigation strategies (such as longer exposure times, active camera cooling, optimisation of pointing coordinates, etc.) are necessary.

6.3.6 SYNTHETIC IMAGES

To test and optimise the exposure time and the guiding software that will process the images taken with the guide cameras we simulated realistic exposures with the guide cameras. We assume Poisson shot noise for all photon/electron-counting quantities (stars, sky, dark current) and normal-distributed readout noise (with $\sigma_e = 5.6e^{-}/s$, see 6.2.3.3). We modelled the point-spread function as a Gaussian

---

[6] https://github.com/sdss/lvmsurveysim

[7] http://healpix.sourceforge.net

Table 6.2: Results of the guide star number analysis. For a magnitude limit of $gmag < 15$, there is a sufficient number of guide stars even for a single camera.

	Single camera			Two cameras in standard orientation			Two cameras with optimal orientation		
	# No. of guide stars			# No. of guide stars			# No. of guide stars		
Mag. Limit	Min.	Med.	Max.	Min.	Med.	Max.	Min.	Med.	Max.
14.0	2	140	1081	11	288	1966	20	313	1967
15.0	6	322	3908	27	660	6683	39	709	7120
16.0	20	704	10747	53	1456	18464	66	1554	19797
17.0	41	1491	33994	98	3069	58460	111	3272	61546
18.0	63	2991	66610	155	6235	125183	175	6671	125183

with a FWHM equal to our requirement (3.5 arcsec). The results for three different simulated images in fields with varying stellar density appear in Figure 6.10.

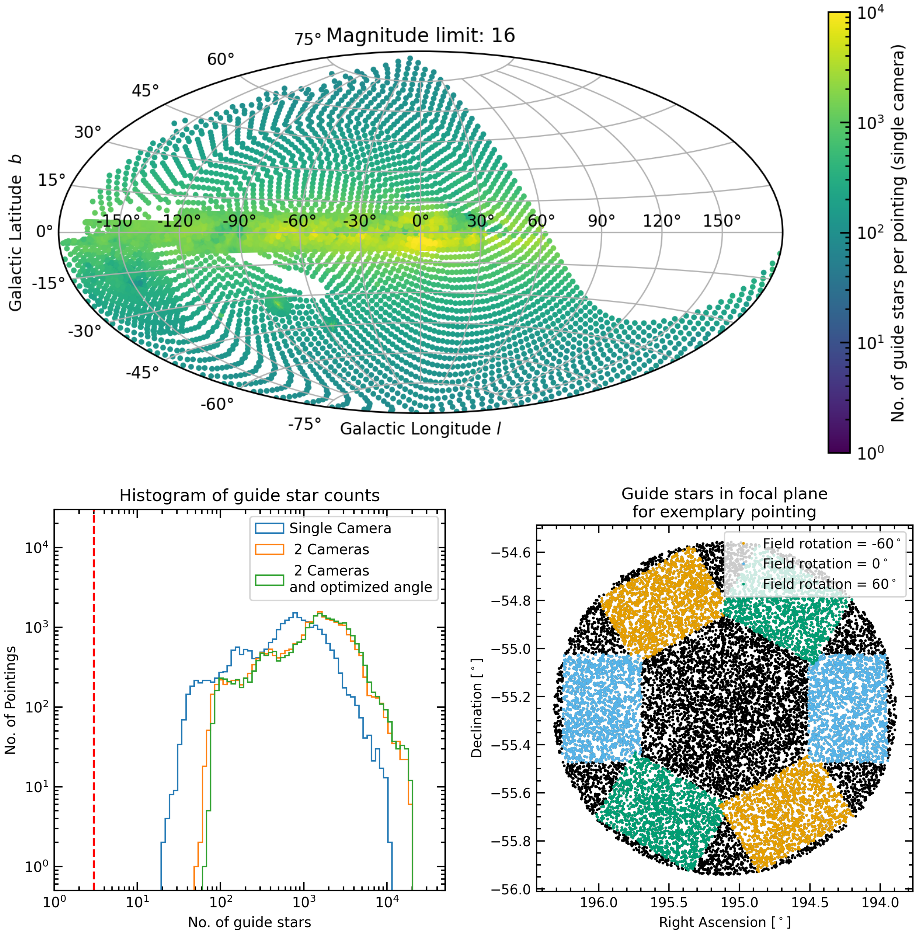

Figure 6.9: Top: A full-sky map in Galactic coordinates. The dots mark the different pointings of the survey and are color-coded with the number of available guide stars brighter than gmag=16. The imprint of the Milky Way with its dust clouds is clearly visible. Lower left: Histogram of the number of available guide stars brighter than gmag=16 for the different A&G camera configurations. The dashed vertical line marks the critical number of 3 guide stars per pointing. All pointings have more stars than that. Lower right: The guide stars within the field of view for an example pointing at a moderately crowded field. The black dots indicate stars brighter than gmag < 16. The coloured dots mark stars within the field of view of the two A&G Cameras at the 3 possible field rotation angles.

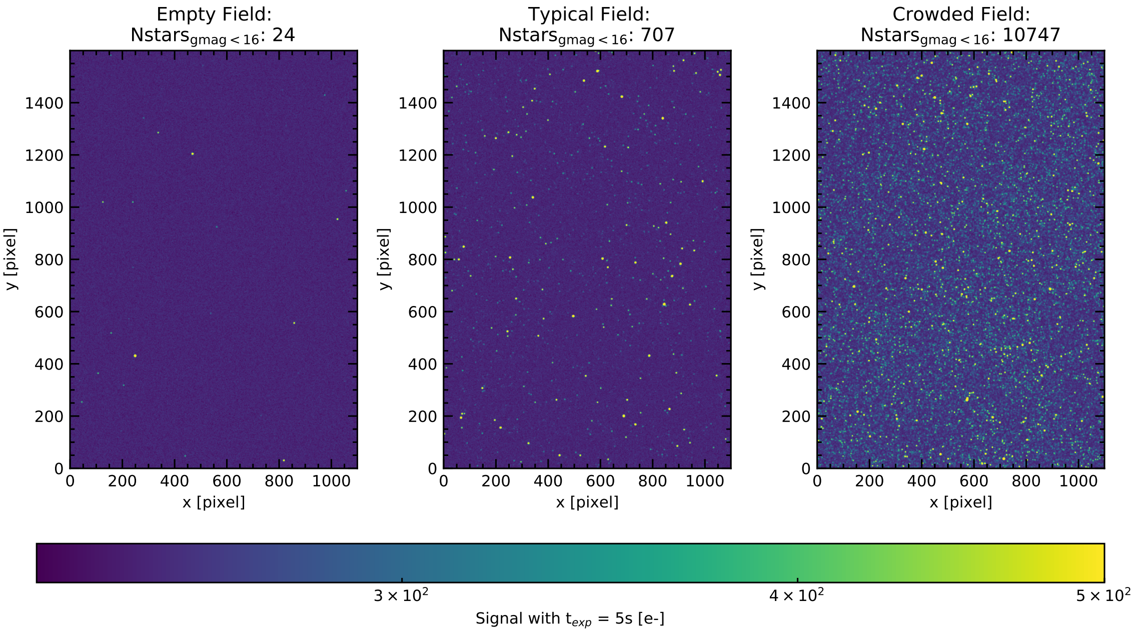

Figure 6.10: Three simulated guide camera images for (left to right) an empty, a typical, and a crowded field.

6.4 FOCAL PLANE METROLOGY

6.4.1 MOTIVATION AND REQUIREMENTS

The focal plane metrology of the LVM telescopes has two phases and two goals:

In the first step, we will align both guide cameras and the IFU to a single reference plane. This will ensure that all these components have a common focus. The requirement for the coplanarity 50 μm is (derived from the rather slow speed of the f/11.42-beam and the requirements on the PSF width).

The goal of the second phase is to measure the exact relative positions. This is necessary to be able to place the IFU fibers on the correct sky positions, based on images taken with the A&G cameras. The requirement of knowing the fibre position to 1 arcsec accuracy leads to a requirement of knowing the relative positions in the focal plane to less than 10 μm.

6.4.2 MEASUREMENT SETUP

We use a *Point Source Microscope* (PSM) (Parks & Kuhn, 2005) from *OPTICAL PERSPECTIVE GROUP* to measure the locations of both the microlenses of the IFU and the pixels of the CMOS sensors of the A&G cameras. The PSM is an autostigmatic microscope that projects the output of a single mode fibre towards a point source in its focal plane. This point source can be used to probe the location of objects in the focal plane, as its location can be determined very accurately due to its small diameter (<5 μm) and its very short depth of focus. We use a long working-distance objective[8], giving a working-distance of 34 mm.

We mount the PSM on three precision linear stages equipped with *Newport DMH-1* digital micrometer heads for fast and precise reading of the positions. The micrometers have a resolution of 1 μm and a stated accuracy of ±2 μm over a range of 25.4 mm. The focal plane is wider than this (see Figure 6.2), so we extend the range of the micrometers using precisely manufactured extension blocks with a known width of either 16 mm or 32 mm. Figure 6.11 shows pictures of the setup.

This setup allows us to measure 3D positions in the focal plane to high accuracy. Using the linear stages, we move the PSM over the edge of a microlens or a specific pixel of one of the camera sensors. By bringing the reflected image of the point source into focus (again with a linear stage), we can ensure that the PSM is always at the same distance from the component being measured.

To avoid having to count single pixels on the camera sensors, we read-out the guide cameras and locate the PSM spot. As the point-source is very small (< 5 μm) we can illuminate individual pixels.

As the the actual IFU (connected to the fibres) and the guiding components will be joined for the first time at the observatory, we used a bare microlens array with the same properties as the nominal microlenses for our tests. We built an adaptor to precisely place it at the right location in the focal plane. Other than that, all components are those that will be used in the final setup.

---

[8] Objective lens: *10X Mitutoyo Plan Apo Infinity Corrected Long WD Objective*

6.4.3 MEASUREMENT PROCEDURE

The measurement procedure has multiple steps:

1. **Stage alignment** As a first step, we have to ensure that the stages are aligned perfectly with the desired focal plane. To do this, we install a diamond-turned target (see Figure 6.11), whose surface defines the focal plane. Then, we use micrometers mounted to the optical table to adjust the stage positions, before fixing the setup in place.

2. **Hybrid measurements on camera sensors** After the stages have been fixed on the table, we remove the target from the focal plane and install the guide cameras. Then, we measure multiple positions on each of the 2 camera sensors. We identify which pixel is illuminated by the PSM by reading out the cameras. At the same time, we log the positions measured with the digital micrometers that move the stages. In principle, 3 measurements would be enough to fully determine the spatial position of each sensor, but to test the precision of our method and improve statistics, we take 9 measurements at different locations on each sensor.

3. **Shimming of camera sensors** The guide cameras are also used to focus the telescope during operation. Therefore, both camera sensors and the microlens array of the IFU have to be in the same plane. If we determine a focus or tilt difference between the reference plane (set by the precisely turned focal plane target, see step 1) and the camera sensors, we will use shims to adjust the position of the cameras. This will likely be the case at the beginning due to manufacturing tolerances.

(Repetition of 2. and 3.) These two steps are iterated, until the two sensors are in the correct plane. After that the as-built positions are measured on last time.

4. **Measurement of as-built microlens positions** We need to locate the centre of each microlens. However, due to reflection and refraction, it is much easier to place the point source at the edge of a microlens. If we take three measurements at the edge of a particular microlens, we already can determine its centre (assuming it is perfectly circular), but again, to have a grasp of our measurement errors and better statistics, we take six measurements per microlens.

6.4.4 DATA REDUCTION

While the three stages directly measure physical positions in the focal plane, we still have to use some mathematics to fully understand the focal plane geometry.

The positions of the camera are determined by finding the 7-parameter linear transformations (3 translations, 3 rotations, scale), that transform pixel coordinates into physical 3D coordinates using a least-squares fit.

The positions of the microlenses are determined by fitting a circle to each of the 6 positions measurements of the edge of each measured lens. After the positions of a few of the individual lenses have

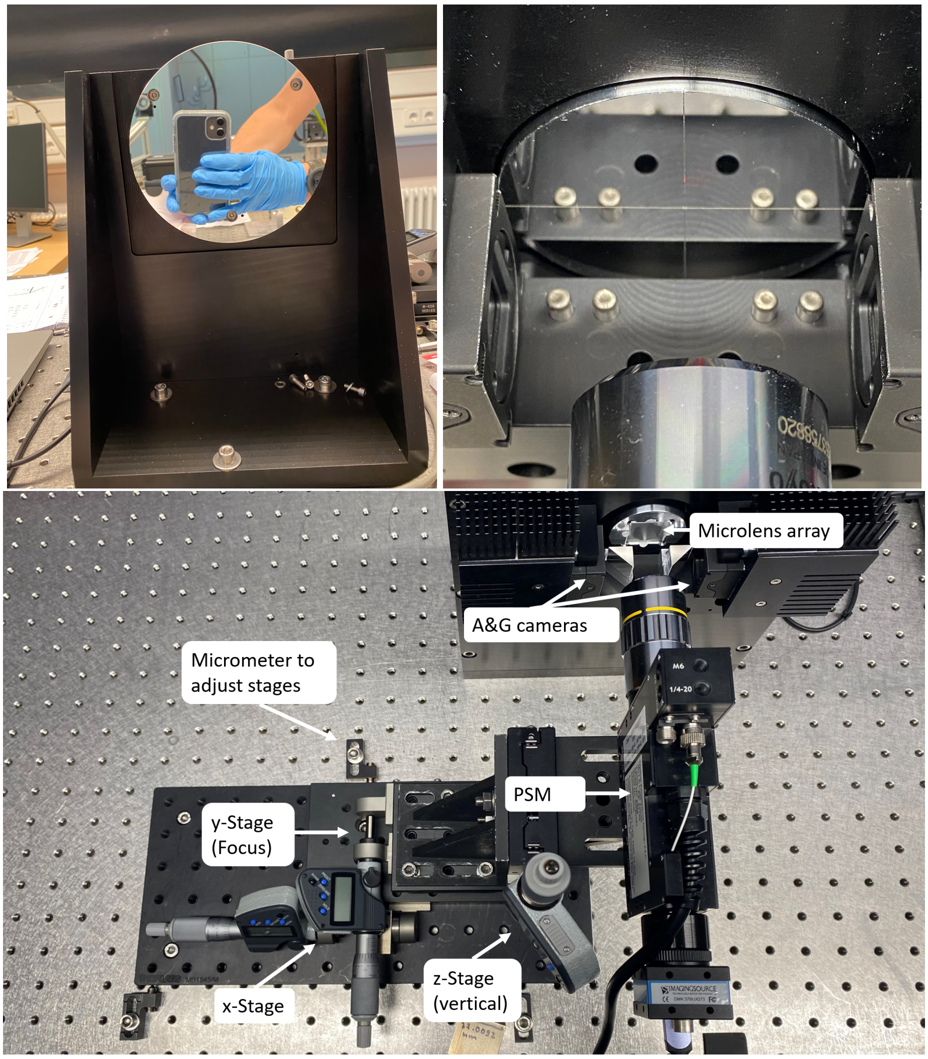

Figure 6.11: Top left: Backside of the focal plane alignment target. Top right: Front of the focal plane alignment target. One can also see the objective lens of the PSM. Bottom: Top-view of the focal plane metrology setup.

been determined, we can determine the global position and orientation of the full microlens array with another linear transformation.

6.4.5 Results

While tests are still ongoing, the first results of this metrology setup are very promising. By comparing the measured physical positions with the on-chip astrometry (i.e. the identified A&G pixels), we can test the consistency of the measurements. The residuals show a RMS of 2 μm (with a P-V of 10 μm), which is consistent with the accuracy of the micrometer heads. This also demonstrates that we are achieving the required precision level.

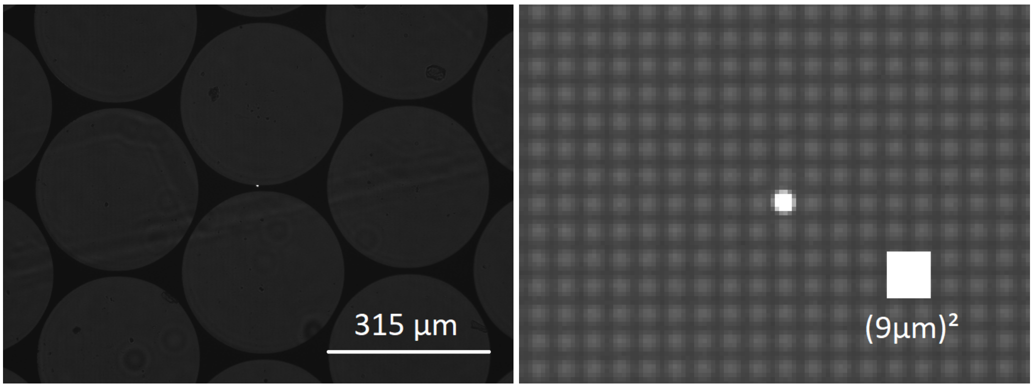

Figure 6.12: The read out of the point source microscope. The left image shows the view of the microlenses, the right image shows (at higher digital magnification) the surface of one of the A&G cameras. Due to the design of the sensor, each electronical pixel (size 9 µm) consists of 2×2 physical units with a size of 4.5 µm. In both images, the point source can be seen as a bright spot in the center.

The coordinates and transformations determined with the PSM measurements were used to accurately calculate the required adjustments to the shims used to align the A&G cameras to the reference focal plane. This proved to be very effective - in 2 iterations of re-shimming we reduced the RMS of the focus deviations from initial $\sim$0.6-0.7 mm to to $\leq$0.005 mm (see Table 6.3), clearly matching our focus requirement of 0.05 mm. Figure 6.13 shows the as-built geometry of our test focal plane as measured with the PSM setup after the 2 iterations of shimming, while Table 6.4 lists the numerical results.

Table 6.3: Focus deviations for two cameras during different iterations of the shimming process.

	Camera 1				Camera 2			
	Focus Deviation [mm]				Focus Deviation [mm]			
	Min.	Mean.	Max.	RMS	Min.	Mean.	Max.	RMS
Iteration 0 (standard shims)	0.598	0.726	0.855	0.729	0.415	0.622	0.830	0.630
Iteration 1 (custom made shims)	-0.060	-0.046	-0.032	0.046	-0.136	-0.086	-0.036	0.089
Iteration 2 (custom made shims)	-0.005	-0.001	0.004	0.002	-0.006	0.003	0.011	0.005

Table 6.4: Preliminary results of the focal plane metrology, after the cameras have been shimmed to adjust for focus deviations.

Component	**x-centre**	**y-centre (focus)**	**z-centre**	**Rotation x axis**	**Rotation y axis**	**Rotation z axis**	**Scale**
Guide camera 1	-32.286 mm	-0.001 mm	0.351 mm	-0.013°	0.026°	-0.209°	9 µm/pixel
Guide camera 2	0.002 mm	0.003 mm	-0.001 mm	0.013°	0.060°	0.136°	9 µm/pixel
Microlens array	-16.079 mm	0.015 mm	-0.128 mm	-0.089°	0.025°	0.141°	330 µm/lens

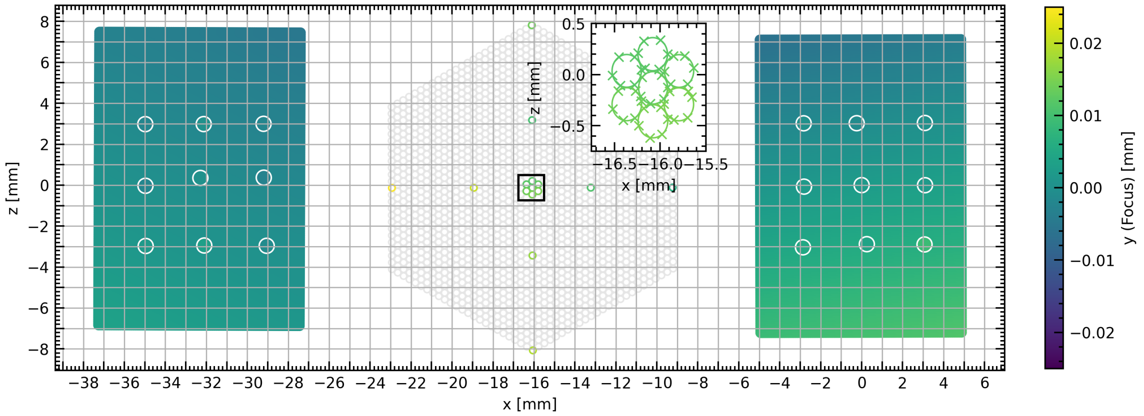

Figure 6.13: The as-built focal plane with positions determined using our high precision metrology setup. The two large rectangles show the inferred positions of the CMOS sensors, colour-coded with the focus deviation, while the hexagon in the middle shows the location of the IFU. Colored circles indicate microlenses, that have been measured. The small insert shows a magnification of the central region of the IFU, the individual measurements taken at the edge of the lenslets are marked with crosses.

6.5 SUMMARY

In this work, we demonstrated the required performance of the LVM acquisition and guiding hardware.

We show that relatively low-cost commercial CMOS cameras offer sky-brightness limited performance, and we reach a sufficient depth for the LVM survey A&G strategy. We reach a magnitude limit of ∼16.5 in 5 s in a full moon night. Even with a magnitude limit of 15 and only a single A&G camera, there are always more than 5 stars available for guiding.

In addition, we present a metrology setup using a point source microscope, which allows us to measure the relative positions of the microlenses of the IFU and the pixels of the guide camera sensors to an accuracy of 2 µm in all three spatial dimensions, allowing for precise focus and tip/tilt adjustments.

Acknowledgments

Funding for the Sloan Digital Sky Survey V has been provided by the Alfred P. Sloan Foundation, the Heising-Simons Foundation, and the Participating Institutions. SDSS acknowledges support and resources from the Center for High-Performance Computing at the University of Utah. The SDSS web site is www.sdss5.org.

SDSS is managed by the Astrophysical Research Consortium for the Participating Institutions of the SDSS Collaboration, including the Carnegie Institution for Science, Chilean National Time Allocation Committee (CNTAC) ratified researchers, the Gotham Participation Group, Harvard University, Heidelberg University, The Johns Hopkins University, L'Ecole polytechnique fédérale de Lausanne (EPFL), Leibniz-Institut für Astrophysik Potsdam (AIP), Max-Planck-Institut für Astronomie (MPIA Heidelberg), Max-Planck-Institut für Extraterrestrische Physik (MPE), Nanjing University, National Astronomical Observatories of China (NAOC), New Mexico State University, The Ohio State University, Pennsylvania State University, Smithsonian Astrophysical Observatory, Space Telescope Science Institute (STScI), the Stellar Astrophysics Participation Group, Universidad Nacional Autónoma de México, University of Arizona, University of Colorado Boulder, University of Illinois at Urbana-Champaign, University of Toronto, University of Utah, University of Virginia, Yale University, and Yunnan University.

This work has made use of data from the European Space Agency (ESA) mission *Gaia* (https://www.cosmos.esa.int/gaia), processed by the *Gaia* Data Processing and Analysis Consortium (DPAC, https://www.cosmos.esa.int/web/gaia/dpac/consortium). Funding for the DPAC has been provided by national institutions, in particular the institutions participating in the *Gaia* Multilateral Agreement.

Some of the results in this paper have been derived using the healpy and HEALPix package.

III. CONCLUSIONS AND OUTLOOK

7 SUMMARY AND CONCLUSIONS

The main focus of this thesis is the kinematics of ω Cen, the most massive globular cluster in the Milky Way and the closest galactic nucleus. In the following, I present a summary of the main results:

A new legacy dataset for studies of ω Cen: In Chapter 3, I describe the creation of a new astrometric and photometric catalog based on an extensive Hubble Space Telescope dataset. This new oMEGACat II catalog is fully public and is the most comprehensive kinematic catalog for any star cluster. The new catalog contains precise proper motion measurements and multi-band photometry for around 1.4 million sources. Thanks to its unique combination of long temporal baseline (leading to high precision proper motions), wide filter coverage (enabling detailed subpopulation studies), and high resolution and depth (enabling the studies of faint stars even in the crowded cluster center) it provides an important legacy dataset for further studies of ω Cen. These studies will allow for a better understanding of the formation history of ω Cen, its mass distribution, and its present-day kinematics.

The dataset is complementary to the recent spectroscopic effort by our collaboration (Nitschai et al., 2023), enabling studies of the cluster kinematics in three velocity dimensions. The data are also complementary to astrometric investigations with the ESA Gaia satellite: While Gaia (with its full sky coverage) is perfectly suited to study the outskirts of ω Cen, it is affected by crowding in the inner regions. Within the half-light radius, our new catalog reaches several magnitudes deeper and contains four times more stars. These two datasets, in combination with detailed dynamical models (see Subsection 8.1.7) will allow us to obtain a complete picture of ω Cen's kinematics.

Robust evidence for an intermediate-mass black hole: The discovery of fast-moving stars in the very center of ω Cen (see Chapter 4) is an important new addition to the long debate about the presence of a black hole in the cluster center. While further work is needed to precisely measure the mass of the black hole in ω Cen (see Section 8.3), these seven stars allow us to place a robust lower limit of 8200 $M_\odot$. This makes the black hole in the center of ω Cen a bonafide IMBH and the closest massive black hole. It is also only the second system (besides the Galactic Center), in which multiple stars on bound orbits around a black hole can be observed.

A detailed view of the kinematics of ω Cen: In Chapter 5, I combine the astrometric and spectroscopic catalogs to provide an updated picture of the kinematics of ω Cen in all three velocity determinations. Our results show a rotation curve that increases with radius until reaching a plateau at $\sim$7 km s^{-1} for $r > 150''$. The rotation along the line-of-sight and in the plane of the sky are consistent and allow a measurement of the inclination of the cluster (see Chapter 3 for the plane of sky rotation and Chapter 5 for the line-of-sight rotation).

In addition to the cluster rotation, we also examine the velocity dispersion of the cluster, finding a monotonic increase towards the cluster center. It rises steadily from ~0.52 $\mathrm{mas\,yr^{-1}}$ (13.4 $\mathrm{km\,s^{-1}}$) at the half-light radius to ~0.81 $\mathrm{mas\,yr^{-1}}$ (20.9 $\mathrm{km\,s^{-1}}$) within the central 10 arcseconds. The velocity dispersion is isotropic in the cluster core but shows increasing radial anisotropy towards larger radii ($\sigma_{\mathrm{PM,tan}}/\sigma_{\mathrm{PM,rad}} = 0.0849 \pm 0.003$ at the half-light radius).

The large number of measurements (~600,000 stars with high-precision proper motions and $\sim 25,000$ with full 3D velocity vectors) also allows us to determine 2-dimensional velocity maps with high spatial resolution. These kinematic maps allow an independent confirmation of the cluster center (coinciding with the photometric center determined in Anderson & van der Marel 2010) and studies of the position angle and the ellipticity of the velocity dispersion field.

Our kinematic measurements are consistent with previous work but provide substantial improvements in precision, spatial resolution, and on-sky coverage. In combination with other datasets for the outskirts of the cluster, the kinematic measurements provide a new reference perfectly suited as input for updated dynamical models of the cluster.

Precise kinematic distance estimation: By combining proper motion measurements and line-of-sight velocities for a consistent sample of stars in the inner region of ω Cen, we can derive a robust kinematic distance estimate of $d = 5445 \pm 41$ pc, the most precise distance to ω Cen available.

Energy equipartition along the main sequence: The new proper motion catalog provides precise velocity measurements for stars spanning a large range of magnitudes and masses. This allows us to measure the degree of energy equipartition at different locations in the cluster. As expected from its young dynamical age, we detect a low degree of energy equipartition in the cluster center ($\eta = 0.088 \pm 0.017$) that further decreases towards larger radii. The radial component of the energy equipartition shows a quicker decrease than the tangential component.

The SDSS-V Local Volume Mapper guiding system: The SDSS-V Local Volume Mapper is a novel widefield integral-field spectrograph that will map the interstellar gas in the Milky Way and other Local Volume Galaxies. I participated in the design, testing, and commissioning phase of the instrument. One of my responsibilities was the guide camera system and the alignment of the focal plane of the LVM telescopes (see Chapter 6). I improved the passive thermal cooling solution of the cameras, leading to better sensitivity and sky coverage. I also developed a new method that allowed me to align and measure the different focal plane elements to micrometer precision. After a successful commissioning campaign (February 2023) at Las Campanas Observatory, Chile, the instrument celebrated its first light, and survey operations are ongoing. I present a preliminary analysis of science verification observations of ω Cen in Section 8.2.

8 NEXT STEPS

8.1 OTHER PROJECTS USING THE OMEGACAT DATA

The work presented in Chapter 3 - Chapter 5 of this thesis was performed within a larger collaboration that aims to disentangle both the formation history and the dynamics of ω Cen by creating a comprehensive spectroscopic, astrometric and photometric dataset. My main contribution to the project was the creation of the Hubble Space Telescope (HST) based astro-photometric dataset (see Chapter 3). This data set is complementary to a large spectroscopic catalog sharing the same spatial coverage. In the following section, I will summarize the many completed and ongoing studies made possible by this unique dataset. I have contributed to these other efforts, mainly by helping with the correct usage of the HST-based catalog, but also through general discussions in the regular meetings of the collaboration and comments on the manuscripts.

8.1.1 VLT MUSE BASED SPECTROSCOPIC CATALOG

This work has been published as Nitschai et al. (2023): "oMEGACat. I. MUSE Spectroscopy of 300,000 Stars within the Half-light Radius of ω Centauri"

The first paper in the oMEGACat series focuses on the creation of a spectroscopic catalog based on observations with the VLT MUSE integral field spectrograph, a large undertaking done by Selina Nitschai. The catalog is based on a large mosaic of 103 individual pointings that were observed either as part of the GTO program "The MUSE Survey of Galactic Globular Clusters" (PI: S. Dreizler, S. Kamann, see also Kamann et al. 2018) and for GO Program 105.20CG.001 (PI: N. Neumayer). Figure 8.1 shows the footprints of the different observations and a reconstructed RGB image. The observations were first reduced using the MUSE pipeline (Weilbacher et al., 2020). Then the individual spectra for more than 300,000 stars were extracted using the `pampelmuse` software package (Kamann et al., 2013). Finally, the spectra were fit using the PHOENIX stellar template library (Husser et al., 2013) in conjunction with the `spexxy` code. These spectral fits yielded metallicities and line-of-sight velocities for over 300,000 stars, and an unprecedented dataset that is one of the foundations for the investigations described in the following.

8.1.2 OVERALL METALLICITY DISTRIBUTION WITHIN ω CEN'S HALF-LIGHT RADIUS

This work has been published as Nitschai et al. (2024): "oMEGACat. III. Multiband Photometry and Metallicities Reveal Spatially Well-mixed Populations within ω Centauri's Half-light Radius"

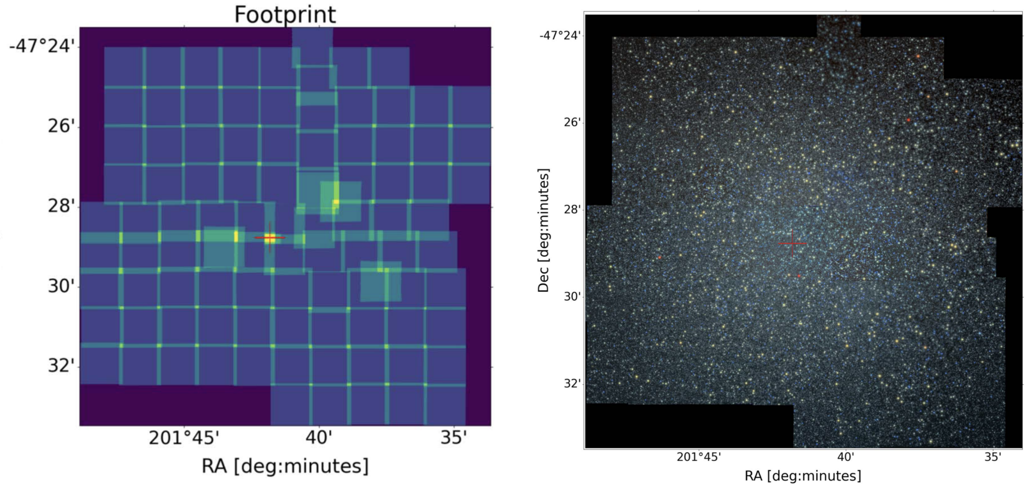

Figure 8.1: *Left:* Footprints of the VLT MUSE observations of the center of ω Cen. The individual observations in Wide-Field-Mode have an extent of $(1')^2$. At the center (red cross), there are multiple observations with the Narrow Field Mode with even higher spatial resolution. *Right:* A RGB reconstruction of the MUSE data of ω Cen using synthetic SDSS i, r, and g filters.
Both figures from Nitschai et al. 2023

This work, led by Selina Nitschai, focused on the spatial metallicity distribution of the red giant branch stars in ω Cen within the combined oMEGACat datasets (HST photometry + VLT MUSE spectroscopy). The comparatively bright magnitude of the red-giant branch stars ($10.5 < m_{\mathrm{F625W}} < 17$) leads to a high signal-to-noise in the spectra and, therefore, to robust metallicity measurements. For the subsample of around 10,000 red giant stars, we found a mean metallicity of $[\mathrm{M/H}]=(-1.614 \pm 0.003)$ with a wide spread ranging from $[\mathrm{M/H}]=-2.04$ to $[\mathrm{M/H}]=-0.67$. The different metallicity sub-populations also split nicely in photometric color-magnitude space: Already a simple $m_{\mathrm{F435W}} - m_{\mathrm{F625W}}$ color-magnitude diagram shows several separate sequences with different spectroscopic metallicities along the red-giant branch (see Figure 8.2). The different stellar populations of ω Cen become even more apparent in the so-called "chromosome map" (Milone et al., 2017a), pseudo-color diagrams using the blue and UV HST filters, that are especially sensitive to the absorption features of light elements. The spectroscopic metallicity information adds a new dimension to the "chromosome map" (see Figure 4 in Nitschai et al. 2024 and Figure 8.5), allowing detailed subpopulation studies. A subsequent analysis of the spatial distribution of the different metallicities found no apparent trend with metallicity, likely due to the shorter dynamical timescales within the center of ω Cen, that lead to well-mixed subpopulations.

8.1.3 ω CEN'S AGE-METALLICITY RELATION

This work has been published as Clontz et al. (2024): "oMEGACat. IV. Constraining the Ages of Omega Centauri Subgiant Branch Stars with HST and MUSE"

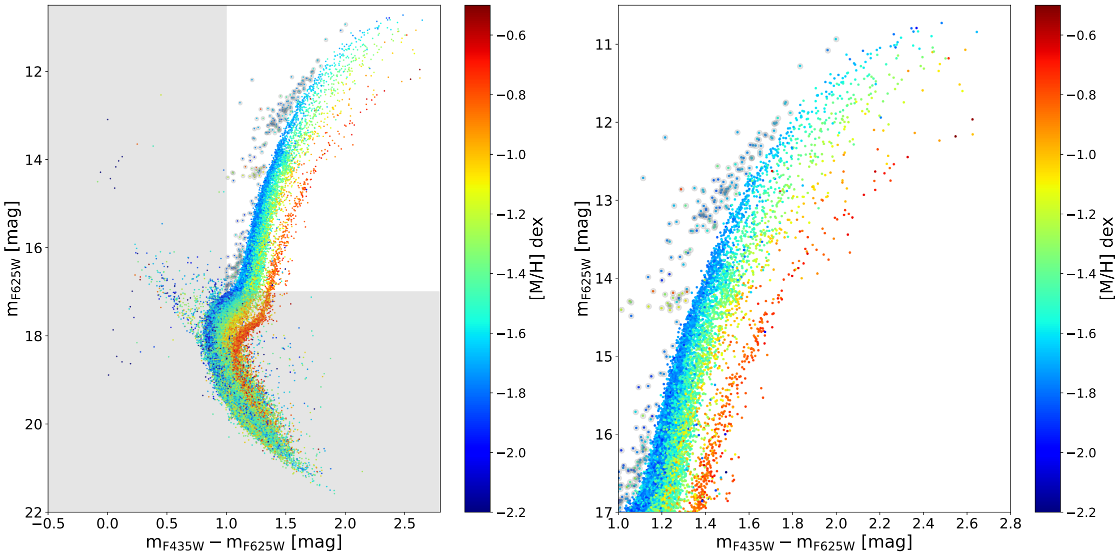

Figure 8.2: *Left:* A color-magnitude diagram based on photometric HST data from the oMEGACat II catalog (Filters: $m_{\mathrm{F435W}}, m_{\mathrm{F625W}}$). It is color-coded with the metallicities from the oMEGACat I catalog. *Right:* A zoom into the red giant branch region, whose metallicity distribution is studied in Nitschai et al. (2024).
Figure from Nitschai et al. 2024

The age-metallicity relation for the stars in ω Cen would give important insights into its formation history. However, the age-spread in ω Cen is debated and estimates range from 0.5 Gyrs (Tailo et al., 2016), 1-2 Gyrs (Joo & Lee, 2013) to 4-5 Gyrs (Villanova et al., 2007).
In this new work, led by Callie Clontz, we revisited this topic, making use of the significantly enlarged stellar sample (provided by our new catalogs) and updated isochrone models. Stellar ages were determined by fitting isochrones in the $m_{\mathrm{F606W}} - m_{\mathrm{F814W}}$ color-magnitude diagram (see Figure 8.3), while also making use of the additional constraints provided by spectroscopic metallicities. We restricted the sample to around 8000 sub-giant stars, as their position in the color-magnitude diagram is less sensitive to Helium variations. The isochrones were built from the Dartmouth Stellar Evolution Database (Dotter et al., 2007, 2008). To accurately model the effect of light elements (C,N,O) we used the relation between the abundance of (C+N+O) and the metallicity as found by Marino et al. (2012).

The resulting age-metallicity distribution is shown in Figure 8.4. When comparing the age distribution in different metallicity bins (Figure 8.4, *left*), we can see an overall trend towards higher metallicities for younger stars, something that is expected in a self-enrichment scenario. However, we also see an apparent bimodal age distribution for most metallicities, which becomes especially visible when plotting individual ages and metallicities (see Figure 8.4, *right*). This bimodal structure shows a tight sequence (indicative of a potential long uninterrupted period of self-enrichment) and a more diffuse sequence, potentially related to an ex-situ population. However, surprisingly, the tight (potential in-situ) sequence lies at lower metallicities. To further constrain the origin of these different sequences, we will target a sample of ~130 stars with high-resolution spectroscopic observations

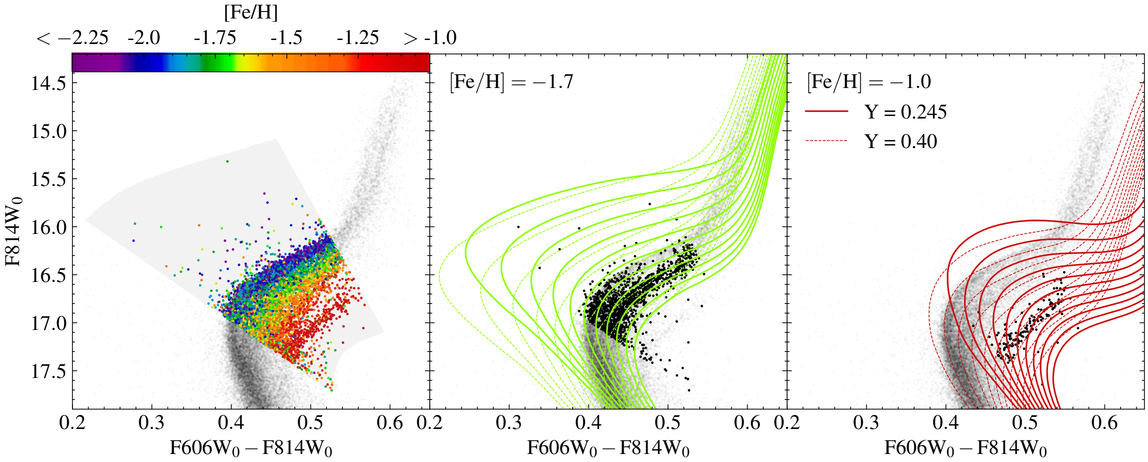

Figure 8.3: All three panels show the $m_{\mathrm{F606W}} - m_{\mathrm{F814W}}$ color-magnitude diagram of ω Cen. In the left panel, we marked the sub-giant branch region selected for studies of the age-metallicity region; the stars are color-coded by their metallicity. In the center panel, we show stars with low metallicity ($-1.75 < [\mathrm{Fe/H}] < -1.65$) and corresponding grids of isochrones with either primordial (Y=0.245, solid lines) or enhanced (Y=0.4, solid lines) Helium fractions. The ages of the isochrones range from 5 to 15 years. The right panel is similar but focuses on stars with high metallicities. One can see that in the selected SGB region, the effect of Helium variations is minimized.
Figure from Clontz et al. 2024

using the VLT FLAMES/GIRAFFE multi-object spectrograph[1]. This will reveal individual elemental abundances and provide information about the origins of the two sequences.

8.1.4 HELIUM ENRICHMENT

This work has been submitted to The Astrophysical Journal and is currently under review. The pre-print is available as Clontz et al. (2025): "oMEGACat V: Helium Enrichment in ω Centauri as a Function of Metallicity"

A spread of Helium abundances is another feature of the multiple stellar population phenomena of many globular clusters including ω Cen (Milone et al., 2018). However, measuring the precise Helium content of stars is observationally challenging, as the Helium sinks below the observable photospheric layers due to diffusion effects. In this new work, led by Callie Clontz, we aim to constrain the Helium mass fraction and its metallicity for a sample of $\sim$7200 red-giant branch stars in ω Cen. We estimate the Helium enhancement by studying the position of stars in the chromosome-diagram (see Figure 8.5, *left*) and by using the spectroscopic metallicities to isolate stars in a narrow range of metallicity. We then use synthetic spectra to correct for the effect of other elemental abundances. This allows us to isolate Helium's contribution to the shape of the chromosome map and measure it.
Our results show that there are subpopulations with significant Helium enhancement at all metallicities. The Helium enhancement increases from $\Delta Y = 0.1$ at low metallicities, towards $\Delta Y \approx 0.15$ at intermediate and high metallicities (Figure 8.5, *lower right*). The fraction of Helium enriched stars

---

[1] Program ID: GO-115.28D6, PI: C. Clontz

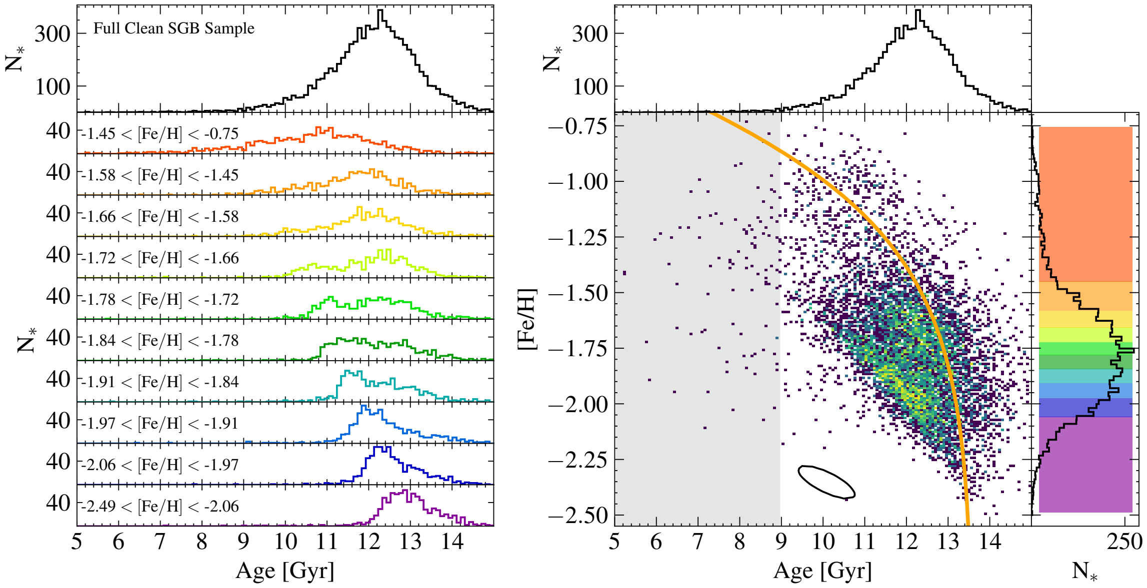

Figure 8.4: This plot shows two representations of the age-metallicity relation of ω Cen. In the left panel we split the dataset into 10 equally populated metallicity bins and study the distribution of stellar ages. In the right panel, we show the distribution of ages and metallicities in a 2D histogram. One can see a bimodal structure with one relatively tight sequence and a more diffuse component. The age-metallicity relation for Gaia-Sausage/Enceladus as measured by Limberg et al. (2022) is indicated with an orange line.
Figure from Clontz et al. 2024

shows a steady increase with metallicity ranging from 10% at [Fe/H]-2.04 to over 90% at [Fe/H]-1.04 (Figure 8.5, *upper right*).

8.1.5 STUDIES OF THE INTERSTELLAR AND INTRACLUSTER MEDIUM

This work is led by Zixian Wang (University of Utah). A publication is currently in preparation.

The large number of stars with high signal-to-noise VLT MUSE spectra contained in the oMEGACat dataset can also directly probe the foreground extinction independent of the photometry. To do this we select a sample of 1119 hot stars ($T_{\rm eff} > 7500$ K) with high S/N and studied the equivalent width of the Na I D absorption line at the line-of-sight velocity $v_{\rm NaI}$ =-14 km s^{-1}, which is proven to correlate with reddening (e.g. van Loon et al., 2009; Poznanski et al., 2012). This is an effective method, as the spectra of these hot stars only contain very small intrinsic absorption features from their photosphere, and the Na I absorption feature is purely caused by the interstellar medium in the foreground. The measured equivalent width shows a clear spatial variation (see Figure 8.6) that is well correlated with the differential reddening maps derived in Chapter 3 (Figure 3.17). We also analyzed the data to probe for any signs of intracluster extinction by searching for the Na I D line at ω Cen's line-of-sight velocity ($\sim$234 km s^{-1}) using stars with $T_{\rm eff} > 10,000$ K, but did not detect any significant effect.

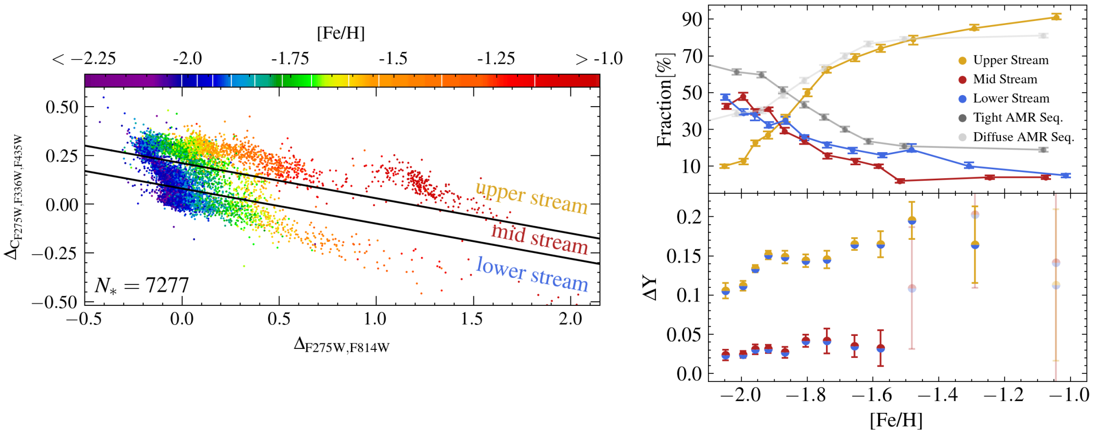

Figure 8.5: *Left:* Pseudo-color ("chromosome") diagram of red giant branch stars in ω Cen based on our HST photometry and color-coded by metallicity. We use this diagram to separate the sample into different streams. The stars on the upper stream show significant Helium enhancements, while the stars on the lower stream have only small (close to primordial) Helium fractions. *Upper right:* Relative contribution of the different streams at different metallicities. *Lower right:* Evolution of Helium enhancement (ΔY) with metallicity.
Figure from Clontz et al. 2025

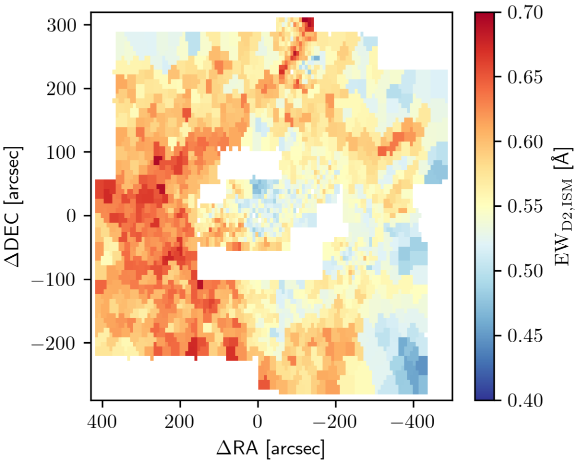

Figure 8.6: Equivalent width of the Na I D line as measured from Voronoi binned MUSE spectra. The Na I absorption feature is caused by the interstellar medium in the line-of-sight and correlates well with the differential reddening correction determined in Figure 3.17. The gaps in the map are due to some pointings being observed with adaptive optics using Sodium laser guide stars (prohibiting observations close to their wavelength).
Figure provided by Zixian Wan, University of Utah

8.1.6 INDIVIDUAL ELEMENTAL ABUNDANCES

The original spectroscopic data-reduction used for the creation of the oMEGACat I catalog (see Nitschai et al. 2023 and Subsection 8.1.1) only fit for the overall metallicity [M/H] in the VLT MUSE spectra of ω Cen's stars. Determining individual abundances would help to further constrain the formation mechanisms for the different subpopulations, but is challenging due to the high signal-to-noise required for such measurements and the comparatively low spectral resolution of the MUSE instrument. At the moment we follow three different approaches to overcome these challenges:

Stacked spectra (Project led by Simona di Stefano, INAF Trieste)
One way to improve the signal-to-noise in the existing MUSE spectra is to stack the spectra of multiple stars belonging to the same subpopulation (as identified using HST photometry). The stacked spectra can reveal weak spectral absorption lines that remain hidden in individual spectra.

Abundance determination using DD-Payne (Project led by Zixian Wang, University of Utah)
Another way to obtain improved abundance constraints for individual stars from low-res spectra is to use machine learning algorithms that have been trained on large datasets with known stellar abundances. One such method is "DD-PAYNE" (Xiang et al., 2019; Ting et al., 2017). It has already been successfully applied to VLT MUSE data (Wang et al., 2022). When applying it to our spectroscopic ω Cen data we can measure the Na-O anti-correlation for a large sample of bright stars, see Figure 8.7. The results are compatible with the high-resolution study of Johnson & Pilachowski (2010).

New high-resolution observations (Project led by Callie Clontz, MPIA & University of Utah)
The most direct way to obtain precise stellar abundances within our sample is to conduct follow-up observations with high-resolution spectroscopy. However, this is only possible for well-justified small samples of bright stars. C. Clontz has successfully proposed a VLT FLAMES program that will measure precise abundances for $\sim$130 subgiant branch stars selected using ω Cen's age-metallicity relation (see also Subsection 8.1.3).

8.1.7 UPDATED DYNAMICAL MODELS OF ω CEN

To infer the mass distribution within ω Cen, we have to compare (or fit) dynamical models with kinematic observations. Several works have done this using a variety of datasets and modeling techniques (e.g. van de Ven et al., 2006; Noyola et al., 2008, 2010; van der Marel & Anderson, 2010; Watkins et al., 2013; Zocchi et al., 2019; Baumgardt et al., 2019b; Bañares-Hernández et al., 2025). Despite these efforts, several properties are still not fully constrained.
Our new kinematic detailed measurements for the inner region of ω Cen provide both a challenge and an opportunity for future dynamical models. Within our collaboration, we are tackling this question using three different modeling methods:

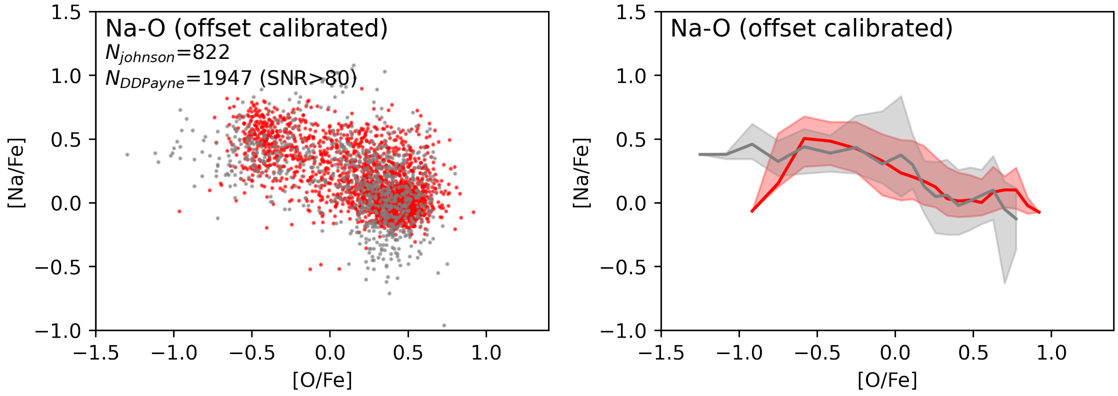

Figure 8.7: *Left:* This plot shows the Natrium (Na) elemental abundance plotted against the Oxygen (O) abundance. Grey dots are measurements from (Johnson & Pilachowski, 2010) obtained using high-resolution spectroscopy, red dots correspond to our new measurements obtained using the DD-PAYNE method on VLT MUSE spectra. The two methods show good agreement. *Right:* Median and width of the Na-O anticorrelation for both datasets.
Figure provided by Zixian Wan, University of Utah

Jeans Modelling (Project led by Renuka Pechetti, Liverpool John Moores University)

Anisotropic Jeans models are a common tool to model stellar kinematics of galaxies (Cappellari, 2008, 2015). They can be used to derive a mass profile based on solving the Jeans equation and have been applied to various globular clusters (see references in Table 1.1).

Orbit-based models (Project led by Peter Smith, MPIA)

Another modeling method, that does not place constraints on the functional form of the distribution function and provides a more flexible (but also computationally more expensive) framework for dynamical modeling are so called Schwarzschild models (Schwarzschild, 1979). In this model, the observed kinematics are described by a superposition of individual stellar orbits. We will use the DYNAMITE code (Jethwa et al., 2020). Currently, this code only supports binned line-of-sight data (see Figure 8.8 for a preliminary application to ω Cen) but future upgrades will allow to also take into account the extensive proper motion information and, eventually, unbinned data from individual stars. These models can also be combined with additional information about the stellar populations within a system, allowing them to constrain the kinematics of subpopulations.

N-Body models (Project led by Holger Baumgardt, University of Queensland)

A different approach to derive the dynamic properties of a globular cluster can be taken by comparing the result of a large grid of N-Body simulations with observed cluster kinematics (see e.g. Baumgardt, 2017; Baumgardt et al., 2019b, and also Figure 4.10). This has the advantage that the N-body models naturally include stellar dynamical effects (such as relaxation and stellar evolution) and will automatically lead to physical solutions. One challenge for this method is the high number of stars in a massive cluster such as ω Cen which contains one or two orders

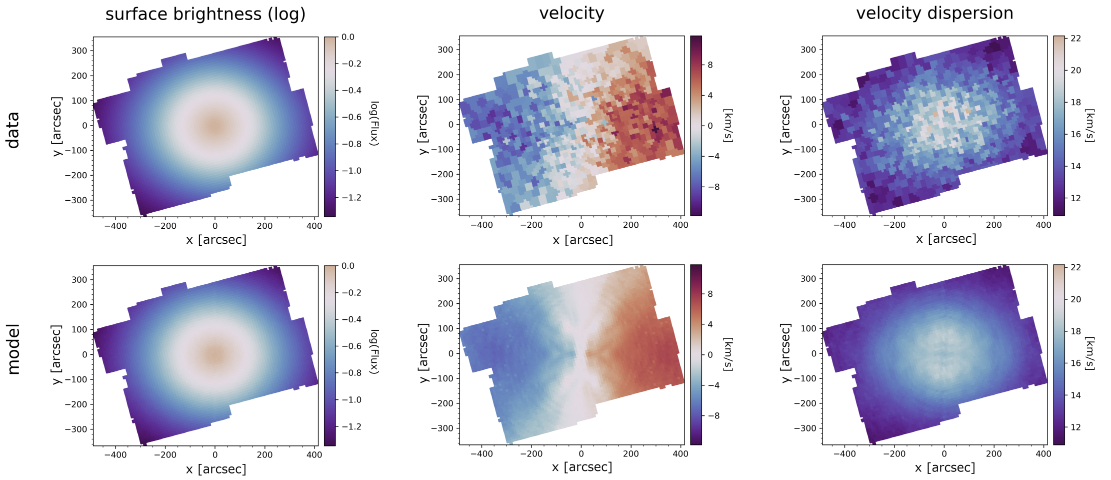

Figure 8.8: This figure shows preliminary results for an orbit-based dynamical model fit to binned line-of-sight velocity data. The upper row shows the observations (including the surface brightness profile, the binned mean line-of-sight velocity, and the velocity dispersion), and the lower row shows the best-fit model.
Figure provided by Peter Smith, Max Planck Insitute for Astronomy, Heidelberg

of magnitude more stars than what can be modeled with direct N-body simulations. Therefore, the simulations have to be rescaled. To better constrain the mass of the IMBH in ω Cen we are currently running N-body models with various IMBH masses and a higher number of particles.

8.1.8 Search for photometric microlensing events

This work is led by undergraduate student Zack Freeman at the University of Utah. I co-supervise him together with Prof. Anil Seth (also University of Utah).

Thousands of stellar mass black holes are expected within the core of ω Cen (Zocchi et al., 2019; Baumgardt et al., 2019a; Dickson et al., 2024; Bañares-Hernández et al., 2025), however, their exact mass and distribution is highly uncertain. One potential way to detect black holes in ω Cen is using the technique of photometric microlensing. The chance alignment between a star in the background and a stellar-mass black hole in the line of sight can lead to an apparent increase in the brightness of the star. Zaris et al. (2020) predicted the rate of detectable events in ω Cen based on assumptions about the black hole distribution. Using a threshold for the minimum detectable magnification of $\Delta\text{mag} = 0.05$ (5 times the photometric precision of HST for bright stars) a rate between $0.1 - 0.4\,\text{yr}^{-1}$ detectable events is expected. The photometric time series of HST observations in the F606W filter with 11 years of continuous observations and a sampling of a few months provides a unique opportunity to search for these events and any detection (or non-detection) would help to constrain the black hole population.

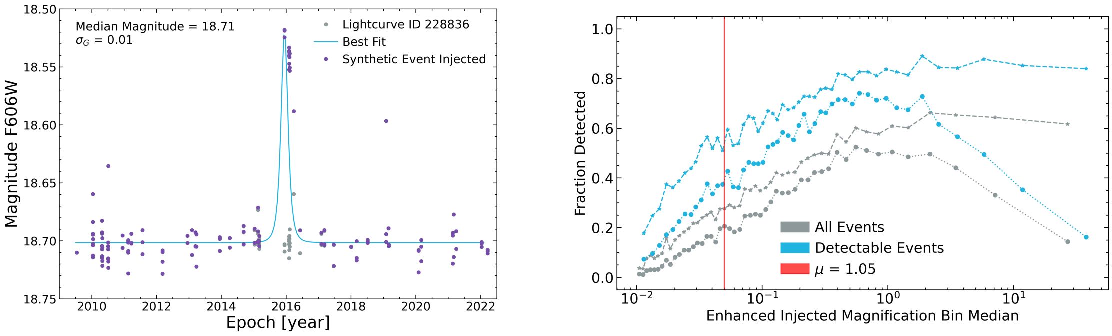

Figure 8.9: *Left:* Example for a synthetic microlensing lightcurve for a star within ω Cen. It is created by taking the real measured star (grey dots) and injecting a synthetic microlensing event (purple dots). The resulting best-fit of a model light curve is shown in light blue. *Right:* This plot shows how the fraction of detected (synthetic) microlensing events depends on the maximum magnification of the event. To optimize our algorithms, we differentiate between all events and detectable events (whose magnified phase is sufficiently sampled by datapoints). For the theoretically detectable events with a magnification of at least 0.05 mag we detect a high fraction of 60-80%.
Figure provided by Zack Freeman, University of Utah

At the time of writing, we are in the end phase of a project aimed at finding these microlensing events in the F606W data. Finding the handful of expected events within more than 100,000 lightcurves is a challenging task, and several potential contaminants (such as hot pixels, diffraction artifacts of bright stars, and close stars) that influence the photometry have to be taken into account. To optimize our search and rejection algorithms, we first created a set of synthetic lightcurves by injecting physically motivated microlensing events into the observed lightcurves (see Figure 8.9, *left*). Preliminary results indicate a high detection fraction of more than 50% for events with $\Delta\text{mag} > 0.05$ (see Figure 8.9, *right*), but both the analysis and the optimization of search algorithms are still ongoing.

8.1.9 SEARCH FOR ASTROMETRIC BINARIES

This work is led by undergraduate student Matthew Whitaker at the University of Utah. I co-supervise him together with Prof. Anil Seth (also University of Utah).

Another way to probe for stellar mass black holes in ω Cen is by searching for binary stars with unseen high-mass companions. This search can be done using multi-epoch spectroscopic observations and has revealed the presence of two stellar-mass black holes in the globular cluster NGC3201 (Giesers et al., 2018). Similar datasets exist for 47 Tuc (Müller-Horn et al., 2025) and ω Cen (Wragg et al., 2024, Saracino et al. *subm.*), however, these studies have found a dearth of short-period binaries that is in tension with model predictions.

Another observation channel that is more sensitive to long-period binaries are astrometric observations. The extensive HST observations of the center of ω Cen provide the necessary astrometric precision and long-temporal baseline for such binary studies. A recent paper (Platais et al., 2024) found four such astrometric binaries in ω Cen (including one neutron star candidate) using 11 years of F606W

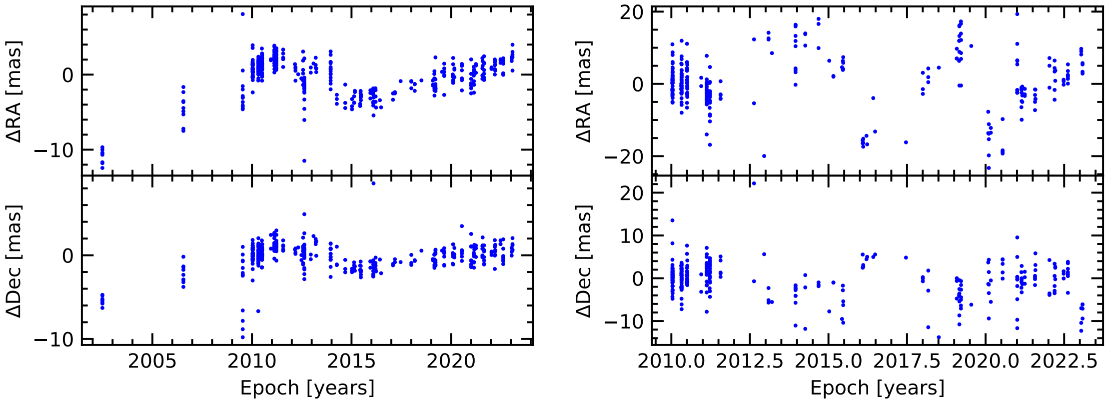

Figure 8.10: This figure shows the astrometric residuals (after subtracting a linear model) for two stars that are showing signs of periodic astrometric accelerations.
Figure provided by Matthew Whitaker, University of Utah

observations.

The dataset analyzed in Chapter 3 includes a longer temporal baseline and a larger number of individual observations due to using all available photometric filters. Also, we used advanced photometric techniques to counteract the effect of crowding on the observations (see Subsection 3.4.6). For this reason, we are currently re-doing the binary search and have already found several interesting candidates. Two examples of astrometric tracks with signs of periodic accelerations are shown in Figure 8.10.

8.2 KINEMATIC STUDIES OF ω CEN USING THE SDSS-V LOCAL VOLUME MAPPER

8.2.1 THE SDSS-V LOCAL VOLUME MAPPER

The SDSS-V Local Volume Mapper (LVM) is a novel wide-field integral field spectrograph, which was designed to map the interstellar gas emission of a large fraction ($> 4300\,\mathrm{deg}^2$) of the Southern Sky, with a focus on the Milky Way plane and the Magellanic Clouds. The instrument consists of four small telescopes in a siderostat configuration, each feeding an integral-field unit. The integral field units are connected to DESI-like spectrographs (Perruchot et al., 2018) that have a spectral range of $3600 - 9800$ Å and a mean resolution of $R \sim 4000$. An overview of the survey and the scientific motivations is given in Drory et al. (2024), and the telescope subsystem developed at the Max Planck Institute for Astronomy is described in Herbst et al. (2024).

8.2.2 MOTIVATION

Due to its coarse spatial scale (37 arcsec/spaxel; a factor of 1000 larger than of the HST observations used in Chapter 3) the LVM instrument is not able to resolve individual stars in a globular cluster such as ω Cen. However, at the same time, its wide field-of-view allows us to measure the integrated light properties of ω Cen in a single observation. By comparing the information we can extract from these integrated light spectra with our detailed observations of resolved stars (with e.g. the HST or the VLT MUSE integral field spectrograph) we can benchmark studies of extragalactic clusters, where resolved observations are not possible. The spatial resolution of the LVM for ω Cen is approximately 1 pc, similar to what can be achieved with VLT MUSE wide field mode at the distance of M31. An earlier demonstration of this type of benchmarking experiment (using rebinned data instead of dedicated observations) is given in Boecker et al. (2020).

8.2.3 OBSERVATIONS AND DATASET

ω Cen was observed by the LVM on 2023-08-22 (1×900 s, LVM exposure number: 3499) and 2024-07-05 (3×900 s, LVM exposure numbers: 20836-20838). The first observation was taken during the early commission phase and, therefore, does not come with a full set of calibrations. The second dataset was taken when the survey was already in full operation and all necessary calibrations were available. For this reason, we focus on the second dataset. The basic data reduction was performed using the standard LVM data-reduction pipeline (DRP), Version v1.1.0 (A. Mejia in prep.).

The dataset consists of three individual integrations, all pointed at the photometric center of ω Cen. A footprint of the observations is shown in Figure 8.11 (*left*). The hexagonal field of view reaches out to around 3 half-light radii of ω Cen. The mean flux in the individual spectra is dependent on the decreasing surface brightness of ω Cen and spans a wide range from ($\overline{f} = 5.4 \times 10^{-13}$ erg $\mathrm{s}^{-1}\mathrm{cm}^{-2}$ Å^{-1}; $(\mathrm{S/N})_{\mathrm{CaI}}$ ≈47) in the center to ($\overline{f} = 6.4 \times 10^{-15}$ erg $\mathrm{s}^{-1}\mathrm{cm}^{-2}$ Å^{-1}; $(\mathrm{S/N})_{\mathrm{CaI}}$ ≈2.9) at the edge of the field, see Figure 8.11 (*upper right*) for a selection of representative spectra.

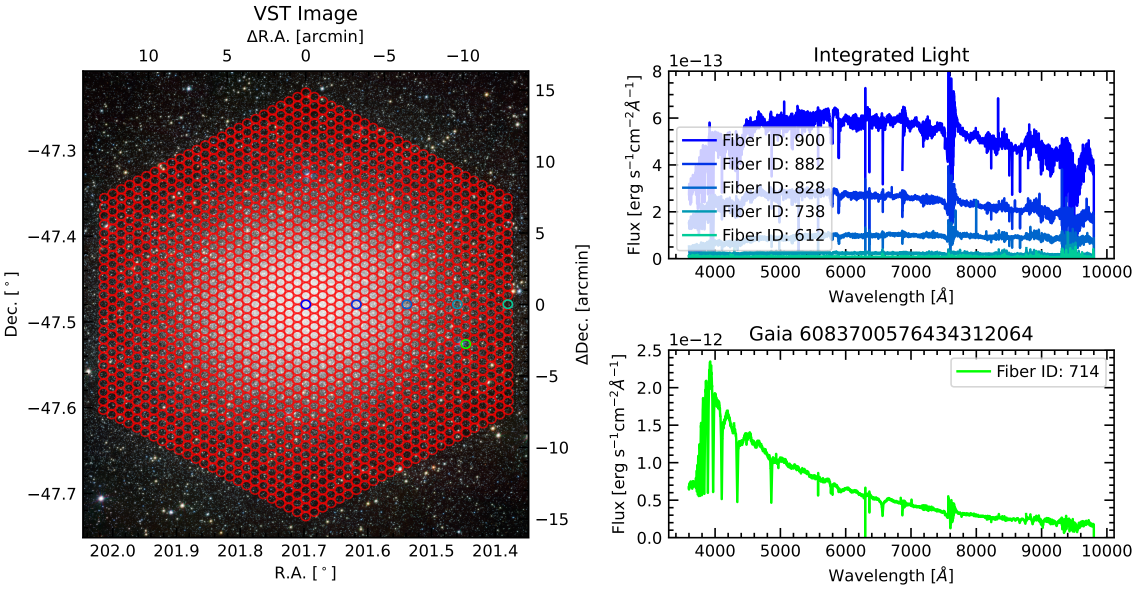

Figure 8.11: *Left:* Footprint of the SDSS-V Local Volume Mapper observations plotted over a wide-field image taken with the VST Survey Telescope. The individual spaxels are indicated as red circles. We mark 6 individual fibers with different colors and show their measured spectra on the right. *Top right:* 5 exemplary spectra from different radii that are dominated by the integrated light of ω Cen. *Bottom right:* Spectrum dominated by the emission of a single, hot, 9th magnitude star.
Background Image Credit: ESO/INAF-VST/OmegaCAM. Acknowledgement: A. Grado, L. Limatola/INAF-Capodimonte Observatory, https://www.eso.org/public/images/eso1119b/*)*

Especially at larger radii (where the flux contribution from ω Cen starts to decrease) individual bright foreground stars can dominate the flux in a spectrum. The most spectacular case is shown in the *lower right* of Figure 8.11, where we see the spectrum of a single hot star with a Gaia G magnitude of 8.8 mag. The star has the Gaia DR3 source ID 6083700576434312064 and is likely an A type star at a distance of ∼500 pc.

To verify the flux calibration and also the astrometric registration of the observations we compare the total flux measured in the individual LVM spaxels with photometric data from the ESA Gaia mission. To do so, we calculate synthetic photometry from the individual LVM spectra in the Gaia G band using the package pyphot (Fouesneau, 2025). Then we determine which Gaia stars (from both DR3, Gaia Collaboration et al. 2023a, and FPR, Gaia Collaboration et al. 2023b) fall into each LVM spaxel and calculate their total magnitude. A comparison between the resulting Gaia flux-maps is shown Figure 8.12, overall we can observe good agreement between the space-based photometry and the flux from the LVM spectra. A detailed investigation of the reason behind individual outliers will be subject to a future analysis.

8.2.4 DETERMINATION OF KINEMATICS USING FULL-SPECTRUM FITTING

To obtain kinematic information we use the full-spectrum fitting code `ppxf` (Cappellari & Emsellem, 2004; Cappellari, 2017, 2023) to fit a superposition of stellar templates to the individual spectra

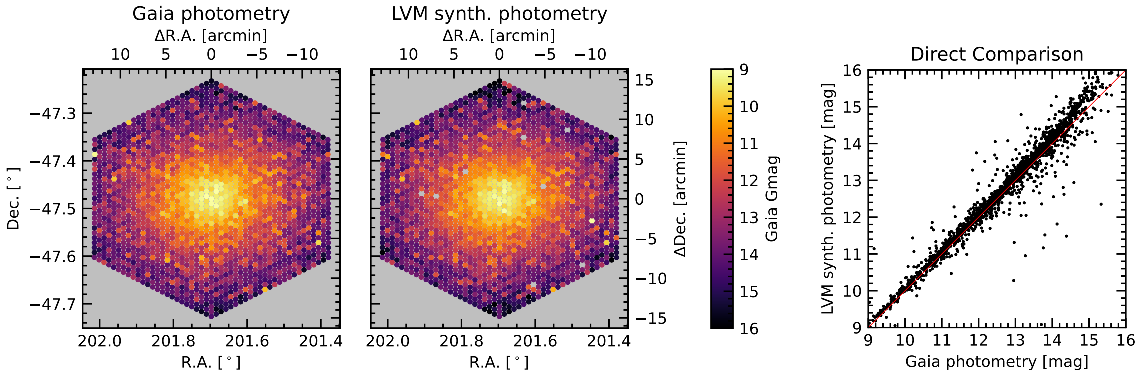

Figure 8.12: The two panels on the right show the total spatial flux distribution of ω Cen in the Gaia G band, either measured by combining the magnitudes of individual sources from the Gaia catalog (*left*), or by creating synthetic photometry using the spectra measured with the Local Volume Mapper (*center*). The rightmost panel directly compares the flux values for the individual spaxels. The good agreement between space-based photometry and ground-based spectroscopy is indicative of successful flux calibration.

in ω Cen. We use a subset of stellar templates from the PHOENIX library (Husser et al., 2013) with metallicities ranging from [M/H]=-2 to 0 and effective temperatures ranging from $T_{\mathrm{eff.}} = 3200\,\mathrm{K} - 11200\,\mathrm{K}$. For the preliminary kinematic analysis, we restrict the spectrum to a relatively narrow range between 8450 Å and 8750 Å, encompassing the three lines of the Calcium triplet. We normalize the spectrum in the selected wavelength range and exclude the region between 8610 Å and 8650 Å, as it shows an emission feature of unclear origin in the low S/N spectra. We then perform the `ppxf` fit with the mean line-of-sight velocity and the velocity dispersion as free parameters. The results for two exemplary individual spectra are shown in Figure 8.13.

To improve the S/N of the spectra we tested different schemes of combining the three integrations and to spatially bin the data. For the preliminary results presented in this work, we combined the normalized spectra of all 3 observations using the median. We also combined the spectra of each spaxel with its 6 neighboring spaxels, while excluding spaxels, in which more than 50% of the flux was contributed by a single source (as measured by Gaia), to remove biases from bright foreground stars. In the future, we plan to optimize this scheme and use adaptive spatial binning techniques such as Voronoi binning.

The resulting map of the mean-line of sight velocity is shown in Figure 8.14. To study the internal rotation, we subtract the systemic velocity of ω Cen ($234\,\mathrm{km\,s^{-1}}$) and a heliocentric correction ($21.57\,\mathrm{km\,s^{-1}}$). One can see a clear rotation pattern with robust measurements reaching around 2 half-light radii. The velocity dispersion is less well-constrained, which is not surprising, given that the line-spread function of the LVM has a width of 1.8 Å (corresponding to $\sigma \approx 27\,\mathrm{km\,s^{-1}}$, larger than the velocity dispersion in ω Cen). The signal-to-noise for the different combined spectra used for the analysis is shown in Figure 8.15. In the center the combined spectra reach high signals-to-noise ratios over 100 (enabling velocity measurements better than $1\,\mathrm{km\,s^{-1}}$). At larger radii the S/N drops below

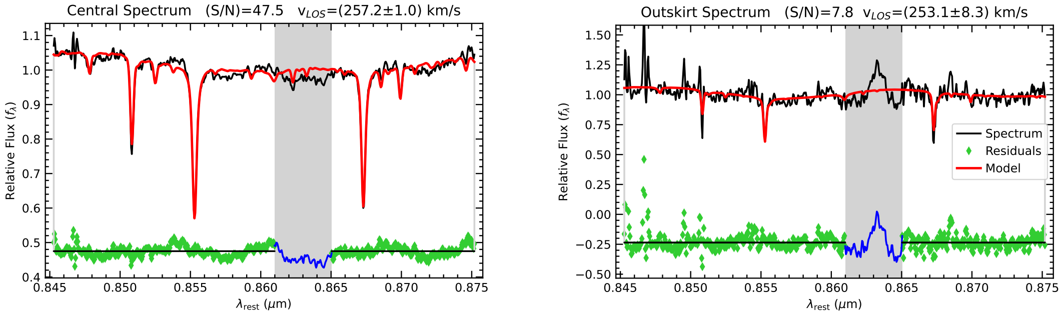

Figure 8.13: This plot shows examples for the results of a `ppxf` fit for a high (*left*) and a low (*right*) signal-to-noise spectrum. The measured normalized spectrum is shown in black, the best fit is shown in red and the residuals are shown in green. The wavelength range shaded in grey is excluded from the fit.

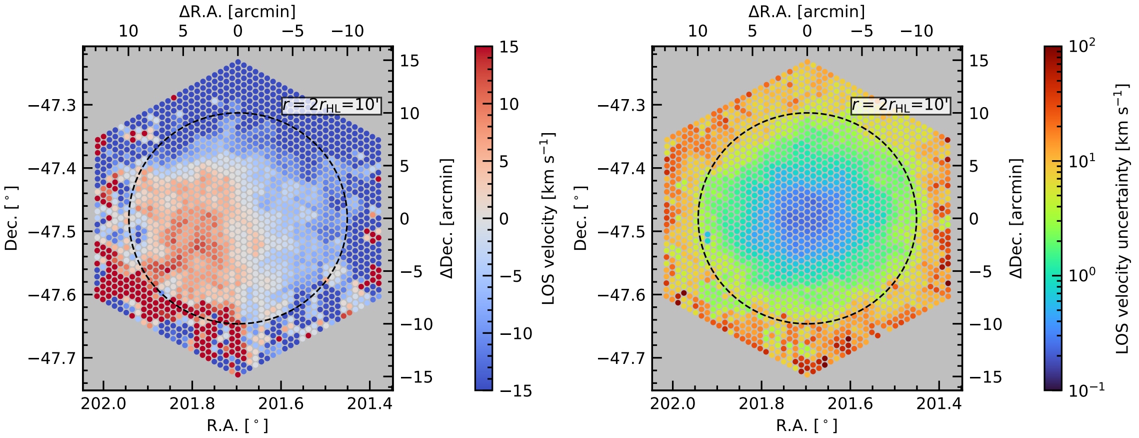

Figure 8.14: *Left:* Line-of-sight velocity map as measured with the LVM. The black dashed circle marks 2 half-light radii (10 arcmin). Beyond this radius, no robust velocities could be measured anymore. *Right:* Formal errors on the line-of-sight velocity measurements. These errors are likely underestimated and in the future we aim to perform a bootstrapping analysis to obtain more robust error estimates.

10, preventing precise measurements.

Within the half-light radius, we can compare the results of our kinematic analysis based on individual MUSE spectra (see Chapter 5; Figure 5.12) with the preliminary Local Volume Mapper results. Figure 8.16 shows a comparison of the mean line-of-sight velocity maps. Both maps show a similar rotation pattern. A direct comparison of velocities from spatially overlapping spaxels and MUSE bins is shown in the right panel of Figure 8.16; it shows good overall agreement, however, the uncertainties on the LVM velocities are too small to explain the scatter between the two datasets.

8.2.5 Next steps

We plan to improve the kinematic analysis of the LVM data by optimizing the binning scheme and by performing a more sophisticated estimation of uncertainties by using e.g. bootstrapping techniques. At larger radii, we can also compare the LVM results to kinematic measurements obtained using

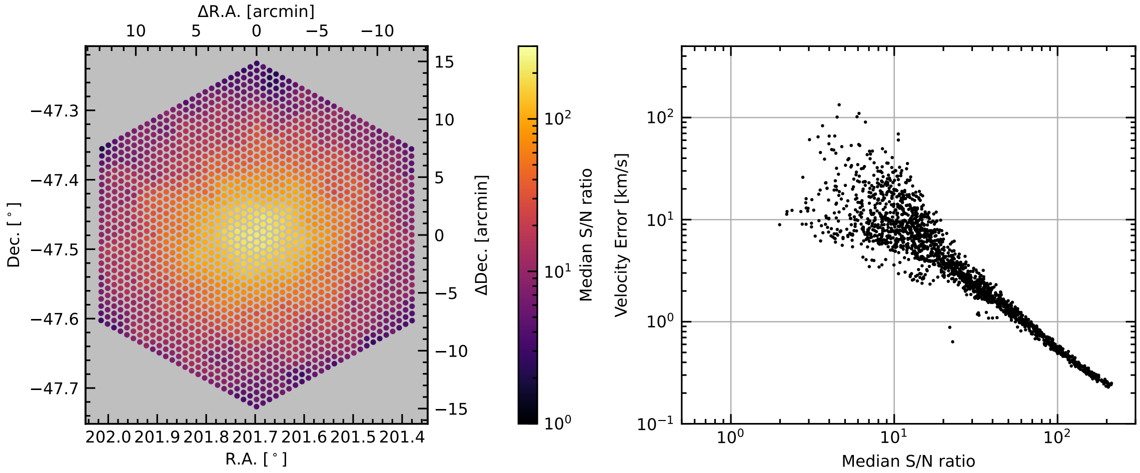

Figure 8.15: *Left:* Mean spectral signal-to-noise ratio for the spectra used to obtain the line-of-sight velocity fit (Figure 8.14). *Right:* Formal velocity errors plotted against the S/N to noise. There is a clear correlation between the two. At a S/N of about 10, the error on the velocity exceeds the expected rotation signal, which has an amplitude of around 7-10 km s^{-1}.

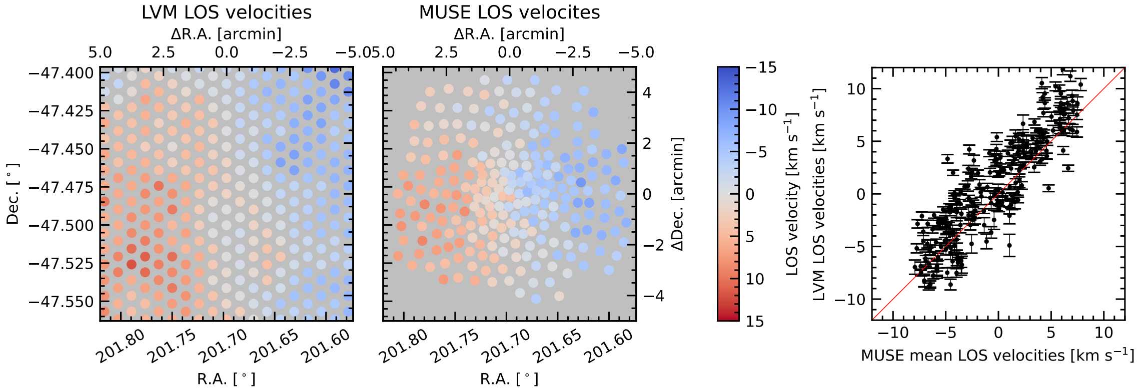

Figure 8.16: This figure shows a comparison between the mean line-of-sight velocity maps obtained either using integrated light with the Local Volume Mapper (*left panel*) or by measuring the mean velocity of individual stars using the oMEGACat I MUSE data (*center panel*, see also Figure 5.12). The direct comparison between spatially coinciding velocity measurements (*right*) shows overall good agreement, although the formal uncertainties on the LVM measurements are likely underestimated.

multi-object spectroscopy measurements as collected in Baumgardt & Hilker (2018).
In a second step in the analysis of the LVM data, we will also plan to use full spectral fitting to recover information on the stellar populations within ω Cen from the integrated light spectra, which then can be compared with the age-metallicity relation determined in Clontz et al. (2024).

8.3 Further constraints on the IMBH in ω Cen

The discovery of fast-moving stars in the center of ω Cen (see Chapter 4) has provided new evidence for an intermediate-mass black hole (IMBH) with a mass of at least 8200 $M_\odot$ based on simple escape velocity arguments. However, the exact mass of the black hole is still poorly constrained. Our statistical analysis and comparisons with N-Body models make a black hole in the range between 20,000 and 40,000 $M_\odot$ plausible (see Figure 4.9 and Figure 4.10). Obtaining better mass constraints is of high importance to confirm the nature of the IMBH and can also provide a unique data point for black-hole scaling relations towards lower masses (see Limberg, 2024, for a recent discussion in this context). In the following, I propose three different observing modes that can help to further characterize this unique system:

8.3.1 Astrometric acceleration measurements

The most direct measurement of the gravitational potential (and mass) of the black hole would be obtained by observing the accelerated motion of stars in its immediate surroundings, in analogy to the observed orbits in the Galactic Center (see Subsection 1.2.2 and Figure 4.11). However, the mass of the ω Cen black hole is likely around 2 orders of magnitude lower than the mass of Sgr A*, leading to much smaller accelerations and longer orbital periods. Assuming a black hole mass of 20,000 $M_\odot$, a star on a circular orbit with a separation of 0.5" would have an orbital period of $\sim$1000 years and experience an astrometric acceleration of $\sim$0.02 mas yr^{-1}.

Still, astrometric accelerations are not fully out of reach: additional observations with JWST NIRCam can yield significantly more precise astrometric measurements due to the better signal-to-noise for the faint, red, fast-moving stars and the slight increase in angular resolution; see Figure 8.17 (*left*) for a comparison between HST and JWST observations. With observations over the next $\sim$5 years, the existing constraints on the accelerations could be decreased by a factor of $\sim$ 2.5 (see Figure 8.17, *right*), leading either to an acceleration detection or meaningful upper limits.

8.3.2 Line-of-sight velocities for the fast-moving stars

Another important piece of information to fully constrain the orbits of the fast-moving stars lies in their line-of-sight velocities. Although the center of ω Cen was targeted with VLT MUSE Narrow Field Mode observations, only 3 of 7 fast-moving stars had a signal-to-noise high enough for line-of-sight velocity measurements. Line-of-sight velocities are still lacking for the four innermost stars, including the three fastest stars in the sample, which are the most constraining stars in terms of IMBH masses. Line-of-sight velocities for these stars could be measured either with deep VLT MUSE observation or with JWST NIRSpec IFU, for the latter an approved program is scheduled for mid-2025 (see Seth et al., 2024). By adding another velocity dimension, we also expect to detect additional fast-moving stars whose 2D velocity (inferred using the proper motions) is still below the escape velocity threshold.

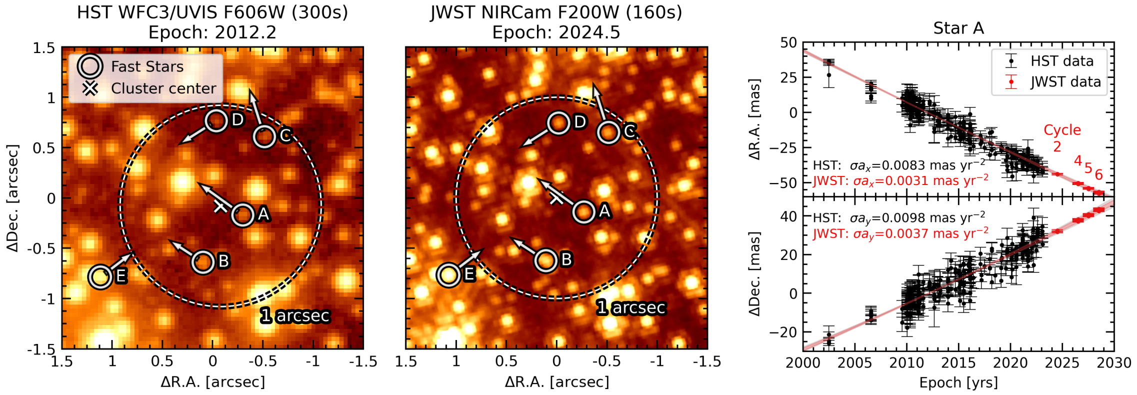

Figure 8.17: The two left panels compare a single HST WFC3/UVIS exposure and a single JWST NIRCam exposure. The JWST data has significantly higher resolution and a higher S/N for faint stars. The right panel shows how a combination of existing astrometric measurements (black) with a future JWST monitoring campaign (red) could yield significantly improved acceleration constraints for Star A from our fast-star sample.
JWST data provided by Oleg Kargaltsev

8.3.3 Accretion constraints

The stringent upper limits on any accretion emission at both X-ray (Haggard et al., 2013) and radio wavelengths (Tremou et al., 2018) make the black hole in the center of ω Cen the most weakly known accreting black hole known with an estimated Eddington luminosity $< 10^{-12}$ (see discussion in Subsection 4.2.2). The spectral energy distribution of other low-luminosity AGN such as Sgr A* peaks at mid-infrared / sub-millimeter wavelengths, making the James Webb Telescope (JWST) and the Atacama Large Millimeter Array (ALMA) the ideal tools to push the sensitivity of accretion searches to even lower limits.

Independent of the detection of the fast stars, a JWST program using deep near- and mid-infrared observations (Kargaltsev et al., 2023) has recently been observed (see Figure 8.17, *left*), and the data reduction is ongoing.

Our team has also successfully applied for observations in ALMA Cycle 11 (PI: Anil Seth, Proposal ID: 2024.1.00979.S). The observations will be conducted in ALMA Band 3 (100 GHz), and using an extended array configuration, leading to beam-sizes of under 0.3 arcsec. Both a non-detection and a detection would provide an important data point in this previously unconstrained part of the spectral energy distribution of the emission from ω Cen's IMBH.

8.4 Future observations with ELT MICADO

The firm lower limit for an IMBH in ω Cen provides an important step for the search for central black holes in massive star clusters in the local universe. However, as ω Cen is not a typical globular cluster but a stripped galactic nucleus, the question of whether regular globular clusters host IMBHs is still unresolved. Our work can serve as a blueprint for future searches, but in some sense ω Cen is a

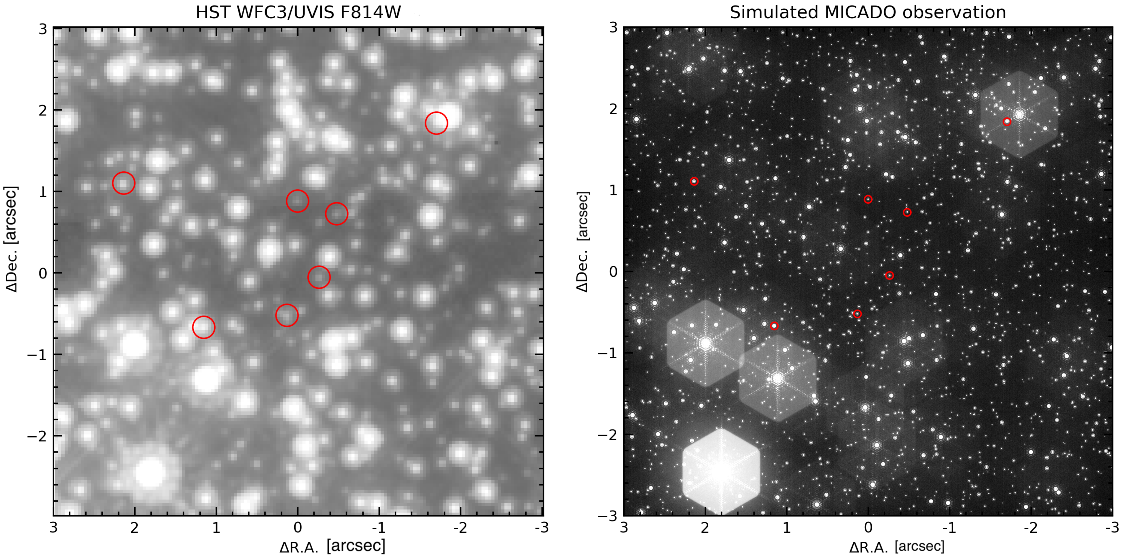

Figure 8.18: In this figure, I compare the state-of-the-art observations of the center of ω Cen with HST WFC3/UVIS (*left*) with simulated future observation with ELT MICADO (*right*). The red circles mark the location of the known fast-moving stars (see Chapter 4). ELT MICADO will be able to fully resolve the cluster, likely leading to the detection of additional fast moving stars even closer to the IMBH.

"relatively easy" case: it is relatively close, not particularly crowded, and has been extensively observed with the HST due to its selection as a calibration field. In addition, its IMBH is fairly massive. For many other globular clusters, even the resolution of the current best telescopes (HST, JWST, and adaptive-optics-assisted ground-based imagers) is not sufficient to resolve their crowded innermost regions, and future instrumentation will be required to enable better observations.

In the next decade, we will see the first light of the Extremely Large Telescope (ELT), built by the European Southern Observatory. With its 39 m diameter main mirror, it will achieve sensitivities comparable to the JWST, but at a four times higher resolution. One of the first instruments will be the near-infrared MICADO instrument (Davies et al., 2021), which will enable diffraction-limited observations between 0.8-2.4 µm. Its pixel scale in high-res mode will be just 1.5 mas, a factor of ~27 better than that of the HST observations used in this thesis.

In the case of ω Cen this will allow to fully resolve the cluster, likely yielding astrometric acceleration measurements and additional faint fast-moving stars even closer to the IMBH; see Figure 8.18 for a comparison of predicted MICADO observations (using the `ScopeSim` simulation software; Leschinski et al. 2020) with state-of-the-art HST observations.

Having high-resolution instruments such as ELT MICADO will be even more important for other more distant or more crowded globular clusters (such as M54, 47 Tuc, NGC 6388). With only a few years of temporal baseline, ELT MICADO observations will enable the detection of or place conclusive limits on the existence of massive black holes in several of the Milky Way's most massive globular clusters and we are awaiting an exciting era of new discoveries.

List of Figures

LIST OF TABLES

Publication list

The following list contains all publications to which I contributed during my PhD. The four first author publications that constitute this thesis are marked in bold.

1. **“oMEGACat. VI. Analysis of the overall kinematics of Omega Centauri in 3D: velocity dispersion, kinematic distance, anisotropy, and energy equipartition” Häberle, Neumayer, Clontz et al.** *(Submitted to ApJ, see Chapter 5)*
2. “oMEGACat V: Helium Enrichment in ω Centauri as a Function of Metallicity” Clontz, Seth, Wang et al. arXiv, arXiv:2412.09783 (2024)
3. “oMEGACat. IV. Constraining the Ages of Omega Centauri Subgiant Branch Stars with HST and MUSE” Clontz, Seth, Dotter et al. ApJ, 977, 14 (2024)
4. “The SDSS-V Local Volume Mapper Telescope System” Herbst, Bizenberger, Blanc et al. AJ, 168, 267 (2024)
5. “The SDSS-V Local Volume Mapper (LVM): Scientific Motivation and Project Overview” Drory, Blanc, Kreckel et al. AJ, 168, 198 (2024)
6. “Author Correction: Fast-moving stars around an intermediate-mass black hole in ω Centauri” Häberle, Neumayer, Seth et al. Nature, 634, E1 (2024)
7. “The GRAVITY+ Project: GRAVITY-Wide and the Beam Compressor Differential Delay Lines” Gravity+ Collaboration, Abuter, Allouche et al. Msngr, 193, 37 (2024)
8. “Hubble Space Telescope proper motions of Large Magellanic Cloud star clusters: I. Catalogues and results for NGC 1850” Niederhofer, Bellini, Kozhurina-Platais et al. A&A, 689, A162 (2024)
9. “Building an ELT simulator in the lab for subsystem testing of METIS/SCAO” Mortimer, Cárdenas Vázquez, Bertram et al. SPIE, 13097, 1309753 (2024)
10. “How to make METIS SCAO work” Bertram, Absil, Bizenberger et al. SPIE, 13097, 1309727 (2024)
11. “The SDSS-V Local Volume Mapper Survey Telescopes: from conception to science” Herbst, Bizenberger, Blanc et al. SPIE, 13094, 1309411 (2024)
12. **“oMEGACat. II. Photometry and Proper Motions for 1.4 Million Stars in Omega Centauri and Its Rotation in the Plane of the Sky” Häberle, Neumayer, Bellini et al. ApJ, 970, 192 (2024)**
13. “oMEGACat. III. Multiband Photometry and Metallicities Reveal Spatially Well-mixed Populations within ω Centauri’s Half-light Radius” Nitschai, Neumayer, Häberle et al. ApJ, 970, 152 (2024)
14. “Building a mini Extremely Large Telescope simulator” Mortimer, Cárdenas Vázquez, Bertram et al. eas..conf, 927 (2024)
15. “The SDSS-V Local Volume Mapper Instrument” Konidaris, Herbst, Froning et al. SPIE, 13096, 130961Z (2024)
16. **“Fast-moving stars around an intermediate-mass black hole in ω Centauri” Häberle, Neumayer, Seth et al. Nature, 631, 285 (2024)**
17. “VizieR Online Data Catalog: Astro-photometry of 23 LMC clusters (Niederhofer+, 2024)” Niederhofer, Bellini, Kozhurina-Platais et al. yCat, 368, J/A+A/689/A162 (2024)
18. “oMEGACat. I. MUSE Spectroscopy of 300,000 Stars within the Half-light Radius of ω Centauri” Nitschai, Neumayer, Clontz et al. ApJ, 958, 8 (2023)
19. **“Validating the local volume mapper acquisition and guiding hardware” Häberle, Herbst, Bizenberger et al. SPIE, 12184, 121846U (2022)**
20. “Construction, testing, and commissioning of the SDSS-V Local Volume Mapper telescope system” Herbst, Bizenberger, Blanc et al. SPIE, 12182, 121821Q (2022)

The following publications are based on work done before the start of my PhD:

1. "Performance and limitations of using ELT and MCAO for 50 µas astrometry" Rodeghiero, Arcidiacono, Pott et al. JATIS, 7, 035005 (2021)
2. "EDEN: Flare Activity of the Nearby Exoplanet-hosting M Dwarf Wolf 359 Based on K2 and EDEN Light Curves" Lin, Chen, Ip et al. AJ, 162, 11 (2021)
3. "Hunting for intermediate-mass black holes in globular clusters: an astrometric study of NGC 6441" Häberle, Libralato, Bellini et al. MNRAS, 503, 1490 (2021)
4. "Performance and limitations of using ELT and MCAO for 50 µas astrometry" Rodeghiero, Arcidiacono, Pott et al. SPIE, 11447, 114471Z (2020)
5. "Development of the MICADO Flat-field and Wavelength Calibration Unit: From Design to Prototyping" Rodeghiero, Häberle, Sauter et al. PASP, 132, 124501 (2020)
6. "EDEN: Sensitivity Analysis and Transiting Planet Detection Limits for Nearby Late Red Dwarfs" Gibbs, Bixel, Rackham et al. AJ, 159, 169 (2020)
7. "Development of the Warm Astrometric Mask for MICADO Astrometry Calibration" Rodeghiero, Sawczuck, Pott et al. PASP, 131, 054503 (2019)
8. "The MICADO first light imager for the ELT: preliminary design of the MICADO Calibration Assembly" Rodeghiero, Pott, Münch et al. SPIE, 10702, 107028U (2018)
9. "The MICADO first light imager for ELT: derotator design status and prototype results" Barboza, Pott, Rohloff et al. SPIE, 10702, 107028T (2018)

BIBLIOGRAPHY

Aarseth S. J., 2003, Gravitational N-Body Simulations

Abbott B. P., et al., 2016, Phys. Rev. Lett., 116, 061102

Abbott R., et al., 2020, Phys. Rev. Lett., 125, 101102

Abbott R., et al., 2023, Physical Review X, 13, 041039

Acernese F., et al., 2015, Classical and Quantum Gravity, 32, 024001

Adamo A., et al., 2020, Space Sci. Rev., 216, 69

Alfaro-Cuello M., et al., 2019, ApJ, 886, 57

Alfaro-Cuello M., et al., 2020, ApJ, 892, 20

Allende Prieto C., et al., 2008, Astronomische Nachrichten, 329, 1018

Anderson A. J., 1997, PhD thesis, University of California, Berkeley

Anderson J., 2003, in Arribas S., Koekemoer A., Whitmore B., eds, HST Calibration Workshop : Hubble after the Installation of the ACS and the NICMOS Cooling System. p. 13

Anderson J., 2006, in Koekemoer A. M., Goudfrooij P., Dressel L. L., eds, The 2005 HST Calibration Workshop: Hubble After the Transition to Two-Gyro Mode. p. 11

Anderson J., 2018, Focus-Diverse PSFs for Five Commonly Used WFC3/UVIS Filters, Instrument Science Report WFC3 2018-14, 19 pages

Anderson J., 2022, One-Pass HST Photometry with hst1pass, Instrument Science Report WFC3 2022-5, 55 pages

Anderson J., King I. R., 2003, AJ, 126, 772

Anderson J., King I. R., 2006, PSFs, Photometry, and Astronomy for the ACS/WFC, Instrument Science Report ACS 2006-01, 34 pages

Anderson J., van der Marel R. P., 2010, ApJ, 710, 1032

Anderson J., et al., 2008, AJ, 135, 2055

Antonini F., Gieles M., Gualandris A., 2019, MNRAS, 486, 5008

Arca Sedda M., et al., 2024, MNRAS, 528, 5119

Aros F. I., Vesperini E., 2023, MNRAS, 525, 3136

Aros F. I., Sippel A. C., Mastrobuono-Battisti A., Askar A., Bianchini P., van de Ven G., 2020, MNRAS, 499, 4646

Askar A., Bianchini P., de Vita R., Giersz M., Hypki A., Kamann S., 2017, MNRAS, 464, 3090

Askar A., Baldassare V. F., Mezcua M., 2023, arXiv e-prints, p. arXiv:2311.12118

Astropy Collaboration et al., 2022, ApJ, 935, 167

Bañares-Hernández A., Calore F., Martin Camalich J., Read J. I., 2025, A&A, 693, A104

Bacon R., et al., 2010a, in McLean I. S., Ramsay S. K., Takami H., eds, Society of Photo-Optical Instrumentation Engineers (SPIE) Conference Series Vol. 7735, Ground-based and Airborne Instrumentation for Astronomy III. p. 773508 (`arXiv:2211.16795`), doi:10.1117/12.856027

Bacon R., Accardo M., Adjali L., Anwand H., Bauer S., Biswas I., Blaizot J., Boudon D., 2010b, in McLean I. S., Ramsay S. K., Takami H., eds, Society of Photo-Optical Instrumentation Engineers (SPIE) Conference Series Vol. 7735, Ground-based and Airborne Instrumentation for Astronomy III. p. 773508 (`arXiv:2211.16795`), doi:10.1117/12.856027

Balbinot E., et al., 2024, A&A, 687, L3

Baldassare V. F., Reines A. E., Gallo E., Greene J. E., 2015, ApJ, 809, L14

Baldassare V. F., Geha M., Greene J., 2018, ApJ, 868, 152

Baldassare V. F., Geha M., Greene J., 2020, ApJ, 896, 10

Baldwin J. A., Phillips M. M., Terlevich R., 1981, PASP, 93, 5

Baldwin A. T., Watkins L. L., van der Marel R. P., Bianchini P., Bellini A., Anderson J., 2016, ApJ, 827, 12

Balick B., Brown R. L., 1974, ApJ, 194, 265

Bastian N., Lardo C., 2018, ARA&A, 56, 83

Baumgardt H., 2017, MNRAS, 464, 2174

Baumgardt H., Hilker M., 2018, MNRAS, 478, 1520

Baumgardt H., Makino J., 2003, MNRAS, 340, 227

Baumgardt H., Vasiliev E., 2021, MNRAS, 505, 5957

Baumgardt H., Hut P., Makino J., McMillan S., Portegies Zwart S., 2003a, ApJ, 582, L21

Baumgardt H., Makino J., Hut P., McMillan S., Portegies Zwart S., 2003b, ApJ, 589, L25

Baumgardt H., Hilker M., Sollima A., Bellini A., 2019a, MNRAS, 482, 5138

Baumgardt H., et al., 2019b, MNRAS, 488, 5340

Baumgardt H., Hénault-Brunet V., Dickson N., Sollima A., 2023, MNRAS, 521, 3991

Bedin L. R., Piotto G., King I. R., Anderson J., 2003, AJ, 126, 247

Bedin L. R., Piotto G., Anderson J., Cassisi S., King I. R., Momany Y., Carraro G., 2004, ApJ, 605, L125

Bedin L. R., King I. R., Anderson J., Piotto G., Salaris M., Cassisi S., Serenelli A., 2008, ApJ, 678, 1279

Begelman M. C., Volonteri M., Rees M. J., 2006, MNRAS, 370, 289

Bekki K., Freeman K. C., 2003, MNRAS, 346, L11

Belczynski K., Bulik T., Fryer C. L., Ruiter A., Valsecchi F., Vink J. S., Hurley J. R., 2010, ApJ, 714, 1217

Bellini A., Bedin L. R., 2009, PASP, 121, 1419

Bellini A., et al., 2009a, A&A, 493, 959

Bellini A., Piotto G., Bedin L. R., King I. R., Anderson J., Milone A. P., Momany Y., 2009b, A&A, 507, 1393

Bellini A., Bedin L. R., Piotto G., Milone A. P., Marino A. F., Villanova S., 2010, AJ, 140, 631

Bellini A., Anderson J., Bedin L. R., 2011, PASP, 123, 622

Bellini A., Anderson J., Salaris M., Cassisi S., Bedin L. R., Piotto G., Bergeron P., 2013, ApJ, 769, L32

Bellini A., et al., 2014, ApJ, 797, 115

Bellini A., Anderson J., Bedin L. R., King I. R., van der Marel R. P., Piotto G., Cool A., 2017a, ApJ, 842, 6

Bellini A., Anderson J., van der Marel R. P., King I. R., Piotto G., Bedin L. R., 2017b, ApJ, 842, 7

Bellini A., Milone A. P., Anderson J., Marino A. F., Piotto G., van der Marel R. P., Bedin L. R., King I. R., 2017c, ApJ, 844, 164

Bellini A., Bianchini P., Varri A. L., Anderson J., Piotto G., van der Marel R. P., Vesperini E., Watkins L. L., 2017d, ApJ, 844, 167

Bellini A., Anderson J., Grogin N. A., 2018a, Focus-diverse, empirical PSF models for the ACS/WFC, Instrument Science Report ACS 2018-8

Bellini A., et al., 2018b, ApJ, 853, 86

Bellm E. C., et al., 2019, PASP, 131, 018002

Belokurov V., Erkal D., Evans N. W., Koposov S. E., Deason A. J., 2018, MNRAS, 478, 611

Bhattacharya S., Heinke C. O., Chugunov A. I., Freire P. C. C., Ridolfi A., Bogdanov S., 2017, MNRAS, 472, 3706

Bianchini P., van de Ven G., Norris M. A., Schinnerer E., Varri A. L., 2016, MNRAS, 458, 3644

Bianchini P., van der Marel R. P., del Pino A., Watkins L. L., Bellini A., Fardal M. A., Libralato M., Sills A., 2018, MNRAS, 481, 2125

Binney J., Tremaine S., 1987, Galactic dynamics

Boecker A., Alfaro-Cuello M., Neumayer N., Martín-Navarro I., Leaman R., 2020, ApJ, 896, 13

Bohlin R. C., 2016, AJ, 152, 60

Böker T., et al., 2022, A&A, 661, A82

Bolton C. T., 1972, Nature Physical Science, 240, 124

Boyce H., Lützgendorf N., van der Marel R. P., Baumgardt H., Kissler-Patig M., Neumayer N., de Zeeuw P. T., 2017, ApJ, 846, 14

Brandl B., et al., 1996, ApJ, 466, 254

Bressan A., Marigo P., Girardi L., Salasnich B., Dal Cero C., Rubele S., Nanni A., 2012, MNRAS, 427, 127

Brodie J. P., Strader J., 2006, ARA&A, 44, 193

Bromm V., Loeb A., 2003, ApJ, 596, 34

Brown W. R., 2015, ARA&A, 53, 15

Brown G. E., Bethe H. A., 1994, ApJ, 423, 659

Buder S., et al., 2021, MNRAS, 506, 150

Cabrera T., Rodriguez C. L., 2023, ApJ, 953, 19

Calamida A., et al., 2017, AJ, 153, 175

Calamida A., et al., 2020, ApJ, 891, 167

Calamida A., Mack J., Medina J., Shanahan C., Bajaj V., Deustua S., 2021, New time-dependent WFC3 UVIS inverse sensitivities, Instrument Science Report WFC3 2021-4, 33 pages

Calamida A., et al., 2022, AJ, 164, 32

Cannon R. D., Stobie R. S., 1973, MNRAS, 162, 207

Cappellari M., 2008, MNRAS, 390, 71

Cappellari M., 2015, arXiv e-prints, p. arXiv:1504.05533

Cappellari M., 2017, MNRAS, 466, 798

Cappellari M., 2023, MNRAS, 526, 3273

Cappellari M., Copin Y., 2003, MNRAS, 342, 345

Cappellari M., Emsellem E., 2004, PASP, 116, 138

Chevance M., et al., 2020, Space Sci. Rev., 216, 50

Chilingarian I. V., Katkov I. Y., Zolotukhin I. Y., Grishin K. A., Beletsky Y., Boutsia K., Osip D. J., 2018, ApJ, 863, 1

Clontz C., et al., 2024, ApJ, 977, 14

Clontz C., et al., 2025, arXiv e-prints, p. arXiv:2412.09783

Colpi M., et al., 2024, arXiv e-prints, p. arXiv:2402.07571

Davies R., et al., 2021, The Messenger, 182, 17

De Silva G. M., et al., 2015, MNRAS, 449, 2604

Della Croce A., Pascale R., Giunchi E., Nipoti C., Cignoni M., Dalessandro E., 2024, A&A, 682, A22

Deng L.-C., et al., 2012, Research in Astronomy and Astrophysics, 12, 735

Desroches L.-B., et al., 2006, ApJ, 650, 88

Dickson N., Hénault-Brunet V., Baumgardt H., Gieles M., Smith P. J., 2023, MNRAS, 522, 5320

Dickson N., Smith P. J., Hénault-Brunet V., Gieles M., Baumgardt H., 2024, MNRAS, 529, 331

Dinescu D. I., van Altena W. F., Girard T. M., López C. E., 1999, AJ, 117, 277

Dong X.-B., Ho L. C., Yuan W., Wang T.-G., Fan X., Zhou H., Jiang N., 2012, ApJ, 755, 167

Dotter A., Chaboyer B., Jevremović D., Baron E., Ferguson J. W., Sarajedini A., Anderson J., 2007, AJ, 134, 376

Dotter A., Chaboyer B., Jevremović D., Kostov V., Baron E., Ferguson J. W., 2008, ApJS, 178, 89

Drinkwater M. J., Gregg M. D., Hilker M., Bekki K., Couch W. J., Ferguson H. C., Jones J. B., Phillipps S., 2003, Nature, 423, 519

Drory N., et al., 2024, AJ, 168, 198

Duras F., et al., 2020, A&A, 636, A73

Eckart A., Genzel R., 1996, Nature, 383, 415

Edelmann H., Napiwotzki R., Heber U., Christlieb N., Reimers D., 2005, ApJ, 634, L181

Einstein A., 1916, Annalen der Physik, 354, 769

Einstein A., 1918, Sitzungsberichte der Königlich Preussischen Akademie der Wissenschaften, pp 154–167

Eisenhauer F., et al., 2003, in Iye M., Moorwood A. F. M., eds, Society of Photo-Optical Instrumentation Engineers (SPIE) Conference Series Vol. 4841, Instrument Design and Performance for Optical/Infrared Ground-based Telescopes. pp 1548–1561 (`arXiv:astro-ph/0306191`), doi:10.1117/12.459468

El-Badry K., et al., 2023a, MNRAS, 518, 1057

El-Badry K., et al., 2023b, MNRAS, 521, 4323

Emsellem E., Monnet G., Bacon R., 1994, A&A, 285, 723

Erkal D., Boubert D., Gualandris A., Evans N. W., Antonini F., 2019, MNRAS, 483, 2007

Event Horizon Telescope Collaboration et al., 2019, ApJ, 875, L1

Event Horizon Telescope Collaboration et al., 2022a, ApJ, 930, L12

Event Horizon Telescope Collaboration et al., 2022b, ApJ, 930, L16

Fabricius C., et al., 2021, A&A, 649, A5

Fahrion K., et al., 2021, A&A, 650, A137

Fan X., Bañados E., Simcoe R. A., 2023, ARA&A, 61, 373

Farrell S. A., Webb N. A., Barret D., Godet O., Rodrigues J. M., 2009, Nature, 460, 73

Feldmeier A., et al., 2013, A&A, 554, A63

Fernández-Ontiveros J. A., López-López X., Prieto A., 2023, A&A, 670, A22

Ferrarese L., Merritt D., 2000, ApJ, 539, L9

Ferrarese L., et al., 2006, ApJ, 644, L21

Ferraro F. R., Sollima A., Pancino E., Bellazzini M., Straniero O., Origlia L., Cool A. M., 2004, ApJ, 603, L81

Forbes D. A., 2020, MNRAS, 493, 847

Forbes D. A., et al., 2018, Proceedings of the Royal Society of London Series A, 474, 20170616

Foreman-Mackey D., et al., 2013a, emcee: The MCMC Hammer, Astrophysics Source Code Library, record ascl:1303.002

Foreman-Mackey D., Hogg D. W., Lang D., Goodman J., 2013b, PASP, 125, 306

Fouesneau M., 2025, pyphot, doi:10.5281/zenodo.7016774

Fowler W. A., Hoyle F., 1964, ApJS, 9, 201

Freeman K. C., 2001, in Deiters S., Fuchs B., Just A., Spurzem R., Wielen R., eds, Astronomical Society of the Pacific Conference Series Vol. 228, Dynamics of Star Clusters and the Milky Way. p. 43

Freeman K. C., Rodgers A. W., 1975, ApJ, 201, L71

Fryer C. L., Kalogera V., 2001, ApJ, 554, 548

Fryer C. L., Belczynski K., Wiktorowicz G., Dominik M., Kalogera V., Holz D. E., 2012, ApJ, 749, 91

Fujii M. S., Wang L., Tanikawa A., Hirai Y., Saitoh T. R., 2024, Science, 384, 1488

GRAVITY Collaboration et al., 2017, A&A, 602, A94

GRAVITY Collaboration et al., 2018, A&A, 615, L15

GRAVITY Collaboration et al., 2019, A&A, 625, L10

GRAVITY Collaboration et al., 2020a, A&A, 636, L5

GRAVITY Collaboration et al., 2020b, A&A, 638, A2

Gaia Collaboration et al., 2016a, A&A, 595, A1

Gaia Collaboration et al., 2016b, A&A, 595, A2

Gaia Collaboration et al., 2021a, A&A, 649, A1

Gaia Collaboration et al., 2021b, A&A, 649, A1

Gaia Collaboration et al., 2023a, A&A, 674, A1

Gaia Collaboration et al., 2023b, A&A, 680, A35

Gaia Collaboration et al., 2023c, A&A, 680, A35

Gaia Collaboration et al., 2024, A&A, 686, L2

Gebhardt K., Kissler-Patig M., 1999, AJ, 118, 1526

Gebhardt K., et al., 2000, ApJ, 539, L13

Gebhardt K., et al., 2001, AJ, 122, 2469

Gebhardt K., Rich R. M., Ho L. C., 2002, ApJ, 578, L41

Gebhardt K., Rich R. M., Ho L. C., 2005, ApJ, 634, 1093

Geffert M., Hilker M., Geyer E. H., Krämer G. H., 2002, in van Leeuwen F., Hughes J. D., Piotto G., eds, Astronomical Society of the Pacific Conference Series Vol. 265, Omega Centauri, A Unique Window into Astrophysics. p. 399

Gehrels N., 1986, ApJ, 303, 336

Genzel R., Eckart A., Ott T., Eisenhauer F., 1997, MNRAS, 291, 219

Genzel R., Eisenhauer F., Gillessen S., 2024, A&A Rev., 32, 3

Gerasimov R., Burgasser A. J., Homeier D., Bedin L. R., Rees J. M., Scalco M., Anderson J., Salaris M., 2022, ApJ, 930, 24

Gerssen J., van der Marel R. P., Gebhardt K., Guhathakurta P., Peterson R. C., Pryor C., 2002, AJ, 124, 3270

Geyer E. H., Hopp U., Nelles B., 1983, A&A, 125, 359

Ghez A. M., Klein B. L., Morris M., Becklin E. E., 1998, ApJ, 509, 678

Ghez A. M., et al., 2008, ApJ, 689, 1044

Giacconi R., Gursky H., Paolini F. R., Rossi B. B., 1962, Phys. Rev. Lett., 9, 439

Gieles M., Zocchi A., 2015, MNRAS, 454, 576

Gieles M., Balbinot E., Yaaqib R. I. S. M., Hénault-Brunet V., Zocchi A., Peuten M., Jonker P. G., 2018a, MNRAS, 473, 4832

Gieles M., et al., 2018b, MNRAS, 478, 2461

Gieles M., Padoan P., Charbonnel C., Vink J. S., Ramírez-Galeano L., 2025, arXiv e-prints, p. arXiv:2501.12138

Giersz M., Heggie D. C., Hurley J. R., Hypki A., 2013, MNRAS, 431, 2184

Giersz M., Leigh N., Hypki A., Lützgendorf N., Askar A., 2015, MNRAS, 454, 3150

Giesers B., et al., 2018, MNRAS, 475, L15

Giesers B., et al., 2019, A&A, 632, A3

Gillessen S., Eisenhauer F., Trippe S., Alexander T., Genzel R., Martins F., Ott T., 2009, ApJ, 692, 1075

Gillessen S., et al., 2017, ApJ, 837, 30

Goldsbury R., Richer H. B., Anderson J., Dotter A., Sarajedini A., Woodley K., 2010, AJ, 140, 1830

Gomez S., Gezari S., 2023, ApJ, 955, 46

Górski K. M., Hivon E., Banday A. J., Wandelt B. D., Hansen F. K., Reinecke M., Bartelmann M., 2005, The Astrophysical Journal, 622, 759

Gravity Collaboration et al., 2023, A&A, 677, L10

Greene J. E., Ho L. C., 2004, ApJ, 610, 722

Greene J. E., Ho L. C., 2005, ApJ, 630, 122

Greene J. E., et al., 2019, arXiv e-prints, p. arXiv:1903.08670

Greene J. E., Strader J., Ho L. C., 2020, ARA&A, 58, 257

Gualandris A., Portegies Zwart S., 2007, MNRAS, 376, L29

Häberle M., et al., 2021, MNRAS, 503, 1490

Häberle M., et al., 2022, in Evans C. J., Bryant J. J., Motohara K., eds, Society of Photo-Optical Instrumentation Engineers (SPIE) Conference Series Vol. 12184, Ground-based and Airborne Instrumentation for Astronomy IX. p. 121846U (`arXiv:2207.05090`), doi:10.1117/12.2629246

Häberle M., et al., 2024a, Nature, 631, 285

Häberle M., et al., 2024b, ApJ, 970, 192

Haggard D., Cool A. M., Heinke C. O., van der Marel R., Cohn H. N., Lugger P. M., Anderson J., 2013, ApJ, 773, L31

Haiman Z., Loeb A., 2001, ApJ, 552, 459

Haller J. W., Rieke M. J., Rieke G. H., Tamblyn P., Close L., Melia F., 1996, ApJ, 456, 194

Han J. J., El-Badry K., Lucchini S., Hernquist L., Brown W., Garavito-Camargo N., Conroy C., Sari R., 2025, arXiv e-prints, p. arXiv:2502.00102

Häring N., Rix H.-W., 2004, ApJ, 604, L89

Harris W. E., 1996, AJ, 112, 1487

Harris W. E., 2010, arXiv e-prints, p. arXiv:1012.3224

Harris W. E., Harris G. L. H., Alessi M., 2013, ApJ, 772, 82

Harris C. R., et al., 2020, Nature, 585, 357

Haywood M., Di Matteo P., Lehnert M. D., Snaith O., Khoperskov S., Gómez A., 2018, ApJ, 863, 113

Heinis S., et al., 2016, ApJ, 826, 62

Helmi A., 2020, ARA&A, 58, 205

Helmi A., White S. D. M., 2001, MNRAS, 323, 529

Helmi A., White S. D. M., de Zeeuw P. T., Zhao H., 1999, Nature, 402, 53

Hénon M., 1961, Annales d'Astrophysique, 24, 369

Hénon M. H., 1971, Ap&SS, 14, 151

Herbst T. M., et al., 2020, in Society of Photo-Optical Instrumentation Engineers (SPIE) Conference Series. p. 114450J, doi:10.1117/12.2561419

Herbst T. M., et al., 2022, in Marshall H. K., Spyromilio J., Usuda T., eds, Society of Photo-Optical Instrumentation Engineers (SPIE) Conference Series Vol. 12182, Ground-based and Airborne Telescopes IX. p. 121821Q, doi:10.1117/12.2629354

Herbst T. M., et al., 2024, AJ, 168, 267

Herschel W., 1789, Philosophical Transactions of the Royal Society of London Series I, 79, 212

Hilker M., Richtler T., 2000, A&A, 362, 895

Hilker M., Kayser A., Richtler T., Willemsen P., 2004, A&A, 422, L9

Hills J. G., 1988, Nature, 331, 687

Ho L. C., Kim M., 2014, ApJ, 789, 17

Hofmann R., Blietz M., Duhoux P., Eckart A., Krabbe A., Rotaciuc V., 1992, in Ulrich M. H., ed., European Southern Observatory Conference and Workshop Proceedings Vol. 42, European Southern Observatory Conference and Workshop Proceedings. p. 617

Høg E., et al., 2000, A&A, 355, L27

Hoyer N., Neumayer N., Georgiev I. Y., Seth A. C., Greene J. E., 2021, MNRAS, 507, 3246

Huang Y., Li Q., Liu J., Dong X., Zhang H., Lu Y., Du C., 2024, arXiv e-prints, p. arXiv:2406.00923

Hulse R. A., Taylor J. H., 1975, ApJ, 195, L51

Hunter J. D., 2007, Computing in Science and Engineering, 9, 90

Husser T. O., Wende-von Berg S., Dreizler S., Homeier D., Reiners A., Barman T., Hauschildt P. H., 2013, A&A, 553, A6

Ibata R. A., Wyse R. F. G., Gilmore G., Irwin M. J., Suntzeff N. B., 1997, AJ, 113, 634

Ibata R., et al., 2009, ApJ, 699, L169

Ibata R. A., Bellazzini M., Malhan K., Martin N., Bianchini P., 2019, Nature Astronomy, 3, 667

Inayoshi K., Visbal E., Haiman Z., 2020, ARA&A, 58, 27

Iorio G., et al., 2024, A&A, 690, A144

Jalali B., Baumgardt H., Kissler-Patig M., Gebhardt K., Noyola E., Lützgendorf N., de Zeeuw P. T., 2012, A&A, 538, A19

Janesick J., Andrews J. T., Elliott T., 2006, in Dorn D. A., Holland A. D., eds, Society of Photo-Optical Instrumentation Engineers (SPIE) Conference Series Vol. 6276, Society of Photo-Optical Instrumentation Engineers (SPIE) Conference Series. p. 62760M, doi:10.1117/12.678867

Janesick J. R., Elliott T., Andrews J., Tower J., Pinter J., 2013, in Widenhorn R., Dupret A., eds, Society of Photo-Optical Instrumentation Engineers (SPIE) Conference Series Vol. 8659, Sensors, Cameras, and Systems for Industrial and Scientific Applications XIV. p. 865902, doi:10.1117/12.2008268

Jethwa P., Thater S., Maindl T., Van de Ven G., 2020, DYNAMITE: DYnamics, Age and Metallicity Indicators Tracing Evolution, Astrophysics Source Code Library, record ascl:2011.007

Johnson C. I., Pilachowski C. A., 2010, ApJ, 722, 1373

Joo S.-J., Lee Y.-W., 2013, ApJ, 762, 36

Jorden P. R., Jerram P. A., Fryer M., Stefanov K. D., 2017, Journal of Instrumentation, 12, C07008

Kaaret P., Feng H., Roberts T. P., 2017, ARA&A, 55, 303

Kacharov N., Neumayer N., Seth A. C., Cappellari M., McDermid R., Walcher C. J., Böker T., 2018, MNRAS, 480, 1973

Kacharov N., et al., 2022, ApJ, 939, 118

Kagra Collaboration et al., 2019, Nature Astronomy, 3, 35

Kamann S., Wisotzki L., Roth M. M., 2013, A&A, 549, A71

Kamann S., Wisotzki L., Roth M. M., Gerssen J., Husser T. O., Sandin C., Weilbacher P., 2014, A&A, 566, A58

Kamann S., et al., 2016, A&A, 588, A149

Kamann S., et al., 2018, MNRAS, 473, 5591

Kargaltsev O. Y., Chen S., Hare J., Pavlov G. G., Posselt B., Yang H., 2023, Hunting for IMBHs in the Omega Centauri Globular Cluster, JWST Proposal. Cycle 2, ID. #4343

Kerr R. P., 1963, Phys. Rev. Lett., 11, 237

King I., 1962, AJ, 67, 471

Kızıltan B., Baumgardt H., Loeb A., 2017, Nature, 542, 203

Klessen R. S., Glover S. C. O., 2023, ARA&A, 61, 65

Kollmeier J. A., et al., 2017, arXiv e-prints, p. arXiv:1711.03234

Konidaris N. P., et al., 2020, in Society of Photo-Optical Instrumentation Engineers (SPIE) Conference Series. p. 1144718, doi:10.1117/12.2557565

Kormendy J., Gebhardt K., 2001, in Wheeler J. C., Martel H., eds, American Institute of Physics Conference Series Vol. 586, 20th Texas Symposium on relativistic astrophysics. AIP, pp 363–381 (`arXiv:astro-ph/0105230`), doi:10.1063/1.1419581

Kormendy J., Ho L. C., 2013, ARA&A, 51, 511

Kormendy J., Richstone D., 1995, ARA&A, 33, 581

Kozhurina-Platais V., Anderson J., 2015, Standard Astrometric Catalog and Stability of WFC3/UVIS Geometric Distortion, Instrument Science Report WFC3 2015-02, 22 pages

Krabbe A., et al., 1995, ApJ, 447, L95

Kremer K., et al., 2020, ApJS, 247, 48

Kroupa P., 2001, MNRAS, 322, 231

Kruijssen J. M. D., 2025, arXiv e-prints, p. arXiv:2501.16438

Kruijssen J. M. D., Pfeffer J. L., Reina-Campos M., Crain R. A., Bastian N., 2019, MNRAS, 486, 3180

Krumholz M. R., McKee C. F., Bland-Hawthorn J., 2019, ARA&A, 57, 227

LIGO Scientific Collaboration et al., 2015, Classical and Quantum Gravity, 32, 074001

LSST Science Collaboration et al., 2009, arXiv e-prints, p. arXiv:0912.0201

Lacy J. H., Townes C. H., Geballe T. R., Hollenbach D. J., 1980, ApJ, 241, 132

Lada C. J., Lada E. A., 2003, ARA&A, 41, 57

Lam C. Y., et al., 2022, ApJ, 933, L23

Lanzoni B., et al., 2013, ApJ, 769, 107

Laporte C. F. P., Johnston K. V., Gómez F. A., Garavito-Camargo N., Besla G., 2018, MNRAS, 481, 286

Larkin J., et al., 2006, in McLean I. S., Iye M., eds, Society of Photo-Optical Instrumentation Engineers (SPIE) Conference Series Vol. 6269, Ground-based and Airborne Instrumentation for Astronomy. p. 62691A, doi:10.1117/12.672061

Leaman R., VandenBerg D. A., Mendel J. T., 2013, MNRAS, 436, 122

Lee Y. W., Joo J. M., Sohn Y. J., Rey S. C., Lee H. C., Walker A. R., 1999, Nature, 402, 55

Lenzen R., et al., 2003, in Iye M., Moorwood A. F. M., eds, Society of Photo-Optical Instrumentation Engineers (SPIE) Conference Series Vol. 4841, Instrument Design and Performance for Optical/Infrared Ground-based Telescopes. pp 944–952, doi:10.1117/12.460044

Leschinski K., Buddelmeijer H., Czoske O., Verdugo M., Verdoes-Kleijn G., Zeilinger W., 2020, in Guzman J. C., Ibsen J., eds, Society of Photo-Optical Instrumentation Engineers (SPIE) Conference Series Vol. 11452, Software and Cyberinfrastructure for Astronomy VI. p. 114521Z (`arXiv:2109.13577`), doi:10.1117/12.2559784

Libralato M., et al., 2018a, ApJ, 854, 45

Libralato M., et al., 2018b, ApJ, 861, 99

Libralato M., et al., 2022, ApJ, 934, 150

Limberg G., 2024, ApJ, 977, L2

Limberg G., Souza S. O., Pérez-Villegas A., Rossi S., Perottoni H. D., Santucci R. M., 2022, ApJ, 935, 109

Lindegren L., et al., 2021, A&A, 649, A2

Liu H.-Y., Yuan W., Dong X.-B., Zhou H., Liu W.-J., 2018, ApJS, 235, 40

Loeb A., Rasio F. A., 1994, ApJ, 432, 52

Longmore S. N., et al., 2014, in Beuther H., Klessen R. S., Dullemond C. P., Henning T., eds, Protostars and Planets VI. pp 291–314 (`arXiv:1401.4175`), doi:10.2458/azu_uapress_9780816531240-ch013

Loose H. H., Kruegel E., Tutukov A., 1982, A&A, 105, 342

Lützgendorf N., Kissler-Patig M., Noyola E., Jalali B., de Zeeuw P. T., Gebhardt K., Baumgardt H., 2011, A&A, 533, A36

Lützgendorf N., et al., 2013, A&A, 552, A49

Lützgendorf N., Gebhardt K., Baumgardt H., Noyola E., Neumayer N., Kissler-Patig M., de Zeeuw T., 2015, A&A, 581, A1

Lynden-Bell D., 1969, Nature, 223, 690

Lynden-Bell D., Wood R., 1968, MNRAS, 138, 495

Maccarone T. J., 2004, MNRAS, 351, 1049

Maccarone T. J., 2005, MNRAS, 360, L30

Maccarone T. J., Servillat M., 2008, MNRAS, 389, 379

Madau P., Dickinson M., 2014, ARA&A, 52, 415

Madau P., Rees M. J., 2001, ApJ, 551, L27

Magorrian J., et al., 1998, AJ, 115, 2285

Maiolino R., et al., 2024, Nature, 627, 59

Majewski S. R., Nidever D. L., Smith V. V., Damke G. J., Kunkel W. E., Patterson R. J., Bizyaev D., García Pérez A. E., 2012, ApJ, 747, L37

Majewski S. R., et al., 2017, AJ, 154, 94

Malhan K., 2022, ApJ, 930, L9

Malhan K., et al., 2022, ApJ, 926, 107

Mann C. R., et al., 2019, ApJ, 875, 1

Mapelli M., 2021, in Bambi C., Katsanevas S., Kokkotas K. D., eds, , Handbook of Gravitational Wave Astronomy. p. 16, doi:10.1007/978-981-15-4702-7_16-1

Mapelli M., Bouffanais Y., Santoliquido F., Arca Sedda M., Artale M. C., 2022, MNRAS, 511, 5797

Marín-Franch A., et al., 2009, ApJ, 694, 1498

Marín Pina D., Rastello S., Gieles M., Kremer K., Fitzgerald L., Rando Forastier B., 2024, A&A, 688, L2

Marino A. F., et al., 2011, ApJ, 731, 64

Marino A. F., et al., 2012, ApJ, 746, 14

Marks M., Kroupa P., Dabringhausen J., 2022, A&A, 659, A96

Massari D., Koppelman H. H., Helmi A., 2019, A&A, 630, L4

Matthews K., Ghez A. M., Weinberger A. J., Neugebauer G., 1996, PASP, 108, 615

Mayer L., Moore B., Quinn T., Governato F., Stadel J., 2002, MNRAS, 336, 119

Mayor M., et al., 1997, AJ, 114, 1087

McGinn M. T., Sellgren K., Becklin E. E., Hall D. N. B., 1989, ApJ, 338, 824

McLaughlin D. E., Anderson J., Meylan G., Gebhardt K., Pryor C., Minniti D., Phinney S., 2006, ApJS, 166, 249

McLean I. S., et al., 1998, in Fowler A. M., ed., Society of Photo-Optical Instrumentation Engineers (SPIE) Conference Series Vol. 3354, Infrared Astronomical Instrumentation. pp 566–578, doi:10.1117/12.317283

Merloni A., Heinz S., di Matteo T., 2003, MNRAS, 345, 1057

Merritt D., Meylan G., Mayor M., 1997, AJ, 114, 1074

Meylan G., Mayor M., 1986, A&A, 166, 122

Michell J., 1784, Philosophical Transactions of the Royal Society of London Series I, 74, 35

Miller M. C., Hamilton D. P., 2002, MNRAS, 330, 232

Miller-Jones J. C. A., et al., 2012, ApJ, 755, L1

Miller-Jones J. C. A., et al., 2021, Science, 371, 1046

Miller B. P., Gallo E., Greene J. E., Kelly B. C., Treu T., Woo J.-H., Baldassare V., 2015, ApJ, 799, 98

Milone A. P., et al., 2017a, MNRAS, 464, 3636

Milone A. P., et al., 2017b, MNRAS, 469, 800

Milone A. P., et al., 2018, MNRAS, 481, 5098

Minniti D., et al., 2011, A&A, 527, A81

Minniti D., et al., 2017, ApJ, 849, L24

Mockler B., Guillochon J., Ramirez-Ruiz E., 2019, ApJ, 872, 151

Morokuma T., et al., 2016, PASJ, 68, 40

Müller-Horn J., Göttgens F., Dreizler S., Kamann S., Martens S., Saracino S., Ye C. S., 2025, A&A, 693, A161

Murray C. A., Candy M. P., Jones D. H. P., 1965, Royal Greenwich Observatory Bulletins, 100, 81

Myeong G. C., Vasiliev E., Iorio G., Evans N. W., Belokurov V., 2019, MNRAS, 488, 1235

Neumayer N., Walcher C. J., 2012, Advances in Astronomy, 2012, 709038

Neumayer N., Seth A., Böker T., 2020, A&A Rev., 28, 4

Newman E. T., Couch E., Chinnapared K., Exton A., Prakash A., Torrence R., 1965, Journal of Mathematical Physics, 6, 918

Nguyen D. D., et al., 2017, ApJ, 836, 237

Nguyen D. D., et al., 2018, ApJ, 858, 118

Nguyen D. D., et al., 2019, ApJ, 872, 104

Nitadori K., Aarseth S. J., 2012, MNRAS, 424, 545

Nitschai M. S., et al., 2023, ApJ, 958, 8

Nitschai M. S., et al., 2024, ApJ, 970, 152

Noyola E., Gebhardt K., Bergmann M., 2008, ApJ, 676, 1008

Noyola E., Gebhardt K., Kissler-Patig M., Lützgendorf N., Jalali B., de Zeeuw P. T., Baumgardt H., 2010, ApJ, 719, L60

Nyland K., Marvil J., Wrobel J. M., Young L. M., Zauderer B. A., 2012, ApJ, 753, 103

Nyland K., et al., 2017, ApJ, 845, 50

Odenkirchen M., et al., 2003, AJ, 126, 2385

Olejak A., Belczynski K., Bulik T., Sobolewska M., 2020, A&A, 638, A94

Ostrov P., Geisler D., Forte J. C., 1993, AJ, 105, 1762

Paduano A., et al., 2024, ApJ, 961, 54

Pagnini G., et al., 2024, arXiv e-prints, p. arXiv:2410.22479

Pancino E., Ferraro F. R., Bellazzini M., Piotto G., Zoccali M., 2000, ApJ, 534, L83

Pancino E., Seleznev A., Ferraro F. R., Bellazzini M., Piotto G., 2003, MNRAS, 345, 683

Parks R. E., Kuhn W. P., 2005, in Hatheway A. E., ed., Society of Photo-Optical Instrumentation Engineers (SPIE) Conference Series Vol. 5877, Optomechanics 2005. pp 102–116, doi:10.1117/12.618165

Pattabiraman B., Umbreit S., Liao W.-k., Choudhary A., Kalogera V., Memik G., Rasio F. A., 2013, ApJS, 204, 15

Pavlík V., Vesperini E., 2021, MNRAS, 504, L12

Pavlík V., Vesperini E., 2022, MNRAS, 509, 3815

Pavlík V., Heggie D. C., Varri A. L., Vesperini E., 2024, A&A, 689, A313

Peñarrubia J., Walker M. G., Gilmore G., 2009, MNRAS, 399, 1275

Pechetti R., et al., 2022, ApJ, 924, 48

Pechetti R., et al., 2024, MNRAS, 528, 4941

Peebles P. J. E., 1972, ApJ, 178, 371

Perera B. B. P., et al., 2017, MNRAS, 468, 2114

Perez F., Granger B. E., 2007, Computing in Science and Engineering, 9, 21

Perruchot S., et al., 2018, in Evans C. J., Simard L., Takami H., eds, Society of Photo-Optical Instrumentation Engineers (SPIE) Conference Series Vol. 10702, Ground-based and Airborne Instrumentation for Astronomy VII. p. 107027K, doi:10.1117/12.2311996

Perryman M. A. C., et al., 1997, A&A, 323, L49

Peterson B. M., 2014, Space Sci. Rev., 183, 253

Pfeffer J., Baumgardt H., 2013, MNRAS, 433, 1997

Pfeffer J., Griffen B. F., Baumgardt H., Hilker M., 2014, MNRAS, 444, 3670

Pfeffer J., Lardo C., Bastian N., Saracino S., Kamann S., 2021, MNRAS, 500, 2514

Platais I., et al., 2023, arXiv e-prints, p. arXiv:2312.16186

Platais I., et al., 2024, ApJ, 963, 60

Plotkin R. M., Markoff S., Kelly B. C., Körding E., Anderson S. F., 2012, MNRAS, 419, 267

Pomeroy R. T., Norris M. A., 2024, MNRAS, 530, 3043

Pooley D., Rappaport S., 2006, ApJ, 644, L45

Portegies Zwart S. F., McMillan S. L. W., 2002, ApJ, 576, 899

Portegies Zwart S. F., Baumgardt H., Hut P., Makino J., McMillan S. L. W., 2004, Nature, 428, 724

Portegies Zwart S. F., McMillan S. L. W., Gieles M., 2010, ARA&A, 48, 431

Poznanski D., Prochaska J. X., Bloom J. S., 2012, MNRAS, 426, 1465

Pryor C., Meylan G., 1993, in Djorgovski S. G., Meylan G., eds, Astronomical Society of the Pacific Conference Series Vol. 50, Structure and Dynamics of Globular Clusters. p. 357

Punturo M., et al., 2010, Classical and Quantum Gravity, 27, 194002

Rantala A., Naab T., Rizzuto F. P., Mannerkoski M., Partmann C., Lautenschütz K., 2023, MNRAS, 522, 5180

Rantala A., Naab T., Lahén N., 2024, MNRAS, 531, 3770

Rees M. J., 1984, ARA&A, 22, 471

Rees M. J., 1988, Nature, 333, 523

Reijns R. A., Seitzer P., Arnold R., Freeman K. C., Ingerson T., van den Bosch R. C. E., van de Ven G., de Zeeuw P. T., 2006, A&A, 445, 503

Reines A. E., 2022, Nature Astronomy, 6, 26

Reines A. E., Greene J. E., Geha M., 2013, ApJ, 775, 116

Remillard R. A., McClintock J. E., 2006, ARA&A, 44, 49

Rieke M. J., et al., 2023, PASP, 135, 028001

Rigaut F., et al., 2021, The Messenger, 185, 7

Robin A. C., Reylé C., Derrière S., Picaud S., 2003, A&A, 409, 523

Rodriguez C. L., et al., 2022, ApJS, 258, 22

Rousset G., et al., 2003, in Wizinowich P. L., Bonaccini D., eds, Society of Photo-Optical Instrumentation Engineers (SPIE) Conference Series Vol. 4839, Adaptive Optical System Technologies II. pp 140–149, doi:10.1117/12.459332

Sahu K. C., et al., 2022, ApJ, 933, 83

Salpeter E. E., 1964, ApJ, 140, 796

Sargent W. L. W., Young P. J., Boksenberg A., Shortridge K., Lynds C. R., Hartwick F. D. A., 1978, ApJ, 221, 731

Scalco M., et al., 2021, MNRAS, 505, 3549

Scalco M., Bedin L., Vesperini E., 2024, A&A, 688, A180

Schmidt M., 1963, Nature, 197, 1040

Schödel R., et al., 2002, Nature, 419, 694

Schwarzschild K., 1916, Sitzungsberichte der Königlich Preussischen Akademie der Wissenschaften, pp 189–196

Schwarzschild M., 1979, ApJ, 232, 236

Searle L., Zinn R., 1978, ApJ, 225, 357

Seth A., Agüeros M., Lee D., Basu-Zych A., 2008, ApJ, 678, 116

Seth A. C., et al., 2014, Nature, 513, 398

Seth A. C., et al., 2024, Weighing the Intermediate Mass Black Hole in Omega Centauri, JWST Proposal. Cycle 3, ID. #5137

Skrutskie M. F., et al., 2006, AJ, 131, 1163

Smith P. J., Hénault-Brunet V., Dickson N., Gieles M., Baumgardt H., 2024, ApJ, 975, 268

Sollima A., Ferraro F. R., Bellazzini M., Origlia L., Straniero O., Pancino E., 2007, ApJ, 654, 915

Sollima A., Baumgardt H., Hilker M., 2019, MNRAS, 485, 1460

Soltis J., Casertano S., Riess A. G., 2021, ApJ, 908, L5

Spera M., Mapelli M., 2017, MNRAS, 470, 4739

Spitzer Jr. L., 1969, ApJ, 158, L139

Spurzem R., Kamlah A., 2023, Living Reviews in Computational Astrophysics, 9, 3

Stasińska G., Cid Fernandes R., Mateus A., Sodré L., Asari N. V., 2006, MNRAS, 371, 972

Stone N. C., Küpper A. H. W., Ostriker J. P., 2017, MNRAS, 467, 4180

Strader J., Chomiuk L., Maccarone T. J., Miller-Jones J. C. A., Seth A. C., Heinke C. O., Sivakoff G. R., 2012, ApJ, 750, L27

Suntzeff N. B., Kraft R. P., 1996, AJ, 111, 1913

Tailo M., Di Criscienzo M., D'Antona F., Caloi V., Ventura P., 2016, MNRAS, 457, 4525

Taylor J. H., Weisberg J. M., 1982, ApJ, 253, 908

Ting Y.-S., Rix H.-W., Conroy C., Ho A. Y. Q., Lin J., 2017, ApJ, 849, L9

Tremaine S. D., Ostriker J. P., Spitzer Jr. L., 1975, ApJ, 196, 407

Tremou E., et al., 2018, ApJ, 862, 16

Trenti M., van der Marel R., 2013, MNRAS, 435, 3272

Trump J. R., et al., 2015, ApJ, 811, 26

Ulvestad J. S., Greene J. E., Ho L. C., 2007, ApJ, 661, L151

Vasiliev E., Baumgardt H., 2021, MNRAS, 505, 5978

Villanova S., et al., 2007, ApJ, 663, 296

Villanova S., Geisler D., Gratton R. G., Cassisi S., 2014, ApJ, 791, 107

Virtanen P., et al., 2020, Nature Methods, 17, 261

Vitral E., Libralato M., Kremer K., Mamon G. A., Bellini A., Bedin L. R., Anderson J., 2023, MNRAS, 522, 5740

Walcher C. J., Böker T., Charlot S., Ho L. C., Rix H. W., Rossa J., Shields J. C., van der Marel R. P., 2006, ApJ, 649, 692

Wang L., Spurzem R., Aarseth S., Nitadori K., Berczik P., Kouwenhoven M. B. N., Naab T., 2015, MNRAS, 450, 4070

Wang L., Iwasawa M., Nitadori K., Makino J., 2020, MNRAS, 497, 536

Wang F., et al., 2021, ApJ, 907, L1

Wang Z., Hayden M. R., Sharma S., Xiang M., Ting Y.-S., Bland-Hawthorn J., Chen B., 2022, MNRAS, 514, 1034

Watkins L. L., van de Ven G., den Brok M., van den Bosch R. C. E., 2013, MNRAS, 436, 2598

Watkins L. L., van der Marel R. P., Bellini A., Anderson J., 2015a, ApJ, 803, 29

Watkins L. L., van der Marel R. P., Bellini A., Anderson J., 2015b, ApJ, 812, 149

Watkins L. L., van der Marel R. P., Libralato M., Bellini A., Anderson J., Alfaro-Cuello M., 2022, ApJ, 936, 154

Weatherford N. C., Chatterjee S., Rodriguez C. L., Rasio F. A., 2018, ApJ, 864, 13

Weatherford N. C., Kıroğlu F., Fragione G., Chatterjee S., Kremer K., Rasio F. A., 2023, ApJ, 946, 104

Webster B. L., Murdin P., 1972, Nature, 235, 37

Weilbacher P. M., et al., 2020, A&A, 641, A28

Whitmore B. C., Zhang Q., Leitherer C., Fall S. M., Schweizer F., Miller B. W., 1999, AJ, 118, 1551

Wiktorowicz G., Belczynski K., Maccarone T., 2014, in de Grijs R., ed., Binary Systems, their Evolution and Environments. p. 37 (`arXiv:1312.5924`), doi:10.48550/arXiv.1312.5924

Wizinowich P. L., et al., 2006, PASP, 118, 297

Wollman E. R., Geballe T. R., Lacy J. H., Townes C. H., Rank D. M., 1977, ApJ, 218, L103

Woolley R. V. D. R., 1966, Royal Observatory Annals, 2, 1

Woosley S. E., 2017, ApJ, 836, 244

Wragg F., et al., 2024, MNRAS, 535, 781

Xiang M., et al., 2019, ApJS, 245, 34

Young P. J., Westphal J. A., Kristian J., Wilson C. P., Landauer F. P., 1978, ApJ, 221, 721

Zaris J., Veske D., Samsing J., Márka Z., Bartos I., Márka S., 2020, ApJ, 894, L9

Zel'dovich Y. B., 1964, Soviet Physics Doklady, 9, 195

Zepf S. E., Ashman K. M., 1993, MNRAS, 264, 611

Zocchi A., Gieles M., Hénault-Brunet V., 2017, MNRAS, 468, 4429

Zocchi A., Gieles M., Hénault-Brunet V., 2019, MNRAS, 482, 4713

Zonca A., Singer L., Lenz D., Reinecke M., Rosset C., Hivon E., Gorski K., 2019, Journal of Open Source Software, 4, 1298

Zubovas K., 2019, MNRAS, 483, 1957

den Brok M., et al., 2015, ApJ, 809, 101

van Leeuwen F., Le Poole R. S., 2002, in van Leeuwen F., Hughes J. D., Piotto G., eds, Astronomical Society of the Pacific Conference Series Vol. 265, Omega Centauri, A Unique Window into Astrophysics. p. 41

van Leeuwen F., Le Poole R. S., Reijns R. A., Freeman K. C., de Zeeuw P. T., 2000a, A&A, 360, 472

van Leeuwen F., Le Poole R. S., Reijns R. A., Freeman K. C., de Zeeuw P. T., 2000b, A&A, 360, 472

van Loon J. T., Smith K. T., McDonald I., Sarre P. J., Fossey S. J., Sharp R. G., 2009, MNRAS, 399, 195

van de Ven G., van den Bosch R. C. E., Verolme E. K., de Zeeuw P. T., 2006, A&A, 445, 513

van der Marel R. P., Anderson J., 2010, ApJ, 710, 1063

van der Marel R. P., Kallivayalil N., 2014, ApJ, 781, 121

Hubble Space Telescope composite image of the central region of ω Centauri

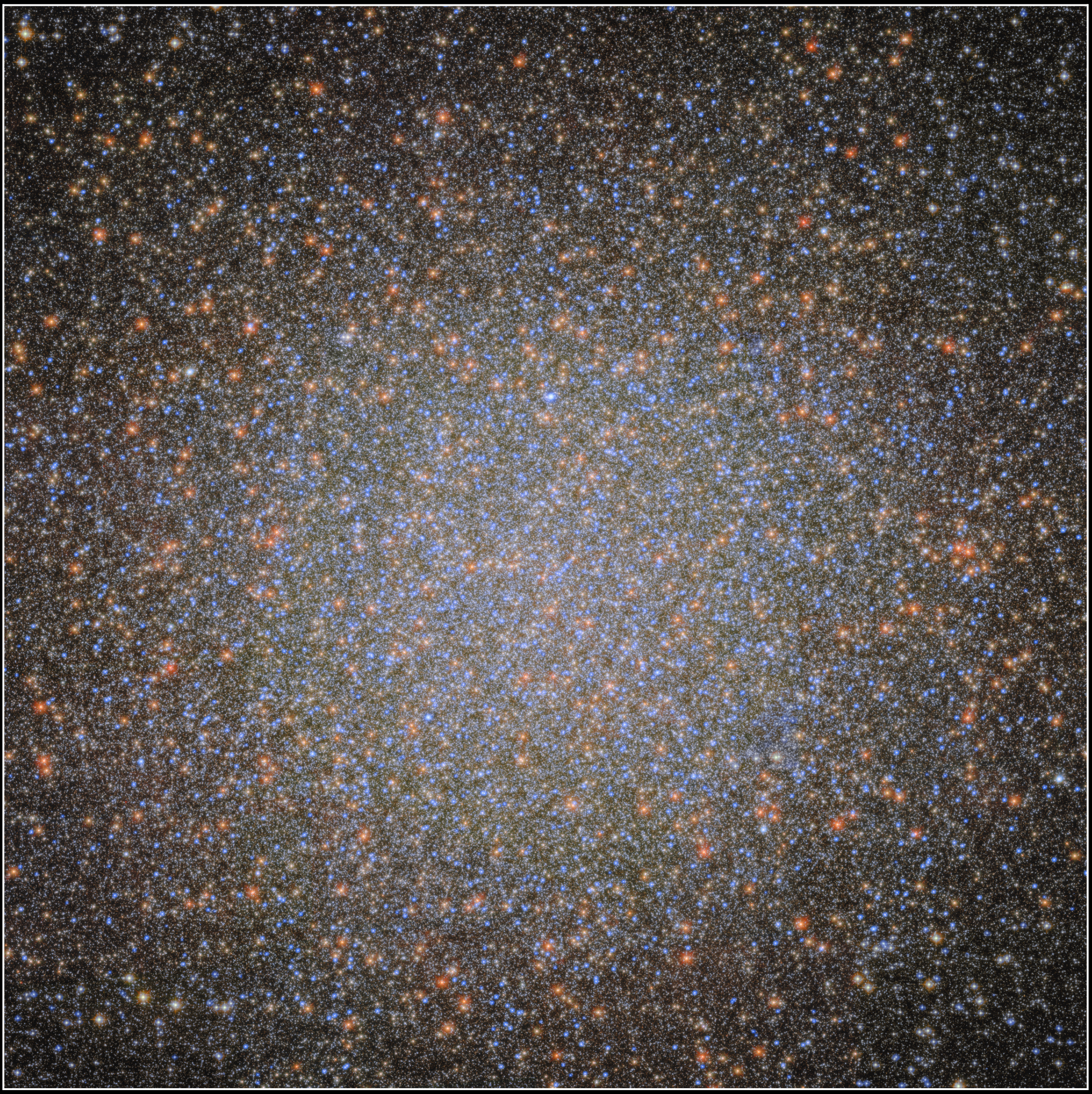

Image credit: ESA/Hubble & NASA, M. Häberle (MPIA)

ω Centauri is a massive globular cluster visible from the Southern Hemisphere.
Its complex stellar populations and its internal dynamic have puzzled astronomers for
decades and hold the key to understanding both its formation history and its mass distribution.

This thesis aims to improve our knowledge of ω Centauri's kinematics by combining
observations from several telescopes and using various techniques,
including photometry, astrometry, and spectroscopy.